
Adaptive image interrogation for PIV

– Application to compressible flows and interfaces –

Proefschrift

ter verkrijging van de graad doctor

aan de Technische Universiteit Delft,

op gezag van de Rector Magnificus Prof.ir. K.C.A.M. Luyben,

voorzitter van het College voor Promoties

in het openbaar te verdedigen op 18 februari 2010 om 15.00 uur

door Raf THEUNISSEN

Ingenieur Luchtvaart en Ruimtevaart

geboren te Genk, België

Dit proefschrift is goedgekeurd door de promotor:

Prof.dr. F. Scarano

Samenstelling promotiecommissie:

Rector Magnificus,

Prof.dr. F. Scarano, Technische Universiteit Delft, promotor

Prof. M.L. Riethmuller, von Karman Institute for Fluid Dynamics België

Prof.dr.ir. A. Hubin, Vrije Universiteit Brussel

Prof.dr.ir. J. Westerweel, Technische Universiteit Delft

Prof.dr.ir. P.G. Bakker, Technische Universiteit Delft

B. Wieneke, LaVision GmbH Duitsland

Dr. T. Astarita, Università di Napoli 'Federico II' Italië

Prof. M.L. Riethmuller heeft als begeleider in belangrijke mate aan de totstandkoming van het proefschrift bijgedragen.

ISBN 978-2-87516-000-3



Vrije Universiteit Brussel

Faculteit Ingenieurswetenschappen

Vakgroep Materialen en Chemie

Research Group Electrochemical and Surface Engineering

Adaptive image interrogation for PIV

- Application to compressible flows and interfaces -

ir. Raf Theunissen

Proefschrift ingediend tot het behalen van de graad van

Doctor in de Ingenieurswetenschappen

Dit proefschrift is goedgekeurd door de promotoren:

Prof.dr. Fulvio. Scarano

Prof.dr.ir. Annick Hubin

Academia 2009-2010

Doctoral Committee:

Prof.dr.ir. Philippe Lataire, Vrije Universiteit Brussel, voorzitter

Prof.dr.ir. Rik Pintelon, Vrije Universiteit Brussel, vice-voorzitter

Prof.dr. Fulvio Scarano, Technische Universiteit Delft, promotor

Prof.dr.ir. Annick Hubin, Vrije Universiteit Brussel, promotor

Prof.dr.ir. Jeroen van Beeck, von Karman Institute, co-promotor

Prof.dr. Steve Vanlanduit, Vrije Universiteit Brussel

Prof.dr. Christophe Schram, von Karman Institute

Dr. Bertrand Lecordier, UMR 6614 Complexe de Recherche

Interprofessionnel en Aérothermochimie

Dr.ir. Sam Dehaeck, Université Libre de Bruxelles

Prof. M.L. Riethmuller (von Karman Institute for Fluid Dynamics) heeft als begeleider in belangrijke mate aan de totstandkoming van het proefschrift bijgedragen.

von Karman Institute for Fluid Dynamics
Environmental and Applied Fluid Dynamics Department

Technische Universiteit Delft
Aerospace Engineering

Vrije Universiteit Brussel
Faculteit Ingenieurswetenschappen
Vakgroep: Materialen en Chemie

Adaptive image interrogation for PIV

Application to compressible flows and interfaces

Cover art: The cover image depicts a PIV snapshot of the flow around a sphere at Mach 6 (J. Haertig *et al.* 2005) and the different stages of the iterative adaptive image interrogation procedure. Clockwise are displayed the detected particle images (undersampled by a factor 2 for clarity) and the standard deviation in measured velocity. These two quantities are combined into a single probability distribution function to assign an adequate sampling mesh (i.e. sampling locations). Interfaces and regions with strong velocity gradients (e.g. shocks) are attributed a higher number of smaller interrogation windows, whereas regions with large flow scales and poor seeding density correspond to a low sampling density. Correlation windows are rotated and stretched parallel to detected interfaces to further increase spatial resolution. The final image depicts the resulting streamline pattern extracted at random locations.

Thesis presented by Raf THEUNISSEN, *M.Sc. in Aerospace Engineering*, in order to obtain the degree of “Doctor”, Technische Universiteit Delft, The Netherlands and Vrije Universiteit Brussel, Belgium, February 2010.

This doctoral thesis is published in the context of a partnership agreement governing the joint supervision and awarding of a doctorate diploma.

Promoters: Prof. Dr. F. Scarano (Technische Universiteit Delft, TU Delft, The Netherlands) and Prof. Dr. Ir. A. Hubin (Vrije Universiteit Brussel, VUB, Belgium)

Supervisors: Prof. M.L. Riethmuller (von Karman Institute for Fluid Dynamics VKI, Belgium)

A selection of doctoral theses published by the von Karman Institute:

Modeling and simulation of dispersed two-phase flow transport phenomena in electrochemical processes

(Th. Nierhaus, Université Libre de Bruxelles and RWTH Aachen, October 2009)

Tunable diode laser absorption spectroscopy characterization of impulse hypervelocity CO₂ flows

(J. Meyers, Université Libre de Bruxelles, September 2009)

Physical models for nonequilibrium plasma flow simulations at high speed re-entry conditions

(M. Panesi, Università degli Studi di Pisa, Italy, 2009)

Aero-thermal impact of purge flow and rotor platform cooling on a transonic HP turbine stage - experimental, numerical and correlation based study

(M. Pau, Università degli Studi di Cagliari, Italy February 2009)

A component environment for high-performance scientific computing design and implementation

(T. Quintino, Katholieke Universiteit Leuven, Belgium, December 2008)

An object oriented and high performance platform for aerothermodynamics simulation

(A. Lani, Université Libre de Bruxelles, Belgium, December 2008)

Efficiency of a HP turbine tested in a compression tube facility

(T. Yasa, Université Catholique de Louvain, Belgium, April 2008)

A full catalogue of publications is available from the library

Adaptive image interrogation for PIV - Application to compressible flows and interfaces

Keywords: PIV, image processing, adaptive interrogation, spatial resolution, aircraft wake vortex, cylinder, shock-wave-boundary layer interaction, interface treatment, Fast Fourier transforms, correlations, vector relocation, robustness, compression ramp, boundary layer, statistical adaptivity, non-isotropic correlation, window overlap ratio, transonic airfoil wake, data analysis, backward-facing step, hypersonic sphere, over-expanded supersonic jet, statistical error, integral time-scale, confidence level, dependent circular block bootstrap

© 2010 by R. THEUNISSEN

D/2010/0238/562, J.P.A.J. van Beeck, Editor-in-Chief

Published by the von Karman Institute for Fluid Dynamics with permission.

All rights reserved. Permission to use a maximum of two figures or tables and brief excerpts in scientific and educational works is hereby granted provided the source is acknowledged. This consent does not extend to other kinds of copying and reproduction, for which permission requests should be addressed to the Director of the von Karman Institute.

ISBN 978-2-87516-000-3

*To my amazing daughter Elissa,
my wonderful wife Silvana,
and my fantastic parents Grietje and Renier.*

A word of thanks...

I cannot believe it; I am actually writing the last part of the thesis; 5 years of hard work have come to an end. And closing the door behind me as a doctoral student, I open with great anticipation the very welcomed door as a husband and father... starting a new life in Switzerland...and working on gas turbine performances. This thesis hasn't been easy to accomplish but I could always fall back on the support of some wonderful people I would like to thank in the following lines.

I would like to thank Prof. Fulvio Scarano. Fulvio, not only have you been an amazing supervisor with great ideas and a critical eye, you went further than many supervisors would, passing many programming (nightly) sessions side by side nourished with your pasta (also thank you Ines). You have become a personal friend with a listening ear and good advice. Prof. Michel Riethmuller I am indebted for allowing me to perform the PhD at the von Karman Institute. By encouraging me to participate at several conferences and workshops I have been able to build up quite some self-confidence.

Special thanks go to Alberto Di Sante, who introduced me the problem discussed in Chapter 7 and with whom I had the pleasure to publish two journal articles. Moreover, Alberto helped me to find the job in Switzerland and I firmly believe he is the only person who immediately knows when I quote from Top Gun.

I would further like to acknowledge Prof. Jeroen van Beeck for all his efforts in arranging the administrative difficulties related to the bi-promotion and Christelle Debeer for coping with all the issues related to the printing of this thesis.

It is difficult for anybody not being part of the scientific world, to understand the dedication required to bring a PhD to a successful ending. Nights, days, weeks (including weekends), months are often sacrificed, only to find out that a promising idea does not work. In those depressing moments, the loving support of close friends or family may provide the necessary strength to keep on going. Especially when such blows have to be endured at high frequency of occurrence. In my case I count myself fortunate to have been able to count on the love of my (now) wife Silvana and my parents. Although my name stands alone as author of this manuscript, they really have been co-authors. *Merci princesse pour ton support. Je sais que ce n'était pas toujours facile. Certainement pas pendant la grossesse, mais finalement on l'a fini avec succès et une super belle petite princesse. Je t'aimerai pour toujours. Liefste oudertjes, het is eindelijk gedaan. Na vijf jaar hard werken hebben we eindelijk het doctoraatsdiploma op zak. Hartelijk bedankt voor al jullie steun en liefde al die vorige, huidige en toekomstige jaren.*

It looks easy enough; saying “thank you”, but reflecting back I have met so many special people at the VKI and I’m too afraid I would forget someone if I started to mention individual names. At this point I therefore cannot resist to refer to a very nice phrase from the all-time epic “The Lord of the Rings”; *I didn't know half of them half as well as I should like, and I liked less than half of them half as well as they deserved.* All of you who are special to me and close to my heart, THANK YOU for all your services (a big thanks to the VKI library, press, reception, technicians and secretary) and the great moments (this part refers mostly to VKI fellow students) we had in climbing, going out, having a drink, tumbling in cars, sharing living spaces, talking, listening etc.

The suitability of the developed PIV image interrogation procedure has been argued mostly by means of image recordings from experiments performed by people other than myself. I would like to gratefully acknowledge the following persons; Vincent Ruwet (cylinder, alveoli), Ray Humble (shockwave boundary layer interaction), Airbus Bremen (aircraft wing vortex), Gerrit Elsinga (boundary layer), Ferry Schrijer (hypersonic double ramp), Annand Ashok (airfoil wake), Damiano Caimano (backward facing step), Jacques Haertig (hypersonic sphere), Anna Jerónimo (over-expanded supersonic jet), Alberto Di Sante (time-resolved diverging channel), Catherine Baivier (large scale windtunnel), Nicolas Buchmann (alveolated tube) and Josu Beloki Perurena (liquid cross-flow).

This work has been supported by the Instituut voor de aanmoediging van innovatie door Wetenschap & Technologie in Vlaanderen (IWT, SBO project nr. 040092).

CONTENTS

Introduction	1
Background.....	1
Operational principle of PIV.....	2
PIV technique development.....	3
PIV algorithm evolution	4
Current limitations	5
Motivation of present work	6
Objectives	8
Thesis outline	9
1 Particle Image Velocimetry	11
1.1 Introduction	13
1.2 Particle tracers	14
1.2.1 Tracking characteristics of particles	14
1.2.2 Illumination	14
1.2.3 Particle imaging	15
1.2.4 Image recording	17
1.3 Image velocimetry modes	18
1.4 Tracer motion evaluation	20
1.4.1 Particle tracking	20
1.4.2 Particle pattern tracking	21
1.5 Image pre-processing	26
1.6 Conclusions	27
2 PIV Image Evaluation	29
2.1 Introduction	30
2.2 Single pass cross-correlation analysis	31

2.2.1	Basic rules for motion analysis	32
2.2.2	Vector validation	35
2.3	Iterative interrogation methods	36
2.3.1	Multi-grid analysis with discrete window offset	36
2.3.2	Multi-grid analysis with window deformation	38
2.3.3	Implementation	40
2.4	Advanced iterative interrogation methods	44
2.4.1	Predictor filtering	44
2.4.2	Performance assessment	46
2.5	Typical PIV experiment: Cylinder wake	49
2.5.1	Background	49
2.5.2	Experimental facility	49
2.5.3	Image evaluation	50
2.6	Conclusions	53
3	Adaptive sampling and windowing interrogation in PIV	55
3.1	Introduction.....	57
3.2	Problem statement.....	58
3.3	Proposed methodology	61
3.3.1	Signal adaptivity	62
3.3.2	Flow adaptivity	63
3.3.3	Combination of signal and flow adaptivity.....	64
3.4	Implementation	66
3.4.1	Signal quantization.....	66
3.4.2	Data interpolation.....	69
3.4.3	Data allocation	71
3.5	Interrogation methodology.....	73
3.6	Performance evaluation	75
3.6.1	Isotropic random fluctuations	75
3.6.2	Transport aircraft wake vortex.....	78
3.6.3	Shock-wave boundary layer interaction.....	81
3.6.4	Cylinder wake flow.....	85
3.7	Conclusions.....	87

4	Improvement of PIV image interrogation near stationary interfaces	89
4.1	Introduction.....	91
4.2	Problem statement.....	92
4.3	Numerical assessment.....	95
4.3.1	Image pre-processing.....	95
4.3.2	Adapted correlation schemes.....	97
4.3.3	Vector relocation.....	99
4.5	Symmetric-mask-exclusion direct cross-correlation implementation.....	101
4.6	Adaptive interrogation near interfaces.....	103
4.7	Experimental assessment.....	105
4.7.1	Subsonic turbulent boundary layer over a flat plate.....	105
4.7.2	Double compression ramp at Mach 7.....	111
4.8	Conclusions.....	114
5	Statistical adaptivity in PIV interrogation	117
5.1	Introduction.....	118
5.2	Proposed methodology.....	120
5.3	Implementation.....	123
5.3.1	Adaptive sampling and window sizing.....	123
5.3.2	Statistical validation.....	125
5.3.3	Non-isotropic correlation.....	126
5.3.4	Number of correlation windows.....	127
5.3.5	Adaptive image snapshot interrogation.....	129
5.4	Experimental application.....	130
5.4.1	Shock-wave boundary layer interaction.....	130
5.4.2	Transonic airfoil wake.....	138
5.5	Conclusions.....	142
6	Experimental assessment of adaptive PIV interrogation	143
6.1	Introduction.....	144
6.2	Hypersonic sphere.....	145
6.2.1	Background.....	145
6.2.2	Experimental facility.....	145
6.2.3	Image evaluation.....	146
6.2.4	Flow diagnostics.....	148

6.3	Backward facing step flow.....	150
6.3.1	Background.....	150
6.3.2	Experimental facility.....	151
6.3.3	Image evaluation.....	151
6.3.4	Flow diagnostics.....	154
6.4	Over-expanded supersonic jet.....	157
6.4.1	Background.....	157
6.4.2	Experimental facility.....	158
6.4.3	Image evaluation.....	159
6.4.4	Flow diagnostics.....	161
6.5	Discussion.....	165
6.6	Conclusions.....	167
7	Statistical analysis of PIV measurements	169
7.1	Introduction.....	170
7.2	Dependent circular block bootstrap.....	174
7.3	Dependent circular bootstrap implementation.....	175
7.4	Practical examples.....	177
7.4.1	Time-resolved PIV in a diverging channel flow.....	177
7.4.2	Classic PIV in a backward facing step flow.....	179
7.5	Conclusions.....	181
8	Summary and perspectives	183
8.1	Summary.....	183
8.2	Perspectives.....	185
8.2.1	PIV in the fast lane.....	185
8.2.2	An everlasting yearn for more spatial resolution.....	186
8.2.3	Extended adaptivity.....	187
8.2.4	Adaptivity philosophy in 3D.....	188
	References	191

A	Adaptive image evaluation: literature survey	205
A.1	Introduction.....	206
A.2	Signal quantization	206
A.2.1	Feature tracking	206
A.2.2	Image statistics.....	208
A.2.3	Particle image segmentation	209
A.3	Data interpolation	209
A.3.1	Adaptive Gaussian Windowing averaging (AGW).....	210
A.3.2	Polynomial fitting	210
A.3.3	Kriging interpolation.....	210
A.3.4	Natural Neighbor interpolation (NN).....	211
A.4	Post-processing: vorticity calculation	212
A.4.1	Differential schemes	212
A.4.2	Least-squares fitting.....	212
B	PIV resolution across normal shocks	215
B.1	Introduction.....	216
B.2	Tracer response	217
B.3	Image evaluation limits to PIV resolution	219
B.3.1	Model shock response for ideal tracers.....	219
B.3.2	Interrogation intrinsic shock response for ideal tracers	220
B.3.3	Model shock response for real tracers.....	221
B.4	Shock position retrieval	222
B.5	Conclusions.....	224
C	Robust image evaluation for sub-optimal PIV recordings	225
C.1	Introduction.....	225
C.2	Implementation	226
C.3	Experimental applications.....	227
C.3.1	Large scale wind tunnel	227
C.3.2	Alveolated bend	229
C.3.3	Liquid ejection in a hypersonic cross-flow	230
C.4	Adaptivity in robust image evaluation: application to an alveolated tube..	231
C.4.1	Background.....	231
C.4.2	Experimental facility.....	231

C.4.3 Image evaluation.....	232
C.4.4 Flow diagnostics	234
C.5 Conclusions.....	235
D Non-isotropic weighting functions in tomographic flow	237
D.1 Introduction.....	238
D.2 Non-isotropic weighting	238
D.3 Performance assessment	240
D.3.1 Synthetic flow field generation.....	240
D.3.2 Results.....	241
D.4 Conclusions and prospects.....	243
Nederlandstalige samenvatting	245
Curriculum Vitae	249

INTRODUCTION

Background

Powerful computers are nowadays able to make flow predictions based on the mathematical treatment of the fluid flow governing equations. Nevertheless, these computations explicitly or implicitly contain simplifications and assumptions and often lack sufficient validation. Experimental approaches on the other hand do not involve simulations but consist of in-situ sampling of Nature's arranged orchestration of physical phenomena.

Till the advent of laser in the 1960's, only probe-based measurement techniques such as pitot-tubes and hot-wires were available for an accurate velocity measurement of flows. The Laser Doppler Velocimeter (LDV) allowed for the first time to investigate by a non-intrusive procedure several types of flows and contributed to the development and verification of theories and models for the prediction and simulation of turbulence (Flack, 1975). Measurements were limited however to one specific spatial location at a time. The determination of the velocity field over an extended flow domain was therefore a time consuming and laborious process. Moreover, it prohibited the direct measurement of spatial velocity gradients, which are of importance in the characterization of turbulence. Not to mention the matter of experimental repeatability; repetition of the experiment while extracting flow information at different spatial locations was only feasible in applications involving steady flows. Unsteady flows on the other hand can only be characterized from a statistical point of view, most notably turbulent flows.



Fig. 1: Instability of smoke from a cigarette. The smoke rises vertically and smoothly for some distance (laminar flow) followed by transition into the turbulent regime due to growing undulations (taken from Van Dyke, 1988).

Flow visualization techniques such as smoke injection, hydrogen bubble wires and streak photography on the other hand, would allow at a glance to visualize and identify the large scale organization of complex flows which mostly undergo transition from laminar to turbulent regimes. A textbook example is the thermal convection of hot air upwards from a burning cigarette (Van Dyke, 1988) visualized by its tendrils of smoke (Fig. 1).

While visualization primarily allows qualitative analyses, quantitative data can be obtained through adequate processing of the recorded image sequences of the visible flow motion i.e. *image velocimetry*. Molecular diffusion in case of laminar flows or the more efficient mixing in case of turbulent flows smears out the distinct boundaries of the visualized coherent structures however, which can be clearly observed in Fig. 1. This smearing complicates the derivation of accurate velocity estimates in the image processing stage and can be circumvented by observing sharp, individual tracer images instead of coherent (smoke) patterns; hence the acronym *particle image velocimetry*.

Operational principle of PIV

The advent of Particle Image Velocimetry (PIV) was obtained by the combined application of a controlled illumination technique (pulsed light sheet) and a flow seeding method based on distinct particle tracers.

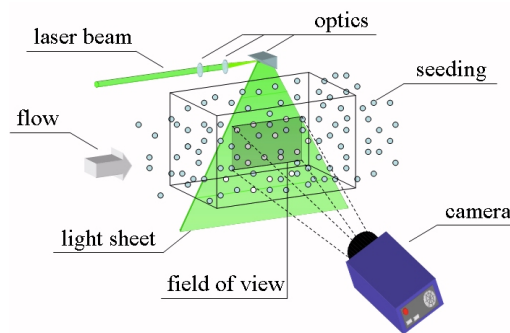


Fig. 2: Typical layout of single-camera image velocimetry.

A typical configuration of a PIV experiment is depicted in Fig. 2 and consists of the following;

1. to visualize the flow, small tracer particles are added which are assumed to ideally follow the fluid motion.
2. a pulsed light source provides illumination of the tracers twice. The separation time between pulses is set taking into account the fluid velocity and magnification factor of the imaging system.

3. cylindrical and spherical lenses shape the light beam into a thin, sheet-like region. The typical size[†] of the measurement domain ranges from $5 \times 5 \text{cm}^2$ to $50 \times 50 \text{cm}^2$.
4. the scattered light from the tracers is imaged through a lens and recorded by a CCD or CMOS sensor at two different time instants.
5. the digital recordings are divided into small interrogation areas (Fig. 3) where the particle displacement is estimated by means of spatial cross-correlation or other statistical operators.

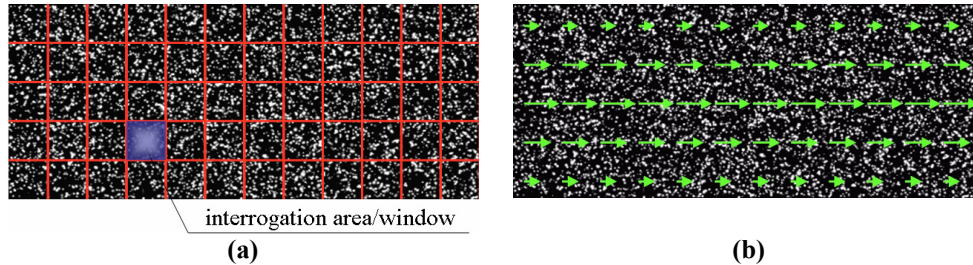


Fig. 3: (a) The image of the recorded light scattered by the tracer particles is divided into small sections called interrogation areas or interrogation windows (b) where the particle displacement is estimated.

PIV technique development

Particle Image Velocimetry experiments nowadays cover the breadth of fluid dynamics; from hypersonic flows (Schrijer *et al.*, 2006) to fundamental turbulence research (Poelma *et al.*, 2006) and artery flow in chicken embryos (Vennemann *et al.*, 2006). The technique's increase in maturity has been documented by hundreds of dedicated scientific papers (Adrian, 2005).

It's success must be ascribed to its non-intrusive character, the simplicity of its principle and the high amount of flow information relative to the short operation time. Additionally, with the advent of new technological advances, this laser-based measurement technique has grown exponentially over the last years in its domain of application. An example where hardware improvements have been beneficial is the case of PIV experiments applied to high speed flows. Powerful lasers now provide sufficient energy over short pulse durations to adequately illuminate the tracers while advanced digital cameras allow short time intervals between exposures. Such developments have made accurate image velocimetry measurements possible in high speed flows up to hypersonic regimes.

The majority of developments in the PIV technique took place in the last 20 to 30 years and were initiated by the Lecture Series organized at the von Karman Institute in 1988. Since, PIV embodies a collection of imaging methodologies, based on the original operational principle, but each aimed at extracting as much velocity related information

[†] Measurement domains below a square millimeter can be obtained, but not with the depicted PIV setup. This technique is commonly known as Micro-PIV (Kähler and Scholz, 2006).

as possible with high resolution. Existing techniques can be classified based on the optical imaging arrangement and targeted flow velocity components;

2D 2C: basic PIV configuration with a single camera (Fig. 2). Velocity components within the thin light plane are measured

2D 3C: two cameras record the scattered light within a thin light sheet from different observation angles (Fig. 4-a). This allows the extraction of the third velocity component (Gauthier and Riethmuller, 1988). This technique is referred nowadays to as Stereoscopic PIV (Prasad, 2000)

3D 2C: A different approach involves scanning, i.e. recording, multiple parallel illumination planes. Afterwards the out-of-plane flow motion is derived by interpolating the 2D velocity fields (Brücker, 1997). The third dimension may also refer to time. With lasers able to operate at high repetition frequencies and digital cameras capable of recording at high frame rates, two dimensional velocity fields are obtained which are resolved in time (Hain and Kähler, 2007).

3D 3C: Fig. 4-b illustrates the use of multiple cameras, which allows the three dimensional reconstruction of the intensity field within an illuminated volume rather than a plane (Elsinga *et al.*, 2008). Image processing then yields fully 3 dimensional velocity fields.

4D 3C: when the 3D 3C experimental setup is equipped with high frame grabbing frequency cameras, time-resolved, 3D velocity fields can be obtained.

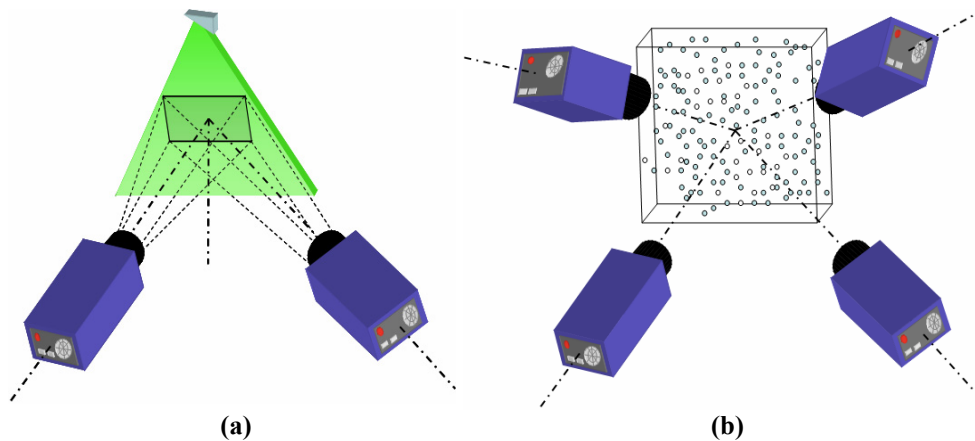


Fig. 4: Examples of camera arrangements for (a) stereo-PIV (2D 3C) and (b) tomographic PIV (3D 3C).

PIV algorithm evolution

In parallel to the evolution in PIV hardware (camera, laser, computing resource, etc.), PIV image evaluation algorithms have become continuously faster and more accurate. In the following, the development in PIV algorithm is briefly discussed with a slightly more elaborate discussion in Chapter 2. An extensive review of the different PIV image evaluation techniques can be found in Scarano (2002) and Willert (2009).

The most straightforward method of extracting tracer motion from a digital image pair was, and still is, cross-correlating common-sized image sections at coincident positions. Because the displacement estimates are calculated in a **single pass** (Willert and Gharib, 1991), stringent restrictions are imposed on the interrogation window size limits to avoid aliasing artifacts or loss of signal. Shifting the sampling areas with respect to one another with a constant, integer, displacement improved the matching of the recorded particle images and the algorithm performances (Westerweel *et al.*, 1997). Of course, prior knowledge of the necessary (displacement) shift is needed and can be retrieved by repeating the image interrogation procedure in **multiple passes** using the recovered displacement field from the previous iteration. In addition to the interrogation area offset, the image pairs can be processed with smaller interrogation windows on a finer grid. Such **multi-grid** approaches offered an additional increase in spatial resolution (Soria, 1996). Further improvements in algorithm accuracy are achieved by incorporating **sub-pixel window shifts** rather than integer values (Lecordier *et al.*, 1999) and by **distorting the imaged area** according to various approximations of the underlying velocity field (Huang *et al.* 1993a, 1993b; Tokumaru and Dimotakis 1995). Nowadays, multiple iterative cross-correlation passes combined with sub-pixel accurate image distortion and recursive interrogation window refinement have become standard practice in PIV image interrogation.

Current limitations

Irrespective of the applied PIV techniques mentioned above, velocity fields are extracted by means of evaluating the digital recordings. Consequently, the measurement quality is dependent on recording conditions. Recordings with strong **image noise** are apt to yield lower accuracy. Especially near interfaces, strong light reflections may occur which have a strong negative effect on measurement accuracy and robustness[†]. Moreover, the **experimental settings** determine the amount of flow detail measurable; the larger the separation time between images the larger the measurable time scale, the higher the magnification factor, i.e. the better the optical resolution or image discretization, the more detailed the flow observation becomes. One only has to look at the effectiveness of long range microscopes to see an example of the drastic improvements in resolution gained by zooming in (Kähler *et al.*, 2006). This additionally brings forward the centrality of proper **seeding** as the tracer spacing and tracer size ultimately define the lower limit in possible resolution.

On the other hand there are limitations imposed by the image interrogation process itself. As a result of the many gatherings among the community of PIV users (PIV Challenges: Stanislas *et al.*, 2003, 2005, 2008), the image processing inherent to PIV has

[†] Accuracy states how close a given velocity measurement is to the actual velocity. A measured velocity is still considered valid if it remains representative of the particle image motion. Otherwise we speak of lack in robustness and the associated error is usually an order of magnitude larger.

reached a certain level of standardization and consensus on the methodology's accuracy and limitations has been established. The response of the PIV technique is linked to the **size of the sensing domain**, i.e. the interrogation area[‡]. A sufficient amount of particle images must be contained within each area to ensure a reliable displacement estimate. However, since each interrogation area yields a single displacement vector representative of the tracer motion inside, the area must not be chosen too large when tracer motion varies spatially as few tracers will then correspond to this estimate. Additionally, **in-plane displacement gradients** are recognized as limitations with respect to the robustness of the statistical operation i.e. cross-correlation tends to fail in case of strong displacement variations. **Out-of-plane displacement** meaning tracer motion perpendicular to the illumination sheet, has a similar degrading effect on the robustness of the image interrogation routines. Although the latter type can be dealt with by more adequate PIV techniques (multiple cameras, thicker light sheet), it remains a problem in planar (2D 2C) PIV and both effects require specialized image evaluation methods and suitable interrogation area sizes.

Motivation of the present work

- **Adaptive resolution**

Current image evaluation routines all interrogate the recordings by means of interrogation areas which are of uniform size throughout the entire image and are placed in a structured fashion, i.e. at regular spacing (Willert and Gharib, 1991). Both the vector spacing and interrogation window size are determined by the user. The search for the optimal image evaluation parameters is both arduous and time consuming since the optimization procedure is generally very specific for each experiment and dependent on the image quality, flow phenomena (steady, unsteady, turbulent, transition, separated, vortices ...), user type (scientific, industry ...), field of application (environmental, combustion, fluid mechanics ...), etc. For each parameter setting the user must evaluate the obtained vector field compromising between spatial resolution and robustness. The decision which parameter setting is best, in principle the interrogation area size, thus ultimately depends on the user. A direct consequence of this trade-off in parameter optimization is a local loss of information; non-optimal experimental conditions occur rather frequently as do non-uniform velocity fields (e.g. jets, wakes, vortices, boundary layer, laminar-turbulent transition, etc.). An image evaluation technique where the

[‡] Many research papers are devoted to comparing the response of PIV to other techniques such as e.g. hot-wire anemometry (e.g. Lavoie *et al.*, 2007). This is to my opinion unfair. The spatial resolution of a hot-wire is directly determined by mainly hardware; the physical dimensions of the wire and its distance from the neighboring interface (Khoo *et al.*, 1997). While it is true that the response of PIV is linked to the geometry of the sensing domain i.e. the correlation window, the resolution is foremost fixed by the covered field of view. The more you zoom in the more detail you may see.

distance between neighboring interrogation windows and the determination of the optimal window size adapts to local velocity field fluctuations and local imaging conditions would thus be a useful contribution, especially when the user dependency can be relaxed[‡] simultaneously.

To clarify the above concept, consider the theoretical example of a wall jet (Fig. 5). The use of large interrogation areas (Fig. 5-top right) yields a structured velocity field containing few vectors. Although such correlation windows provide few outliers (i.e. high robustness), the resulting flow field is not representative of the underlying truth (Fig.5-bottom right). Small interrogation windows (Fig.5-bottom left) on the other hand lead to dense velocity measurements (i.e. many vectors or high resolution) but clearly with numerous outliers which undermine the measurement confidence. The current example also addresses the limitation imposed by setting interrogation parameters globally. The outer-jet region consists of nearly uniform flow, sufficing a sampling by few large interrogation areas. On the contrary, strong spatial flow variations are encountered in the jet's core region where sampling must be denser and smaller interrogation areas must be applied (Fig 5-bottom right).

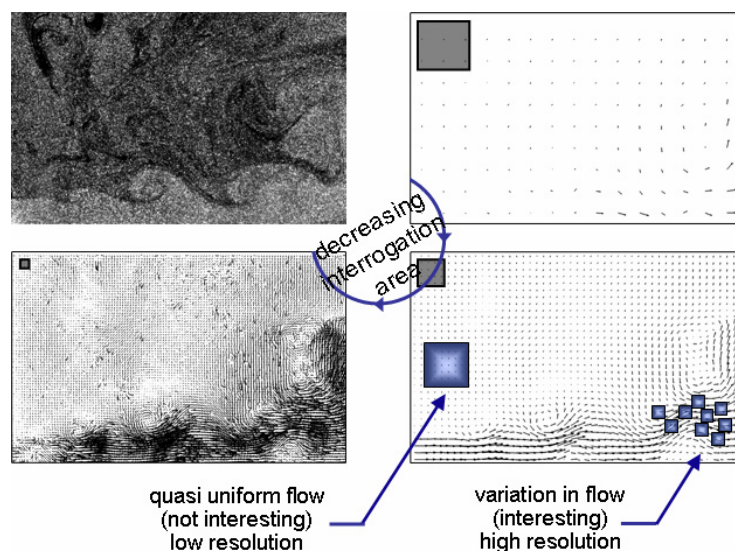


Fig. 5: Illustration of trade-off in interrogation parameter setting; large interrogation areas yield robust velocity estimates whereas the use of small areas leads to more representative flow fields marked by measurement outliers. Additionally, flow variation demands adequate sampling of the flow. (Top-Left) Contrast enhanced PIV snapshot of a walljet. Resulting vector fields with window-sizes of (Top-Right) 64×64 pixels² (Bottom-Right) 20×20 pixels² (Bottom-Left) 8×8 pixels². (Bottom Right) Adequate sampling in terms of window sizing and window spacing.

[‡] This statement has been supported by the Editorial Board of the scientific journal *Measurement Science and Technology*, who awarded the paper on adaptivity in PIV (Theunissen *et al.*, 2007) stating that their selection was influenced by the perceived utility of the contribution to the numerous investigators who utilize PIV methods.

- **PIV measurement near interfaces**

Accurate measurement of flow velocities near interfaces is generally recognized as problematic due to strong spatial variations in, not only flow characteristics, but also imaging conditions. Light reflections and signal (i.e. seeding) discontinuity near the interface require specific image interrogation routines. Although the treatment of interfaces has been the topic of many research studies (e.g. Tsuei and Savas, 2000), current image evaluation procedures do not allow a variation in image treatment or processing parameters from one image area to the other as a result of the constraint imposed by global interrogation parameter settings. Concomitantly the problem of insufficient measurement resolution discussed above is once more emphasized.

- **PIV data reduction**

After the experimentalist has obtained Giga-bytes of velocity data, the difficult task of post-processing is at hand. Although one can extract fanciful quantities such as e.g. the viscous dissipation (Piiro *et al.*, 2003), the data analysis is often limited to mean velocity and turbulence intensity. At this point one can wonder about the meaning of these average values in terms of flow physics; how sure are we that by averaging all the measurements we have a correct estimate for the mean flow field? Because this question has been subject of scrutiny many a times, a variety of statistical approaches have been reported in literature to estimate the confidence interval of the measurements, with equally varying outcome. A unique and generally applicable methodology is thus lacking.

Objectives

Once the images have been recorded the task of the image interrogation software is to retrieve as much velocity information as possible, as accurate as possible and with adequate resolution to yield experimental data with the highest affinity to the underlying flow field. Exactly this goal is emphasized within the presented work by pursuing the following objectives;

1. Alleviate the constraint of global interrogation parameter settings which impose limitations on achievable resolution.
2. Increase the reliability and resolution of PIV image processing near stationary interfaces.
3. Ensure the proposed interrogation methodologies to be generally applicable in terms of varying flow and imaging conditions
4. Reduce computational/user effort and minimize the need of expertise by introducing a certain degree of autonomy in the selection of interrogation parameters.
5. Improve the confidence estimation in the determination of flow statistics.

Thesis outline

In this chapter the general aspects of Particle Image Velocimetry have been introduced. In its simplest form this optical measurement technique provides two dimensional instantaneous velocity data within a planar slice of the flow. Over the years PIV has matured as measurement technique and has gained popularity among the scientific and industrial communities. Despite numerous developments, the inherent image evaluation is limited in resolution due to the adopted structured sampling and global interrogation settings. Moreover, image analysis near stationary interfaces has been identified as a problem area.

The remainder of this thesis discusses a possible approach to overcome the above difficulties. In **chapter 1** a description of the PIV technique is given regarding the experimental components. The involved image interrogation in its basic form is presented while a detailed elaboration on advanced image evaluation follows in **chapter 2**.

Image recordings are often performed under non-optimal experimental conditions and pose particular difficulties for conventional interrogation approaches where the flow sampling follows the nodes of a Cartesian grid while adopting uniform processing parameters. In **chapter 3** adaptivity criteria are proposed which allow the process of image interrogation to optimize the inherent parameters and enhance the resolution where possible while avoiding a user-defined trade-off between robustness and resolution. The adaptivity criteria include signal and flow adaptivity, responding respectively to underlying questions *where is it possible to extract velocity information, where is it necessary and how can we extract the most information?* Combined these drive the interrogation parameter settings. Chapter 3 further includes a detailed description of the adaptivity implementation and an assessment of the proposal based on experimental recordings[†].

Chapter 4 addresses the lack in interrogation robustness and accuracy near stationary interfaces. A modified correlation scheme is proposed to improve robustness while an extension of the adaptive interrogation reported in chapter 3 aims at enhancing the measurement resolution.

While so far the focus lied on the analysis of instantaneous flow fields, the interest often lies in averaged quantities. To reduce the computational effort, image interrogation can then be adapted to mean signal and flow statistics. This is the topic in **chapter 5**.

[†] The use of synthetic images to demonstrate improvements has been reduced to a minimum within this work. Synthetic images, although very useful during the development of novel algorithms, can always be “tweaked” and may return unrealistic improvements by reduction of image noise, lowering the degree of image discretization, changing the imposed seeding density, increasing optical resolution etc. Moreover, the inadequacy of computer generated images to reflect true conditions has been the topic of many discussions in the PIV research community. Therefore synthetic images are conducive in visualizing an inherent tendency, but improvements in image analysis performance can only be demonstrated by using real images and comparing the results with reference values obtained by a more accurate method.

Adaptive PIV interrogation is further assessed in **chapter 6** by the application to three experimental flow cases; a hypersonic sphere, a backward facing step and an over-expanded supersonic jet. The image evaluation is for each case discussed in detail, emphasizing limitations and improvements of the advanced interrogation methodology.

The application of a statistical technique known from econometrics to PIV measurements is the subject in **chapter 7**. It is shown that the proposed bootstrapping method is capable of yielding unique and robust confidence level estimates, especially for time-resolved measurements.

A summary and perspectives of the applicability of the reported work is included in **chapter 8**.

To finalize this introduction, a small comment concerning the programming of the routines reported within this thesis; all routines have been written in Matlab[®] to facilitate any future continuation of the work. Its user-friendliness and multitude of built-in routines made Matlab[®] the most adequate choice. Moreover, most engineering students are nowadays well-familiar with this programming language or had at least a brush with the basics during their studies. Special care has been taken to optimize the computational efficiency by vectorizing mathematical operations. The contrived and implemented special programming “tricks” are not reported herein for sake of conciseness. Last but not least, operations deemed computationally intenser have been translated into so-called MEX (Matlab Executables) files, which are written in C++ language to limit their execution time.

CHAPTER 1

PARTICLE IMAGE VELOCIMETRY

Abstract

This chapter presents the fundamental principles of the PIV technique and covers the theoretical and practical aspects regarding the choice of tracer particles, illumination, particle imaging and image recording. Different types of image velocimetry modes are introduced as a function of the applied seeding concentration. The chapter also discusses the extraction of quantitative particle motion estimates from image recordings on an individual basis or on the basis of particle image ensembles. The mathematical background on the statistical cross-correlation operator is presented and approaches to reach sub-pixel accuracy are discussed.

Nomenclature

δ	Dirac function
δ_x	fractional displacement in horizontal direction (pixel)
δ_z	depth of focus (meter)
Δt	snapshot time separation (seconds)
$\vec{\Delta x}$	tracer displacement vector between exposures (meter or pixels)
Δx_m	measured tracer displacement (meter)
Δz_0	laser sheet thickness (meter)
ε_{δ_x}	fractional error (pixel)
$\varepsilon_{\Delta x}$	displacement measurement error (meter or pixels)
λ	light wavelength (meter)
λ_m	minimum resolvable length scale (meter)
λ_p	tracer spacing (pixels or meter)
ρ, ρ_p	fluid density, particle density (kilogram meter ⁻³)
μ	dynamic fluid viscosity (kilogram meter ⁻¹ second ⁻¹)
τ	particle relaxation time (seconds)
ϕ	cross-correlation function

cov	covariance
c_r	ratio between particle image diameter and pixel size
C	seeding density (particles per pixel ² or ppp)
\vec{d}	relative shift in the correlation plane (pixels)
d_r	particle image diameter (meter or pixel)
d_o	diffraction spot diameter (meter or pixel)
d_p	particle diameter (meter)
d_r	dimension of pixel element (meter)
D	aperture diameter (meter)
$\vec{D} = (\Delta x, \Delta y)$	uniform tracer displacement (pixels)
DCC	Direct Cross-Correlation
DSR	Dynamic Spatial Range
f	lens focal length (meter)
$f_{\#}$	f-number
fps	frames per second
FFT	Fast Fourier Transform
\vec{g}	gravitational acceleration vector (meter second ⁻²)
(i, j)	image coordinates
I_o	peak intensity
I_a, I_b	intensity distributions recorded at time 't _o ' and 't _o +Δt'
$\overline{I_a}, \overline{I_b}$	mean intensities
I_s	scattered light intensity
l_{xy}	dimension of image plane (meter)
L_{XY}	dimension of object plane (meter)
LSV	Laser Speckle Velocimetry
m, n	spatial correlation shifts (pixels)
m_p, n_p	integer locations of the correlation peak (pixels)
M	magnification factor
N_I	image density
N_S	source density
PIV	Particle Image Velocimetry
PTV	Particle Tracking Velocimetry
r_o	diffraction spot radius (meter or pixel)
SSD	Sum of Squared Differences
t	time (seconds)
\vec{u}	fluid velocity vector (meters per second)
\vec{u}_p	tracer velocity vector (meters per second)
W_S	correlation window size (pixels)
\vec{x}	tracer position vector
z_o, Z_o	lens to image plane and lens to object plane distance (meter)

1.1 Introduction

The PIV technique hinges on the principle of evaluating instantaneous fluid velocities by recording and evaluating the position of images produced by small tracers suspended in the fluid at successive time instants. Though image velocimetry originates from flow visualization (e.g. VKI LS 1986, Tokumaru and Dimotakis 1995), the main difference lies exactly in the visualization approach. While for the latter the aim is to make certain flow structures visible by selective seeding of the flow regions, for particle image velocimetry a homogenous seeding must be established. Flow structures become visible only when the velocity field has been determined.

Following the work of Westerweel (1997), the velocity of the flow $\vec{u}(t)$ is measured indirectly as a function of the tracer displacement $\overline{\Delta\vec{x}}(\vec{x}, t_0, \Delta t)$ between images recorded within a finite time extent Δt as mathematically expressed in (1.1). Here, $\overline{u_p}(t)$ represents the tracer's velocity which in the ideal case is identical to the fluid velocity. Given the discrete nature of the temporal sampling, this equation simplifies to (1.2) under the assumption of a sufficiently small time separation Δt to neglect the effect of flow acceleration.

$$\overline{\Delta\vec{x}}(\vec{x}, t_0, \Delta t) = \int_{t_0}^{t_0 + \Delta t} \overline{u_p}(\vec{x}, t) dt \quad (1.1)$$

$$\overline{\Delta\vec{x}}(\vec{x}, t_0, \Delta t) = \vec{x}(t_0 + \Delta t) - \vec{x}(t_0) = \overline{u_p}(\vec{x}, t) \cdot \Delta t \quad (1.2)$$

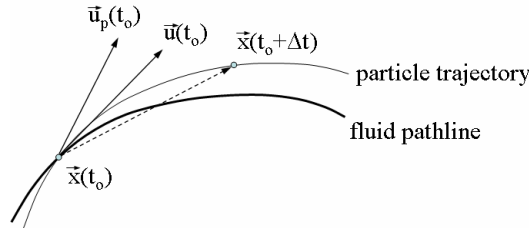


Fig. 1.1: The displacement of the tracer particles is an approximation of the fluid velocity (following Westerweel, 1997).

Since the velocity of the fluid is inferred from the motion of the tracer particles, their properties are key parameters to be assessed (Melling, 1997). Ideal tracers follow exactly the fluid motion without altering the flow or fluid properties. In a practical situation the ideal tracers can only be approximated as depicted in Fig. 1.1. Fluid mechanics then prescribes small particle diameters to minimize the relative velocity between fluid and tracers while on the other hand, the conflicting requirement of efficient light scattering favors larger particle diameters. In the remainder of this chapter a brief discussion is presented on the main parameters to be taken into account in setting up a typical PIV experiment (Raffel *et al.*, 1998).

1.2 Particle tracers

1.2.1 Tracking characteristics of particles

The tracer motion can be theoretically estimated by the results for a spherical particle of diameter ‘ d_p ’ moving in the fluid in Stokes flow regime (Melling, 1997);

$$\frac{d\vec{u}_p}{dt} = \frac{\vec{u} - \vec{u}_p}{\frac{d_p^2(\rho_p - \rho)}{18\mu}} + \vec{g} \quad \text{where} \quad \frac{1}{\tau} = \frac{18\mu}{\rho_p d_p^2} \quad (1.3)$$

where ‘ \vec{g} ’ refers to the gravitational force, ‘ ρ_p ’ to the density of the particle, ‘ ρ ’ to the fluid density and ‘ μ ’ to the dynamic viscosity of the fluid. The relaxation time ‘ τ ’ is characteristic of a particle’s capability to follow a sudden velocity change in the flow. Ideally, ‘ τ ’ is smaller than the smallest time scale of the flow which imposes stringent conditions on the seeding properties, especially in compressible flows. To obtain particles following the flow with fidelity, small values of ‘ τ ’ are thus desirable and can be achieved by either using a seeding material with low density or by reducing the tracer particle diameter.

While adequate tracer response requires small diameters, the particles must remain visible. For spherical particles, Mie light scattering theory predicts the intensity ‘ I_s ’ of the scattered light to be a strong function of both the particle’s size parameter ‘ $I_s \sim (d_p/\lambda)^2$ ’ and refractive index. Clearly high intensities necessitate large diameters while constraining the choice in seeding material.

As a compromise, particles of 0.5 to 3 micrometer diameter are typically applied for experiments conducted in gaseous flows while larger particles of 10 to 100 micrometer can be used in liquid flows. Because the flow can only be characterized at those random spatial locations sampled by a particle, a high seeding density with a homogeneous distribution is a desirable condition.

1.2.2 Illumination

The camera projects the three dimensional environment onto a two dimensional image. Concomitantly, resolved motion will be constraint to two dimensions and cannot be extended to three dimensions without additional information. For the obtained displacement field to be a non-ambiguous representation of the fluid motion the illuminated volume must therefore be reduced to a slice. The limited thickness of

typically 1mm furthermore minimizes the disturbances in image quality as a result of out-of-focus particles[†] (Stanislas and Monnier 1997).

The duration of the light pulses is important and determines the degree to which the particle images are frozen during the pulse exposure. While streak photography has been applied earlier, its range of applications is limited to two dimensional fields to avoid numerous truncations in streak formation (Adrian, 1991). Moreover, the disadvantage of this early method is the poor accuracy of the measurement based on the estimation of the length of the traces. Instead, short pulses are more appropriate requiring high energy light sources since the recording device receives only a fraction of the scattered light which itself is limited in energy due to the small particle sizes.

Lasers are widely used in PIV because of their ability to emit coherent light with high energy density which can easily be transformed into a thin sheet of light by means of cylindrical and spherical lenses. The most common is the Nd:YAG laser, which can provide as much as 400mJ of monochromatic light ($\lambda=532\text{nm}$) with a pulse duration of 5 to 10 nano-seconds (10^{-9} seconds) and repetition rates typically between 10 and 50Hz. The time separation between successive laser pulses requires meticulous selection taking into account

- a) the influence of random noise sources[‡]
- b) errors inherent to fluid acceleration (Boillot and Prasad, 1996).
- c) temporal resolution; irrespective of tracers being ideal, the flow field is sampled at discrete moments yielding velocity estimates averaged over the separation time (Westerweel, 1997).
- d) a minimization of the loss of particle images due to the out-of-plane velocity component (Lin and Perlin, 1998).

1.2.3 Particle imaging

When illuminating the seeded flow, impinged light is scattered by the individual tracers and spread through a lens system onto the recording plane (Fig. 1.2-a). Because seeding particles are small (in the order of the incident light wavelength), the imaged light (Mie-scattering) pattern does not appear as a magnified circle but forms a diffraction pattern. This Fraunhofer diffraction pattern is characterized by concentric rings and can be mathematically described by the Airy function (Fig. 1.2-b). The latter represents the impulse function of the optical system and can be conveniently approximated by a Gaussian distribution.

[†] Particles are in focus when the light sheet thickness ' Δz_0 ' is less than the object focal depth ' δz ', which is determined by the optical system (par. 1.2.3); $\delta z \approx 4 \cdot (1 + M^{-1})^2 \cdot f_{\#}^2 \cdot \lambda$

[‡] The flow velocity 'u' is derived from the measured marker displacement ' Δx_m ' between consecutive image snapshots separated by a time delay ' Δt ' as; $u = (\Delta x_m + \epsilon_{\Delta x}) / \Delta t$. Here ' $\epsilon_{\Delta x}$ ' refers to the unavoidable error on the pixel displacement estimate, on average in the order of 0.01 pixels (Willert, 2009). By reducing the time separation between recordings this error term gains importance, lowering the accuracy of the velocity measurement.

The diameter of the diffraction spot ‘ d_o ’ is defined by the first minimum of the Airy disc and reads (Hecht, 2002)

$$d_o = 2.44 \cdot r_o = 2.44 \cdot (1 + M) \cdot \lambda \cdot f_{\#} \quad (1.4)$$

where ‘ λ ’ refers to the light wavelength, ‘ M ’ the magnification and ‘ $f_{\#}$ ’ the f-number. Both magnification and f-number, and as a result also the size of the diffraction spot, depend on the optical system characteristics;

$$M = \frac{z_o}{Z_o} \quad \text{and} \quad f_{\#} = \frac{f}{D} \quad \text{where} \quad \frac{1}{f} = \frac{1}{z_o} + \frac{1}{Z_o} \quad (1.5)$$

with ‘ D ’ symbolizing the aperture diameter. The resulting particle image diameter ‘ d_{τ} ’ can be expressed as (Adrian and Yao, 1984)

$$d_{\tau} = \sqrt{(M \cdot d_p)^2 + d_o^2} \quad (1.6)$$

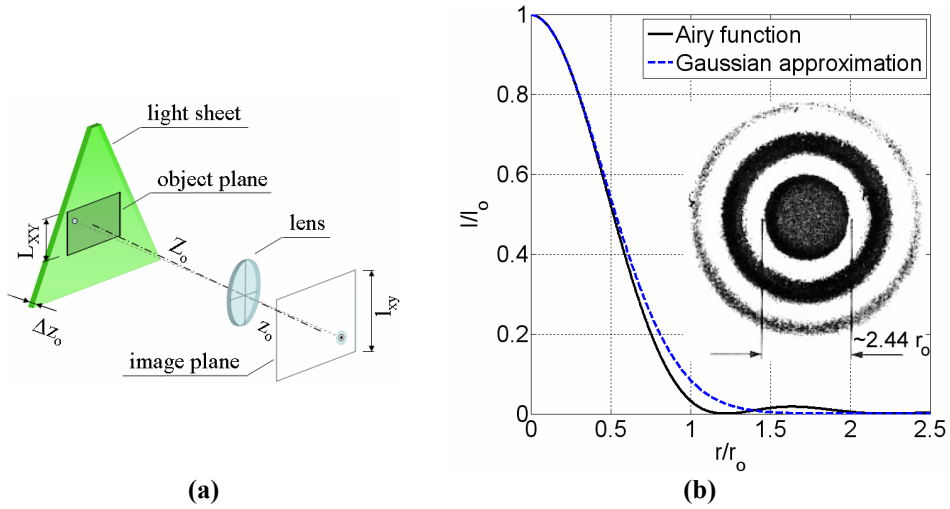


Fig. 1.2: (a) Optical arrangement of PIV optics (b) the radial intensity profile of the Airy function and the corresponding Gaussian approximation.

While particle images must be sharp and small to distinguish them against the sensor noise, the most important consideration in optimizing a PIV setup for a given experiment is the size of the particle with respect to the resolution of the recording medium. If the particle image diameter is too small with respect to the sensor elements, the image is under-sampled yielding uncertainty in locating the image centroid and mean bias errors in the displacement. This effect is known as *peak-locking*. Here the analogy with a chessboard patterns can be drawn. Suppose the white squares represent the particle

images. When shifting two overlaying patterns, white squares overlap either again a white square (correlation) or their counterparts (no correlation). Correlation peaks will thus appear only at integer shifts, expressed in terms of number of squares. At high flow velocities and/or high magnification, measurement errors of a pixel may easily convert into several meters per second giving rise to unacceptable inaccuracies. In general the particle image is recommended to cover about two pixel units (Westerweel, 1993).

1.2.4 Image recording

Historically photographic film was first applied as recording medium. The shutter of a photographic camera was opened for a sufficient amount of time during at least two consecutive light pulses. Accordingly, the recorded images would contain multiple tracer exposures, making it difficult to distinguish the temporal sequence of the tracer images (e.g. Marzouk and Hart, 1998). Moreover, tedious processing of the photographic film meant a difficult on-line control of experimental parameters in terms of focusing and appropriate tracer concentration.

Nowadays, because of recent advances in electronic imaging, electronic image sensors with high resolution provide immediate access to a digitized image ready for immediate processing. Accordingly, electronic image sensors have forced the photographic film aside and have become standard practice in image velocimetry. Of these, Charge Coupled Devices or CCD have found the most widespread use. CCD sensors are composed of several sensitive elements, pixels, arranged in a rectangular array. Continuous light distributions impinging on the sensor are spatially discretized by the pixel elements who convert light into electrical charge. Sensor areas are typically in the order of 1000×1000 pixels with pixel sizes of $10 \times 10 \mu\text{m}^2$.

At this point the concepts of *digital image resolution* and *Dynamic Spatial Range (DSR)* are introduced. The former is defined as the number of pixel elements per millimeter in the object space ($\sim l_{xy}/d_r \cdot 1/L_{XY}$) and is relevant to adequately resolve images incident on the sensor (cf. peak-locking effect discussed in 1.2.3). Dynamic spatial range (Adrian, 1997) relates to the level of measurable detail and is expressed as the ratio between the field-of-view in object space ' L_{XY} ' and the smallest resolvable spatial variation ' λ_m ';

$$\text{DSR} = \frac{L_{XY}}{\lambda_m} \sim \frac{l_{xy} \cdot c_r}{M} \quad \text{since} \quad L_{XY} = \frac{l_{xy}}{M} \quad \text{and} \quad \lambda_m \sim \frac{d_r}{c_r} = \frac{1}{c_r} \quad (1.7)$$

Large dynamic spatial resolution allows the measurement of small-scale variation embedded in larger scale motion, as occurs in e.g. turbulence. The field-of-view in the fluid is directly defined by the dimensions of the recording medium ' l_{xy} ' and magnification through geometrical optics. The minimum resolvable scale is related to the image sampling rate ' c_r ' on the basis that the more pixels per particle image, the better the accuracy in determining the displacement. For a given optical arrangement (read, magnification), the DSR can thus be increased either by reducing the dimensions of the

pixel elements ‘ d_r ’, and improving the digital image resolution, and/or by enlarging the overall sensor area ‘ l_{xy} ’. This explains the current tendency in CCD development (Table 1.1).

A third noticeable evolution is the reduction in frame separation time. Especially in high speed flows, the temporal resolution must be high to limit the loss of particle images between recordings. In the case of high-speed imaging (thousands of frames per second) this requires short exposure times and strong illumination with fast read-out. Here CMOS[†] image sensors provide a cost-effective alternative with respect to traditional CCD cameras.

Table 1.1: Examples of CCD camera data

Manufacturer/Model	Kodak Megaplug ES 1.0	PCO SensiCam QE	LaVision Imager Pro X 4M
Resolution (pixels²)	1008×1018	1376×1040	2048×2048
Pixel size ‘d_r’ (μm)	9	6.45	7.4
Frame rate (fps)	30	10	14

1.3 Image velocimetry modes

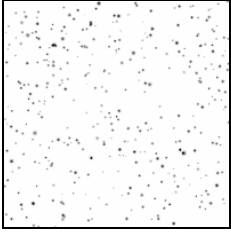
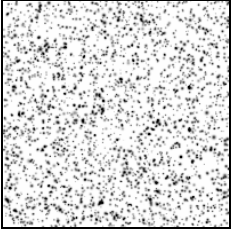
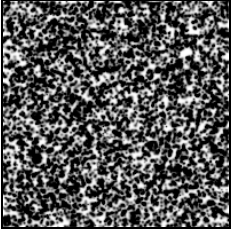
Image velocimetry is subdivided into different classes based on the amount of injected and imaged seeding tracers (Adrian, 1991). Different operation modes are distinguished, relating to the source density ‘ N_s ’ and image density ‘ N_I ’ (Adrian and Yao, 1984) who are symbolically defined as follows

$$N_s = \frac{C\Delta z_0}{M^2} \frac{\pi}{4} d_\tau^2 \approx \frac{\pi}{4} \frac{d_\tau^2}{\lambda_p^2} \quad \text{and} \quad N_I = \frac{C\Delta z_0}{M^2} W_s^2 \approx \frac{W_s^2}{\lambda_p^2} \quad \text{with} \quad \frac{C\Delta z_0}{M^2} \approx \frac{1}{\lambda_p^2} \quad (1.8)$$

where ‘ C ’ is the number density of particles, ‘ Δz_0 ’ the light sheet thickness, ‘ M ’ the image magnification, ‘ d_τ ’ the particle image diameter and ‘ λ_p ’ the typical inter-particle distance. The source density indicates whether the image consists of individual, $N_s \ll 1$, or overlapping, $N_s \gg 1$, particle images, while the image density relates to the average number of particle images within an interrogation domain of area ‘ W_s^2 ’ (cf. Fig. 1.5). Examples of the working ranges for the different image classes are presented in Table 1.2.

[†] CMOS stands for Complementary Metal Oxide Semiconductor. Traditionally CCD cameras provided higher quality images. However, CMOS quality is getting better and better with each new generation of chip design.

Table 1.2: Image velocimetry modes (gray scales inverted for clarity)[†].

PTV	PIV	PIV (LSV)
$N_S \ll 1, N_I \ll 1$	$N_S \ll 1, N_I \gg 1$	$N_S \gg 1, N_I \gg 1$
		

Criteria for applying Particle Image Velocimetry (PIV) are a low occurrence of particle images overlapping while maintaining a sufficient number present within each interrogation area. Data is obtained by tracing an ensemble of particle images which constitute a pattern convected by the flow. Particle Tracking Velocimetry (PTV) and Laser Speckle Velocimetry (LSV) occupy the two extremes of the spectrum of information density. Particle Tracking Velocimetry acts on the premise that the displacement of individual, identifiable markers in the object plane can be measured from one image to the next. Accordingly, PTV operates at the low image and source density ensuring a correct pairing between identified particles. In the case of high levels of seeding concentration, particles can no longer be unambiguously identified in the image due to interference between their images. In Laser Speckle Velocimetry velocity information was originally extracted from the Young's interference fringes appearing when a coherent light beam passes through two transparencies of speckle images which are placed one over one another and slightly displaced (Meynart, 1983). However, as these speckles still contain sufficient texture, the interrogation procedures common in PIV remain adequate as demonstrated by the application of PIV-image analyses to for example smoke images (Fawcett and Komerath 1991) and even Schlieren images (e.g. Jonassen *et al.*, 2006).

[†] Because of the application of the PIV concept to a broad range of imaging conditions it is to the author's belief now permitted to deviate from the traditional categorization of image velocimetry into three separate classes but instead merge PIV and LSV into a single class.

1.4 Tracer motion evaluation

The experiment is not concluded until the velocity information is obtained. Mathematical operators determine the most probable displacement of the captured particle images. The nature of the operator and adopted processing strategy depends on the velocimetry operation mode (Fig. 1.3).

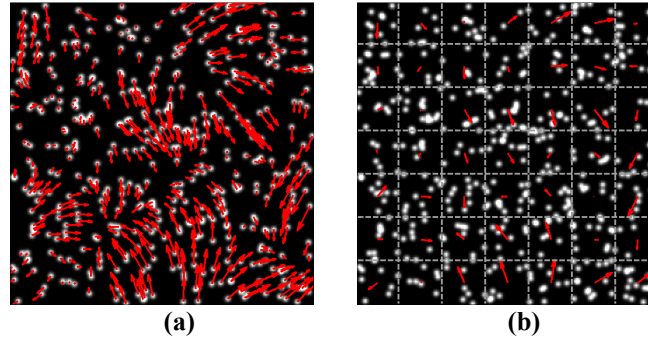


Fig. 1.3: (a) With PTV velocity components for individual particle images are determined whereas (b) PIV yields the representative displacement of particle patterns inside interrogation windows (dashed grid).

1.4.1 Particle tracking

PTV operates on the most straightforward principle of tracking individual particle images throughout the recording sequence, (Fig. 1.3-a). As the spatial resolution in image velocimetry is ultimately limited by the distance between tracer particles[†], tracking individual particles would theoretically define the upper limit in achievable resolution. Assessments based on computer generated images demonstrated PTV to yield resolutions two to three times higher compared to PIV (Marxen *et al.*, 2000). Notwithstanding, practice rather shows the opposite as seeding densities and turbulent velocity fluctuations are kept way below those encountered in PIV, mainly to ensure sufficiently high success rates in pairing particle images (Malik *et al.*, 1993). The problem of ambiguous particle pairing is illustrated in Fig. 1.4-b. Despite such drawbacks, PTV remains extremely suitable in the extraction of quasi steady particle trajectories.

By making a prediction of the particles' shift, based for instance on a previous cross-correlation analysis, particle pairing ambiguity can be greatly reduced allowing an extension of PTV into high image densities (Cowen and Monismith 1997). Hybrid routines combine PIV and PTV and improve the spatial resolution proportional to the

[†] Spatial resolution determines the smallest measurable flow scale. The goal is to reach the highest resolution for the more details are known, the better the flow phenomena can be described and understood. Flow features with a wavelength shorter than twice the distance between particles cannot be recovered from the data according to the Nyquist sampling criterion (Agüí and Jiménez, 1987).

allowed increase in image density (Keane *et al.*, 1995). The concept is depicted in Fig. 1.4. Even so, hybrid techniques lean on the spatial response of PIV. Consequently in case of flow structures with higher spatial frequency, no noticeable improvement should be expected. PTV is at best complementary to PIV vis-à-vis resolution.

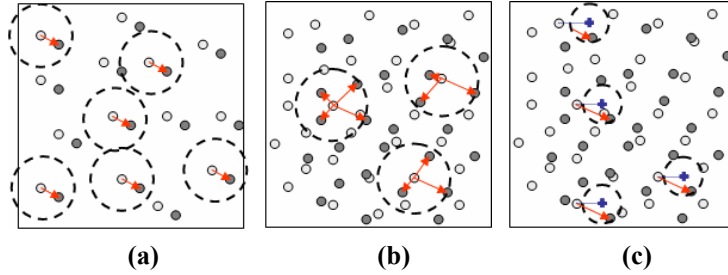


Fig. 1.4: Particle Tracking Velocimetry; (a) at low image density particle pairing (\rightarrow) can be performed unambiguously between the particle images recorded at time ‘ t_0 ’ (light gray) and a time-instant later (dark grey) (b) at higher image densities or larger displacements multiple matches are possible within the search area (---) (c) when applying a predictor (+) the search area can be reduced yielding an increase in successful pairing.

Accuracy and precision in tracking methodologies remain inferior to PIV mainly due to the uncertainty in locating the particle images centroids (Stanislas *et al.*, 2005). While fruitful attempts have been made in elevating accuracies to levels equivalent in PIV (Theunissen *et al.*, 2004), precision remains a weak point. The supremacy of PIV is to be credited to its statistical nature i.e. it operates on tracer ensembles rather than individual particle images. Combined with its non-intrusive nature and whole field measurement capacity, it is this resilience in robustness which makes PIV attractive and conducive in most experimental applications.

1.4.2 Particle pattern tracking

PIV operates on ensembles of particle images, captured within regularly spaced interrogation windows (Fig. 1.3-b). The aim is to extract the spatial shift ‘ $(\Delta x, \Delta y)$ ’ of the particle patterns by means of a statistical operator. The tracking of features throughout an image sequence is essentially based on finding the similarity of corresponding gray-level patches by minimization of disparity between pixel intensity values within windows of fixed size at two time moments ‘ t_0 ’ and ‘ $t+\Delta t$ ’ (Fig. 1.5). Nowadays, the method of choice[†] in retrieving the spatial shift ‘ $(\Delta x, \Delta y)$ ’ of the particle patterns is the statistical technique of spatial cross-correlation.

[†] An alternative measure of the disparity is the search for a minimum in the summation of squared intensity differences (SSD) within the interrogation areas (Lucas and Kanade, 1981);

$$SSD = \sum_{i,j \in W_s} [I_a(i,j) - I_b(i+m,j+n)]^2 = \sum_{i,j \in W_s} I_a^2(i,j) + \sum_{i,j \in W_s} I_b^2(i+m,j+n) - \sum_{i,j \in W_s} I_a(i,j)I_b(i+m,j+n)$$

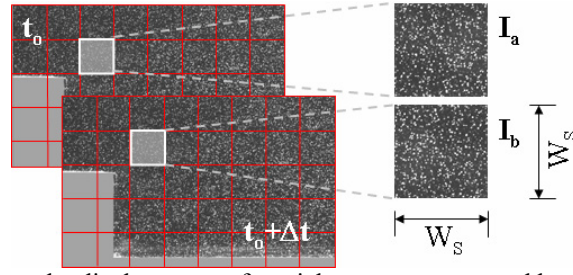


Fig. 1.5: PIV determines the displacement of particle patterns, captured by the regularly spaced so-called interrogation windows of area ' W_s^2 ' (red lines), from images separated by a time-step ' Δt '.

- **Mathematic background**

As anticipated, most PIV interrogation techniques nowadays rely on the cross-correlation operator to retrieve the flow velocity between particle image pairs. The application of this operator intrinsically refers to an optimization process whereby the correlation function ' ϕ ' between the continuous distributions ' I_a ' and ' I_b ' is maximized in function of the parameter ' \vec{d} ' i.e. the relative spatial displacement

$$\max_{\vec{d}} [\phi(\vec{d})] = \max_{\vec{d}} \left[\int I_a(\vec{x}) I_b(\vec{x} + \vec{d}) d\vec{x} \right] \quad (1.9)$$

with the intensity field ' I_a ' described through the expression

$$I_a(\vec{x}) = \sum_h^M I_o(\vec{x}_h) \delta(\vec{x} - \vec{x}_h) \quad \text{with} \quad \vec{x} = (x, y, z) \quad \text{where} \quad z \in \left[-\frac{\Delta z_o}{2}, \frac{\Delta z_o}{2} \right] \quad (1.10)$$

where $I_o(h)$ is the peak intensity level associated to the h^{th} particle located at ' $\vec{x}_h = (x_h, y_h, z_h)$ '.

A detailed analysis regarding the properties of the cross-correlation operator is given in e.g. Keane and Adrian (1992), Westerweel (1993) and Raffel *et al.* (1998) and is reduced to a minimum in the current paragraph. In the present discussion the hypothesis is made that the displacement between the two exposures is restricted to a uniform, planar translation ' \vec{D} ', leading to a resulting intensity field in the second exposure ' I_b '[†]

Several image processing algorithms apply this technique in the estimation of the underlying velocity distribution (e.g. Gui and Merzkirch 2000). However, the last term in the above equation refers to a standard correlation indicating that the spatial shift (m,n) producing a minimum in SSD corresponds to a correlation maximum. Note that in the above definition the intensity distributions are already in discretized form

[†] Because of particles entering and exiting the interrogation windows, the number of particle images ' M ' and ' N ' differs.

$$I_b(\vec{x}) = \sum_k^N I_o(\vec{x}_k + \vec{D}) \delta(\vec{x} - \vec{x}_k - \vec{D}) \quad \text{with} \quad \vec{D} = (\Delta x, \Delta y, 0) \quad (1.11)$$

With (1.10) and (1.11) the continuous cross-correlation function of the intensity distributions (1.9) becomes

$$\phi(\vec{d}) = \sum_h^M \sum_k^N I_o(\vec{x}_h) I_o(\vec{x}_k - \vec{D}) \int \delta(\vec{x} - \vec{x}_h) \delta(\vec{x} - \vec{x}_k - \vec{D} + \vec{d}) d\vec{x} \quad (1.12)$$

The integration is non-zero only for $\vec{x}_h = \vec{x}_k + \vec{D} - \vec{d}$. Accordingly, two contributions to the correlation function are distinguished;

1. $\vec{x}_h \neq \vec{x}_k$ represents the contribution due to particle images at different exposures that do not correspond to the same physical particle and is referred to as *spurious pairing*. This correlation noise term is statistically evenly distributed over the correlation space with low amplitude peaks.
2. $\vec{x}_h = \vec{x}_k$ produces a high correlation peak for a separation vector ' \vec{d} ' in the correlation plane at a location distant from the origin that corresponds to the, sought for, uniform displacement ' \vec{D} '. This component corresponds to the correlation of particle image pairs, produced by the same particle.

This principle of extracting displacement estimates by means of intensity cross-correlation is illustrated in Fig. 1.6.

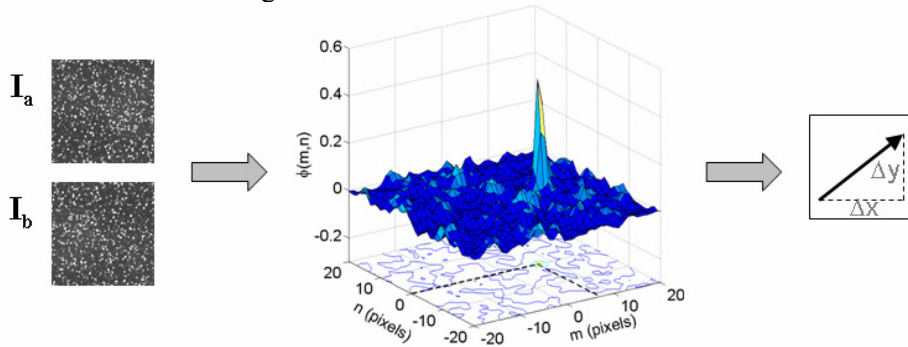


Fig. 1.6: After cross-correlating interrogation windows ' I_a ' and ' I_b ', the peak location (dashed lines) of the correlation coefficient ' $\phi(m,n)$ ' indicates the relative pixel shift between the intensity distributions.

- **Discrete normalized cross-correlation**

The electronic sensor area integrates the light intensity over small, individual and finite pixel elements. Although the intensity distributions ' I_a ' and ' I_b ' are accordingly spatially discretized, the operational principle of the correlation operator remains valid. A detailed

mathematical formulation is provided in Westerweel (1993), but it suffices to note that (1.9) in discrete form reads as

$$\phi(m, n) = \sum_{i,j} I_a(i, j) \cdot I_b(i + m, j + n) \quad (1.13)$$

The coordinates corresponding to the location of the correlation maximum quantify again the pattern shift. Because in practice interrogation windows contain spatial variations in particle motion, the returned displacement can be thought of as the volume averaged displacement of the captured particle images. However, it is more precise to denote it as the most representative displacement or yielding the best pattern match (i.e. the most probable displacement).

To reduce the sensitivity of the correlation function expressed in (1.13) to intensity changes between exposures, a normalization is introduced (Huang *et al.*, 1997);

$$\phi(m, n) = \sum_{i,j=1}^{W_s} \frac{(I_a(i, j) - \bar{I}_a)}{\sqrt{\sum_{i,j=1}^{W_s} (I_a(i, j) - \bar{I}_a)^2}} \cdot \frac{(I_b(i + m, j + n) - \bar{I}_b(m, n))}{\sqrt{\sum_{i,j=1}^{W_s} (I_b(i + m, j + n) - \bar{I}_b(m, n))^2}} \quad (1.14)$$

The proposed normalization has the advantage of making the result independent of linear transformations. The mean subtraction eliminates the contribution of the DC term in the correlation map (originating from the mean intensity correlation), which would otherwise introduce a strong bias error.

- **Correlation by means of Fast Fourier Transforms**

The calculation of ‘ ϕ ’ directly in the spatial domain as presented in (1.14) is referred to as direct cross-correlation (DCC) and requires the mean intensities of the two exposures to be computed in a different way. Whereas ‘ \bar{I}_a ’ is determined only once before the correlation operation, ‘ \bar{I}_b ’ must be calculated each time a new pixel offset ‘(m,n)’ between the two distributions is chosen.

Willert and Gharib (1991) introduced the implementation of Fourier transforms in the calculation of ‘ ϕ ’ as a simplification and significant speed-up (1.15). The use of Fourier transforms (FFT) neglects the spatial dependency of ‘ \bar{I}_b ’ sufficing a mean intensity value subtraction in the interrogation areas prior to the correlation operation.

$$\phi = \text{FFT}^{-1}(\text{FFT}(I_a^*) \cdot \text{FFT}(I_b^*)) \quad \text{with} \quad I^* = \frac{I - \bar{I}}{\text{cov}(I)} \quad (1.15)$$

- **Sub-pixel accuracy**

Having obtained the correlation map pertinent to a selected interrogation window, the correlation peak can be localized with only half a pixel accuracy because of the discrete nature of the image recordings.

The optics applied in PIV are for the majority of applications diffraction-limited. The diffraction pattern can be mathematically described by the Airy function and approximated by a Gaussian (paragraph 1.2.3). Accordingly, the correlation function can be considered to be a discrete representation of the convolution between several continuous Gaussian functions, which mathematics predicts to ultimately retrieve a Gaussian anew. Following Westerweel (1993) sub-pixel accuracy can ipso facto be achieved by estimating the peak location of the continuous Gaussian function underlying the correlation (Fig. 1.7-a). While Whittaker interpolation outperforms the Gaussian fit, the latter is generally chosen for its trade-off between accuracy and computational simplicity (Roesgen, 2003).

Sub-pixel accuracy in each component of the displacement estimate can be obtained by a three-point Gaussian fit to the detected correlation peak. The fitting equation for the horizontal displacement component is presented in (1.16).

$$\delta x = \frac{0.5 \cdot (\log \phi_{m_p-1, n_p} - \log \phi_{m_p+1, n_p})}{\log \phi_{m_p-1, n_p} - 2 \log \phi_{m_p, n_p} + \log \phi_{m_p+1, n_p}}, \phi_{m_p+i, n_p} = \phi(m_p + i, n_p) \quad (1.16)$$

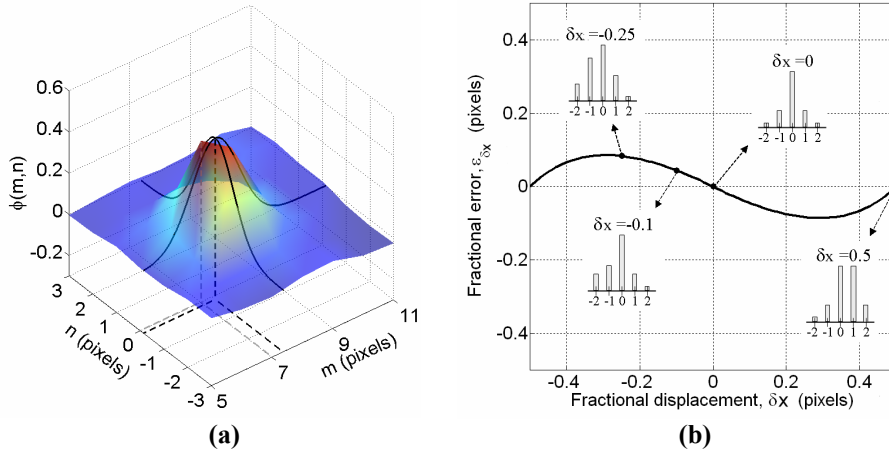


Fig. 1.7: (a) Zoom of the correlation peak in Fig. 1.6. Gray dashed lines indicate the integer peak position. Dashed black lines point towards the sub-pixel position. The latter is obtained by fitting Gaussian functions (black line) to the discrete correlation function. While originally the retrieved shift equaled $\Delta x=7$ and $\Delta y=0$, peak fitting yields $\Delta x=7.36$ and $\Delta y=-0.14$. (b) Fractional error for Gaussian peak fitting vs. fractional displacement following Westerweel (1993). Included in the figure are typical correlation maps at different fractional displacements.

As a result of correlation asymmetry a certain amount of error will always be introduced despite the estimation of the correlation peak through interpolation (Fig. 1.7-b). This bias error or fractional error ' $\epsilon_{\delta x}$ ' defined as the difference between the measured and imposed fractional displacements, although small, can significantly degrade the measurements when small velocity fluctuations are to be detected and becomes prominent in the display of derivative field quantities such as e.g. vorticity (Scarano and Riethmuller, 1999).

Though the measurement accuracy can be greatly improved by peak-fitting function, it is important to stress the importance of experimental conditions. Individual particle images must cover two to three pixels to avoid a systematic under-estimation of the fractional displacement (Westerweel 1998; cf. section 1.2.3).

1.5 Image pre-processing

Ideal PIV images consist of a completely black background on which the particle images are superimposed as bright spots. Image recordings inevitably suffer from noise originating from the CCD sensor array (thermal noise) or non-ideal experimental conditions (background light, day light, light reflections from interfaces, etc.). While some sources of image noise can be removed or at best minimized by appropriate filtering, others, such as thermal camera noise, are embedded into the recorded signal making their removal close to impossible.

Statistical de-noising methods exist (e.g. Katkovnik *et al.*, 2002), but tend to minimize high frequency contents within the image which, in case of PIV images, would undoubtedly remove also the particle images. Consequently the objective must be to enhance the image quality by modifying the recorded intensity distribution towards ideal conditions.

Image pre-processing steps may involve actions such as enhancement of intensity gradients (e.g. Westerweel, 1993), intensity histogram redistribution (e.g. Roth and Katz 2001), temporal and/or spatial intensity filtering (e.g. Fore *et al.* 2005, Wereley *et al.* 2002^a) etc. The most common approach however to remove background noise is by mere background subtraction. A background image is typically constructed by spatial filtering of the image recording. The filter operator can either be a local intensity averaging or a determination of the local intensity minimum whereas the availability of a large collection of image snapshots allows full exploitation of the statistical nature of noise. Wereley *et al.* (2002^b) compose their background image by selecting the pixel-wise minimum intensity throughout the data set, whereas Stitou and Riethmuller (2001) take into account the ensemble average and standard deviation statistics in intensity. To remove background noise, Lourenco and Krothapalli (2000) took this idea one step further and rebuilt the PIV image by transferring detected particle images onto a black background. Though this method eliminates spurious background due to reflections and parasite illumination, its effectiveness is strongly dependent on particle segmentation performance.

Overall the degradation in image quality cannot be attributed to a single parameter but is dependent on an interplay of factors. The optimal type of image treatment must

therefore be selected for each case individually. Nevertheless, background subtraction in general already provides a sufficient primary reduction in background noise.

1.6 Conclusions

One of the most widely applied measurement techniques nowadays is image velocimetry. PIV is non-intrusive and provides instantaneous flow velocity within a field of view from recorded image pairs of the seeded flow. While the experimental setup requires meticulous preparation its concept is rather simple and is founded on the principle of flow visualization. In this chapter the working principle of Particle Image Velocimetry is described covering the sequence of choice of seeding, illumination, particle imaging and recording.

Pivotal in the selection of tracer particle diameter and material is the inherent relaxation time to minimize the particle's lag with respect to the flow. Because of the consequent small particle image diameters, high energy light sources are required for which lasers provide the best solution. Moreover, lasers allow short duration light pulses to ensure frozen markers on the image recording. The projected particle image is for typical applications diffraction limited and the physical background has been presented. To eliminate the probability of pronounced bias errors in the displacement measurement, it comes out that particle image must cover at least two sensor elements. Regarding image recording, advances in electronic imaging have pushed digital CCD cameras to the foreground with on-going developments to reduced pixel dimensions and enlarged sensor arrays.

Different velocimetry modes can be distinguished as a function of the image seeding density with accompanying motion-extraction methodologies. While PTV evaluates the motion of individual markers, PIV extracts the displacement of tracer ensembles by means of the statistical cross-correlation operator. The underlying mathematics of cross-correlation have been presented and dominating maxima in the resulting signal are shown to correspond to representative tracer displacements. Because of the discretized representation of the continuous image recording, displacement accuracies are limited to integer pixel values but can be improved to sub-pixel levels by Gaussian fitting of the correlation peak.

Given the statistical nature of PIV image interrogation, performance limitations are imposed related to the quality of the signal and its evaluation. Whereas idealized recording conditions may be approximated by image pre-processing, adequate data validation criteria and advanced interrogation methodologies are needed to overcome basic restrictions in correlation effectiveness. These are the topic in the following chapter.

CHAPTER 2

PIV IMAGE EVALUATION

Abstract

Though cross-correlation is an effective method in the determination of purely translational motion, the basic statistical technique is inadequate to resolve strong velocity variations common to the majority of fluid dynamical applications. This chapter introduces the limitations of and basic rules for motion analysis by means of cross-correlation. To increase the range of applicability, advanced iterative interrogation algorithms have been developed over the years with the intention to improve both reliability and spatial response. The concept, implementation and assessment of such interrogation techniques are presented within this chapter. These methods form the foundations upon which the interrogation methodology developed within the PhD framework has been built. Finally, the discussion is concluded by the demonstration of image evaluation applied to a typical PIV experiment conducted on the wake behind a cylinder.

Nomenclature

β	bias error (pixels)
$\delta\xi_0^k$	fractional displacement obtained at k^{th} iteration (pixels)
Δt	time separation between successive recordings (seconds)
$\Delta x, \Delta y, \Delta z$	particle displacement along respective axes e.g. $\Delta x = u \cdot \Delta t$ (pixels)
ε	acceptable sub-pixel accuracy, error in intensity reconstruction (pixels)
ε_n	estimate of correlation noise (pixels)
$\varepsilon_{\delta x}$	fractional displacement error (pixels)
ε_{mod}	error in reconstruction due to modulation effects (arbitrary unit)
λ	imposed sinusoidal wavelength (pixels)
λ_m	minimum measurable flow length scale (pixels)
ξ_0^k	raw displacement field obtained at k^{th} iteration (pixels)
ξ^k	filtered and/or validated displacement field obtained at k^{th} iteration (pixels)
σ	random error (pixels)
ϕ	cross-correlation

ω_z	out-of-plane vorticity component ; $\omega_z = \partial v / \partial x - \partial u / \partial y$ (pixel/pixel)
C_ξ^k	displacement corrector for ξ obtained at k^{th} iteration (pixels)
F_0	fraction of particles lost due to out-of-plane motion
F_1	fraction of particles lost due to in-plane motion
h	vector spacing (pixels)
I_a, I_b	intensity distribution recorded at time ' t_0 ' and ' $t_0 + \Delta t$ '
k	iteration number
K	number of refinements
m, n	spatial shifts in horizontal and vertical direction (pixels)
N	number of samples
$N_1 F_0 F_1$	effective particle image density
r_c	normalized median threshold
t	time (seconds)
u, v	horizontal and vertical velocity components (pixels)
u_0	imposed sinusoidal amplitude (pixels)
WOR	window overlap ratio
W_S	correlation window size (pixels)
$W_{Sx,y,z}$	correlation window size along respective axes (pixels)
$\lfloor X \rfloor$	rounded value of variable X towards minus infinity
X_m	measured value of variable X
\overline{X}_m	ensemble average value of measured variable X
$X_{\max, \min}$	maximum and minimum value of variable X

2.1 Introduction

The basic particle image interrogation methodology presented so far is extremely suitable in the description of smooth flow fields i.e. in the assumption that the velocity difference between tracers belonging to the same interrogation area is negligible. Limits in spatial resolution become apparent however in case of stronger variations in tracer displacement, which are common to the majority of fluid dynamical applications.

The final achievable resolution depends on several parameters; the seeding density or inter-particle spacing, the digital imaging resolution expressed in pixels/mm (cf. section 1.2.4), the sampling rate (number of vectors per mm) and the spatial response of cross-correlation. The latter two contributions are inherent to the image evaluation technique and related to the interrogation window sizes as will be shown in this chapter. PIV's spatial response has therefore been a topic intensively covered with the aim to alleviate the resolution limit imposed by the finite dimensions of the interrogation window (e.g. Nogueira *et al.* 1999, 2005; Scarano 2003; Astarita 2007).

Furthermore, the effect of velocity gradients must be taken into account, especially when dealing with vortex dominated or turbulent flows that contain displacement fluctuations which result in random motion of seed particles. The appearance of a unique displacement as assumed in section 1.4.2 thus becomes highly unlikely and will cause a

failing of the correlation operator. Moreover, particles' out-of-pattern motions decrease the effectiveness of the statistical operator since they are imaged only once in either of the interrogation windows. This absence in particle image pairs is associated to particles entering or escaping the interrogation volume between laser pulses.

A general consensus has been reached in the PIV community on methodologies minimizing the effect of out-of-plane and out-of-pattern motion. Adequate measures have been extensively reported in literature and are discussed hereafter. In essence, each method aims at restoring the displacement uniformity within each selected interrogation area and maximizing the number of particle image doublets.

2.2 Single-pass cross-correlation analysis

The operating principle of basic PIV image analysis has been introduced in the previous chapter;

1. image pre-processing may be performed to reduce the influence of noise sources.
2. image recordings are divided into sub-sections of equal size, called interrogation areas or correlation windows.
3. corresponding windows between consecutive exposures are analyzed by means of spatial cross-correlation to extract the most probable motion of the ensemble of tracer markers that belong to the interrogation regions.
4. the correlation peak is fitted with a Gaussian distribution to achieve displacement estimates with sub-pixel accuracy.
5. the position of the correlation peak is converted into velocity knowing the optical magnification and time separation between two exposures

Denoting the light intensity distributions ' I_a ' and ' I_b ' at time instants ' t_0 ' and ' $t_0+\Delta t$ ' respectively, the local image displacement is evaluated as the absolute maximum in the cross-correlation function (2.1) and corresponds to the best match between the distributions in a statistical sense.

$$\phi(m, n) = \sum_{i,j} I_a(i, j) \cdot I_b(i + m, j + n) \quad (2.1)$$

According to this definition, the correlation operator only takes into account linear shifts ' (m,n) ' between the two images as a single parameter and acts as a rigid-block matching. In practice however, fluid motion is significantly more complex than pure translation and situations are often encountered (e.g. vortical flow, turbulent flow, flows with shock-waves, etc.) where basic cross-correlation is inadequate to yield representative motion estimates and may even fail entirely.

Failure is referred to situations where the highest correlation peak does not correspond to the particle average displacement. The causes for degradation in the correlation peak can be several; low seeding density, high image noise levels (CCD noise, background

noise, reflections, degraded optical access, etc.) and a strong velocity gradient. The purpose of data validation is then to detect the local occurrence of spurious vectors and increase the confidence level of the measurements.

Moreover, the spatial response of the correlation technique at this stage is poor and resembles that of a moving average, as will be shown in the remainder. Efforts in PIV image processing development are therefore aimed at improving the technique's response and alleviate factors limiting the robustness of the correlation operator. First, basic rules to consider in image evaluation with standard cross-correlation are discussed to appreciate advanced interrogation routines.

2.2.1 Basic rules for motion analysis

- *Minimization of loss of particle pairs due to out-of-plane motion*

PIV intrinsically estimates the displacement of image features, i.e. particle patterns. An adequate number of particle images is firstly needed to constitute a discernable pattern. At high image densities, particle images will furthermore overlap at each imposed correlation shift '(m,n)' (Fig. 2.1-a) requiring a sufficient number of tracer images to ensure a correlation peak related to the best overall match dominating this correlation noise level (Hart and Meinhart, 2003). Performances of the correlation operator are therefore strongly related to the number of particle image pairs.

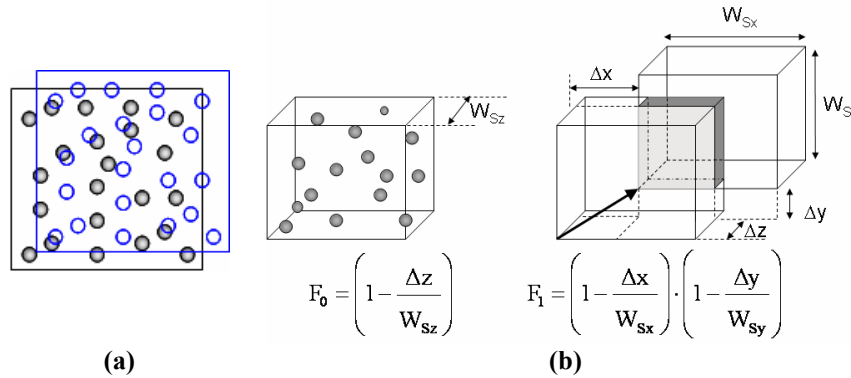


Fig. 2.1: (a) More than one particle image overlaps at any window offset, resulting in an increase in the relative correlation noise level compared to the peak correlation. (b) Assuming an interrogation volume with dimensions '(W_{Sx}, W_{Sy}, W_{Sz})', the effective particle image density is related to 'N_I' (in this example N_I=15 particle images) and the particles' in-plane motion '(Δx, Δy)' and out-of-plane motion 'Δz'. The volume ratio between the gray cube and original interrogation volume corresponds to 'F₀·F₁' (Keane and Adrian, 1992).

Because of in-plane motion, particle images escape the interrogation windows during the separation time. Furthermore, fluid motion perpendicular to the light sheet causes out-of-plane motion and consequently distortions of the traceable particle pattern. Keane and Adrian (1992) introduced the term *mean effective particle image density*, denoted as

' $N_1 F_0 F_1$ ', where the factors ' F_1 ' and ' F_0 ' represent respectively the in-plane and out-of-plane motion and ' N_1 ' denotes the particle image density. This effective density can be thought of as the number of common particle images recorded at two time instants within an interrogation volume (Fig. 2.1-b) or in other words the number of corresponding particles contributing to the correlation peak. On the basis of practical experience and following an assessment based on computer generated PIV images, Keane and Adrian proposed the following criteria to optimize the PIV performance;

The amplitude of the correlation peak is proportional to the number of image pairs present. Accordingly, the minimum number is 2 because this low density does not give enough pairs to unambiguously define the correct pairing of images or yield a sufficiently high correlation peak. The **image density** ' N_1 ' should in general be at least 15 to have a correlation peak above the noise in 90% of the cases.

Because interrogation areas have a fixed spatial location in the image analysis, particle motion between exposures causes certain particles to leave the interrogation volume either within or perpendicular to the plane defined by the laser sheet. To limit the reduction in the correlation peak amplitude as a result of this loss of particles, **maximum displacements** must be limited to $1/4^{\text{th}}$ the interrogation volume (Fig. 2.1-b). This recommendation is generally known as *the one-quarter rule*. Note that the constraint on the out-of-plane component can be relaxed to some extent by increasing the light sheet thickness (cf. section 1.2.2).

$$\Delta x/W_{S_x} \leq 0.25, \quad \Delta y/W_{S_y} \leq 0.25 \quad \text{and} \quad \Delta z/W_{S_z} = \Delta z/\Delta z_o \leq 0.25 \quad (2.2)$$

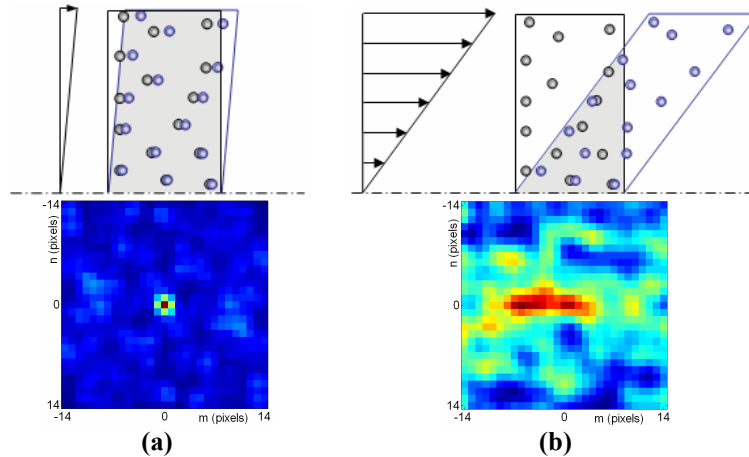


Fig. 2.2: (a) weak (0.01 pixel/pixel) and (b) strong (0.5 pixel/pixel) velocity gradient with typical correlation maps. Velocity gradients decrease the number of common particle images (the effective area is visualized by the gray overlapping area) in case of fixed, rigid interrogation windows (black rectangles) while retaining particles with lower velocities. If the windows would distort according to the reigning flow velocity (blue windows) all tracers would be retrieved.

Many applications of PIV involve turbulent flows exhibiting small scale velocity fluctuations, associated to **large spatial velocity gradients**. These gradients cause

additional disturbances in the image patterns as cartooned by Fig. 2.2, degrading the quality of correlation between the rigid interrogation windows pertinent to reliability and accuracy. With increasing velocity gradient the area of overlap decreases, indicating fewer particles contribute to the correlation (lower reliability). Due to the variety in captured displacements, the correlation peak broadens and flattens yielding increasing uncertainties in peak localization. The distortions in correlation map are clearly visible in Fig. 2.2. Moreover, the images of particles having smaller velocities remain inside the windows, biasing the displacement estimate towards lower values (less accuracy). Keane and Adrian (1990) therefore propose an upper limit of 5% for the displacement differences within the interrogation window with respect to the mean displacement.

- **Cross-correlation spatial response**

The spatial response of a spatial operator refers to its capability in accurately representing the various length scales present within a flow. Under ideal recording conditions (a black background with superimposed a homogeneous spatial distribution of particle images having identical diameters and identical peak intensities) the cross-correlation is known to return a volume averaged displacement (Willert and Gharib, 1991). Length scales smaller than the physical dimensions of the interrogation windows will be attenuated as a result of the correlation operation's low-pass filtering effect. Although the frequency response of the correlation function has a complex non-linear behavior, a qualitative approximation can be obtained using the moving average frequency response as a model (Nogueira *et al.*, 1999).

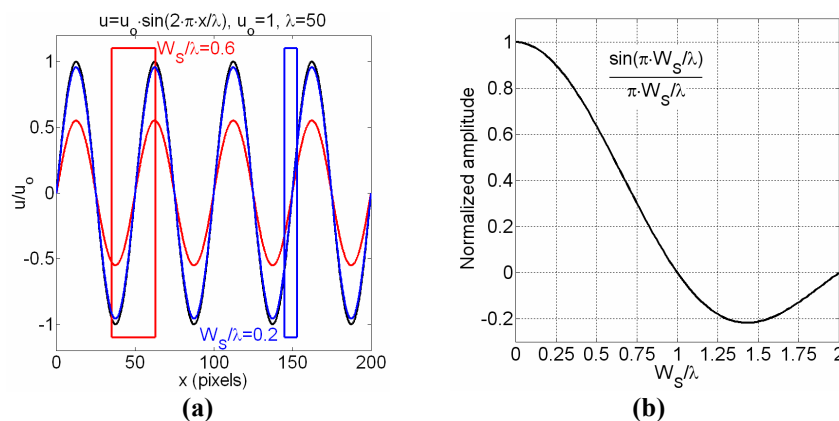


Fig. 2.3: (a) Starting from a given sinusoidal displacement field (—) moving averaging filters of various size (—, —) are applied. The amplitude of the filtered sinusoids (—, —) decreases with increasing filter kernel. (b) Plotting the ratio between retrieved and imposed amplitude versus normalized window size yields the spatial response (—).

Figure 2.3-a graphically explains the reasoned similarity by considering a sinusoidal displacement field. The modulation in amplitude of the filtered sinusoids becomes appreciable at larger values of the normalized filter kernel. Based on these considerations,

accurate measurement (within 10%) of the velocity spatial fluctuations would require a window-size below 20% of the spatial wavelength of the velocity distribution (Fig. 2.3-b) as reported by Scarano (2002). In other words, the smallest resolvable physical length scale with PIV, ' λ_m ', must be sampled by at least 5 windows of size ' λ_m '. This emphasizes the necessary accuracy-resolution trade-off. Decreasing the window size enhances the spatial response but lowers the accuracy on the basis of the reduced image density and equation (2.2). Clearly the interrogation window size requires a meticulous selection.

- ***Interrogation cell overlap***

On the account of widespread applications reported over the last decade, a general consensus has been reached on the PIV technique's limits in spatial resolution. The limiting factors have been identified as under-sampling of the continuous flow field either through insufficient seeding or too coarse vector spacing and volume averaging (Nogueira *et al.*, 2005). Whereas the limits imposed by seeding spacing can only be controlled experimentally, volume averaging is governed by the applied window size and light-sheet thickness. The vector spacing ' h ' is prescribed in the processing stage by imposing a certain window overlap ratio ' WOR ';

$$h = (1 - WOR) \cdot W_s \quad (2.3)$$

The minimum detectable wavelength, i.e. ' λ_m ' at which the measured amplitude equals zero (Fig 2.3), theoretically corresponds to the adopted window size ($W_s/\lambda_m=1$). Ensuring adequate flow sampling by a sampling rate at least two times the frequency encountered in the flow translates into the typical minimum window overlap ratio of 50%;

$$h \leq 0.5 \cdot \lambda_m \rightarrow 2 \cdot (1 - WOR) \cdot W_s \leq \lambda_m \rightarrow WOR \geq 0.5 \quad (2.4)$$

In these conditions the error is dominated by the modulation effect.

2.2.2 Vector validation

Measurement results with PIV may contain spurious displacements which degrade the reliability and accuracy of statistical flow information (Westerweel, 1994). In general, spurious displacement estimates are the result of interrogation spots containing insufficient particle-image pairs, causing random correlation peaks to dominate the true peak in amplitude. An accustomed measure of the correlation peak's ascendancy and reliability is the *signal-to-noise ratio* defined as the amplitude ratio between the highest and second highest correlation peak. High ratios indicate high certainty in valid peak detection allowing a threshold criterion to act as first displacement validation. A typical threshold in signal-to-noise of 1.5 is often imposed.

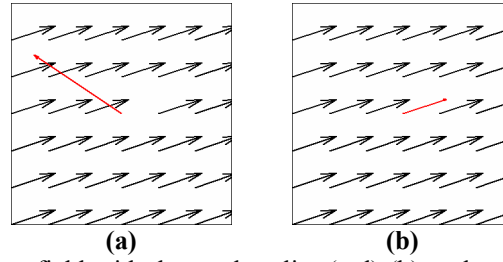


Fig. 2.4: (a) Uniform vector field with detected outlier (red) (b) replacement of outlier by linear interpolation.

Stray vectors show unphysical deviations in magnitude and direction from nearby vectors (Fig. 2.4-a). Accordingly Westerweel (1994) proposes detection through a comparison of each vector with its close neighbors considering the local velocity median and standard deviation. In line of this observation the recent normalized median test (Westerweel and Scarano, 2005) has been introduced for its robustness and efficient detection capability also in situations where multiple outliers appear. If the vector does not satisfy the condition presented in (2.5), the vector is excluded from the data-set and substituted by an interpolation of neighboring values (Fig. 2.4-b). Typical values for the threshold ‘ r_c ’ range between 2 and 4.

$$\frac{|\xi_i - U_m|}{r_m + \varepsilon_n} \leq r_c \quad \text{where} \quad \begin{aligned} U_m &= \text{median}(\xi_k) \\ r_m &= \text{median}(|\xi_k - U_m|) \end{aligned} \quad \text{with } k=1 \dots n \quad (2.5)$$

where ‘ ξ_i ’ represents the analyzed vector and ‘ ε_n ’ is a conservative estimate of the cross-correlation noise (≈ 0.1 pixels). The median of the vectors $\{\xi_1, \dots, \xi_n\}$ within the neighborhood of ‘ ξ_i ’ is represented by ‘ U_m ’. Vectors falling within a spatial extent (from the location of ‘ ξ_i ’) of 1.5 times the locally reigning window size are considered to be neighbors. The normalization factor ‘ r_m ’ is estimated as the median of the deviations between the neighboring vectors and the median ‘ U_m ’.

2.3 Iterative interrogation methods

2.3.1 Multi-grid analysis with discrete window offset

The selection of the interrogation window size in case of basic cross-correlation is based on a compromise between accuracy and spatial resolution (cf. section 2.2.1). On one hand smaller windows improve the spatial resolution, but on the other hand the window must be sufficiently large to provide a sufficiently large effective particle image density and ensure a detectable correlation peak.

As a result of the finite extent of the interrogation windows, the selected segments of image signal can be modeled as the product between the complete image signal and top-

hat windows. The auto-correlation of these distributions thus creates a weighting of the original correlation map with higher values close to the origin (Westerweel, 1997). As a result, basic cross-correlation yields displacement measurements which systematically underestimate the actual particle image displacement. This velocity bias is appreciable when observing the negative sign of the mean error in displacement (Fig. 2.5). Corrections for this effect are based on a proper normalization of the correlation function or the use of interrogation windows with different sizes (Westerweel, 1997).

An alternative solution is provided by discrete window offset (Westerweel *et al.* 1997, Scarano and Riethmuller 1998); interrogation windows are offset by the integer part of the particle image displacement. This technique compensates for the in-plane loss of pairs and yields a more accurate result compared to the original analysis (Fig. 2.5). Figure 2.5 demonstrates the advantage of sub-pixel window offset over discrete window offset; bias errors are practically removed and random errors are reduced to levels in the order of 10^{-3} pixels.

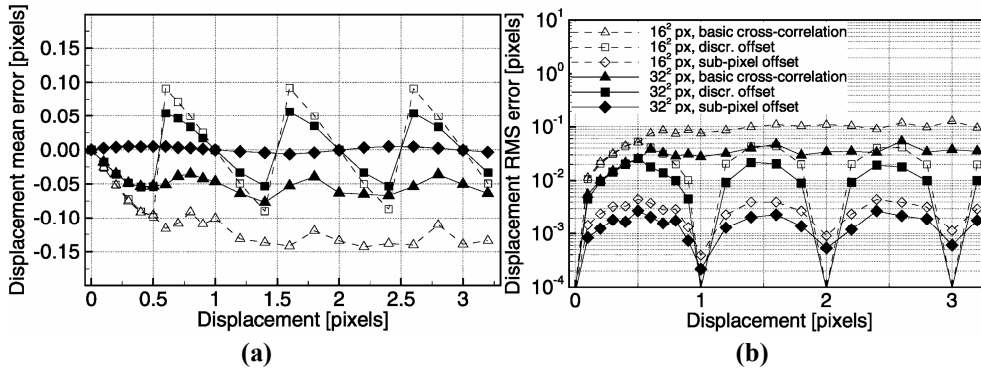


Fig. 2.5: (a) Mean displacement error (imposed – measured displacement) and (b) displacement RMS error as a function of the displacement for different window sizes and offset procedures based on synthetic images (taken from Scarano and Riethmuller, 2000).

The local displacement of each interrogation area is anticipated by a flow pattern obtained by a previous interrogation, which implies the need of adopting an iterative procedure.

As the window shift technique alleviates the constraint on the interrogation window size to maximize the number of particle doublets imposed by the one-quarter rule, smaller window sizes can be applied to simultaneously improve the correlation's spatial response and dynamic velocity ranges about three orders of magnitude[†] (Adrian, 1997). This is the underlying rationale of multi-grid analyses.

[†] The dynamic range is a measure of the technique's ability to represent velocity differences and is defined as $(u_{\max} - u_{\min}) / u_{\min} = c_1 W_s / \lambda_m - 1$. Ratios close to unity imply poor spatial resolution as minimum measurable wavelengths ' λ_m ' are in the order of the interrogation window size ' W_s '. For basic cross-correlation, the ratio ' c_1 ' between the maximum in-plane displacement and the window

At the start of the process the interrogation window size is set respecting the one-quarter rule for the in-plane motion. The subsequent iteration consists of reducing the window sizes and using the previously coarse result to guide the integer window offsets.

2.3.2 Multi-grid analysis with window deformation

To overcome the problems inherent to velocity variations within interrogation areas, smaller interrogation volumes must be applied. These bound the displacement variation within but are in conflict with the image density requirements. A reduction in time separation between the images also circumvents the problematic, yet exacerbates to unacceptable relative displacement errors (Boillot and Prasad, 1996).

The possibility to iteratively describe the velocity field allows an estimation of not only the displacement field but also the spatial distribution of the velocity gradients. In the correlation matching procedure, the domain transformation by rigid blocks (cf. equation 2.1) is replaced by an approximation in space of the displacement distribution (2.6). Accordingly, the affine motion provides a better representation of the actual fluid motion by taking into account the deformation of fluid elements due to shear, rotation or dilation and maximizes the number of matching particle images between the two exposures. As shown in Fig. 2.6 the displacement distribution can be approximated by different orders of domain transformation. A first order, linear, interpolation generally suffices.

$$\phi(\vec{d}) = \int I_a(\vec{x}) I_b(\vec{x} + \vec{d} + \nabla \vec{d} \cdot \vec{x}) d\vec{x} \quad (2.6)$$

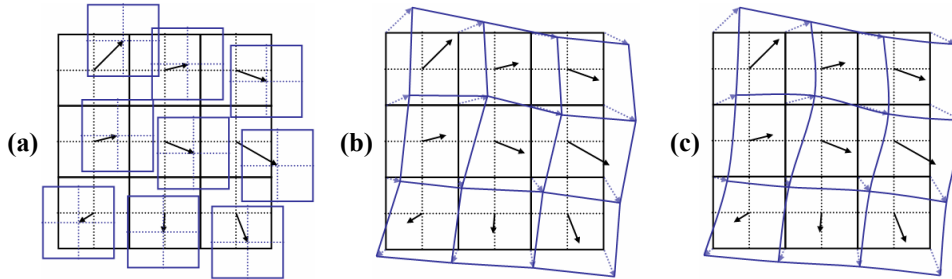


Fig. 2.6: Schematic of the adopted iterative domain transformations; (a) rigid body (b) first (c) high order. Black lines represent the domain at time ' t_0 ', blue lines the one at ' $t_0 + \Delta t$ '.

linear size, equals $\frac{1}{4}$ according to the one-quarter rule (section 2.2.1). With velocity uncertainties in the order of 0.1 pixels (Willert and Gharib, 1991), and typical window sizes of 32 pixels, a dynamic range of two orders of magnitude is obtained. With window discrete offset and multigrid resolution, the uncertainty is reduced to 0.01pixels (Fig. 2.5) and the maximum displacement may exceed the window size yielding an increase in dynamic range by at least an order of magnitude

By recursively distorting the images following a predicted displacement field (Huang *et al.* 1993^{a,b}; Scarano and Riethmuller 2000) demonstrated that a velocity gradient up to 0.5 pixels can be followed.

It is evident that a proper image interpolation procedure is needed to evaluate intensity values at non-integer positions. Because of this fractional window offset, the fractional pattern displacements intrinsically diminishes iteratively to zero which practically minimizes any effect of peak-locking (Scarano, 2002). The latter is evidenced by the systematic analysis performed by Scarano and Riethmuller (2000) shown in Fig. 2.5; bias errors remain below 0.01 pixels with RMS levels reduced to 10^{-3} pixels. Additionally, deformation of the interrogation areas compensates for the in-plane loss of pairs due to velocity gradients (as indicated by the blue sheared window in Fig. 2.2) augmenting the correlation-peak amplitude, reducing the gradient bias and allowing a further improvement of the dynamic velocity range.

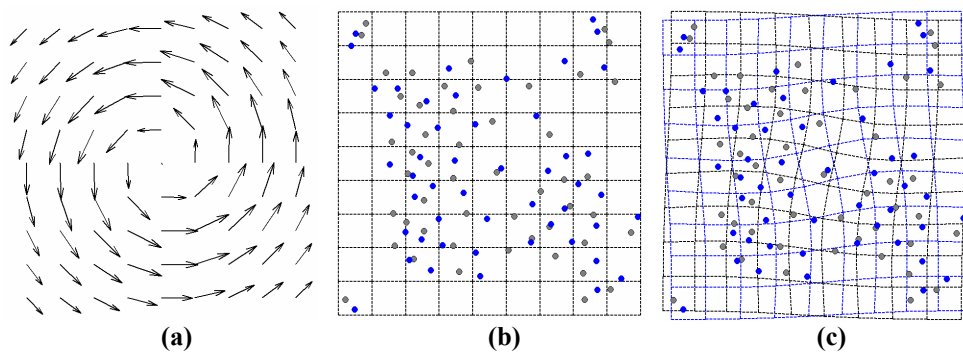


Fig. 2.7: Example of window distortion. (a) imposed vortex flow. Compared to the rigid and fixed correlation windows (b) distortion of the corresponding interrogation cells (c) allows a better matching of the particle patterns recorded at time ‘t’ (●) and ‘t+ Δt ’ (●) by assuming the estimated deformation of the fluid elements.

Figure 2.7 visually explains the latter benefit by considering the example of rotational flow; following the vortical flow pattern in Fig. 2.7-a, particle images recorded at time instant ‘t’ (●) shift towards their new position at time ‘t+ Δt ’ (●). When keeping the interrogation windows fixed and rigid (Fig. 2.7-b), particles move out of the windows and cause a loss in particle image pairs (i.e. no matching between gray and blue particles within a window). The latter becomes especially evident near the vortex center where stronger displacement gradients occur. The reduction in effective image density will consequently cause a spurious vector. On the contrary, when the images are deformed (Fig. 2.7-c), corresponding interrogation windows retain particle image pairs thereby increasing the probability of correlating the same particles with each other and increasing the probability of detecting a valid correlation peak.

2.3.3 Implementation

The above mentioned interrogation improvements have become general concepts in the PIV community and standard in commercialized PIV software (e.g. DaVis^{LaVision}, FlowManager^{Dantec Dynamics}, etc.). Nowadays, image interrogation procedures are typically composed of the main steps shown in Fig. 2.8. Within this paragraph, further details are provided concerning their implementation.

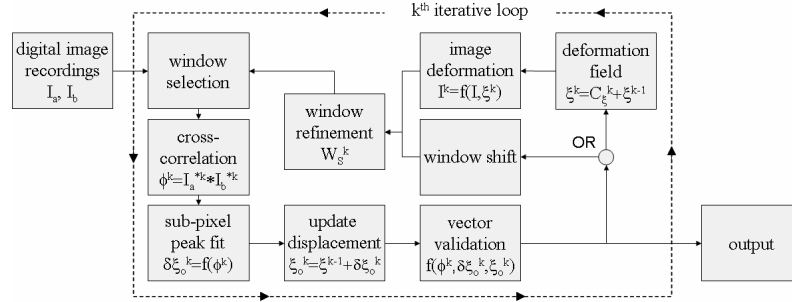


Fig. 2.8: Layout of a typical iterative image interrogation routine adopting discrete window offset or image deformation ($\xi = u, v$).

- **Window refinement**

Windows are iteratively reduced according to relation (2.7), which imposes a gradual refinement;

$$W_S^k = W_S^K + (W_S^0 - W_S^K) \cdot \left(\frac{K - k}{K} \right)^2 \quad \text{where } W_S^K = \frac{W_S^0}{2^K} \quad \text{and } k=0, 1, \dots, K \quad (2.7)$$

where ‘K’ refers to the number of refinement steps and ‘k’ the iteration number. The initial window size ‘ W_S^0 ’ can be chosen arbitrarily but must not exceed one-fourth of the maximum displacement to minimize in-plane loss of particle images and assure a detectable correlation peak (Keane and Adrian, 1990). The lower limit in possible final window size ‘ W_S^K ’ remains dominated by the need of a sufficient quantity of corresponding particle images to avoid spurious/erroneous displacement estimates. The number of refinement steps must therefore be selected with meticulous care.

- **Vector validation**

For iterative algorithms the validation is even more crucial because the deleterious effect of an outlier at early iterations can compromise the final result to a relatively large extent. Prior to the interpolation sequence, a thorough validation procedure is therefore needed as to eliminate spurious vectors.

Besides the two criteria introduced in section 2.2.2, additional criteria can be proposed which are based on the knowledge that the fractional displacement should gradually decrease towards zero as a result of iterative image distortion. The first measure consists in a recursive reduction of the correlation peak's search area centered on the origin. Typically halving the radius aids in effectively minimizing the probability of detecting stray random correlation peaks. The second related criterion considers the convergence of the displacement estimates;

$$\left| \frac{C_{\xi}^k}{\varepsilon + \text{median}\{C_{\xi}^n\}} \right| \leq 2 \quad \text{with } n=0,1,\dots,k-1 \quad \text{and } C_{\xi}^k = \xi^k - \xi^{k-1} \quad \text{and } \xi=u, v \quad (2.8)$$

where the displacement in ξ -direction measured in the k^{th} iteration is symbolized by ' ξ^k ' and ' ε ' is an estimate of the acceptable sub-pixel accuracy. While an accuracy of 0.1 pixels suffices for displacements in excess of a pixel, sub-pixel displacements may require more stringent accuracies;

$$\varepsilon = 10^{r-1} \quad \text{with } r = \left\lfloor \frac{1}{\log(10)} \log \left(\sqrt{\sum_{\xi=u,v} \text{med}_{\xi}^2} \right) \right\rfloor - 1 \quad \text{and } \text{med}_{\xi} = \text{median}\{\xi^n\} \quad (2.9)$$

The empirical relation (2.9) ensures the required sub-pixel accuracy to be an order of magnitude below the total displacement. As an example, a displacement corrector ' C_{ξ}^k ' of 0.1 pixels with a median of 0.01 pixels yields according to (2.8) a valid ratio of 0.90 for ' $\varepsilon=0.1$ '. While this corrector would be acceptable for displacements in excess of a pixel, this level of accuracy is unsuitable for sub-pixel displacements ($\xi^k < 1$ pixel). This stringent restriction is incorporated by requiring higher sub-pixel accuracy, one order below the displacement measurement i.e. ' $\varepsilon=0.01$ ' (yielding an invalid ratio of 5).

- ***Image deformation***

To enlarge the measurable velocity gradient range, matching between regions which undergo transformation has to be improved. Interrogation windows are deformed (read, images are distorted) respectively forwards and backwards by half the imposed displacement as depicted in Fig. 2.7-c and expressed in equation (2.10). This central difference interrogation philosophy has been proven to produce second order accuracy, compensating to an extent for the effect of particle path curvature (Wereley and Meinhart, 2001).

$$I_a^k = I_a \left(i - \frac{u^k}{2}, j - \frac{v^k}{2} \right) \quad \text{and} \quad I_b^k = I_b \left(i + \frac{u^k}{2}, j + \frac{v^k}{2} \right) \quad (2.10)$$

The predictor ' ξ_o^k ' guiding the image deformation is iteratively updated; the window displacement evaluated at the $k-1^{\text{th}}$ iteration is corrected by the term ' $\delta\xi_o^k$ ' which follows from the cross-correlation of the deformed images;

$$\xi_o^k = \xi^{k-1} + \delta\xi_o^k \quad (2.11)$$

In this work the deformation is given by a continuous first order approximation of the discrete displacement field by means of bi-linear interpolation over all the pixels (Fig. 2.6-b). Though linear interpolation is in general less accurate compared to higher order interpolation schemes (e.g. Tokumaru and Dimotakis, 1995), it has the advantage of requiring less CPU time. Moreover, in comparison with the error introduced by modulation, the increase in accuracy is negligible at larger window overlap ratios.

- **Interrogation cell overlap**

The statement that the increase in accuracy is negligible at larger window overlap ratios when applying higher order interpolation schemes to predict the displacement field for image deformation, is argued with a numerical example. One-dimensional sinusoids of various wavelength ' λ ' are considered which are sampled by regularly spaced windows of size ' W_s ' (Fig. 2.9-a). The spacing is defined by equation (2.3). The response of the correlation windows is modeled as a moving average and retrieved values are interpolated pixel-wise to calculate the difference between the original and reconstructed sinusoid (Fig. 2.9-b).

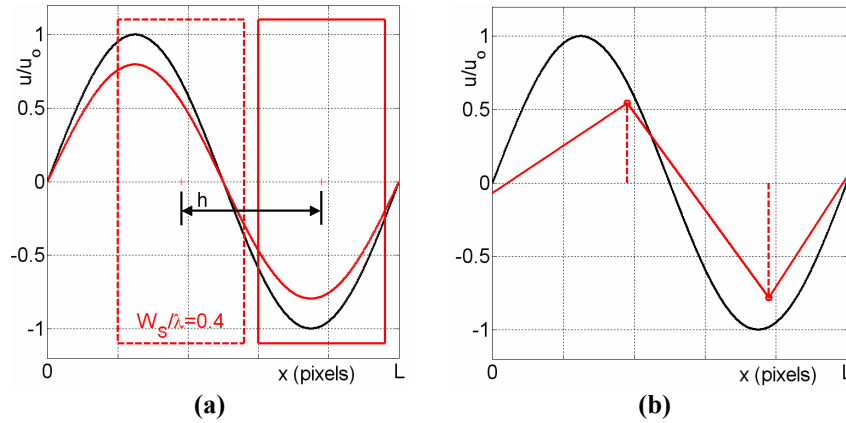


Fig. 2.9: (a) The imposed sinusoid $u_o \cdot \sin(2\pi x/\lambda)$ (black line) is sampled by windows of various size at discrete locations separated by distance ' h ' (equation 2.3). The response of the correlation operator is assumed to be that of a moving average. (b) The difference between the reconstructed sinusoid from the discrete samples (red line) and the original sinusoid is used as a measure for the reconstruction error.

In Fig. 2.10 the evolution of the absolute reconstruction error $|\varepsilon|$, integrated over a wavelength and normalized with imposed amplitude u_o (2.12), is plotted versus normalized window size for different window overlap ratios and a linear and quadratic interpolant (Dogson, 1997). The reconstruction error gains amplitude with W_s/λ , which is to be anticipated in view of growing modulation effects (ε_{mod}). Vector spacing proves to be important as increasing window overlap ratios provoke a reduction in error. Moreover, in case of high overlap coefficients, the reconstruction error is clearly dominated by ε_{mod} given by (2.13).

$$\frac{|\varepsilon|}{u_o} = \frac{1}{u_o \lambda} \int_0^\lambda |u_o \sin(2\pi \frac{x}{\lambda}) - u(x)| dx \quad (2.12)$$

$$\begin{aligned} \frac{\varepsilon_{\text{mod}}}{u_o} &= \frac{1}{u_o \lambda} \int_0^\lambda |u_o \sin(2\pi \frac{x}{\lambda}) - u_{\text{mod}} \sin(2\pi \frac{x}{\lambda})| dx \\ &= \frac{1}{\lambda} \left(1 - \text{sinc}\left(\frac{W_s}{\lambda}\right)\right) \cdot \int_0^\lambda |\sin(2\pi \frac{x}{\lambda})| dx = \frac{2}{\pi} \left(1 - \text{sinc}\left(\frac{W_s}{\lambda}\right)\right) \end{aligned} \quad (2.13)$$

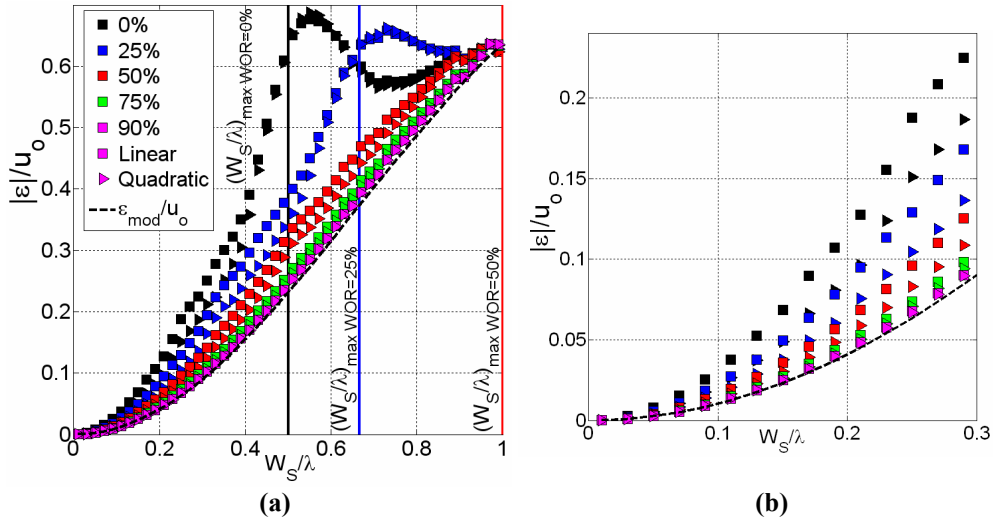


Fig. 2.10: Numerical comparison between linear and higher order interpolations modeling the correlation operation as a moving averaging filter in case of a sinusoidal displacement $u_o \cdot \sin(2\pi x/\lambda)$. The displacement estimates at discrete locations were interpolated pixel-wise over a single wavelength from which the reconstruction error could be determined. (a) Evolution of the error with normalized window size for different window overlap ratios. (b) Zoom for $W_s/\lambda < 0.3$.

Nyquist's sampling criterion combined with the relation between sample spacing h ($h/\lambda_m \leq 1/2$) and window overlap ratio 'WOR' (equation 2.3) imposes an upper bound for the normalized window size indicated by the vertical lines. Above the limit value the sinusoid is subject to under-sampling rendering accurate reconstruction impossible,

independent of the interpolant order. When proper sampling is ensured, application of the higher order interpolant offers a reduction in reconstruction error only for low WOR. However, the advantages remain questionable; the gain in error reduction when changing between linear and quadratic interpolation is marginal compared to the total reconstruction error. Overlap ratios of 75% turn out to be a good trade-off between computational effort and error since discrepancies with 90% WOR are minute inherent to an over-sampling.

Concluding, as the normalized window size approaches zero or overlap ratios in the order of 75% are selected, lower order interpolation schemes show to be sufficient as higher order schemes are no longer beneficial and modulation effects dominate the error transmission. Moreover, only overlap factors of at least 75% ensure that the signal modulation is solely associated to the window size and not to the data spacing which is in agreement with Schrijer and Scarano (2008) and Astarita (2007).

- ***Image interpolation***

Since the images must be deformed with sub-pixel accuracy, intensity re-interpolation is necessary. Scarano and Riethmuller (2000) implemented the cardinal function interpolation following Hall (1979) related to the image reconstruction. Image reconstruction however has a broad range of applications such as e.g. medical imaging and computer graphics and each discipline offers its own number of research articles devoted to finding the best image interpolation scheme (e.g. Mitchell and Netravalli 1988, Dodgson 1997, Thévenaz *et al.* 2000). Overall, the preferred schemes are those involving splines of various orders (Lehmann *et al.*, 2001). Astarita and Cardone (2005) and Kim and Sung (2006) indeed separately conclude quintic B-spline interpolation to offer the best trade-off between accuracy and computational time after conducting a performance assessment of various schemes based on synthetic images. In parallel, Lecordier and Trinité (2006) showed B-spline interpolation to have better performances compared to the cardinal function based on real particle images. While retaining the accuracy, the computational effort involved showed a drastic decline.

In the remainder of the presented work, quintic B-spline interpolation will be applied when image re-interpolation is involved. The algorithmic implementation is based on the procedure described by Unser *et al.* (1993^a, 1993^b) which yields a considerable reduction in execution time.

2.4 Advanced iterative interrogation methods

2.4.1 Predictor filtering

One of the main results of the worldwide PIV Challenges (Stanislas *et al.*, 2005, 2008) is the recognition that iterative image deformation has become a standard interrogation method, where the most straightforward approach of setting the predictor equal to the value obtained from the previous interrogation is adopted. While this approach avails in

coping with flows exhibiting large velocity gradients, Nogueira *et al.* (1999) reported the occurrence of a numerical instability causing the growth of a sinusoidal wave when using multigrid PIV methods incorporating equation (2.11).

The nature of this unstable behavior has been linked to the negative amplitude response shown in Fig. 2.3. Analyses have shown that flow wavelengths $2/3$ times the applied window size are amplified corresponding to the maximum of the first sign reversal in the spatial response (Scarano, 2004) as explained in Fig. 2.11. In the idealized case of a sinusoidal velocity field with ' $W_s/\lambda=1.5$ ', the measured displacement at the centre of the interrogation window is the opposite of the imposed. Consequently, images are deformed in opposite directions, increasing the deformation between matching particle patterns tending towards a higher probability in formation of spurious vectors (Nogueira *et al.*, 2001). When implementing successive iterations this process will diverge and unrecoverable errors will occur.

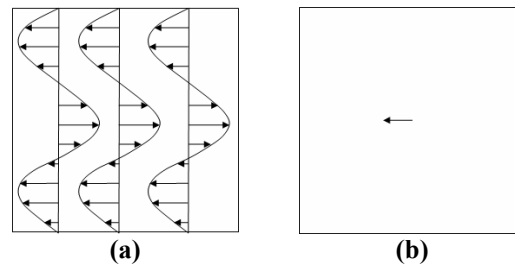


Fig. 2.11: Example of instability origin (a) interrogation window containing a sinusoidal displacement field, $W_s/\lambda=1.5$ (b) measured displacement.

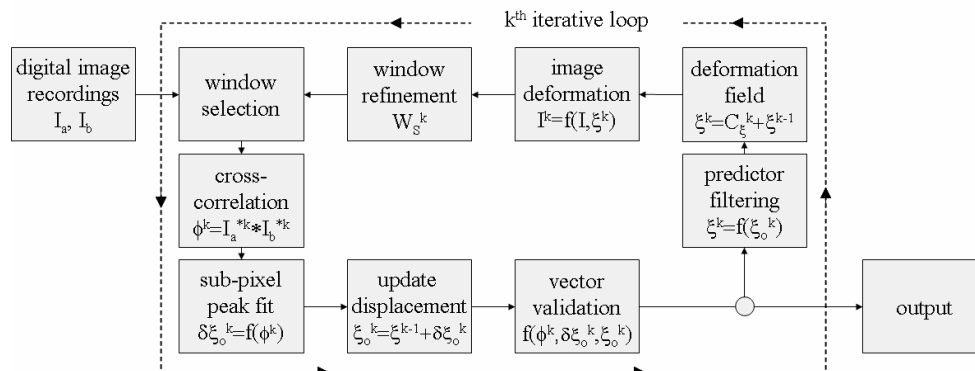


Fig. 2.12: Flow diagram of a iterative predictor-corrector image interrogation with predictor filtering (Note, ξ may represent either the u displacement component or the v -component).

With the aim of stabilizing the iteration scheme, Schrijer and Scarano (2008) investigated both numerically and theoretically filtering methods for the predictor and reported a second order polynomial least-squares regression to yield limited modulation effects with simultaneous reduction in RMS values. Based on their findings, the current work implements the 2nd order polynomial regression model defined in (2.14) involving

all neighboring displacement estimates within a radius of $\frac{3}{2} \cdot W_S^k$. Once the unknown coefficients have been determined, the displacement values ξ_o^k are substituted by their counterparts ξ^k prescribed by the analytic function.

$$\xi_i^k(x_i, y_i) = a_{\xi,i} x_i^2 + b_{\xi,i} y_i^2 + c_{\xi,i} x_i y_i + d_{\xi,i} x_i + e_{\xi,i} y_i + f_{\xi,i} \quad (2.14)$$

The flow chart of the predictor-corrector iterative loop (Fig. 2.8) has been repeated in Fig. 2.12 with the additional stage of predictor filtering. The option of window shifting has been omitted since the window deformation also includes the case of window shifting.

2.4.2 Performance assessment

- *Synthetic images*

The performance of the advanced iterative image interrogation routine described afore is assessed by means of synthetic images (Stitou, 2003). Zero background intensity arrays of 256-by-256 pixels² were populated by particles at random locations followed by an integration of the Gaussian particle image intensity distributions over the virtual sensor. A pixel fill factor of 0.7 was adopted. The maxima in particle intensity amplitude were selected randomly between 0 and 255 corresponding to 8bit images. A normal distribution in particle image size was assumed with a mean particle image diameter of 3 pixels and a standard deviation of 1 pixel. In total the generated images contained 5243 particles corresponding to a particle density of 0.08 particles per pixel.

- *Spatial resolution*

Figure 2.13 shows the spatial response of the implemented interrogation procedure considering a 1D sinusoidal displacement field of varying wavelength λ and a constant amplitude of 2 pixels, omitting image noise. The image interrogation was performed with window sizes of 33 pixels, imposing a window overlap ratio of 90% to exclude influences of poor vector spacing (cf. Fig. 2.9 and Fig. 2.10). Measured amplitudes were extracted from a sinusoidal fit to the resulting displacement fields.

Evident from Fig. 2.13 is the non-linear behavior of the cross-correlation routine. The spatial response clearly exhibits an evolution surpassing that of the moving average filter, the latter being defined as $\text{sinc}(W_S/\lambda)$. Whereas the moving average returns 80% of the imposed amplitude for wavelengths 2.8 times the imposed window size ($W_S/\lambda \approx 0.36$), this lower limit is now further reduced to a factor of about 2 ($W_S/\lambda \approx 0.6$).

The attenuation of sub-grid scales is of importance especially in turbulence measurements. To ensure sufficient resolution Westerweel *et al.* (1996) applied arguments similar to those found in DNS simulations; $(W_S \cdot W_S \cdot \Delta z)^{1/3} < \pi \cdot \eta$, where Δz refers to the laser sheet thickness and η the Kolmogorov length scale. When flow

integral length scales are less than around ten times the size of the interrogation cells, Spencer and Hollis (2002) report significant errors in second-order statistics calculated from the velocity field measured with the conventional metrologies. With increasing order of the involved statistics, requirements become more stringent yielding spatial resolutions of around twice the Kolmogorov scale to enable the measurement of 90% of the turbulent energy dissipation (Saarenrinne *et al.* 2001, Baldi and Yanneskis 2004). As the window size can now be enlarged while retaining a sufficiently low modulation, the robustness of the interrogation method can be increased. Vice versa, for a given window size the modulation error is decreased yielding more accurate velocity estimates.

In view of the above the use of a window overlap factor above 0.5 is justified in case of iterative image deformation. In fact, for an overlap factor of 0.5, the effect of discrete sampling would introduce an error significantly larger than the modulation error. The two errors instead become comparable when an overlap factor of 0.75 is used.

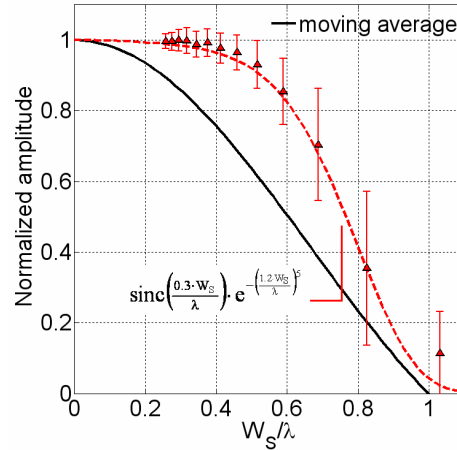


Fig. 2.13: Spatial response of the implemented interrogation procedure when applying uniform window sizes placed on a structured grid with 90% window overlap. Error bars indicate 95% confidence level.

- **Accuracy**

Particle images were uniformly displaced with intervals of 0.05 pixels to assess the accuracy of the interrogation algorithm. Both ideal conditions and more realistic conditions were considered simulating image noise with a mean intensity of 40 gray levels and a variation of 10. The interrogation was performed with two refinement steps starting with window sizes of 81 pixels² and 63 pixels² yielding final window sizes of 33 pixels² and 15 pixels² respectively. A global window overlap ratio of 75% was applied resulting in a number of velocity samples ‘N’ at least 25 10⁴.

$$\beta = \frac{1}{N} \sum_{i=1}^N (u_{m,i} - u) = \overline{u_m} - u \quad \text{and} \quad \sigma = \sqrt{\frac{1}{N} \sum_{i=1}^N (u_{m,i} - \overline{u_m})^2} \quad (2.15)$$

Bias error ' β ' and random error ' σ ' are presented in Fig. 2.14 and are defined in (2.15) in accordance with Gui and Wereley (2002) where ' $u_{m,i}$ ', ' u ' and ' $\overline{u_m}$ ' are respectively the measured, the imposed and the mean measured displacements.

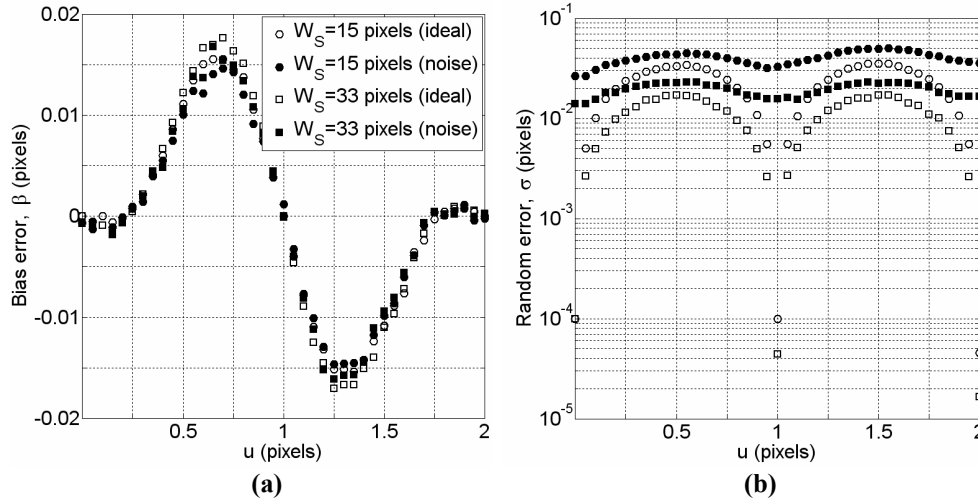


Fig. 2.14: (a) Bias measurement error (b) Random measurement error for different window sizes and imaging conditions.

The bias error is observed to have a periodicity of two pixels crossing zero at integer displacements which is in agreement with the observations of Scarano and Riethmuller (2000) and Astarita and Cardone (2005). The period of two pixels can be easily explained by noting the symmetric image deformation in equation (2.10). Only when the imposed displacement is a multiple of 2 are both images displaced over an integer number of pixels leading to zero errors in intensity reconstruction. The latter would correspond to the asymmetric situation where one of the two images is translated over one pixel.

A slight peak-locking can still be observed as measured displacements are biased towards integer values. In the present work the bias error reaches absolute maxima of 0.015 pixels at displacements of one plus-minus a quarter pixel whereas the research mentioned afore reported maxima at fractional displacements of 1 ± 0.5 pixels. This discrepancy is thought to be the result of the difference in implemented predictor filter.

Whereas the introduction of image noise or enlarging the interrogation area leads to minimal variations in bias error, the effects become more pronounced in the random error. Minima in random error are again reached for zero fractional displacements and maxima of in average 0.013 pixels are attained for fractional offsets of half a pixel, yielding a dynamic velocity range of almost three orders of magnitude when considering a maximum displacement of typically 8 pixels. Enlarging the interrogation area is clearly beneficial in reducing the variation in error while image noise yields an increase in ' σ ', as to be expected.

2.5 Typical PIV experiment: Cylinder wake

A typical PIV experiment is considered in the following to illustrate the interrogation routine improvements discussed within this chapter. As benchmark, the case of the wake flow behind a cylinder at a Reynolds number ' Re_D ' of 2000 (based on the diameter) has been considered as it contains challenging flow features; strong spatial gradients in the separated shear layers and vortical structures convected downstream.

2.5.1 Background

The flow behind a submerged cylinder is likely to be the most famous and well-studied flow in fluid mechanics. Depending on the Reynolds number (based on the cylinder diameter; ' Re_D ') intricate and complex 3D patterns appear in the unstable wake (Williamson, 1996).

As the laminar boundary detaches from the cylinder a turbulent wake is formed. The wake consists of pairs of vortices shed alternatively from the upper and lower part of the cylinder (Fig. 2.15-a). The vortices are arranged in two staggered rows with opposite sense of rotation; the so-called *street vortex* (Fig. 2.15-b). Even though the wake becomes more complex and turbulent with increasing Reynolds number, the alternate shedding can still be detected up to $Re_D \approx 10^7$. For the current Reynolds number of 2000, literature (Lienhard, 1966) reports a Strouhal number for vortex shedding of 0.21 ± 0.05 .

Vortex streets occur in almost any bluff body flow and are of importance to engineering structures. As the vortices (with opposite circulations) are shed off alternately, an oscillating lift force is generated. A frequency of vortex shedding close to the natural frequency of some mode of vibration of the structure will result in an appreciable lateral vibration which may lead to structural failures.

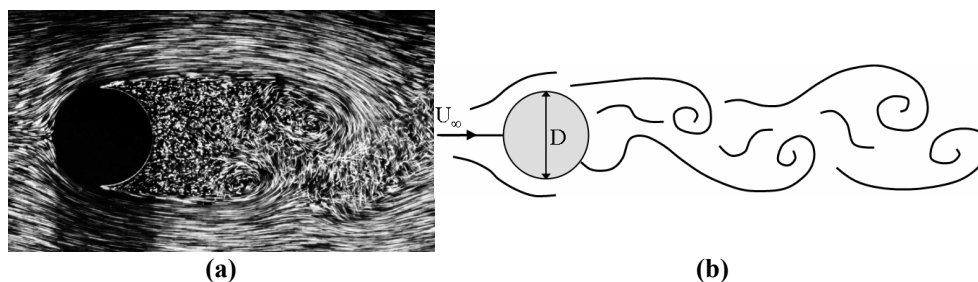


Fig. 2.15: (a) Boundary layer separation for a circular cylinder at $Re_D=2000$ (taken from Van Dyke, 1988). The pocket of slow (with respect to the freestream velocity ' U_∞ ') fluid motion behind the cylinder is visible as well as the onset of the oscillating wake (b) Schematic of the oscillating wake pattern.

2.5.2 Experimental facility

Experiments were conducted in a low-speed windtunnel with a turbulent free stream velocity of 3.1 m/s. A cylinder of 1cm in diameter was placed in a test-section height of

9.5 cm. Measurements were performed in the vertical mid-plane to avoid wall interferences.

Oil droplets with mean diameters of $1\mu\text{m}$ provided the necessary flow seeding. Droplets were generated by a Laskin's nozzle seeding generator which works on the principle of oil vaporization to produce smoke.

An 8bit TSI camera (640×480 pixels²) recorded the scattered intensities within a thin laser sheet ($\sim 1\text{mm}$ thickness). The light sheet was formed by letting the laser beam emanated by an Nd-Yag laser pulsating at 10Hz pass a spherical and cylindrical lens before being reflected vertically towards the test section by a prism. With an optical resolution of 6.87 pixels/mm the recordings covered a field of view of 70×93 mm². The time separation between image snapshots was set to 0.2 milliseconds with a corresponding maximum displacement of 7 pixels in the sensor spatial domain.

An exemplary PIV snapshot is presented in Fig. 2.16. The vortex shedding is emphasized by spatial variations in seeding density. The cylinder is situated to the left of the image and is accompanied by strong light reflections. With the laser sheet entering the test-section from the top, a shadow region is cast below the cylinder. Moreover, an oblique strip of high light intensity is visible further downstream, which is caused by impurities (i.e. scratches or dust) in the lens, prism and walls. The wake in the immediate vicinity of the cylinder suffers from poor optical access due to impurities on the transparent walls of the test-section. Imaging conditions are clearly far from optimal for PIV analysis, but remain representative as ideal experimental conditions are not always achievable and the presented problems may occur rather frequently.

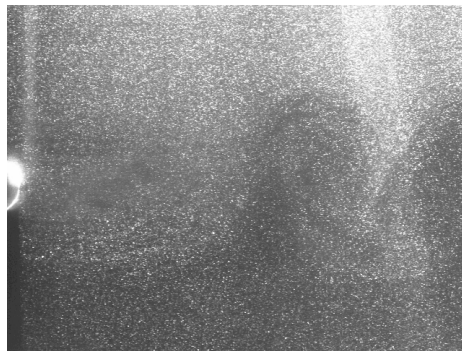


Fig. 2.16: Instantaneous PIV image of the wake flow behind a circular cylinder at $Re_D \approx 2000$.

2.5.3 Image evaluation

Image interrogation routines based on basic cross-correlation and multigrid routines (incorporating predictor filtering) are considered in the following. Basic image evaluation was performed with correlation window sizes of 65 and 21 pixels and 75% mutual window overlap yielding vector spacings of 16 and 5 pixels respectively. In the multigrid structure initial window sizes were set to 65 pixels and reduced to 21 pixels within 5

iterations. As the maximum displacement was in the order of 5 pixels, all selected window sizes fulfilled the one-quarter criterion introduced in (2.2).

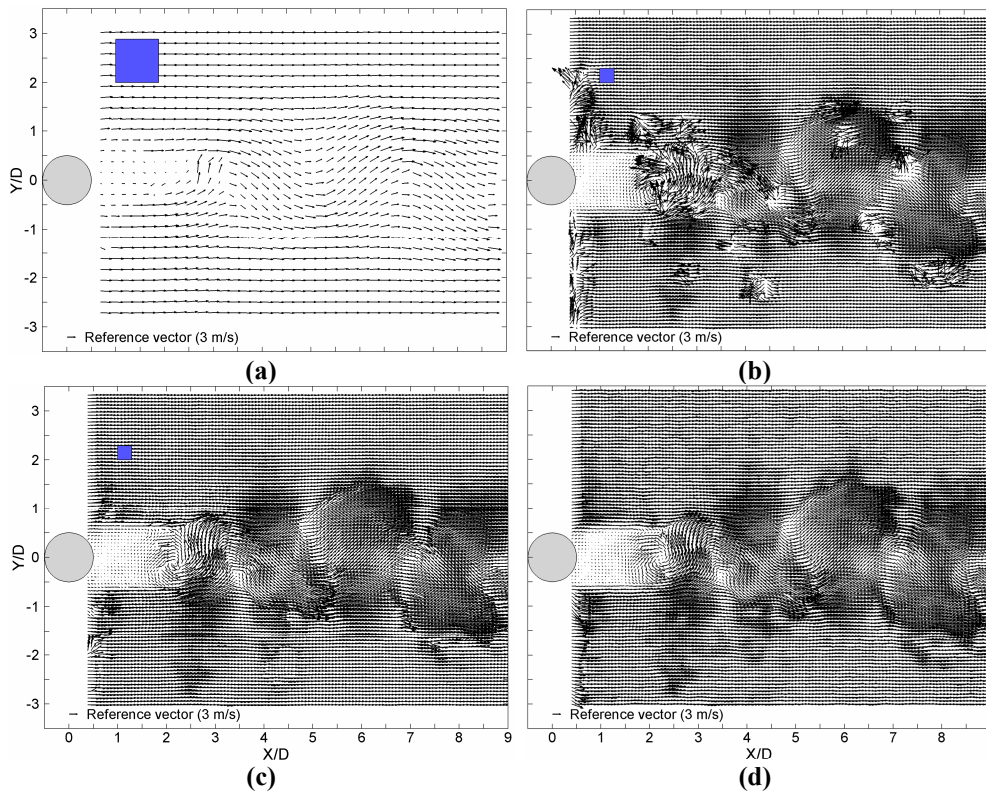


Fig. 2.17: Velocity field underlying the exposure in Fig. 2.16 obtained with different interrogation routines (WOR=75%). (a) basic cross-correlation with window sizes of 65 pixels, no vector validation (b) basic cross-correlation with window sizes of 21 pixels, no vector validation (c) basic cross-correlation with window sizes of 21 pixels, vector validation (d) multigrid analysis reducing initial windows of 65 pixels to 21 pixels in 5 iterations, no vector validation. Blue squares indicate the adopted interrogation area sizes.

Instantaneous velocity fields underlying the exposure shown in Fig. 2.16 are presented in Fig. 2.17-a for basic correlation with 65 pixels correlation windows. The use of large correlation windows yields a poorly resolved flow field though robust. Reducing the interrogation window size results in an improved flow sampling and spatial response, however at the expense of robustness as can be verified by the patches of displacement outliers (Fig. 2.17-b). Especially the near-cylinder wake suffers from multiple outliers as a result of strong velocity gradients whereas erroneous vectors in the shadow region of the cylinder are caused by insufficient seeding density. Fig. 2.17-c vividly illustrates the importance of vector validation as the proposed outlier detection criteria are able to minimize the occurrence of false displacement estimates. The decoupling between

accuracy and spatial resolution inherent to the multigrid allows the same resolution as the basic correlation operation adopting window sizes of 21 pixels while maintaining robustness (Fig. 2.17-d). As the image is iteratively deformed, the tracer motion distribution is approximated which allows a reduction in correlation window size while maximizing the number of particle image doublets.

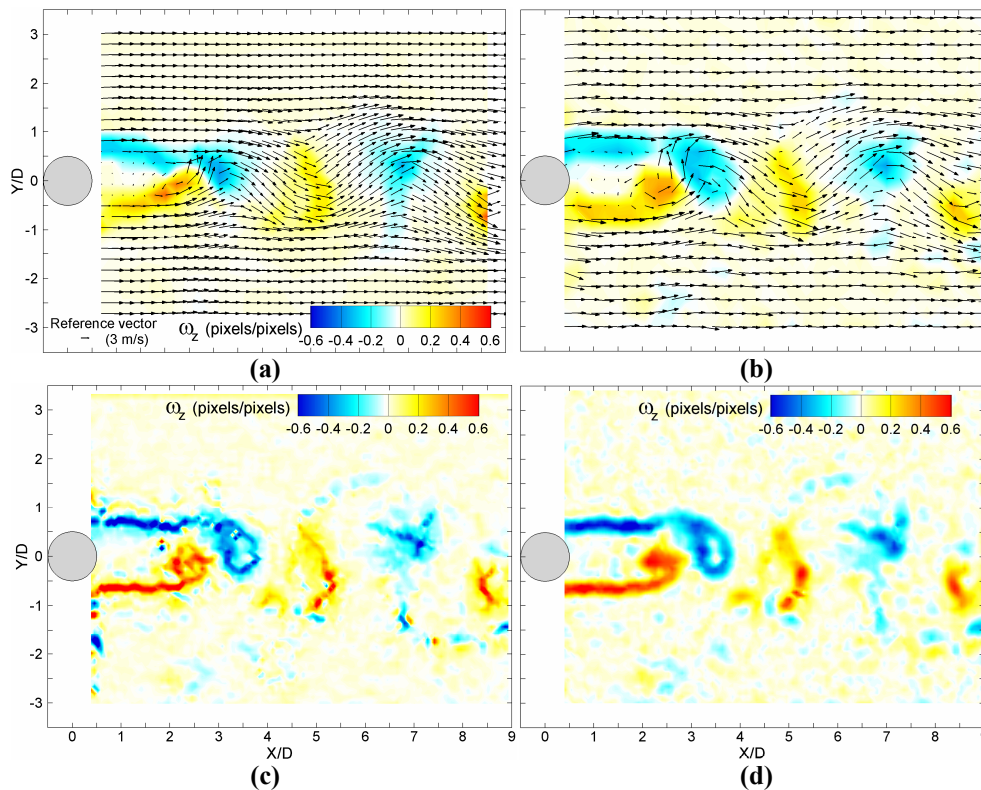


Fig. 2.18: Vorticity fields underlying the exposure in Fig. 2.16 obtained with different interrogation routines. (a) basic cross-correlation with window sizes of 65 pixels, 75% WOR with data validation (b) multigrid analysis reducing initial windows of 65 pixels to 21 pixels in 5 iterations, 0% WOR, with vector validation (c) basic cross-correlation with window sizes of 21 pixels, 75% WOR, with vector validation (d) multigrid analysis reducing initial windows of 65 pixels to 21 pixels in 5 iterations, 75% WOR, with vector validation.

Imposing a window overlap ratio of 0%, the vector spacing of the multigrid analysis is almost equivalent to that of basic interrogation with $W_S=65$ pixels (Fig. 2.18-a vs. -b). Comparing the vorticity fields however, the multigrid routine is more adequate to represent the shear layers emanating from the cylinder hemispheres and vortex cores with higher vorticity. This may serve as an indicator for improved resolution. After all, the velocity resulting from cross-correlation is a volume averaged representation of the tracer motion.

Especially in regions of strong velocity gradients i.e. the separated shear layers and vortex core regions, the application of small rigid correlation windows is inappropriate which explains why the vorticity field obtained with basic cross correlation adopting interrogation windows of 21 pixels in size is noisy and less coherent (Fig. 2.18-c) compared to the multigrid approach (Fig. 2.18-d).

2.6 Conclusions

Basic analysis of the PIV recordings is performed via the two-dimensional spatial cross-correlation function over relatively small interrogation areas, obtained by image segmentation into so-called interrogation windows. Insufficient seeding and high velocity gradients have a detrimental effect on the reliability of the cross-correlation operation. Allowable window sizes are limited respecting seeding density and displacement magnitudes to ensure a sufficient number of particle image pairs within. By distorting the interrogation windows the condition of zero velocity gradients within the flow is approached. This allows a drastic increase in number of retained particle image pairs, relaxing the sizing requirement in function of the maximum displacement measured. Consequently, window sizes can be iteratively refined enhancing the ability to represent large velocity differences and spatial resolution of the interrogation process.

To maximize the number of particle doublets, background-subtracted images are iteratively deformed to enhance the matching between image regions. Quintic B-splines have been currently implemented to perform the intensity re-interpolation. To increase the spatial resolution correlation windows are gradually reduced with iteration number, but must be ensured to contain an effective particle image density of at least 7. A filtering of the displacement field prior to the image deformation sequence further improves the spatial resolution. Vectors are validated based on iterative convergence of the displacements, signal to noise and neighbor similarity.

An assessment of the iterative multigrid routine based on computer generated PIV images attested the improved spatial response with respect to that of the basic correlation method. Given a modulation factor of 0.8 the minimum measurable wavelength is reduced from more than 3 times the window size to less than 2 times the window size. Simultaneously, the bias measurement error expressed in pixels could be limited to 2 orders of magnitudes with a random error of the same amplitude yielding a dynamic range of nearly three orders of magnitude. Application to experimental image recordings of a turbulent cylinder wake confirmed these performance enhancements compared to basic correlation routines.

However, the achieved interrogation quality depends strongly on the selection of final interrogation window size and window overlap, both of which need to be set by the user. Based on the enhanced spatial response and optimal trade-off in accuracy and computation effort in image reconstruction, the overlap factor has been argued to be at least 75%.

Interrogation parameters such as number of refinements, final window size and window overlap ratio are not chosen arbitrarily but are methodical choices made by the

user. Based on his experience, the user must select these parameters such that the image analyses will yield the sought for quantities, representative of the underlying truth in those regions of interest to him.

CHAPTER 3

ADAPTIVE SAMPLING AND WINDOWING INTERROGATION IN PIV[†]

Abstract

This chapter proposes a cross-correlation based PIV image interrogation algorithm that adapts the number and location of interrogation windows as well as their size to the image properties and to the velocity field. The proposed methodology releases the (commonly adopted) constraint that the window size has to be uniform all over the image as well as the distance between neighboring vectors. Especially in non-optimal experimental conditions where the flow seeding is inhomogeneous this leads either to loss of robustness (too few particles per window) or measurement precision (too large or coarsely spaced interrogation windows).

Two criteria are investigated namely adaptation to the local signal content in the image (i.e. seeding density) and adaptation to the local velocity field properties (i.e. spatial velocity variations). The location and size of the interrogation windows is locally adapted to the image signal (i.e. seeding density) and flow length scale (i.e. velocity variance). Also the local window spacing (commonly set by the overlap factor) is put in relation with the spatial variation of the velocity field.

The suitability of the method to analyze images from real experimental conditions is illustrated by three test cases; a shock-wave boundary-layer interaction, an aircraft vortex wake and a cylinder wake flow. Additionally synthetic images of isotropic random velocity fluctuations are considered where the limitation of a uniform interrogation approach clearly appears. The examples show that the spatial sampling rate can be adapted to the actual flow features and that the interrogation window size can be arranged such to follow the spatial distribution of seeding particle images and flow velocity fluctuations. In comparison with the uniform interrogation technique, the spatial resolution is locally enhanced while in poorly seeded regions the level of robustness of the analysis (signal-to-noise ratio) is kept almost constant.

[†] This work has been partly published in Theunissen *et al.*, 2007, Measurement Science and Technology.

Nomenclature

Δ	vector spacing (pixels)
ε	measurement error (pixels or meter second ⁻¹)
$\kappa_{0,1}$	particle segmentation constants related to intensity pedestal and variation
λ_f	spatial wavelength of flow fluctuation (pixels)
λ_m	minimum measurable wavelength (pixels)
λ_p	particle spacing (pixels)
λ_w	spacing between neighboring measurement points (pixels)
φ	two dimensional sampling rate (expressed in samples per pixel ² or spp)
σ_u	velocity standard deviation (pixels)
ω_z	out-of-plane vorticity component ; $\omega_z = \partial v / \partial x - \partial u / \partial y$ (pixel/pixel)
(x_i, y_i)	projected spatial location corresponding with a probability $p(x_i, y_i)$
A	amplitude of flow fluctuation (pixels)
b	transport aircraft model wingspan (meter)
c	conditional density function, vector containing interpolation coefficients
C, M	cumulative density functions 1D and 2D respectively
D	cylinder diameter (meter)
f	exact node value
h	grid spacing in case of uniform sampling (pixels)
$I_{\max, \min}$	maximum and minimum intensity respectively
I_p	particle intensity
k	modulation factor
$[L_x, L_y]$	spatial domain dimensions (pixels)
m	marginal density function
N_I	number of particles within the interrogation window
N_W	number of interrogation windows
$p(x_i, y_i)$	probability density function
S_d	local seeding density (particles per pixel ² or ppp)
SN	Signal-to-Noise Ratio
u, v	velocity component in horizontal and vertical direction (pixels)
\bar{u}	interrogation window-averaged velocity (pixels)
w_i	weighting function
WOR	interrogation window overlap ratio
W_S	interrogation window size (pixels)
W_S^*	calculated interrogation window size based on seeding density (pixels)
X	downstream distance from aircraft wing (meter)
$\{X\}$	total collection of values of variable X
$\{X\}_S$	collection of values of variable X within the vicinity S

3.1 Introduction

Currently most interrogation parameters, namely the size of the interrogation window (' W_s ') and overlap factor ('WOR') are set by the user and applied uniformly throughout the image, independent of variations in seeding density (defined as the number of particles per pixel) or flow property, even in the multigrid analysis. Since the progressive window refinement is applied uniformly over the entire image, the interrogation process is unaware of the possible spatial non-homogeneity either on the side of seeding density or in terms of velocity fluctuations. Non-homogeneous information distribution occurs in the majority of the flows of interest. From this consideration a need arises to adopt more flexible interrogation algorithms. Previous studies have been dedicated to overcome this problem. At least two approaches can be identified being Particle Tracking Velocimetry (PTV) and the second consists in making the correlation based interrogation more flexible.

Particle Tracking Velocimetry (Hassan and Canaan 1991, Keane *et al.* 1995) algorithms are based on the tracking of individual particle images and allow in principle the highest spatial resolution, i.e. one vector for each detected particle. However, pairing particle images in the presence of a large out-of-plane component still causes a lack of robustness. For this reason PTV algorithms were limited to flows with low seeding density, with clear limits in spatial resolution. The super-resolution approach (Keane *et al.* 1995, Stitou and Riethmuller 2001) incorporates conventional cross-correlation PIV followed by sub-grid particle tracking within the interrogation window. Despite the increased pairing success rate, tracking individual particles was shown to introduce larger noise due to the low precision of particle to particle matching (Spencer and Hollis, 2005; PIV challenge 2005). Because cross-correlation PIV analysis provides an average displacement of an ensemble of tracers still representative of the in-plane motion, the advantage over PTV is the relative increase in robustness and precision (about a factor 3 according to the 2005 PIV challenge). An additional point is that PTV performances are still strongly dependent on the choice of the detection, pairing and validation algorithms and the technique has not yet reached a sufficient level of standardization. As such, every single user applies specific rules and algorithms to optimize the analysis for the given problem.

For the analysis of PIV images by cross-correlation few attempts have been reported in literature to adapt the cross correlation analysis to the spatial variations in the seeding density (Rohály *et al.* 2002, Susset *et al.* 2006) or cross-correlation signal as proposed by Wieneke and Susset (2004), who used the Signal-to-Noise-ratio (SN-ratio) as a criterion to increase the interrogation window. The SN-ratio is defined as the ratio between the amplitude of the highest correlation peak versus the second highest. Rohály *et al.* (2002) adapted the window-size to the correlation signal within a reversed hierarchical structure. The proposed method starts with the smallest window size (2×2 pixels) and locally adds correlation maps (i.e. larger interrogation areas) until a reliable signal peak is found. Susset *et al.* (2006) performed grid refinement and modified the window size depending on whether or not a valid result was obtained in the previous iteration. Both methods improved the spatial resolution through the ability to use larger windows in areas with

low seeding density and to reduce the size in areas of high density. Indeed, application to experimental images showed promising performances. However, the degradation of the correlation signal can also occur due to velocity gradients (none of the mentioned methods applies window deformation), therefore introducing an ambiguous behavior of the SN-ratio with respect to the interrogation window size. Adjustment of the window size to the correlation signal can be seen as a signal adaptivity mechanism and to a small extent flow adaptation. Despite all improvements, study of the cross-correlation map does not allow to distinguish between a drop in Signal-to-Noise ratio due to a lack in seeding particles or due to velocity gradients. On the other hand several procedures have been presented to incorporate adaptation to the spatial flow fluctuations. An algorithm to vary the interrogation window size with respect to the local velocity fluctuations has been proposed by Scarano *et al.* (2002) for the analysis of vortex wakes. The shape of the windows can also be adapted to the local flow properties namely flow direction (Di Florio *et al.*, 2002) or the velocity field curvature (Scarano, 2003). The application of the above methods showed best results when applied within an iterative structure. Recently Becker *et al.* (2008) proposed adaptation of the interrogation parameters based on a variational approach minimizing an error function. The latter takes into account the influence of window size, eccentricity, displacement gradients and image noise on the velocity measurement accuracy. Though the method showed significant improvements, it however does not account for degradation in accuracy due to improper flow sampling or spatial variation in signal content.

The present study investigates separately the aspects of non-homogeneous seeding density and that of spatial velocity fluctuations, proposing a method that adapts the windows and sampling rate of the interrogation to varying seeding and flow properties by removing the unnecessary constraint of uniform windowing and placement of interrogation areas on a Cartesian mesh. The first part of the chapter introduces the problem in general terms discussing the concept of adaptive interrogation and its need under critical experimental conditions. The following section presents the implementation of the adaptive interrogation procedure followed by the application to computer generated images of homogeneous fluctuations and experimental images from the wake vortex behind a transport aircraft model and a supersonic flow over a shock-wave boundary layer interaction.

3.2 Problem statement

When performing PIV measurements of complex flows, in some parts of the investigated domain a high spatial resolution might be required i.e. small windows, whereas in other regions of the flow a lower spatial resolution may be sufficient. The conventional interrogation is optimized in a global sense and non-optimal conditions are often accepted in some regions of the measurement domain, which in turn introduces spurious vectors (when seeding density is too low) or large uncertainties due to poor spatial resolution. Two typical examples are shown where the user encounters a dilemma between the interrogation window size with respect to the seeding density, flow scales,

non-homogeneous image and flow properties. Here non-homogeneous image properties relate to non-homogeneous illumination, the presence of interfaces, areas with no seeding at all etc. but not to variations in density within the seeded areas.

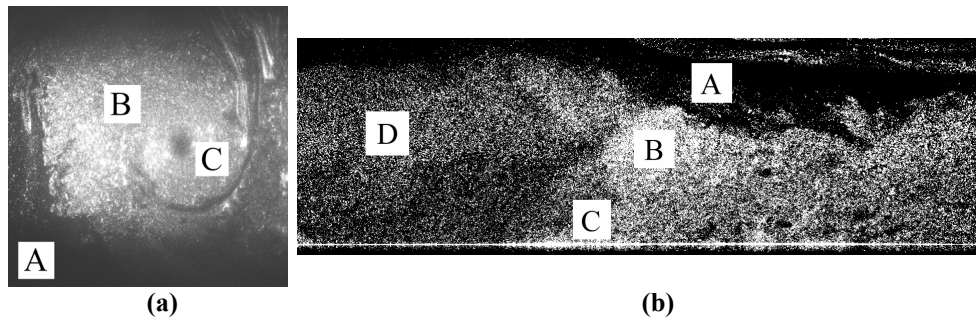


Fig. 3.1: PIV recordings of inhomogeneously seeded flows (a) aircraft vortex wake (b) Shock-wave Boundary Layer interaction.

The first image shown in Fig. 3.1-a is a recording with inhomogeneous seeding and illumination of a wake vortex behind a transport aircraft. As the external flow area 'A' is poorly illuminated, the particle image density is at such a level, that no interrogation windows should be placed. Flow data can be extracted only in an area of about 80% of the image size, in which again a gradient in seeding density and flow scales can be found; region 'B' in the external flow has optimum illumination and seeding while a lower seeding level and smaller flow scales can be found in the vortex core ('C'). Fig. 3.1-b depicts an image of a shock-wave boundary layer interaction, characterized by an intrinsically non-homogeneous seeding density due to compressibility effects (shocks) and temporal intermittency. Uniform flow regions (supersonic domains) are separated by sharp flow features (shocks, expansions). Empty regions as in 'A' would ideally require larger windows to collect enough particle images to yield a robust cross-correlation analysis. As no extra information on the flow itself can be obtained from 'A', only few velocity vectors would suffice. Region 'D' points in the uniform flow upstream of the oblique shock, where small fluctuations in the velocity are to be expected. After the oblique shock impinges on the wind tunnel wall at 'C' where a turbulent boundary layer has fully developed (Humble *et al.*, 2006) a complex interaction exist in region 'B', characterized by sharp flow features in the form of the oblique shock and a thin shear layer emanating from the interaction point. In order to capture the large displacement difference associated to these features, a high spatial sampling rate is required. Preventing the shock to be smeared out, would additionally necessitate the use of small interrogation windows to limit the well-known spatial filtering effect (Scarano, 2002). Based on this line of thought the flow sampling rate should be varied throughout the recording with a higher sampling rate in 'B' and 'C' and a relatively lower one in 'A' and 'D'.

The resulting velocity field of the analysis with a constant interrogation window size distributed along a uniform mesh are presented in figures 3.2 and 3.3. When analyzing the images with 64×64 windows and an overlap factor of 75% the number of outliers is limited (Fig. 3.2-a, Fig. 3.3-a). Nevertheless, because the seeding distribution is

inhomogeneous, the poorly seeded flow in the peripheral regions of the vortex still introduces a large number of outliers. Due to the filtering effect the vortex core is most probably enlarged and will result in a smearing out of the expected vorticity peak. The shock wave and the flow close to the wall are sampled with relatively coarse spacing and with a window size probably larger than optimum. As such the spatial resolution is insufficient to adequately characterize the flow across the shock and the boundary layer properties.

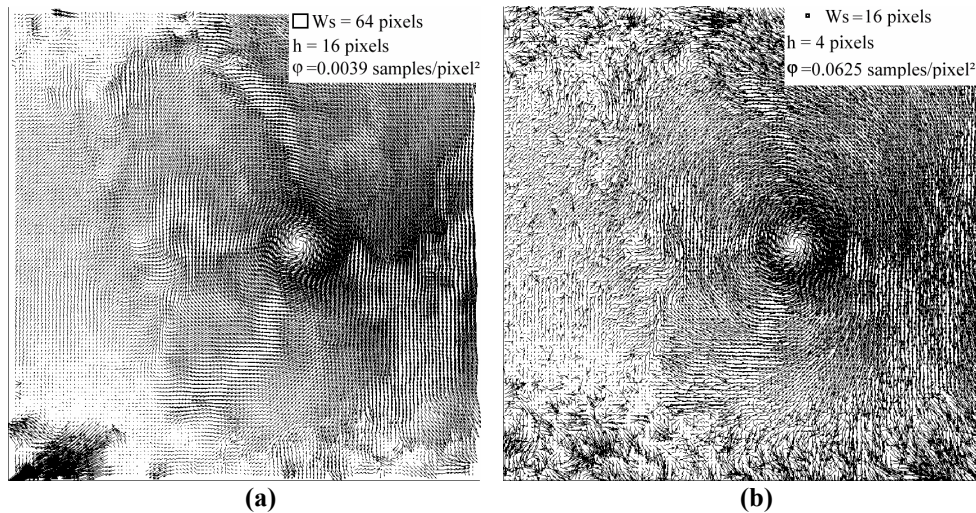


Fig. 3.2: PIV analysis with uniform window size and uniform sampling rate ('WOR' of 75%) of the recordings of the vortex wake. (a) ' W_s ' of 64 pixels, (b) ' W_s ' of 16 pixels (velocity field is undersampled by factor 4 in both directions for readability).

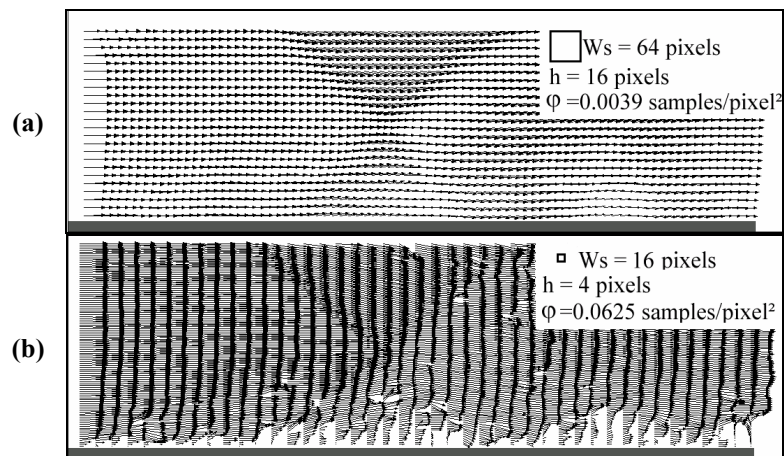


Fig. 3.3: PIV analysis with uniform window size and uniform sampling rate ('WOR' of 75%) of the recordings of the shockwave-boundary layer interaction. (a) ' W_s ' of 64 pixels, (b) ' W_s ' of 16 pixels (velocity field is undersampled by factor 8 in horizontal direction for readability).

Fig. 3.2-b and Fig. 3.3-b present the results of the analysis performed with interrogation windows of 16×16 pixels and an overlap of 75% (' $h=4$ ') yielding a spatial sampling rate of ' $1/h^2=0.0625$ ' samples per pixel². With the improved spatial resolution the shock locations in case of the shockwave-boundary layer interaction become now visible. The decrease in final window-size improved the spatial resolution, but also increased the number of outliers elsewhere in the recording since too few tracers will be captured to perform a reliable correlation. Moreover, in case of the vortex wake the flow spatial sampling rate is almost everywhere higher than necessary, since most of the high-frequency information is concentrated at the vortex core, which occupies less than 10% of the overall measurement area. These conflicting settings oblige the user to opt either for a high vector resolution in certain areas with a large number of outliers in other regions or for a low resolution with fewer outliers. Based upon a compromise between robustness/precision and resolution a window size of 32×32 is chosen in most cases.

3.3 Proposed methodology

The above examples demonstrate the need of suppressing the unnecessary constraint of uniform spatial sampling (Cartesian grid) and constant interrogation window size over the whole domain of analysis. Instead, the measurement points should be chosen with a spatial density according to the local amount of available signal and flow scales.

Signal theory dictates that the smallest detectable wavelengths are determined by the Nyquist theorem, requiring a fluctuation to be sampled at least twice. From an experimental standpoint, this concept is of little use since one should know or estimate a-priori how the velocity fluctuations are spatially distributed and what is their wavelength in order to apply the appropriate flow seeding. In experimental practice one tries to obtain the highest possible seeding density before multiple scattering or multiphase flow effects or excessive facility contamination occur.

The window size ' W_s ' is set by the user as a compromise between robustness and spatial resolution. The spatial sampling rate ' ϕ ', defined as the number of samples per pixel² (spp), can then be varied through the window overlap ratio 'WOR'. A uniform sampling with a grid spacing of ' h ' pixels corresponds to a two-dimensional spatial sampling frequency ' $\phi = h^{-2} = [(1-WOR) \cdot W_s]^{-2}$ '. For non-uniform sampling however the spacing, ' $\lambda_w(x,y)$ ', between neighboring measurement points varies throughout the image and the spatial sampling rate may be defined as:

$$\phi(x, y) = \frac{1}{[\lambda_w(x, y)]^2} \quad (3.1)$$

In the proposed methodology two main criteria are set for the adaptive windowing and sampling; signal adaptivity and flow adaptivity.

3.3.1 Signal adaptivity

In order to maintain an approximately constant number of particle images, ' N_I ', within the interrogation window (Adrian, 1991) ' W_S ' should be inversely proportional to the local seeding density ' S_d ' (in particles per pixel). The minimum amount of image pairs necessary to obtain a robust and accurate estimate of the displacement is somehow still under debate and may depend on the interrogation algorithm. However, the effective particle image density or number of particle image pairs ranges between 4 and 10 (Westerweel, 1994; Raffel et al, 1998). The available signal in the PIV recordings hence dictates the information that can be extracted from them, in turn determining the optimal size and location of the interrogation windows. The implementation of this criterion involves image pre-processing in order to estimate the amount of signal in the images (scattered light from the seeding particles).

A straightforward approach well known in Particle Tracking Velocimetry is to count individual particles over selected areas (Agüí and Jiménez 1987, Takehara and Etoh, 1999). The particle detection algorithm is based on intensity background removal (sliding minimum subtraction, Wereley *et al.* 2002^b) and local intensity thresholding (see paragraph 3.4.1). For the required ' N_I ' the evaluation of ' S_d ' returns the value of the window sized based solely on signal content ' W_S^* '. The signal adaptivity criterion in principle reads as

$$W_S^* = \frac{N_I}{S_d(x, y)} \quad (3.2)$$

while the spatial sampling rate ' φ ' is directly proportional to ' S_d ' (3.3)

$$\varphi \propto S_d \quad (3.3)$$

An example of signal adaptation is shown in Fig. 3.4. A computer generated PIV image has been produced with inhomogeneous seeding density decreasing from left to right (Fig. 3.4-b). Following equations (3.2) and (3.3) more and smaller windows (represented by the red squares) are placed in those areas with a higher seeding density whereas the lower seeded regions are sampled more sparsely with enlarged interrogation windows.

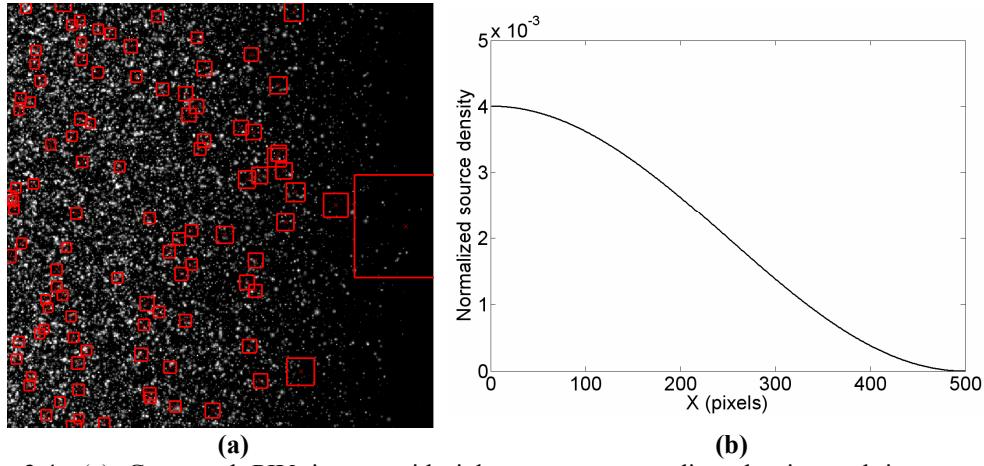


Fig. 3.4: (a) Generated PIV image with inhomogeneous seeding density and interrogation windows (red squares) (b) imposed, normalized seeding density.

3.3.2 Flow adaptivity

The flow fluctuations can be characterized by their amplitude ‘A’ and spatial wavelength ‘ λ_f ’. Knowing their value would allow to optimize the window size and to make an accurate estimate of the measurement error associated to the limited spatial resolution (Scarano, 2003). Contrary to signal adaptation however both parameters are unknown a-priori and the flow adaptivity criterion can only be implemented within a recursive structure. Eventually, the resolution limits for the minimum wavelength that can be described ‘ λ_m ’ turns out to be as follows, ‘ $\lambda_m > 2 \cdot \lambda_p$ ’, ‘ $\lambda_m > k \cdot W_s$ ’ and ‘ $\lambda_m > 2 \cdot \Delta$ ’, where ‘ λ_p ’ represents the particle spacing, ‘ Δ ’ the vector grid node distance, ‘ W_s ’ the interrogation window size and ‘k’ a modulation factor (Nogueira *et al.*, 2005). The presented methodology takes the estimator for the local spatial velocity fluctuations as the local velocity standard deviation over a kernel as large as the average interrogation window size. By increasing the number of samples in those areas with high values for the standard deviation, the limitation set by the vector grid node distance is relaxed (read, spatial resolution is increased). Minimizing W_s , but preserving the robustness, will further decrease ‘ λ_m ’.

After cross-correlation of the sampling windows a velocity field with pixel spacing is obtained through a linear interpolation of the individual vectors (cf. paragraph 3.4.2). The calculation of the velocity standard deviation is then defined as

$$\sigma_u(x, y) = \sqrt{\frac{1}{W_s^2} \sum_{j=-\frac{W_s}{2}}^{+\frac{W_s}{2}} \sum_{i=-\frac{W_s}{2}}^{+\frac{W_s}{2}} [u(x+i, y+j) - \bar{u}]^2 + [v(x+i, y+j) - \bar{v}]^2} \quad (3.4)$$

$$\text{with } \bar{u} = \frac{1}{W_S^2} \sum_{i=-\frac{W_S}{2}}^{+\frac{W_S}{2}} \sum_{j=-\frac{W_S}{2}}^{+\frac{W_S}{2}} u(x+i, y+j) \quad \text{and} \quad \bar{v} = \frac{1}{W_S^2} \sum_{i=-\frac{W_S}{2}}^{+\frac{W_S}{2}} \sum_{j=-\frac{W_S}{2}}^{+\frac{W_S}{2}} v(x+i, y+j) \quad (3.4)$$

In the above expression u is the horizontal velocity component varying throughout ‘ W_S ’, ‘ \bar{u} ’, ‘ \bar{v} ’ and ‘ σ_u ’ are the local mean and standard deviation within the kernel respectively. The spatial sampling rate ‘ φ ’ is also set directly proportional to ‘ σ_u ’ (3.5).

$$\varphi \propto \sigma_u \quad (3.5)$$

The following example illustrates the above described concept of flow adaptivity. Consider a jet-like Gaussian velocity distribution (Fig. 3.5-b). The sampling rate is scaled according to the standard deviation and shows two peaks. The interrogation windows scaled by the standard deviation, according to (3.4), are shown in Fig. 3.5-a, with a minimum size in the region of largest velocity gradients.

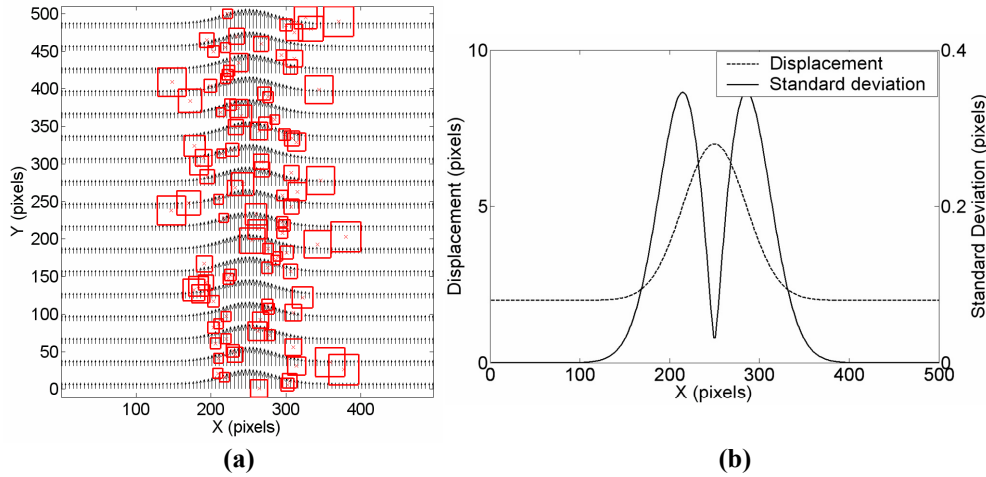


Fig. 3.5: (a) imposed velocity field with interrogation windows (red squares) (b) imposed velocity profile and calculated standard deviation profile using moving windows of 27 pixels in width.

3.3.3 Combination of signal and flow adaptivity

At the beginning of the iterative process, ‘ W_S ’ is chosen large enough such to obey the $\frac{1}{4}$ rule (Adrian, 1991). In the subsequent steps, the windows are gradually modified in size adapting locally to the seeding density distribution ‘ S_d ’ and the velocity standard deviation ‘ σ_u ’. The algorithm used for the combined adaptation of the local window size reads as (3.6)

$$W_S = (1 + C_0 k) \cdot W_S^* \quad \text{where} \quad k = \frac{\sigma_{\text{ref}} - \sigma_u}{\sigma_{\text{ref}}} \quad \text{and} \quad \sigma_{\text{ref}} = \text{median}(\sigma_u) \quad (3.6)$$

In the above equation ‘ W_S^* ’ is the window size based on the evaluation of the local seeding density (3.2). The empirical constant ‘ C_0 ’ is set at 0.3 to limit the effect of flow adaptivity correction with respect to the signal adaptivity criterion (30% variation with respect to ‘ W_S^* ’). The range of ‘ k ’ is limited between -1 and 1 in order to avoid too large fluctuations of ‘ k ’ (and therefore ‘ W_S ’) in case of spurious vectors.[†]

Implementation of signal and flow adaptivity results in spatial distributions for both the velocity standard deviation and seeding density. The normalized product of a modified ‘ σ_u ’ and ‘ S_d ’ is used to produce a spatial distribution for a single scalar i.e. the spatial sampling rate ‘ φ ’ (3.7). This is needed because the projection of the sampling positions is based on a single scalar distribution. The modified velocity variance ‘ σ_u^* ’ ensures regions of higher velocity variance to be attributed the majority of sampling locations.

$$\varphi = \frac{S_d \cdot \sigma_u^*}{\iint_{\text{image}} S_d \cdot \sigma_u^* dx dy} \quad \text{where} \quad \sigma_u^* = \sqrt{\max(\sigma_u - \sigma_{\text{ref}}, 10^{-6})} \quad (3.7)$$

During the first interrogation no information on the velocity distribution is available. Therefore the sampling rate will be based only on ‘ S_d ’. To distribute the sampling points in accordance with the value of the sampling rate ‘ φ ’ use is made of the 2D transformation method (Secord *et al.*, 2002), which is summarized in the following paragraph. By updating the velocity field within an iterative structure, the local sampling rate and local window overlap factor will vary accordingly. The latter implies that every iteration the number of correlation windows may be freely adapted. Estimates for the number of windows can be based on statistical evaluations as discussed further in chapter 5. However, in the current implementation, the number of windows ‘ N_w ’ is a constant and is determined solely by the number of identified particle images, imposed minimum number of tracers within the window ‘ N_t ’ and mean area overlap ‘WOR’ (3.8). The latter is defined by the user prior to the interrogation process. Equation (3.8) further ensures the

[†] At this point it is worth mentioning that trials have been performed to relate the window size to the effective image density. For each correlation window of size ‘ W_S ’, the number of particle image pairs ‘ N_{pairs} ’ between image snapshots at ‘ t ’ and ‘ $t+\Delta t$ ’ is determined with the aid of the displacement field determined in the previous iteration. Imposing an effective number of particles images of 10, the updated, correct window size is given by $W_S \cdot (10/N_{\text{pairs}})^{1/2}$. Though correct in principle, it is argued that because of sub-grid scales a correct estimate of particle pairing is impossible, not to mention the effect of out-of-plane motion. This problem is typically encountered in particle tracking and poses a stringent limitation in the PTV technique’s spatial resolution (Spencer and Hollis, 2005).

upper limit in number of retrieved vectors to be restricted by the number of tracers who dictate the amount of extractable flow information.

$$N_w = \frac{\text{Number of detected particles}}{N_t \cdot (1 - \text{WOR})^2} \quad (3.8)$$

The combination of ‘ σ_u ’ and ‘ S_d ’ represents the relative importance of the information contained over different areas in the image. As soon as the local velocity fluctuation increases, the displacement standard deviation will increase, requiring a higher sampling rate in that region (Fig. 3.6-a). Concerning the signal distribution the more is the available signal, the closer smaller windows can be placed to each other, increasing the sampling rate and finally the spatial resolution. Eventually the PIV image with seeding density and velocity profile as depicted in Fig. 3.4-b and Fig. 3.5-b respectively are analyzed with windows of non-uniform size located according to the calculated sampling rate (Fig. 3.6-b).

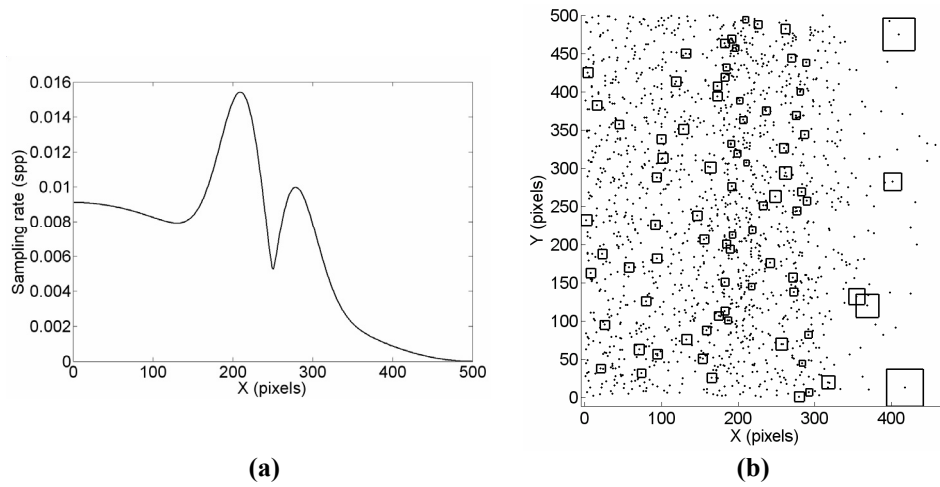


Fig. 3.6: (a) Sampling rate obtained as a linear combination between the velocity standard deviation and seeding density (b) image of 16000 interrogation windows distributed according to the sampling rate. The squares depict the size of randomly selected interrogation windows, calculated according to equation (3.6).

3.4 Implementation

3.4.1 Signal quantization

In PIV, seeding particles sample the a-priori unknown velocity distribution which allows an estimation of the convective velocity through appropriate image analysis. More exotic approaches involving intensity eigenvalues and image statistics have been proven

inadequate in the estimation of the tracer, read signal, concentration (cf. Appendix A). The most straightforward approach is the identification and localization of the individual particle images.

The extraction of individual particles is challenging; apart from uneven brightness levels in background, random noises are often superimposed. The latter complicates identification based on intensity gradients e.g. in feature detection with automatic scale selection (Lindeberg, 1993). Takehara and Etoh (1999) proposed the floating computation of the cross-correlation between the target image and a function representing a typical particle image. The latter commonly has a Gaussian character considering its close affinity with the Airy distribution of the point spread function of a diffraction limited lens (Adrian and Yao, 1984). The mask method is however very sensitive to random noise requiring conducive thresholding in the selection of particle-related correlation function amplitudes. More straightforward particle segmentation involves an intensity threshold criterion (Guezennec and Kiritsis, 1990), which must be locally defined as reported by Ohmi and Li (2000) to incorporate spatial fluctuations in background intensity amplitudes.

Whereas the pixelwise statistical threshold proposed by Stitou and Riethmuller (2001) necessitates a sufficiently large collection of reference images the tracer distinction implemented in this work is conditioned to single snapshots and hinges on three considerations;

1. Instead of accuracy and high detection success rate, which are both important in analyses related to particle tracking (Marxen *et al.* 2000, Theunissen *et al.* 2004), robustness in the estimation of signal quantity is preponderant. This negates the need of sub-pixel accuracy.
2. Pixel intensities originating from particle images are in general easily discernable from those belonging to noise.
3. The correlation operation is sensitive to elevated image intensities (Young *et al.*, 2004), requiring the signal of importance to differ sufficiently from the surroundings and background.

Combined these are translated in the following segmentation criterion; symbolizing the collection of detected local maxima and minima in intensity by ' $\{I_{\max}\}$ ' and ' $\{I_{\min}\}$ ' respectively, a local intensity peak ' I_p ' (element of ' $\{I_{\max}\}$ ') is classified as a particle image when satisfying equation (3.9).

$$I_p - \kappa_0 \geq 3.5 \cdot \kappa_1 \quad \text{with} \quad \kappa_1 = \text{median}(\{I\}_S - \kappa_0) \\ \text{and} \quad \kappa_0 = \text{median}(\{I_{\min}\}_S) \quad (3.9)$$

Terms ' κ_0 ' and ' κ_1 ' relate respectively to the DC intensity pedestal and surrounding gray levels. Factor 3.5 has been empirically determined and incorporates sufficient discernment between candidate pixel intensity and surrounding intensities. Subscript 'S' refers to those pixel intensities within the spatial vicinity 'S' centered on ' I_p ' (typically around 15 pixel units). An example of the proposed segmentation criterion's performance when applied to an experimental intensity profile is depicted in Fig. 3.7-a. High intensity

amplitudes can be easily spotted visually and are classified as particle images accordingly. Those surrounded by stronger intensity variations on the other hand complicate the identification and have a lower occurrence of being categorized as particle image-related. The latter is furthermore consistent when considering their negligible influence on the correlation function. In case of a randomized intensity distribution (Fig. 3.7-b), none of the detected maxima are affiliated to particle images, demonstrating the robustness of the proposed criterion.

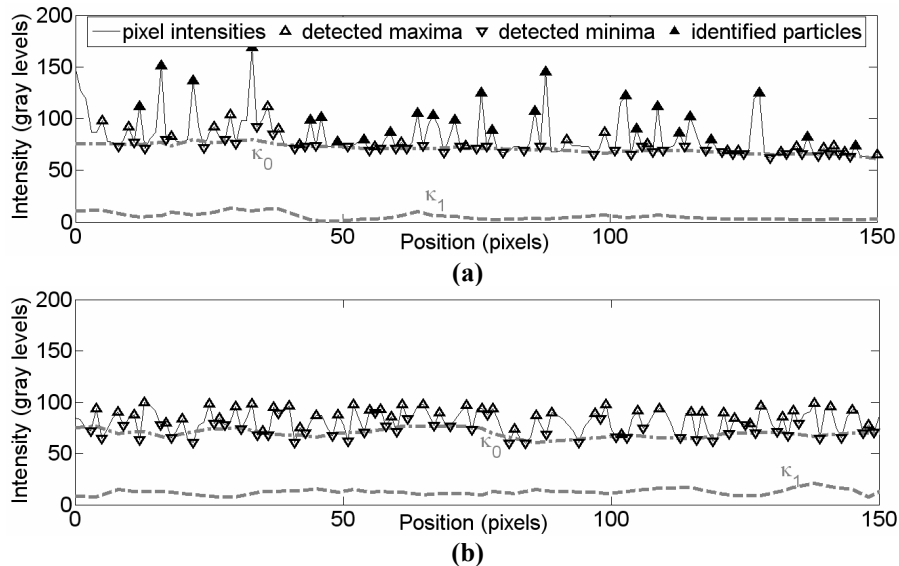


Fig. 3.7: Segmentation criterion defined in (3.9) applied to (a) an experimental intensity profile (b) random pixel intensities.

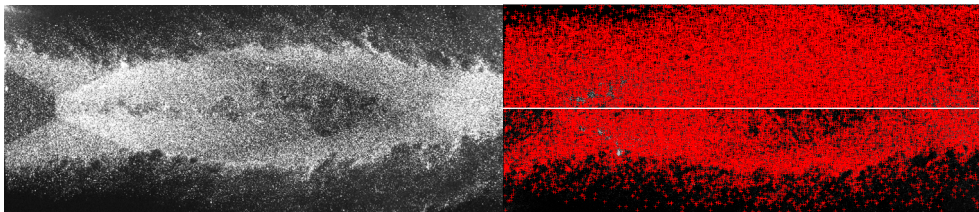


Fig. 3.8: (Left) PIV image of supersonic jet with enhanced contrast for clarity (Right-top) Detected particle images (+) based on (3.9). (Right-bottom) Results from segmentation criterion defined in (3.9) combined with dynamic intensity range threshold. The central jet region is clearly more discernable as well as the seeded protuberances at the jet's edge.

Strong seeding density gradients are typically encountered in compressible flows, which concomitantly produce high scattering intensities. An example is shown in Fig. 3.8 which depicts the PIV recording of a supersonic jet (see also section 6.4). In this case areas with heightened intensities should not be categorized as having increased background noise levels, but as zones with high information content. By introducing a

further threshold on the dynamic intensity range ' $I_p/\max(\{I_{\max}\}) > 0.5$ ' these regions can be isolated more adequately as demonstrated in Fig. 3.8.

The convolution between a binary image containing the detected particle locations and a window of unit intensity yields the number of detected tracers captured within the sliding window for each pixel location. By repeating the procedure for various window sizes the inherent quadratic dependency between particle image density and window size, ' $N_I = a \cdot W_S^2 + b \cdot W_S$ ', can be extracted by means of a parabolic fit where coefficient 'a' directly relates to the searched for concentration estimate.

3.4.2 Data interpolation

- **Linear interpolation**

To enlarge the measurable velocity gradient range, matching between regions which undergo transformation has to be improved. To do so, the images are deformed based on a continuous first order approximation of the displacement field. Though linear interpolation is in general less accurate compared to higher order interpolation schemes, it has the advantage of requiring less CPU. For this reason displacements were chosen to be linearly interpolated over all the pixels from an unstructured mesh of points using the nearest neighbors, i.e. using for each pixel the three nodes of the circum-triangle based on a Delaunay triangulation (Sambridge *et al.*, 1995).

$$\underline{X} \cdot \mathbf{c} = \mathbf{f} + \boldsymbol{\varepsilon} \quad \text{where} \quad \underline{X} = \begin{bmatrix} x_1 & y_1 & 1 \\ x_2 & y_2 & 1 \\ x_4 & y_4 & 1 \end{bmatrix}, \quad \mathbf{c} = \begin{bmatrix} c_1 \\ c_2 \\ c_3 \end{bmatrix} \quad \text{and} \quad \mathbf{f} = \begin{bmatrix} f_1 \\ f_2 \\ f_3 \end{bmatrix} \quad (3.10)$$

$$f_p = c_1 \cdot x_p + c_2 \cdot y_p + c_3 \quad (3.11)$$

Calling 'P' the point which to interpolate to, the nodes of the circum-triangle of 'P' are used to construct a linear system of equations. Considering Fig. 3.9, the circum-triangle of 'P' corresponds to triangle 1-2-4 resulting in the set of equations presented in (3.10). The vector containing the measurement error is symbolized by ' $\boldsymbol{\varepsilon}$ '. In general ' $\boldsymbol{\varepsilon}$ ' is omitted from the equation as the measurement error is typically unknown a-priori and the summation of the exact values ' \mathbf{f} ' and error are combined into the measured values. The solution of the system yields the coefficients ' c_1 ', ' c_2 ' and ' c_3 ' allowing the evaluation of the interpolated value at 'P' (3.11).

- **Natural Neighbor interpolation**

Natural Neighbor (NN) interpolation has been selected to redistribute the data onto a final Cartesian grid to facilitate the post-processing of the obtained displacement field. The Natural Neighbor scheme has been selected in view of its low computational

intensity and robustness compared to more common interpolation schemes such as Adaptive Gaussian Windowing, Krigging and polynomial fitting (cf. Appendix A).

NN-interpolation is initiated by constructing the Voronoi cells given the unstructured node locations. Voronoi diagrams divide the plane into a set of regions, one for each node, such that all points in a particular region are closer to its node than any other node (Fig. 3.9-a). Delaunay tessellation is formed by connecting the nodes whose Voronoi cells have common boundaries. For any point 'P' (Fig. 3.9-a), the neighborhood support is given by the natural neighbors defined as the nodes whose triangulation relationships would be modified by the insertion of point 'P' (Fig. 3.9-b). A straightforward means to arrive at the same end is to use the empty circumcircle criterion (Sakumar *et al.*, 1998); the natural neighbors are those points whose circumcircle of the Delaunay triangulation contains point 'P' (Fig. 3.9-a). For the case cartooned in Fig. 3.9-a, point 'P' has 6 natural neighbors.

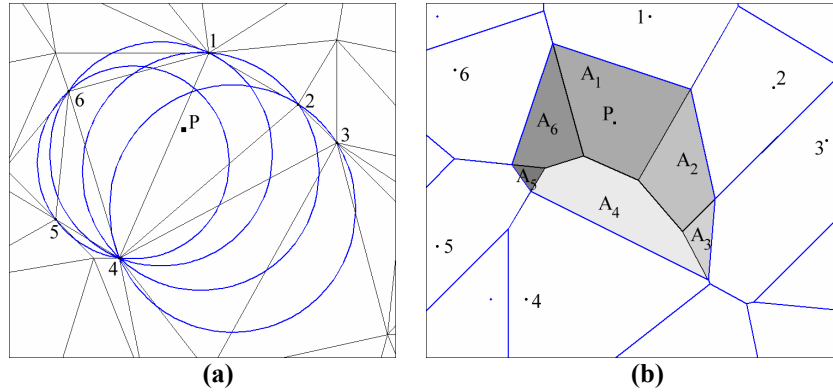


Fig. 3.9: Nearest neighbor interpolation (a) Delaunay triangulation (gray) with circum-circles (blue). Data points 1-6 are the nearest neighbors of point P. (b) Voronoi diagram before (black) and after (blue) insertion of point P.

The Voronoi cell about 'P' (blue lines) overlaps all the original cells of its natural neighbors. The interpolation weights attributed to the extent of neighboring functional values are related to the ratio of the area of the overlapping Voronoi cells to the total area of the Voronoi cell about 'P'. In the example case, the interpolated value at 'P' is therefore defined as

$$f_p = \frac{1}{\sum_{i=1}^6 A_i} \cdot \sum_{i=1}^6 A_i f_i \quad (3.12)$$

The interpolation algorithm has been implemented adopting the routine descriptions of Sambridge *et al.* (1995) and modifications suggested by Triguí (2005).

3.4.3 Data allocation

- *PDF weighted 2D point distribution*

Lets consider a number of points to be distributed in space with the probability density function 'p' as depicted in Fig. 3.10-a. The calculation of the cumulative probability function 'C' (3.13) allows to project randomly distributed points onto the target space (3.14), approximating the required sampling distribution (Fig. 3.10-b). For the purpose of illustration, regular separated points were chosen.

$$C(x) = \int_0^x p(\eta) d\eta \quad (3.13)$$

$$x_i = C^{-1}(p_i) \quad (3.14)$$

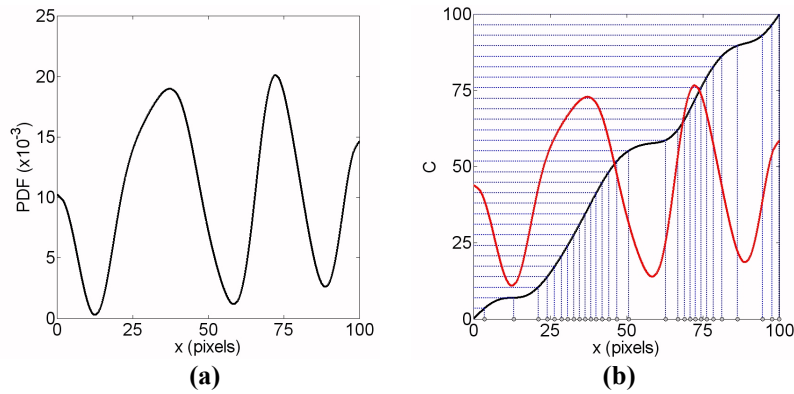


Fig. 3.10: (a) 1D probability density function (b) and its cumulative density function and regular sampling of its inverse. The red line serves as a mere heuristic of the original PDF.

The procedure can be extended to two-dimensional signals. Given a 2D probability density function 'p(x,y)' defined on a domain with size '[L_x,L_y]', then the marginal density function 'm' and its cumulative density function 'M' are given by the integrals in (3.15). Random values for the probability in x- and y-are chosen, 'p_{x,i}' and 'p_{y,i}'. By taking the inverse of the cumulative density function 'M', the y-location of point 'i' is retrieved (3.16). Given 'y_i' the x-coordinate 'x_i', is determined by transforming 'p_{x,i}' according to the pdf at 'y_i' i.e. 'p(x,y_i)' by using the conditional density function 'c' and its cumulative 'C' (3.17). The x-location is then given by the inverse of the latter function (3.18).

$$M(y) = \int_0^y m(\eta) d\eta \quad \text{where} \quad m(y) = \int_0^{L_x} p(x, y) dx \quad (3.15)$$

$$y_i = M^{-1}(p_{y,i}) \quad (3.16)$$

$$C(x|y_i) = \int_0^x c(\eta|y_i) d\eta \quad \text{where} \quad c(x|y_i) = \frac{p(x, y_i)}{m(y_i)} \quad (3.17)$$

$$x_i = C^{-1}(p_{x,i}|y_i) \quad (3.18)$$

- **Sample re-distribution**

A mesh returned by the 2D transformation method described by Secord *et al.* (2002) is of poor quality as can be seen in Fig. 3.11. Similar to grid adaptation in computation fluid dynamics, a mesh smoothing is applied prior to the re-interpolation process.

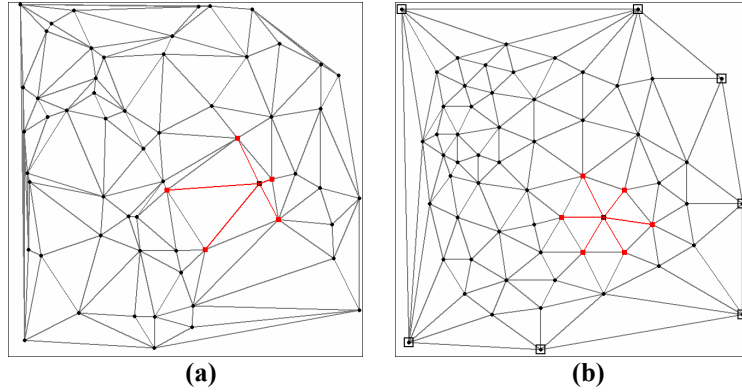


Fig. 3.11: Mesh smoothing (a) original sampling distribution (b) distribution of sampling points after 3 Laplacian smoothing iterations. Points lying on the convex hull (\square) remain unchanged.

Following a Laplacian smoothing operation (Zhou and Shimada, 2000), the measurement points are redistributed to the center of gravity of the area spanned by its neighboring nodes (Fig. 3.11-b) without changing the connectivity. Doing so the Delaunay triangles are equilateralized and the grid quality is enhanced. For a given circum-circle's radius the area of the inscribed triangle is maximized when it is equilateral. The smoothing operator thus maximizes the determinant of ' \underline{X} ' in (3.10) and minimizes the influence of the measurement uncertainty ' ϵ ' concomitantly when solving the linear system (Simpson, 1994).

- **Grid spacing**

To facilitate the post-processing of the irregularly spaced data a redistribution of the velocity data towards a Cartesian grid is in order. The new Cartesian grid spacing ' h ' should respect the typical spacing of the unstructured field to keep the same data density since over-sampling does not add extra information. Proper sampling of the original data and flow structures is already ensured by taking into account the estimated spatial distribution of flow length scales yielding a structured nodal distance at least equal to the smallest unstructured sample spacing; regions of strong velocity gradients (high variance)

are attributed a local increase in sampling density while regions with low velocity gradients are sampled by few windows.

Each Delaunay triangle is replaced by a circle of equal area and whose radius serves as indicator for the sample spacing ' λ_w '. A weighted averaging of all radii (3.19) results in the final grid spacing where the applied weighting function must minimize the bias caused by sporadically small distances and put more importance to smaller radii. An example of such a weighting function is given in equation (3.19) prescribing typical final grid spacings in the order of 2 pixels.

$$h = \frac{1}{N_w} \sum_{i=1}^{N_w} w_i \lambda_{w_i} \quad \text{where} \quad w_i = 1 - \tanh\left(\pi \left[\frac{\lambda_{w_i} - \min(\lambda_w)}{\max(\lambda_w) - \min(\lambda_w)} \right]^{\frac{1}{2}}\right) \quad (3.19)$$

3.5 Interrogation methodology

Fig. 3.12 schematically displays the outline of the implemented algorithm. The displacement is determined at the chosen locations by cross-correlating the interrogation windows with an iterative algorithm which applies window deformation following the WiDIM algorithm described in section 2.3.2 (Scarano and Riethmuller, 2000). Five multi-grid steps are applied, followed by two iterative loops.

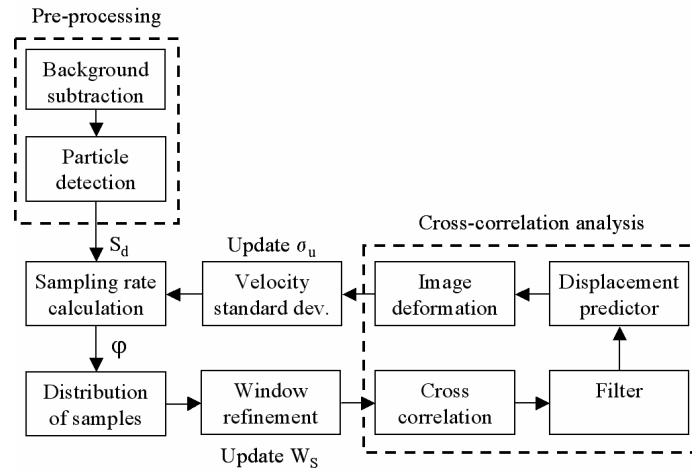


Fig. 3.12: Blockdiagram of the implemented interrogation method.

In the image deformation sequence, the displacements are linearly interpolated over all the pixels from an unstructured mesh of points using the nearest neighbors, i.e. locating for each pixel the three value points based on a Delaunay triangulation (Sambridge *et al.*, 1995). Prior to the interpolation, the predictor corrector iterative interrogation is stabilized with a Least-Squares Fit (Schrijer and Scarano, 2008), which consists in re-interpolating each determined displacement vector using a 2nd Order Least-Squares Fit.

As the window size adaptation is driven by the velocity spatial fluctuations, the recently proposed normalized median test combined with criteria based on signal-to-noise ratio and iterative convergence in displacement corrector has been implemented as validation procedure to eliminate spurious vectors (cf. paragraphs 2.2.2 and 2.3.3). Erroneous vectors are replaced by a linear interpolation of their direct neighbors.

Contrary to conventional interrogation processes, the proposed methodology returns displacement vectors placed on an unstructured grid. To allow further post-processing of velocity data the algorithm makes use of Natural Neighbour interpolation of the data to obtain a structured representation (Sambridge *et al.*, 1995). Though the NN interpolation allows a direct computation of the first order derivatives, it was found that the final results were noisy. In order to retrieve more smooth results for derivative operations, 2nd order polynomials were fitted onto the structured grid allowing a direct evaluation of e.g. the vorticity.

The vortex image presented in Fig. 3.1-a served as a test case to allow a comparison in CPU time between WiDIM and the proposed adaptive methodology. Square windows of 41×41 pixels² with an overlap of 75% were imposed in the WiDIM process. The adaptive sampling and omission of superfluous correlation windows allowed the implemented technique to reduce the computation time by a factor two compared to the classical approach. Fig. 3.13 depicts the distribution in computation time over the different subprocesses for the two image processing methods. Distorting the images and cross-correlating the interrogation windows are in general the most computationally demanding. Fig. 3.13-b further indicates that the extra computational time associated with mapping and interpolation accompanying the sampling on an unstructured grid does not exceed 25% of the overall CPU time.

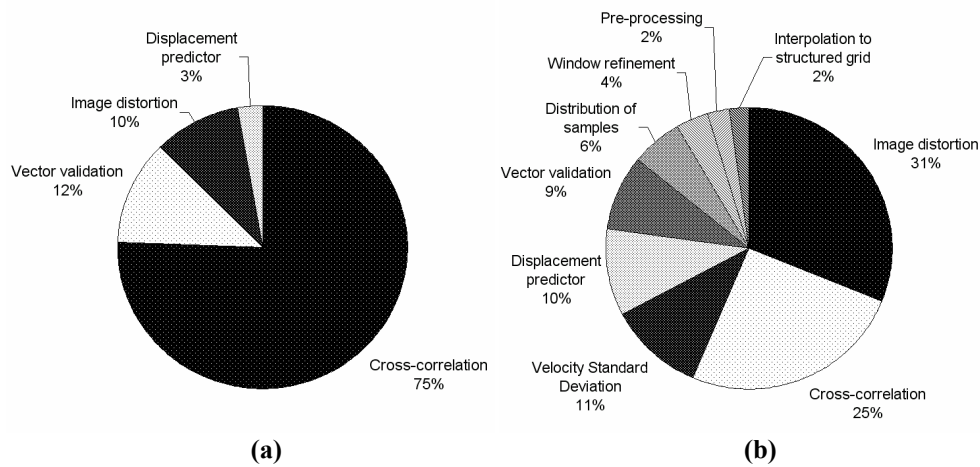


Fig. 3.13: Distribution in computational time (a) WiDIM (b) Adaptive PIV.

3.6 Performance evaluation

In this section the performances of the method incorporating the proposed adaptive criteria is compared with the improved WiDIM algorithm of DUTAE (Stanislas *et al.*, 2005). The latter can be considered as state of the art, based on the conventional approach of structured image sampling with uniformly sized and spaced interrogation windows. The assessment is based on four flows of very different nature. Computer generated images of isotropic turbulence represent a theoretical case, whereas the experimental wake vortex images behind a transport aircraft are more of industrial interest. The shock-wave boundary layer interaction (Humble *et al.*, 2006) on the other hand can be considered to be a state of the art aerodynamics problem while the cylinder wake flow is a well-known problem in academics.

Improvements related to the adaptivity criteria are assessed on the basis of performance indicators with respect to the different quantities of interest depending on the considered flow;

- In case of homogeneous and isotropic velocity fluctuations, performances are related to the capability of accurately measuring the various spatial scales. In terms of power spectra, this translates in accurately representing the underlying spectra up to wave numbers as high as possible.
- The wake vortex image has typical characteristics for recordings taken in industrial conditions (inhomogeneous illumination and seeding). The performance heuristics are here the robustness with respect to illumination and seeding while resolving the flow in more detail around the vortex core. The improvements can therefore be quantified by means of the vorticity statistic.
- The shock-wave boundary layer interaction is characterized by various flow domains exhibiting spatially strong variations in flow scales and seeding density. The response of the adaptive approach to the required spatial resolution in the different image domains is considered in this case to be the performance indicator.

Improvements in case of the cylinder wake can be judged on the basis of a more detailed representation of the flow field. Here, similar to the vorticity scalar in the wake vortex images, the λ_2 parameter introduced by (Jeong and Hussain, 1997) enables to quantify to a certain extent the achieved performance improvements as the parameter is in direct relation with the interrogation inherent modulation effects and the proposed approach's capability of measuring spatial velocity gradients..

3.6.1 Isotropic random fluctuations

To quantify the capacity of the proposed interrogation method in the characterization of turbulent flows, synthetic PIV images simulating isotropic turbulence were generated. Imposing a seeding concentration of 0.2 particles per pixel, $5 \cdot 10^4$ particles were randomly distributed onto a 500-by-500 pixel array. Image discretization was taken into account by integrating the Gaussian shaped intensity profiles over a 70% central effective sensor area. To emulate homogeneity in the velocity field, a pixelwise random isotropic displacement field with maxima of 5 pixels in absolute value was smoothed in three

consecutive passes by a moving Gaussian filter. The simulated flow length scales are controlled by the variance of the moving kernel as demonstrated in Fig. 3.14; larger variances yield smoother displacement fields and therefore larger length scales. Under the assumption of the known velocity map to be invariant in time, the evolution of particle positions can be determined by Euler integration.

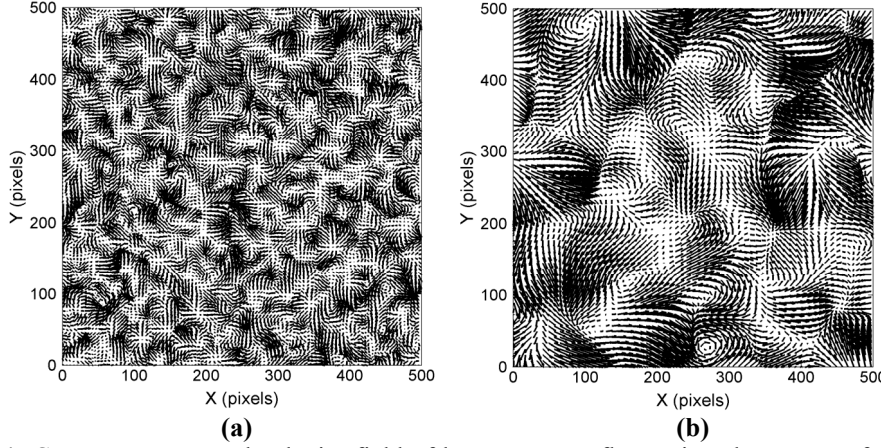


Fig. 3.14: Computer generated velocity field of homogeneous fluctuations by means of Gaussian smoothing with a variance of (a) 21 pixels and (b) 71 pixels. Vectors are undersampled and scaled for readability.

The produced velocity fields are qualitatively very similar to those from DNS simulations (Lecordier *et al.*, 2001). Nevertheless, a simple flow field cannot fully simulate the complex structure of a real flow. The purpose of this test case is therefore merely to evaluate the behavior of the interrogation method in a turbulent-like flow field containing small fluctuations.

To provide a reference, images were analyzed with the structured, more conventional, WiDIM method discussed in Chapter 2 (symbolized as \blacksquare). Because adaptivity (represented by \bullet) predicted a minimum window size of 11 pixels, the structured routine applied final windows of equal size with an overlap factor of 0.75, leading to a vector spacing of 3 pixels and a total of around 28000 correlation windows.

The suitability in representing velocity fluctuations of various length scale is expressed through the longitudinal power spectrum ‘ E_{uu} ’, which has been calculated as

$$E_{uu}(p, 1 : N) = \left| \text{FFT}(u_m(p, 1 : N)) \right|^2 \quad \text{and} \quad E_{uu}(N + p, 1 : N) = \left| \text{FFT}(u_m^T(p, 1 : N)) \right|^2$$

$$E_{uu}(k) = \frac{1}{N+N} \sum_i E_{uu}(i, 1 : N) \quad (3.20)$$

where $p=1, \dots, N$ and $k = \frac{2\pi}{N} \cdot \frac{n-1}{h}$ with $n=1, \dots, N$

In (3.20) ‘ h ’ represents the grid spacing between the entries of ‘ u_m ’, the latter being an array of dimensions ‘ $N \times N$ ’.

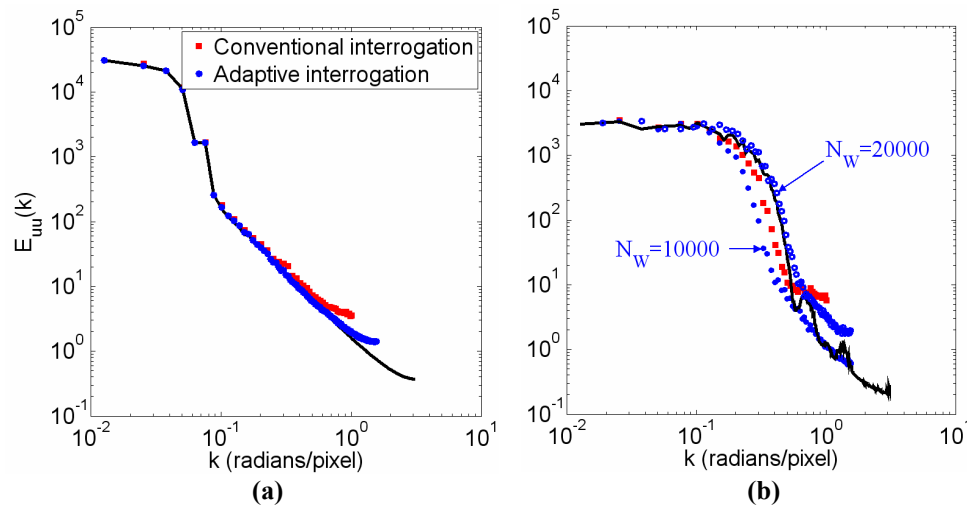


Fig. 3.15: Synthetic isotropic random fluctuations (a) Longitudinal power spectrum of the horizontal velocity component in case of a smoothing variance of 71 pixels. (b) E_{uuu} spectrum for a smoothing variance of 21 pixels. Black lines represent the imposed spectrum[‡].

Considering the homogeneous distributions in seeding density and spatial velocity fluctuations, sampling rate as well as window sizes will not exhibit strong spatial variations. In flows containing large coherent structures (Fig. 3.14-b), modulation effects are less important and the spectra of both adaptive and conventional methodologies nearly superimpose (Fig. 3.15-a). In that case the measured spectra coincide perfectly with the imposed spectrum for small wavenumbers ‘ k ’ i.e. large flow structures. In highly turbulent conditions (Fig. 3.15-b) the combined effect of spatial modulation and an insufficient number of imposed adaptive sampling windows ($N_w=10^4$) prevents a faithful reconstruction of the power spectrum. The spectrum of the adaptive technique clearly infers an incorrect representation of lower wavenumbers. While smaller flow scales seem to be well measured based on the spectrum, these small fluctuations are artificial byproducts stemming from measurement errors. Doubling the concentration of sampling windows ($N_w=20 \cdot 10^3$), thus equalizing the number of interrogation areas applied by the conventional, structured, interrogation analysis, yields an enhanced spectral response (Fig. 3.15-b, \bullet). With exception of the small flow scales, the spectrum now faithfully approaches the truth contrary to the conventional routine.

Two remarks finalize the discussion on the application of adaptive interrogation to computer generated images of homogeneous fluctuations;

1. The total number of correlation windows with the structured and adaptive approach generally amounted to 20000 and 10000 respectively. Even though this involves

[‡] The spectral lobes at higher wave number are directly reminiscent of the moving averaging operator used in the generation of the velocity field underlying the synthetic PIV images of homogeneous fluctuations.

reduction by a factor two, adaptive interrogation generally retains the spatial resolution and as such, in addition to being fully automated, certainly offers a benefit.

2. The smallest length scale, in other words the largest wavenumber, measurable is ultimately limited by the finite tracer spacing. This further enforces the statement made in the introduction that studies such as the current are inappropriate in describing quantitatively the achievable spatial resolution of PIV as a measurement technique because of the strong dependency on experimental conditions. Moreover, in case of a large range in flow scales the achieved performance in measuring power spectra will be heavily dependent on the adopted velocity interpolation schemes and original vector density as proclaimed by Lindken *et al.* (2003) and Vedula and Adrian (2004).

3.6.2 Transport aircraft wake vortex

- **Background**

When an aircraft wing generates lift, the pressure difference between top and bottom of the airfoil creates wingtip vortices. These are tubes of circulating air which are left behind by the wing and trail from the tip of each wing as vividly illustrated in Fig. 3.16.

To characterize vortex structures, information is needed on both size and strength within the core. Because the rate of rotation is a derivative operation on the individual velocity components, a high spatial resolution is needed which can be achieved by a sufficient number of correlation windows with reduced dimensions. On the other hand, these core regions contain the highest spin velocities which consequently causes a reduction in seeding as a result of strong centrifugal forces (Fig. 3.17-a). The quantity of interest, vorticity, is a derivative operation and its education is consequently sensible to erroneous displacement estimates or even small deviations. Correlation windows must therefore be also sufficiently large to ensure robustness. Once the velocity distribution is known, mathematical models can be fitted to estimate the vortex size. Again, the importance of accuracy and resolution is eminent.



Fig. 3.16: Wing-tip vortices of descending aircraft visualized by clouds (with permission of Steve Morris; www.airliners.net).

- **Experimental conditions**

An aircraft model scale 1:48 is towed at 3m/s in a water tank where 2C-PIV measurements are performed at a fixed station. The aircraft configuration at a few degrees incidence generates powerful vortical structures emanating from wingtips, winglets and flaps. After a single vortex has formed, the circulatory motion persists with a considerable strength and lifespan downstream (Rossow, 1999). Such flow experiment has been selected because of some challenging and peculiar features which are foreseen to complicate the analysis with conventional interrogation routines. First, the imaged region covering a field of view of $1.3 \times 1.3 \text{m}^2$ is neither uniformly seeded nor illuminated. Second, the flow properties are strongly non-uniform with small-scale fluctuations concentrated in a very small portion of the imaged flow, namely the vortex core.

- **Image evaluation and flow diagnostics**

Fig. 3.17-a shows the recording of the wake vortex at ' $X/b=30$ ', with the inherent large spatial variation in seeding where ' X ' is the distance downstream of the model and ' b ' is the aircraft wingspan relating to a value of 1.25m. By adapting the sampling rate to the seeding density and to the velocity standard deviation, samples are located in the region of interest, i.e. around the vortex core. Making use of the information on the velocity spatial fluctuations and that on the seeding density, a higher spatial resolution (higher sampling rate and smaller window size) can be obtained within the vortex core ensuring a better representation of its characteristics (Fig. 3.17-b).

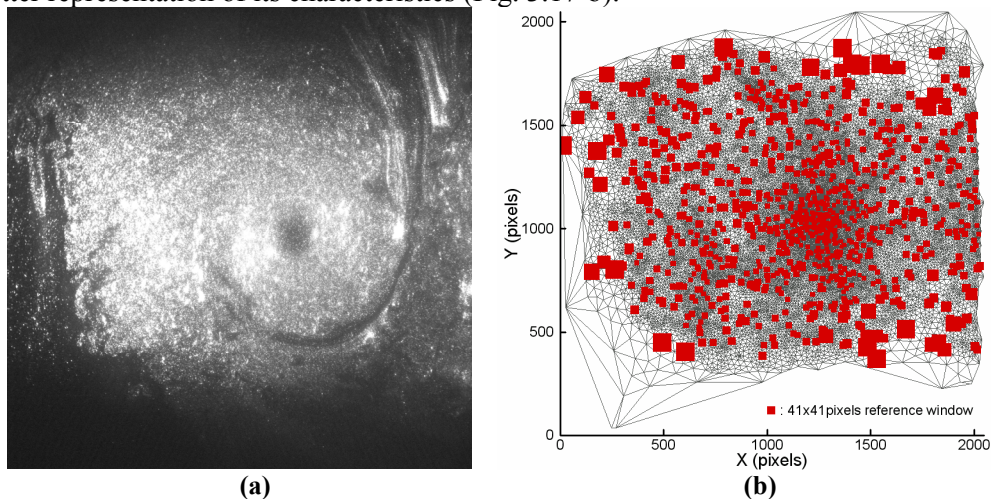


Fig. 3.17: Aircraft wake vortex (a) instantaneous recording and (b) adaptive sampling (red squares represent selected interrogation areas, scaled with a factor 2 for readability).

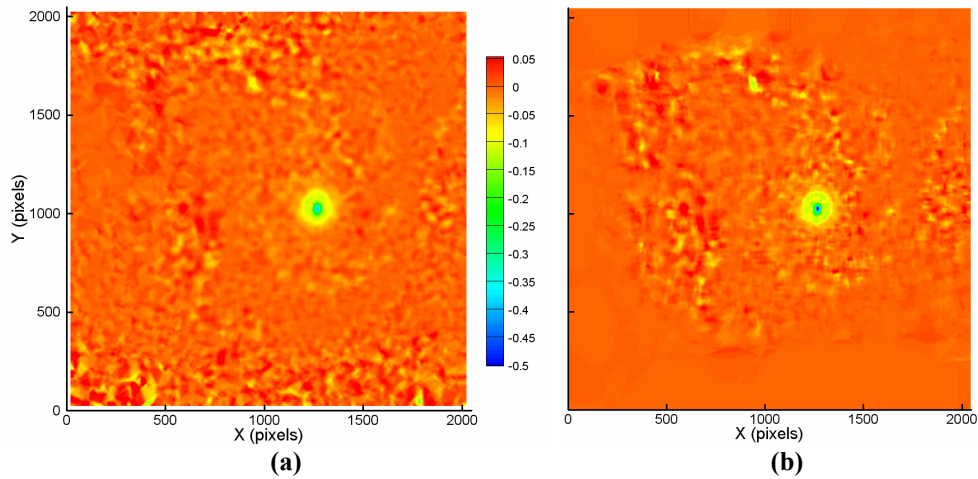


Fig. 3.18: Vorticity field (pixels/pixels) of the wake vortex (a) uniform sampling (b) adaptive sampling.

As discussed in the introduction, processing the recorded images with a structured grid requires a trade-off for the choice of interrogation area, between the number of outliers and spatial resolution. A constant sample area of 41 by 41 pixels with an overlap of 75% was applied. The large number of outliers appearing strongly affects the representation of the vorticity field (Fig. 3.18-a vs. -b). Moreover, because of the fixed distance between interrogation windows, the sampling of the vortex core is relatively poor ($h=10$ pixels or $\phi=0.01\text{spp}$), which results in an under estimation of the peak vorticity (-0.4 pixels/pixels) compared to the peak of -0.6 pixels/pixels obtained by adaptive PIV. The adopted methodology in the eduction of vorticity was a polynomial fitting (2nd order) in a least squares sense to the displacement field (Fouras and Soria 1998). Further details on the extraction of vorticity by means of polynomial fitting can be found in Appendix A.

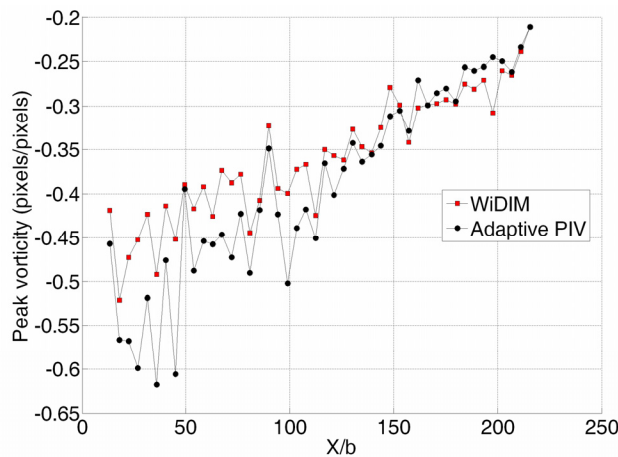


Fig. 3.19: Time history of the peak vorticity (■) WiDIM (●) Adaptive PIV.

The time history of vortex structure properties is important to determine the behavior of the vortex in the mid-field and far-field. Fig. 3.19 shows the time history of peak vorticity as obtained from WiDIM and from the adaptive method. Although the diagram shows more scatter for the adaptive methodology, a constant underestimate can be observed for the data obtained from WiDIM. For ' $X/b > 100$ ' the discrepancy reduces as a result of the increase in vortex core radius.

3.6.3 Shock-wave boundary layer interaction

- **Background**

As a result of the pressure rise across the incident shock, the boundary layer thickens and the resulting streamline curvature generates compression wavelets which merge into a reflected shock. This reflected shock-wave has a low frequency dynamic which is associated with the behavior of the incoming boundary layer. Having crossed the reflected shock, the incident shock reflects from the thickened layer as a Prandtl-Meyer expansion. If the pressure gradient is sufficient, the boundary layer may even separate. The typical features observed are illustrated schematically in Fig. 3.20.

Whole-field quantitative information is needed to make a complete characterization of the spatial structure associated with the shock-wave turbulent boundary layer and the dynamical aspects of the flowfield. In view of the boundary layer influencing the unsteady motion of the reflected shock, a good characterization is in order. Besides the oblique shocks, also the boundary layer must therefore be attributed a high spatial resolution, categorically in capturing the recirculation zone.

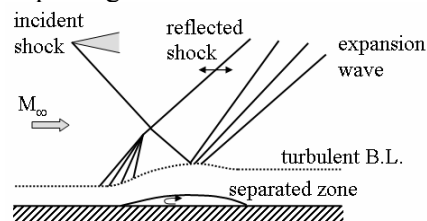


Fig. 3.20: Conceptual drawing of the features observed in the reflection of shocks from walls with turbulent boundary layers (following Shapiro, 1953).

- **Experimental conditions**

Experiments were performed in a Mach 2.1 free-stream where the oblique shock-wave generated by a wedge (deflection angle of 10 degrees) impinges on the wind tunnel wall where a turbulent boundary layer has fully developed (Humble *et al.*, 2006). This case has been chosen because the flow seeding density experiences considerable spatial variations due to the flow compressibility (shown in Fig. 3.21). Moreover, seeding intermittency (Fig. 3.21) in the region of interaction makes the experimental conditions even more critical for a robust interrogation. From the flow features point of view, the challenging

aspects are represented by the shock waves as well as the large range of flow scales associated to the turbulent boundary layer.

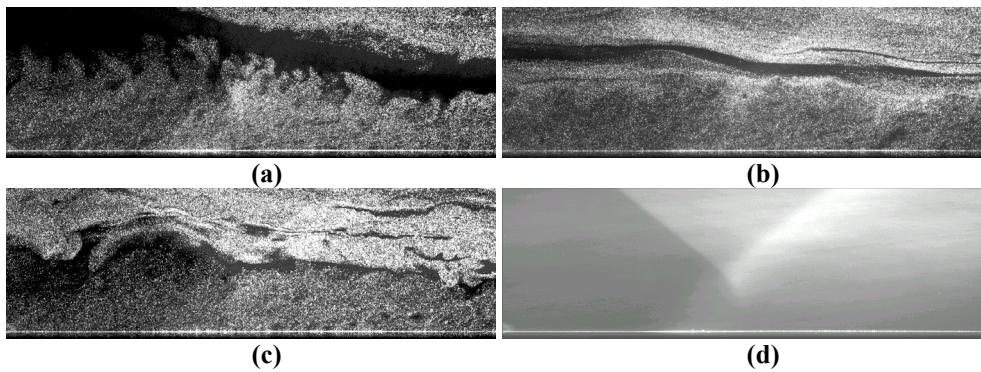


Fig. 3.21: (a)-(c) Instantaneous PIV recordings of the shock boundary layer interaction at different time instances (d) Ensemble averaged image intensity (400 image pairs).

- **Image evaluation and flow diagnostics**

The analysis was performed over 400 image pairs. The images were processed with the adaptive scheme and WiDIM-based interrogation algorithm (cf. Chapter 2). In the latter case the interrogation was performed with 21 by 21 pixels² and 75% overlap. For comparison at the end of the image interrogation process, the unstructured data was re-interpolated onto a grid of 5 pixels spacing.

Fig. 3.21 shows the typical conditions encountered during the experiment. The seeding level close to the wall is relatively homogeneous due to vigorous turbulent mixing, however the external flow is affected by intermittency caused by the limited mass flow output of the seeding supply system. Turbulent structures also affect locally the seeding distribution with centrifugal forces that reduce the seeding level in the core of the vortices. The mean scattering pattern (Fig. 3.21-d) clearly shows the variation of seeding density associated to the flow density, which changes sharply across shock waves.

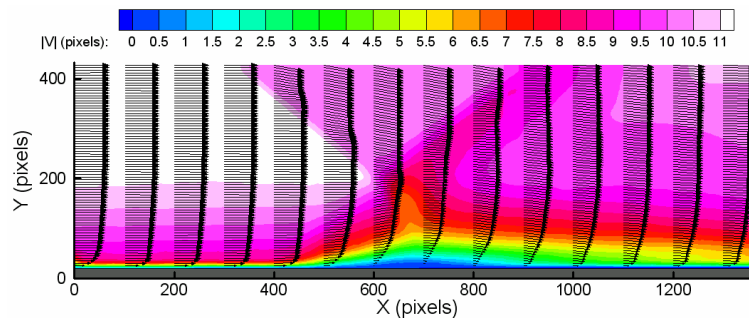


Fig. 3.22: Ensemble averaged velocity field with velocity profiles for the shock-wave boundary layer interaction.

The contours of velocity magnitude clearly show the incident and reflected shocks as well as the boundary layer before and after the intersection (Fig. 3.22). From the spatial distribution of the mean interrogation window size, one can conclude that the adaptive algorithm automatically reduces the window size in the boundary layer and to some extent across the shocks. The uniform flow regions are therefore sampled with windows in the range of 37 to 45 pixels (Fig. 3.23). Across the λ -structure and after the interaction with the boundary layer, the variation in displacement is expected to increase. The window size is accordingly automatically scaled to a value ranging between 13 and 21 pixels. The flexibility in window sizing further allowed a gradual reduction of the calculated window size towards the interface with a maximum factor of 3/2. This reduction was simultaneously accompanied by an increase in sampling rate. The instantaneous sampling distribution corresponding with image (a) presented in Fig. 3.21 is shown in Fig. 3.24. The adaptive sampling methodology places windows concentrated in those areas with sufficient tracers and in the area where the complex interactions take place.

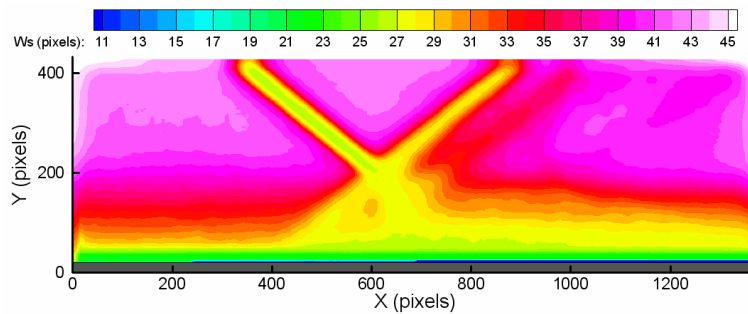


Fig. 3.23: Ensemble averaged window-size distribution for the shock-wave boundary layer interaction.

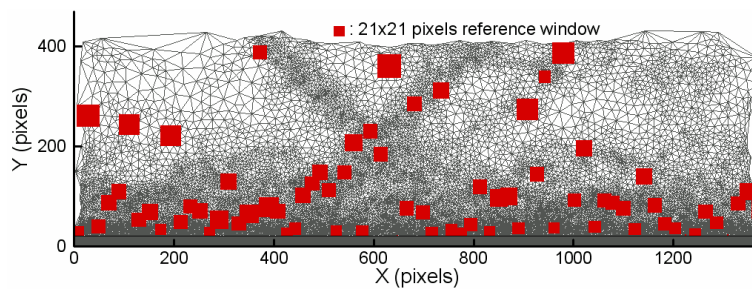


Fig. 3.24: Unstructured mesh for a single snapshot (Fig. 3.21-a) of instantaneous velocity field for the shock-wave boundary layer interaction. Red squares represent selected interrogation areas.

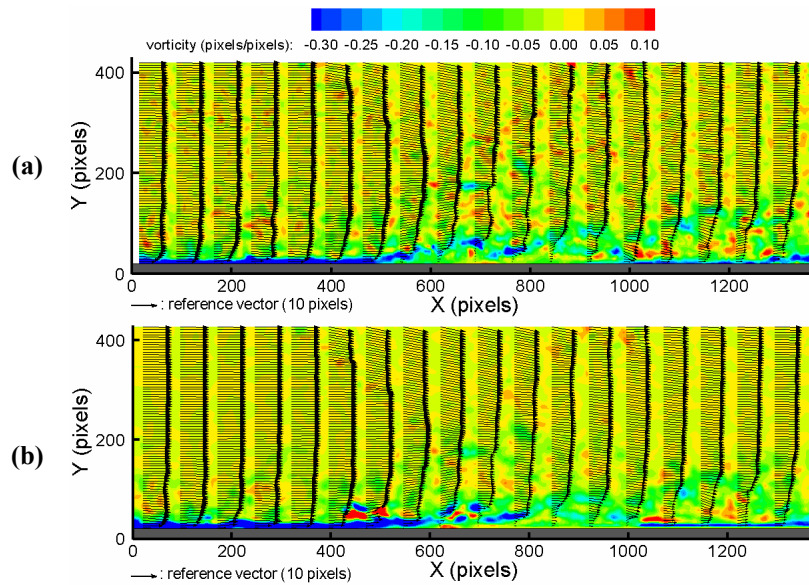


Fig. 3.25: Shock-wave boundary layer interaction instantaneous displacement field corresponding to image (a) in figure 3.21, with (a) uniform sampling (b) and adaptive sampling.

The instantaneous displacement field corresponding to image (a) in Fig. 3.21, is depicted in Fig. 3.25. Contour levels are based on the calculated vorticity. Within the free stream regions, spurious peaks can be noticed when processing the image with WiDIM (Fig. 3.25-a), indicating the presence of outliers. The adaptive methodology (Fig. 3.25-b) on the other hand provides less noisy vorticity contours. Due to the augmented sampling rate near the wall, the adaptive methodology is furthermore able to return a smoother boundary layer velocity profile, especially upstream of the interaction region. Square windows of 21 pixels in size were used in the interrogation with WiDIM. According to the proposed window-size distribution by the adaptive process (Fig. 3.23) this is the minimum size to be applied in the bulk of the flow. Overall, the differences between the two methodologies are therefore small.

Ensemble averaged velocity profiles obtained with both the adaptive and conventional methodology reveal no large differences in the bulk of the flow nor in the shock-wall interaction region (Fig. 3.26-a). However, close to the wall a slight improvement can be observed with the velocity profile approaching zero more systematically for the adaptive method. The extracted profiles of velocity fluctuations (Fig. 3.26-b) show again that the adaptive and conventional analysis are quite comparable for this flow case, except for the trends approaching the wall where the adaptive method better captures the peak. Moreover, downstream of the interaction a slightly lower level of fluctuations is observed, which is ascribed to a lower occurrence of outliers.

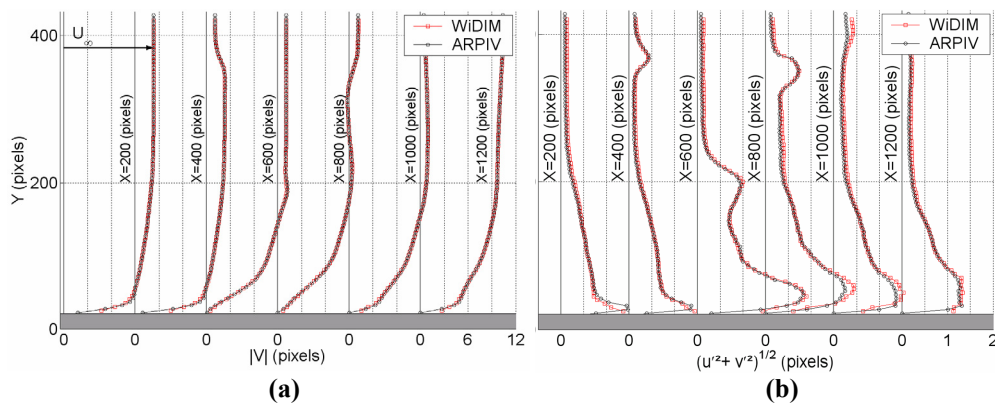


Fig. 3.26: Extracted profiles of the ensemble averaged (a) total displacement and (b) RMS in the displacement for the shock-wave boundary layer interaction. (□) WiDIM (○) Adaptive PIV.

3.6.4 Cylinder wake flow

The test case concerning the wake flow behind a circular cylinder placed in a turbulent flow (diameter-based Reynolds number ' Re_D ' of around 2000) has been previously encountered in Chapter 2 and is repeated here. An exemplary PIV snapshot is presented in Fig. 3.27-a. At a Reynolds number of 2000 the downstream von Karman vortex street emanating from the separated shear layers is fully turbulent yielding strongly three-dimensional vortical structures. The cylinder can therefore be considered as a challenging test case for any interrogation metrology in the eduction of vorticity.

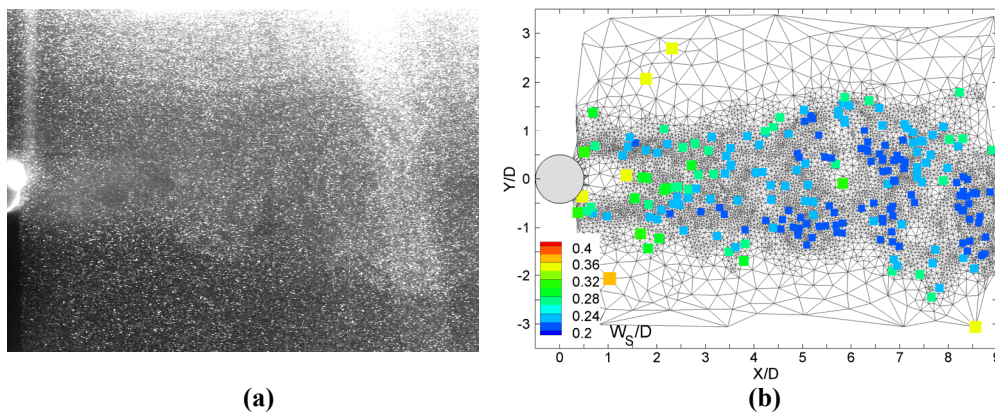


Fig. 3.27: (a) PIV snapshot of the cylinder wake flow ($Re_D \approx 2000$) (b) Adaptively imposed instantaneous sampling locations and correlation window sizes.

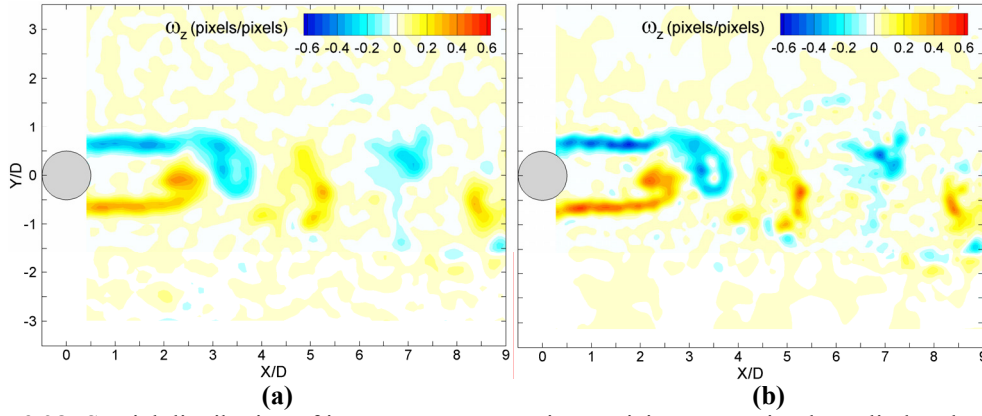


Fig. 3.28: Spatial distribution of instantaneous spanwise vorticity over a circular cylinder obtained by (a) conventional PIV image interrogation ($W_s/D \approx 0.29$) and (b) adaptive interrogation ($0.2 \leq W_s/D \leq 0.35$).

The degree of adaptivity is vividly visible in the distribution of correlation windows depicted in Fig. 3.27-b. The detached shear layers and wake are attributed high densities in correlation windows compared to the outer flow. The typical sample spacing in the wake region is 2 pixels. In total 8000 correlation windows sampled the flow with (square) window sizes ranging between 15 pixels ($W_s/D \approx 0.2$) and 19 pixels ($W_s/D \approx 0.26$) in the wake and 25 pixels ($W_s/D \approx 0.35$) in the free stream. For comparison the image snapshot was analyzed by the conventional metrology discussed in Chapter 2. Final correlation windows of 21×21 pixels² ($W_s/D \approx 0.29$) were adopted with an overlap coefficient of 75% yielding a vector about every 5 pixels.

The attainable enhancement in spatial resolution is evinced by the vorticity fields (Fig. 3.28). While the overall topology is identical, the adaptive approach yields more detail and predicts vorticity values which are around 50% higher in both the vortex cores and shear layer. The improved ability to detect vortices is further illustrated by observing the λ_2 -field defined by Jeong and Hussain (1997) in (3.21).

$$\lambda_2 = \left(\frac{\partial u}{\partial x} \right)^2 + \left(\frac{\partial u}{\partial y} \frac{\partial v}{\partial x} \right) \quad (3.21)$$

Equation (3.21) has been implemented through 2nd order polynomial fitting (cf. Appendix A). As indicated by Fig. 3.29, negative values identify the vortex cores. In case of adaptive image interrogation parameters, ' λ_2 ', besides being more detailed, reaches higher values in absolute magnitude and is better resolved in the core regions. The latter is beneficial in the identification of isolated vortices and in accurately locating the vortex cores.

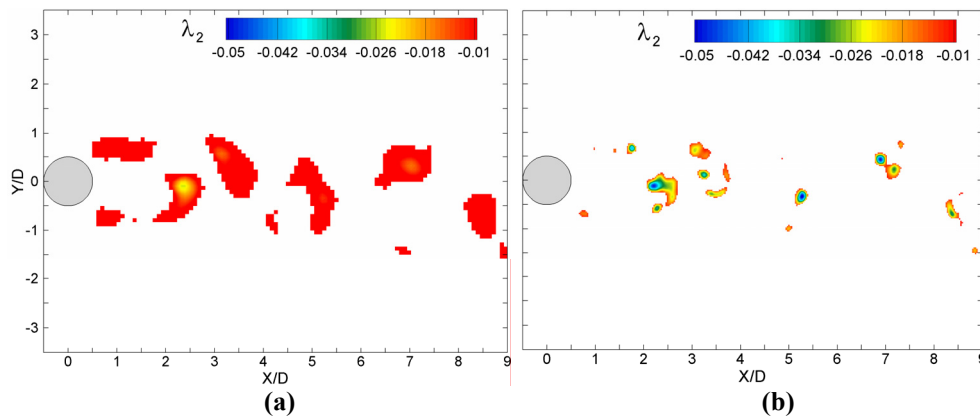


Fig. 3.29: Spatial distribution of instantaneous λ_2 -fields obtained by (a) conventional PIV image interrogation ($W_s/D \approx 0.29$) and (b) adaptive interrogation ($0.2 \leq W_s/D \leq 0.35$).

3.7 Conclusions

An adaptive image interrogation method is proposed with the purpose of increasing robustness and spatial resolution. The location, number and size of the interrogation windows is related to the local amount of particle images (i.e. seeding) and magnitude of the velocity fluctuations. The general criteria for flow adaptivity are stated treating separately signal adaptivity and flow adaptivity. The implementation of the adaptive methodology requires that interrogation windows are placed on an unstructured grid, which requires a technique for projection according to a target probability density function. The combination of the two criteria results in a single parameter describing the distribution of measurement windows.

While the limit in achievable spatial resolution is given by the particle size and distance between particle images, in current practice this theoretical limit is not used due to the compromise between spatial resolution and robustness in global sense. The proposed method decouples the mechanism allowing to put more and smaller windows where the flow requires it and using less of these unnecessary small windows in regions where the flow does not require it i.e. more uniform or potential regions.

Applied to computer generated images of homogeneous fluctuations, the adaptive metrology improved the measurement of the longitudinal power spectrum despite a force reduction in number of adopted correlation windows. Three experimental test cases have been chosen to further assess the proposed methodology; an aircraft vortex-wake, a cylinder wake and a shockwave boundary-layer interaction. In the first cases the method automatically allowed to reduce the number of outliers in poorly illuminated regions, still keeping a high resolution in the vortex core. In the third case the comparison with respect to a non-adaptive method yielded less pronounced differences, due to smaller variations of the image properties, except in case of seeding intermittency, which might occur in high speed flows. Even when the performance of the adaptive technique did not yield a

net improvement on the measurement, the fact that limited user input was needed (tuning window size and overlap factor) can be regarded as a significant improvement.

Given the marginal improvements near the static interface, further efforts are to be directed towards refined implementation of the criteria such as boundary treatment.

CHAPTER 4

PIV IMAGE INTERROGATION NEAR STATIONARY INTERFACES[†]

Abstract

In the following chapter the problem posed by interfaces when present in PIV measurements is addressed. Different image pre-processing, processing and post-processing methodologies with the intention to minimize the interface effects are discussed and assessed using Monte Carlo simulations.

Image treatment prior to the correlation process is shown to be incapable of fully removing the effects of the intensity pedestal across the object edge. The inherent assumption of periodicity in the signal causes the FFT-based correlation technique to perform the worst when the correlation window contains a signal truncation. Instead, an extended version of the masking technique introduced by Ronneberger et al. (1998) is able to minimize the interface-correlation, resolving only the particle displacement peak. Once the displacement vector is obtained, the geometric center of the interrogation area is not the correct placement. Instead, the centre of mass position allows an unbiased representation of the wall flow (Usera et al., 2004).

The aforementioned concepts have been implemented in the adaptive interrogation methodology where additionally non-isotropic resolution and re-orientation of the correlation windows is applied near the interface, maximizing the wall-normal spatial resolution. The increase in resolution and robustness are demonstrated by application to a set of experimental images of a flat-plate, subsonic, turbulent boundary layer and a hypersonic flow over a double compression ramp.

[†] This chapter has been partly published in Theunissen *et al.*, 2008, Experiments in Fluids.

Nomenclature

*	cross-correlation operation
δ	boundary layer thickness (pixels)
$\Delta x, \Delta y$	horizontal and vertical image correlation offset (pixels)
Δt	image time separation (seconds)
(η, ξ)	interface-fitted coordinate system
θ	boundary layer momentum thickness (meter)
κ, B	logarithmic-law constants
ρ	radius of curvature (pixels)
ν	kinematic viscosity (meters ² per second)
ϕ	correlation coefficient
a.i.i.	adaptive interface interrogation; increased sampling and non-isotropic window rotation
AR	Aspect Ratio
conv.	conventional interrogation methodology
$d\xi$	wall-normal distance (pixels)
DCC	Direct Cross-Correlation
enh.	correlation enhancements; vector relocation and SME-DCC
FFT	Fast Fourier Transform
FOV	Field Of View
I	intensity distribution
I_a, I_b	intensity distributions recorded at respectively time 't' and 't+ Δt '
I^0	undisturbed image intensity distribution
k_R, k_B	intensity scaling parameter for reflections and background intensity
MA	Moving Average
PDF	Probability Density Function
PIV	Particle Image Velocimetry
S	step function
SF_{max}	user-defined maximum stretching factor
SME	Symmetric Mask Exclusion
T	top hat function
u	wall-tangent velocity component (pixels)
u'	fluctuating wall-tangent velocity component (pixels)
u^+, y^+	inner-law variables
u_τ	wall-friction velocity (meters per second)
U_∞	freestream velocity (pixels)
V	total velocity (pixels)
WOR	Wall Overlap Ratio
W_s	correlation window size (pixels)
W_s^+	non-dimensional window size expressed in wall units
WU	Wall Unit; 1 WU = u_τ/ν
(x,y)	CCD coordinate system

4.1 Introduction

Nowadays, the majority of image processing algorithms involve a correlation operation between two images to extract the motion of detectable features. The problem of PIV measurements close to interfaces due to the presence of strong reflections and/or appearance of ghost particles is widely recognized (Stanislas *et al.*, 2003). These reflections constitute detectable features (Shi and Tomasi, 1994) and will create anomalies within the correlation-map, biasing the measured displacements towards zero and decreasing the reliability of the image analysis. Lindken and Merzkirch (2002) made use of fluorescent particles and shadowgraphy in an attempt to filter out these unwanted reflections. Depardon *et al.* (2005) on the other hand reduced the effect of optical disturbances by painting the complete test section and object with fluorescent paint. By placing the camera under the Brewster angle with the interface, Lin and Perlin (1998) were able to minimize the mirror-like behavior. Especially when dealing with curved interfaces or multiphase flows, a change in camera orientation is not always the simplest and most straightforward solution. In addition, surface treatments are not always possible. The truncation in signal density (i.e. seeding density) and velocity gradients imposed by the submerged object are known to cause an additional distortion in the correlation maps (Gui *et al.* 2003, Keane and Adrian 1990) leading to less accurate tracer displacement estimates. In these cases adjustment of the experimental setup will not avoid the degrading influence of the signal truncation. Consequently it is interesting to investigate the possibility to minimize the effects arising from interfaces in the image processing stage.

Current image analysis software samples the recordings at fixed locations within a Cartesian grid where the user selected parameters (correlation window size and overlap) are applied globally. As such, the processing parameters set are not optimal near interfaces. One therefore commonly resorts to PIV algorithm improvement or image enhancement prior to the correlation operation. The performance of several image pre-processing, image processing and data post-processing routines are assessed within this chapter when the field of view involves a static interface using computer generated PIV images.

In case of an interface, the windows overlapping it are susceptible to a lack of tracer particle images making the estimate of the displacement less reliable (Keane and Adrian, 1992). Ideally the interface is completely excluded from the correlation process while taking into account a sufficient number of tracers by careful positioning and orientation of the correlation windows. The second part of this chapter therefore presents an extension of the adaptive PIV algorithm. To improve the robustness of the PIV technique, correlation windows are rotated parallel to the interface boundary. Considerable improvements in resolution are achieved by augmenting the sampling rate near the object interface, while applying a stretching factor proportional to the radius of curvature of the object's surface.

4.2 Problem statement

Performing PIV measurements near interfaces, the experimentalist is confronted with the appearance of non-uniform image properties in the wall-normal direction and reflections, which are usually more intense than the individual particle images. Under this circumstance the image interrogation by cross-correlation is strongly affected. The mathematical expression of the cross-correlation operation between the intensity distributions ‘ I_a ’ and ‘ I_b ’ is presented in (4.1) for clarity.

$$\phi(m, n) = \sum_{i,j=1}^{W_s} \frac{(I_a(i, j) - \bar{I}_a) \cdot (I_b(i + m, j + n) - \bar{I}_b(m, n))}{\sqrt{\sum_{i,j=1}^{W_s} (I_a(i, j) - \bar{I}_a)^2 \cdot \sum_{i,j=1}^{W_s} (I_b(i + m, j + n) - \bar{I}_b(m, n))^2}} \quad (4.1)$$

Calculating ‘ ϕ ’ in the spatial domain through direct cross-correlation (DCC), requires mean intensities ‘ \bar{I}_a ’ and ‘ \bar{I}_b ’ to be computed in a different way. Whereas the former is determined only once before the correlation operation, the latter must be calculated each time a new pixel offset ‘(m,n)’ between the two distributions is chosen. The use of Fourier transforms on the other hand neglects the spatial dependency of ‘ \bar{I}_b ’ sufficing a mean intensity value subtraction in the interrogation areas prior to the correlation operation.

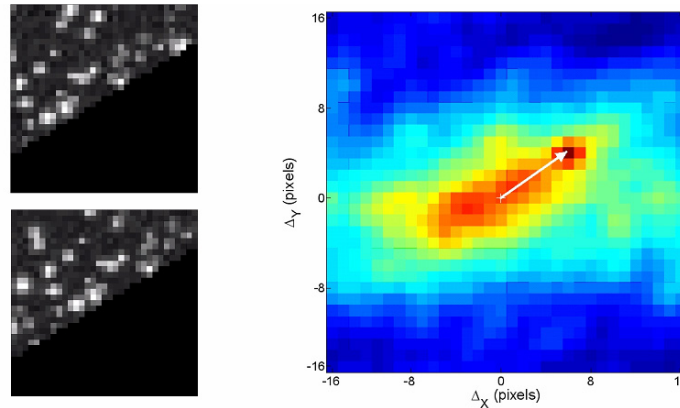


Fig. 4.1: Computer generated images with correlation map. White arrow indicates true imposed tracer displacement.

An example of the distortion in the correlation map due to the presence of a step in the intensity distribution across the interface is shown in Fig. 4.1. The interface is represented as delimiting the region where particle images are present from an ideally dark region. The location in the correlation map indicating the displacement of the tracer particles is highlighted by the white arrow. However, a wide region of high-intensity is present around the origin, decreasing the peak detectability. Approaching closer to the wall will

ultimately lead to an erroneous measurement of the displacement, either biased towards the origin or even false peak detection.

In Particle Image Velocimetry the signal consists of tracer particles sampling the flow from which velocity information can be extracted. The interface region may either contain no particle images (typical for opaque-diffuse surface properties) or contain some particle images due to light reflection at the wall (e.g. metallic objects, glass, etc.). In the first case the light intensity may drop at the interface causing a step-like discontinuity. In the latter case the intensity level is kept approximately constant while differences in refraction index between fluid and interface give additionally rise to strong reflections. A further discontinuity in background noise can be encountered across the interface due to an absence of secondary particle intensity scattering.

In their simplest form this signal truncation and reflection across the interface may be modeled by a step ‘S’ and top hat function ‘T’ respectively. Fig. 4.2 pictorially presents the decomposition of a PIV recording of intensity ‘I’, affected by the truncation and reflection, into a summation of the product between the undisturbed image ‘I^o’ and the step, and the scaled step and top hat functions. The mathematical expression is presented in (4.2). The first term models the signal truncation while the last terms represent respectively the truncation in background noise and presence of reflections. Scaling parameters ‘k_B’ and ‘k_R’ are introduced and can be time-dependent if reflections vary in intensity between recordings.

$$I \approx (I^o \cdot S) + k_B \cdot S + k_R \cdot T \quad (4.2)$$

According to (4.3) the cross-correlation of the signals ‘I_a’ and ‘I_b’ can be decomposed into the correlation of each term individually and cross-terms. The influence exerted by the step and top hat on the correlation map will therefore depend on the prominence of the truncation and will affect the entire correlation-map. For conciseness only the dominant terms in (4.3), being the autocorrelations and cross-correlation, are depicted in Fig. 4.2.

$$I_a * I_b \approx \underbrace{(I_a^o \cdot S) * (I_b^o \cdot S)}_{\text{cross-correlation}} + \underbrace{k_B^2 \cdot (S * S) + k_R^2 \cdot (T * T)}_{\text{auto-correlations}} + \underbrace{k_B \cdot ((I_a^o + I_b^o) \cdot S) * S + k_R \cdot ((I_a^o + I_b^o) \cdot S) * T + 2 \cdot k_B k_R \cdot (S * T)}_{\text{cross-terms}} \quad (4.3)$$

From visual inspection the distortion in the measured signal’s correlation can be traced back to the cross-correlation of the undisturbed images and the autocorrelation maps of the DC components (‘S’ and ‘T’). These anomalies, which have maximum amplitudes at the origin, will undoubtedly cause a systematic error in the measured displacement, i.e. a bias towards zero, and in the worst case lead to spurious vectors due to poor signal peak detectability.

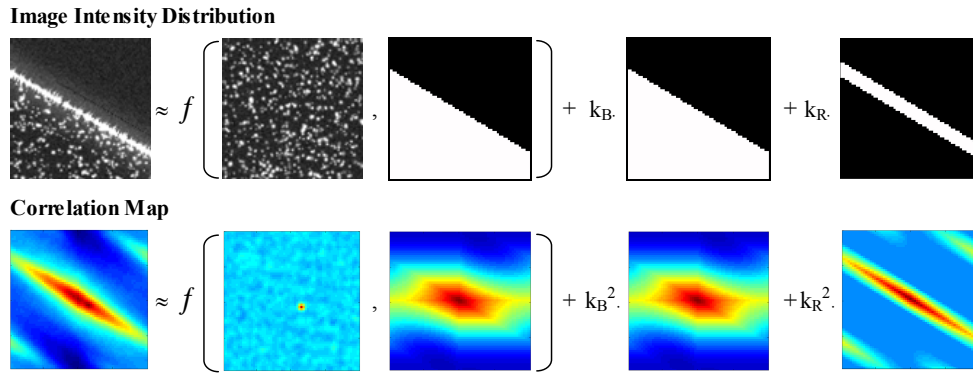


Fig. 4.2: (Top) The signal truncation can be represented as a multiplication between the undisturbed image and binary masks belonging to the intensity pedestal and reflections. (Bottom) Depicting only the dominant terms, the correlation of the images can be approximated as a summation of the cross-correlation of the undisturbed images and the individual autocorrelations.

If coefficients ' k_B ' and ' k_R ' could be estimated as well as the interface location and extent, the influence exerted by the reflection and background truncation could be minimized, correcting the cross-correlation to

$$I_a * I_b \approx (I_a^o \cdot S) * (I_b^o \cdot S) \quad (4.4)$$

Possible means to estimate the coefficients are related to background intensity characterization (e.g. sliding mean filter, statistical minimum pixel intensity, etc.) while the interface can be detected through proper morphological operations (e.g. image erosion, edge detection, etc.). The signal truncation however cannot be removed by mere intensity-related transformations but must instead be dealt with by an adequate correlation method. Additionally, the presence of an interface manifests itself in a positional uncertainty in vector location. When the correlation window overlaps the interface, the centroid of the measurement area is moved from the center of the interrogation area towards one side. Attributing the vector to the geometrical centre of the interrogation window is therefore no longer suitable. Viscous effects moreover cause a difference in motion between flow and submerged object, leading to gradients in the velocity field close to the interface. In combination with improper vector location this is reported to bias the measurement (Keane and Adrian, 1992).

In conclusion the following problems are identified as crucial for PIV measurements in wall proximity;

- (a) signal truncation at the wall,
- (b) presence of spurious light reflected from the wall,
- (c) biased velocity estimates and
- (d) insufficient wall-normal spatial resolution.

The remainder of the chapter describes possible solutions to points (a) and (b) by means of image pre-processing and correlation schemes. Furthermore, point (c) is

addressed recalling the vector-relocation technique. Finally the possible improvement of wall-normal resolution is handled by an adaptive algorithm based on non-isotropic resolution. The proposed methods are presented with computer simulated particle images and further assessed under experimental conditions.

4.3 Numerical assessment

Different pre- and processing methodologies will be assessed by means of Monte Carlo simulations with computer generated PIV images (Okamoto *et al.*, 2000). The generated PIV images all had a maximum intensity level of 255 corresponding to a depth of 8bits. The background was simulated with a uniform component of 16% and a fluctuating term (i.e. pixel noise) of 3%. A seeding concentration of 0.08 particles per pixel² was applied where particles were distributed randomly in a Gaussian shaped laser sheet. Gaussian particle images were integrated over a pixel array with fill factor 0.7 representing the virtual sensor. A normal distribution was applied for the particle image diameters with a mean of 3 pixels and variance of 1 pixel.

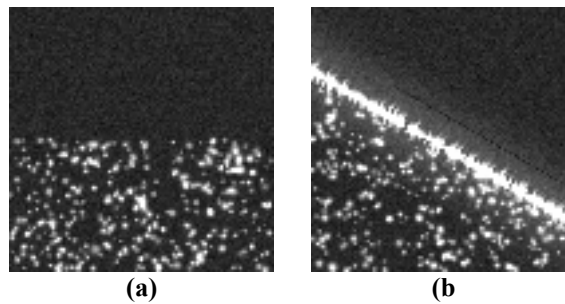


Fig. 4.3: Synthetic images: (a) Image type 1, 0° wall inclination. (b) Image type 2, 30° wall inclination.

Two types of images were generated; the first image type contained a simple transition from the flow region to the object without interface. Reflections and flare were imposed in the second image type. For each of the image types the interface was placed either at 0° inclination or 30° to simulate respectively flat or inclined walls (Fig. 4.3). Tracer particles were uniformly displaced parallel to the interface by a finite amount. Interrogation windows were set to 33 pixels and did not overlap. For the two image types the case of 50% wall overlap ratio (WOR) between the correlation windows and interface was considered while preserving a high enough number of particle image pairs for reliable correlation.

4.3.1 Image pre-processing

In absence of temporal fluctuations in reflection and flare, background subtraction is in principle able to adequately remove the truncation and reflection terms ' $k_B \cdot S$ ' and ' $k_R \cdot T$ '

in the original image (4.2). According to Wereley *et al.* (2002^b) the proper way is to select at each pixel location the minimum intensity over an ensemble of PIV image recordings. Having eliminated reflection and noise truncation (or in case of ideal intensity transition from flow to object, cf. image type 1), the intensity distribution involves only signal truncation. Comparison between correlation maps of the original and background subtracted image shows an almost complete removal of the reflection's and flare's autocorrelation (Fig. 4.4-a vs. -b). However, when coefficients ' k_B ' and ' k_R ' vary between images, background subtraction is unable to provide a valid noise estimate for each image individually, resulting in a distorted correlation map with only a minimal reduction in width of the reflection's autocorrelation (Fig. 4.4-e vs. -d).

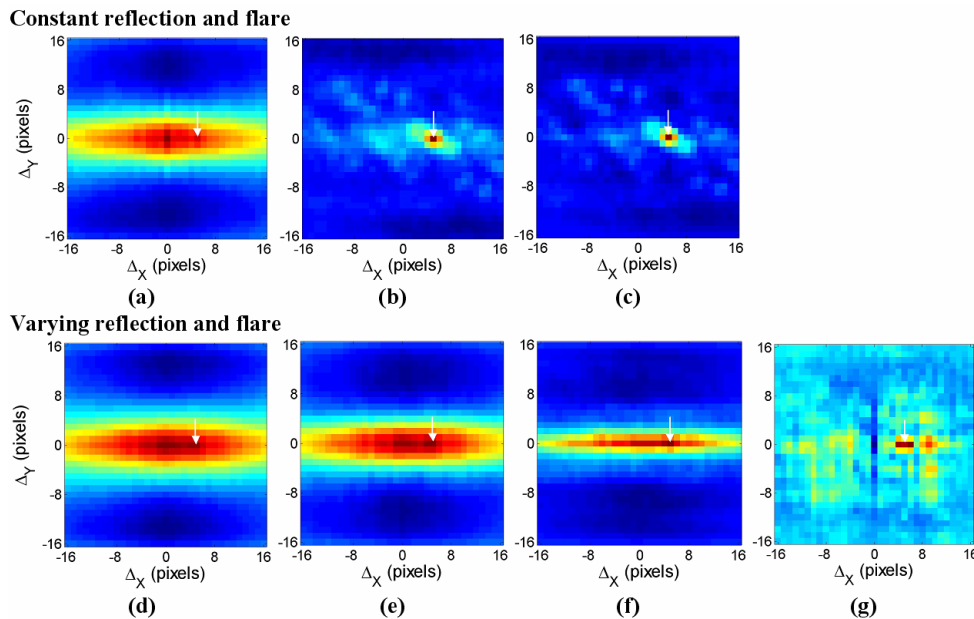


Fig. 4.4: Typical correlation maps for images of interfaces at 0 degrees inclination with constant (top) and varying reflection and flare (bottom). Imposed displacement peaks are indicated by the arrows. (a-d) no pre-processing (b-e) background subtraction according to Wereley *et al.* (2002^b) (c-f) background subtraction and intensity fill within masked area (g) image subtraction according to Honkanen and Nobach (2005).

Recalling the definition of the cross-correlation operation (4.1), the remaining mean intensity pedestal will create an additional distortion. A direct approach is therefore to equalize the gray-scale values inside image areas covering the flow and interface. Having identified the area within the correlation window containing flow-related information, its mean intensity is pasted within the masked area. Fig. 4.4-c indicates this operation to slightly enhance the peak detectability in case no reflection or flare is present. Otherwise, the improvement is more pronounced and the pasting operation furthermore reduces the DC component within the correlation map (Fig. 4.4-f).

However, as image properties commonly have a spatial variation in the direction perpendicular to the interface, the mean intensity is not an accurate estimation for the amplitude of the pedestal. A pixel-wise approach will therefore be more accurate, such as e.g. the image subtraction proposed by Honkanen and Nobach (2005). Pedestals and reflections are removed from image pairs by subtracting each consecutive image within a pair i.e. $I_b - I_a$. The autocorrelation function of the signal truncation is no longer present and a distinct correlation peak is retrieved (Fig. 4.4-g). Nevertheless the subtraction also removes objects with displacements smaller than one particle image width, which makes it unsuitable for boundary layers where the displacement gradually decreases towards zero when approaching the interface.

In conclusion, some attenuation of the effects of a stationary reflection can be achieved by means of local minimum intensity subtraction from each image. The problem of signal truncation can be partly addressed by masking techniques involving equalization of the mean intensity throughout the image. However, as image pre-processing does not allow a complete removal of the artifacts prior to the correlation operation, the correlation operator itself must be adapted in an attempt to reduce the prominence or effect of the autocorrelations related to the DC components.

4.3.2 Adapted correlation schemes

Since Willert and Gharib (1991) introduced the concept of digital image processing techniques in PIV, the use of Fast Fourier Transforms (FFT) for the image cross-correlation operation has become widespread. FFT is however sensitive to signal dependency both in the amplitude and phase domain. This is noticeable by the large peak at the origin of the correlation map originating from the image's DC component (Fig. 4.5-a). In this case the particle displacement peak is hidden and cannot be recovered. For this reason Wernet (2005) proposes to filter the Fourier transform of each interrogation area such that only the phase contributes to the cross-correlation. After filtering, the correlation map shows two distinct Dirac-functions at the origin and most probable tracer displacement (Fig. 4.5-b). However, when dealing with sub-optimal conditions (number of effective particle image pairs) it was observed that the central peak can outgrow the true peak, decreasing detectability.

Results from Monte Carlo simulations with synthetic images of the second type for wall overlap ratios of 50% are presented in Table 4.1. Filtering the Fourier transform reduces the displacement error. Largest displacement errors are obtained with unfiltered FFT when correlation windows are not parallel to the interface i.e. 30 degree inclination. Though the filtered version shows to be an improvement in this case, the method is more susceptible to random errors due to a lack in tracer images causing frequently peak detection at the origin. The latter explains the higher RMS error for the filtered FFT method.

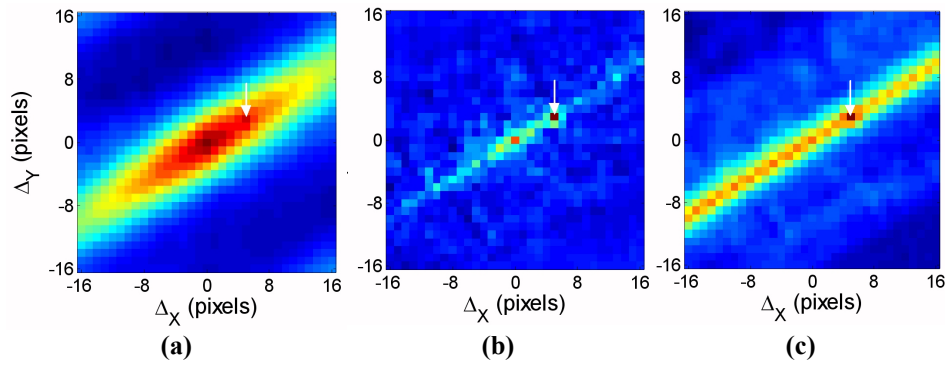


Fig. 4.5: Typical correlation maps for images as shown in Fig.4.3-b. The imposed displacement peak is indicated by the white arrow. Correlation using (a) FFT (b) FFT with filtering (Wernet 2005) (c) Symmetric Mask Exclusion Direct Cross-Correlation.

Table 4.1: Displacement error and RMS error after application of different correlation schemes to synthetic images of type 2, imposing uniform displacement of 5 pixels over flat walls at 0 and 30 degrees inclination. Correlation windows of 33 pixels, no mutual overlap and 50% WOR. Single correlation iteration.

Correlation method	Displacement error		Displacement RMS	
	0 deg. incl.	30 deg. incl.	0 deg. incl.	30 deg. incl.
FFT no filtering	-80%	<-100%	32.8%	6.8%
FFT with filtering	-4%	-27%	14.6%	48%
SME-DCC	0%	-0.2%	2.8%	0.6%

A simpler solution is to completely avoid signal truncation by excluding the interface region from the interrogation area. Ronneberger *et al.* (1998) applies direct cross-correlation (DCC) with an additional masking of the first interrogation window to exclude pixels covered by the interface from the correlation. DCC is beneficial in case of low seeding density as it utilizes an enlarged search area in which the smaller interrogation window is shifted. This explains its improved performances concerning displacement error and RMS error (Table 4.1). In addition, direct correlation does not assume periodicity in the image pattern as is the case with FFT. Here the application of pixel exclusion in both interrogation windows is proposed and will refer to the method by the acronym SME-DCC (Symmetric Mask Exclusion Direct Cross-Correlation). The correct numerical implementation of SME-DCC is deemed important and is dealt with in paragraph 4.5. With DCC the prominence of the autocorrelation peak of the DC component has decreased compared to the original map (Fig. 4.5-c). Moreover, the correlation peak has almost constant height, minimizing any bias towards the origin and reducing the possibility of false peak detection around the origin. At larger wall overlap ratios ($\geq 70\%$), the true peak is engulfed by the rim and can no longer be detected.

4.3.3 Vector relocation

Conventionally the obtained displacement vectors are attributed to the centre of the interrogation area. Tsuei and Savas (2000) discuss that when the centre of the correlation domain is located on a rigid stationary wall the obtained non-zero displacement vector is erroneous. The problem thus reduces to a proper repositioning of the vector representing the tracers' ensemble displacement when correlation windows overlap with the interface.

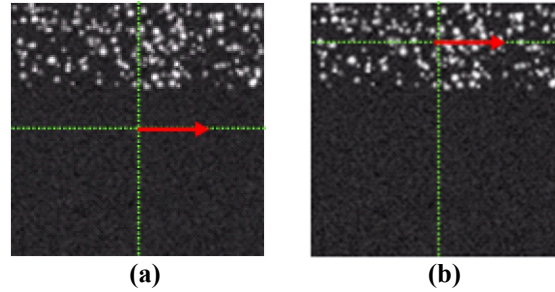


Fig. 4.6: Vector attribution (a) to the geometrical centre of the correlation window (b) to the centroid of the seeded area within the correlation window.

According to Willert (2000) a more correct approach is to position the velocity vector at the centre of gravity of the signal contained inside each correlation window whereas Young *et al.* (2004) locate the vector to the position of maximum intensity in the multiplication plane[†]. Similarly Lindken *et al.* (2003) place the displacement vector at the centroid of the multiplication plane. While these relocation approaches may enhance the spatial resolution in free stream conditions, their strong dependence on the recorded image intensities induce strong errors near interfaces owing to the presence of reflections. Instead, Usera *et al.* (2004) proposes to place the vector in the geometrical centre of the truncated correlation window which offers a more representable attribution as shown in Fig. 4.6.

In the present study the effect of vector relocation following the latter approach is assessed using synthetic data of a boundary layer with exponential velocity profile of equation;

$$u(y) = 3 \cdot (1 - e^{-\beta \cdot y}) \quad \text{where} \quad \beta = -\frac{\log(0.01)}{20} \quad (4.5)$$

The boundary layer thickness was set to 20 pixels. Correlation windows did not overlap mutually such as to study the effect of the velocity gradients for a single WOR between window and interface. The correlation operation was performed with SME-DCC. As reference, the response of a moving averaging filter (MA) on the imposed velocity

[†] The multiplication plane is the matrix containing the pixel-wise multiplications between the intensity fields of the two images shifted by the determined optimal displacement.

distribution is plotted. The applied kernel size was 33 pixels excluding signal inside the interface in the averaging operation.

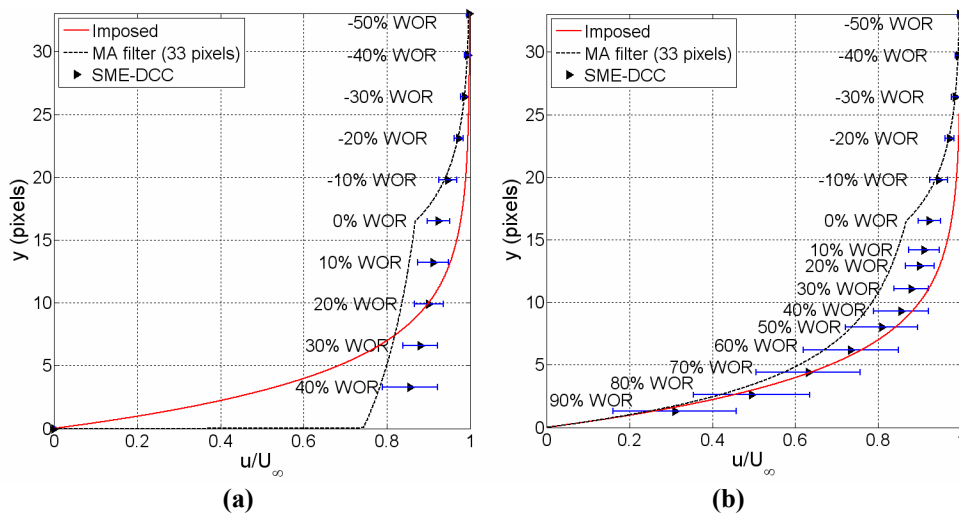


Fig. 4.7: Measured displacements for an imposed exponential velocity profile (red line) after a single iteration with a correlation window of 33 pixels applied to synthetic images of type 1 at different WOR with the interface at 0 degrees inclination. (a) Vector positioned in the geometrical center of the interrogation window (b) relocation of the vector to the centroid of the seeded area within the correlation window. Horizontal bars correspond to 95% confidence level.

Without vector relocation the maximum overlap possible between correlation window and interface is 50%. At higher overlaps the geometrical centers of the windows fall inside the interface in which case the vectors are set to zero displacement to satisfy the no-slip condition. The latter causes a strong discontinuity in the velocity profile near the wall, which is more pronounced in the MA profile (Fig. 4.7-a). More accurate displacement estimates are obtained by placing the vector in the geometrical centre of the information containing part of the correlation window. Relocation allows wall overlap ratios exceeding 50%, accompanied however by a higher displacement measurement uncertainty (Fig. 4.7-b). Nevertheless, the obtained values better follow the imposed profile and the discontinuity near the wall has disappeared.

As shown in Scarano and Riethmuller (2000), the MA offers a good approximation of the cross-correlation's response when there is a low variation in displacement within the correlation window. In case of highly sheared flows, the equivalence between MA and cross-correlation does not hold anymore. When displacement gradients exceed a particle diameter, correlation peaks detach (Westerweel, 2007). The non-linear response of the cross-correlation accordingly favors regions with less displacement variance. In the case of a boundary layer these zones correspond to the free-stream, biasing the measured displacement to higher values compared to the linear averaging operator. With increasing wall overlap ratio (WOR) the discrepancy between the moving average (MA) filter and cross-correlation response thus augments. This non-linear behavior further causes an

increase in displacement RMS, as indicated by the enlarged confidence intervals (Fig. 4.7), which agrees with the findings of Keane and Adrian (1990).

4.5 Symmetric-mask-exclusion direct cross-correlation implementation

Previously the direct cross-correlation (DCC) approach was demonstrated to be conducive in retrieving tracer displacements when the correlation window overlapped with an interface. The direct calculation is however resource intensive as for a square window of size ' W_S ' it involves in the order of ' W_S^4 ' number of calculations. In contrast, Fast Fourier Transforms (FFT) are able to considerably reduce this number to the order of ' $W_S^2 \cdot \log(W_S)$ '. The benefits of a frequency based correlation are eminent, which is the reason why the DCC has been translated into a simple sequence of FFT operations.

Similar to the digital mask methodology proposed by Gui *et al.* (2003), the normalized correlation coefficient is defined as

$$\phi(m, n) = \frac{\sum_{i,j=1}^{k \cdot W_S} F(i, j) \cdot m_b(i + m, j + n) \cdot (I_b(i + m, j + n) - \bar{I}_b(m, n))}{\sqrt{\sum_{i,j=1}^{k \cdot W_S} m_b^2(i + m, j + n) \cdot (I_b(i + m, j + n) - \bar{I}_b(m, n))^2}} \quad (4.6)$$

$$\text{where } F(i, j) = \frac{m_a(i, j) \cdot (I_a(i, j) - \bar{I}_a)}{\sqrt{\sum_{i,j=1}^{k \cdot W_S} m_a^2(i, j) \cdot (I_a(i, j) - \bar{I}_a)^2}} \quad (4.7)$$

To separate the seeded flow from the object area, binary masking arrays ' m_a ' and ' m_b ' are introduced for the first and second recording respectively (Fig. 4.8-e,-f). After expanding the multiplicative operation in the nominators of (4.6) and (4.7), each of the individual terms involves a cross-correlation, which can be performed by means of fast Fourier transforms. However, while ' F ' needs to be computed only once before the correlation operation, both mean intensity ' \bar{I}_b ' and mask ' m_b ' require recalculation for each offset (m,n). The latter necessitates a direct approach for the computation of ' ϕ ', rendering the presented scheme computationally intensive.

Following the FFT-based free shape correlation (Ronneberger *et al.*, 1998), the interrogation area in the first image is extended and padded with zeros to equal the size ' $k \cdot W_S$ ' of the larger search area in the second partial image (Fig. 4.8-a,-b,-c,-d). This zero padding operation can be automatically taken into account by the binary mask ' m_a '. When measurement points are located on a structured grid factor ' k ' is set to 2. With every iteration the disparity between the deformed images will converge to zero,

eventually allowing values of 'k' approaching unity. In case of window rotation and non-isotropic sizing the dimensions of the enlarged search area are given by ' $k_{\eta} \cdot W_{S\eta}$ ' and ' $k_{\xi} \cdot W_{S\xi}$ ' respectively in wall-tangent and normal direction (Fig. 4-10), where

$$k_{\eta,\xi} = 1 + \frac{\min(W_{S\eta}, W_{S\xi})}{2 \cdot W_{S\eta,\xi}} \quad (4.8)$$

To negate the need of repetitive computation of ' $\bar{I}_b(m,n)$ ' and ' $m_b(m,n)$ ', the introduction of a third binary mask 'W' of similar size as the search area is proposed containing unity values inside the interrogation area and zero otherwise as depicted in Fig. 4.8-g. Consequently, the mean operator can be translated into a correlation involving 'W', ' m_b ' and ' I_b ' (4.9). Calculation of ' $\bar{I}_b(m,n)$ ' in equation (4.9) is hence reduced to a one-time correlation operation by means of two Fourier transforms. Hereafter determination of ' \bar{I}_b ' at (m,n) becomes a mere lookup action. Concisely, the direct cross-correlation function can be expressed as a series of FFT operations (4.10), which drastically reduces the computational effort compared to the direct spatial computation.

$$\bar{I}_b(m,n) = \frac{\sum_{i,j=1}^{k \cdot W_s} m_b(i+m, j+n) \cdot I_b(i+m, j+n)}{\sum_{i,j=1}^{k \cdot W_s} m_b(i+m, j+n)} = \left[\frac{W * (m_b I_b)}{W * m_b} \right]_{(m,n)} \quad (4.9)$$

$$\phi = \frac{F * (m_b I_b) - \bar{I}_b (F * m_b)}{\sqrt{(W * m_b I_b^2) - \bar{I}_b^2 (W * m_b)}} \quad \text{where} \quad \bar{I}_b = \frac{W * m_b I_b}{W * m_b} \quad (4.10)$$

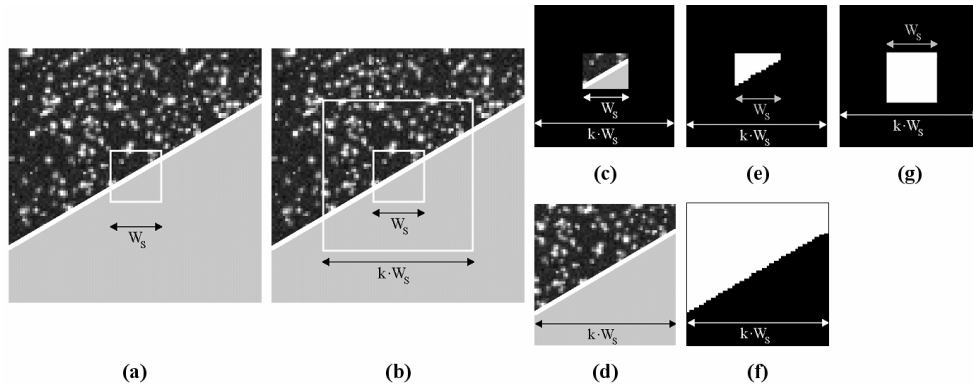


Fig. 4.8: (a) Image with selected interrogation area of size 'WS' (b) second snapshot with extended search area 'k·WS' (c) extended and padded interrogation area 'Ia' (d) selected search area 'Ib' (e) mask 'ma' (white =1) (f) mask 'mb' (g) mask 'W' used in calculation of mean intensity and covariance.

4.6 Adaptive interrogation near interfaces

Summarizing the previous results, the image pre-processing may enable to substantially attenuate the effect of reflections responsible for poor peak detectability. The latter is further enhanced exchanging the FFT method with SME-DCC. Finally the bias error can be compensated (if enough correlation signal is given) by a vector relocation technique. The problem however remains when reflections cannot be completely accounted for and when the interface is not aligned with the coordinates of the pixel grid. Moreover, as drawn in Fig. 4.7, even applying vector relocation, the spatial resolution close to the wall is in most cases the limiting factor for a PIV measurement.

In this section the earlier discussed schemes are implemented within the adaptive interrogation algorithm previously developed. The imposed adaptivity properly locates interrogation windows with the intention to sample regions with higher seeding densities and flow variances more densely with reduced window sizes. Briefly, the source density is mapped through a particle detection algorithm which allows dictation of the necessary window size by imposing a local image density. Estimates for the spatial fluctuations in the flow are taken as the spatial standard deviation of the velocity. Selected window sizes are inversely proportional to the seeding density and velocity standard deviation. Through a linear combination of velocity variance and source density the information concerning the signal distribution and flow scales is used in order to produce a single normalized distribution for the spatial sampling rate. A 2D transformation method distributes the window locations according to this sampling rate.

In the present case the aim is to keep constant the number of particle images when moving the interrogation area closer to the wall. This can be achieved by allowing the interrogation area to gradually expand in the direction tangent to the wall (assuming the flow to have a displacement parallel to the interface close to the object), resulting in a non-isotropic wall-normal resolution enhancement. The evolution of the window aspect ratio 'AR' with wall-normal distance 'dξ' is described by the following relation

$$AR(d\xi) = \frac{W_{S\eta}(d\xi)}{W_{S\xi}(d\xi)} = SF_{\max} \cdot \begin{cases} 1 & \text{if } d\xi < \beta \\ 1 - \tanh\left(\pi \frac{d\xi - \beta}{4\beta}\right) & \text{if } d\xi \geq \beta \end{cases} \quad (4.11)$$

where 'β' assumes a general value of 15 pixels, based on the typical lower size limit for a square interrogation window. Subscripts 'η' and 'ξ' refer to wall-tangent and normal abscissa of the coordinate system aligned with the interface (Fig. 4.10).

Equation (4.11) incorporates a user-defined maximum stretching factor 'SF_{max}', with representative values ranging between 2 and 6. Both rotation and stretching will increase the effective interrogation areas as cartooned in Fig. 4.9, which has a beneficial effect on the correlation robustness (Adrian, 1991). Enforcing simultaneously a reduction in total correlation window size further limits any spatial modulation. Following the principles of adaptive interrogation, the sampling rate is modified approaching the wall, increasing the windows' mutual overlap such to minimize the error due to coarse spatial sampling (Theunissen *et al.*, 2006^b). The latter can be achieved by adequate weighting of the

sampling rate imposed by e.g. the convolution between a Gaussian kernel and the eroded, binary image of the detected interface boundaries.

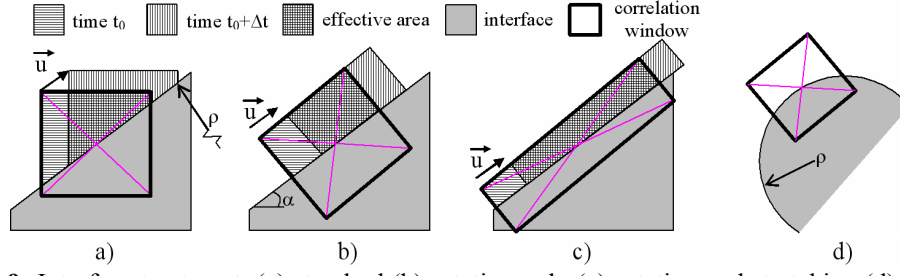


Fig. 4.9: Interface treatment: (a) standard (b) rotation only (c) rotation and stretching (d) effect of curvature.

The proposed methodology may be generalized for the case of curved interfaces by including the interface curvature radius ' ρ ' as an additional parameter to control the window aspect ratio;

$$AR(d\xi) = SF_{\max} \cdot \left[1 + (SF_{\max} - 1) \cdot \min \left(1, \frac{W_s|_{d\xi=0}}{|\rho|} \right) \right]^{-1} \cdot \begin{cases} 1 & \text{if } d\xi < \beta \\ 1 - \tanh\left(\pi \frac{d\xi - \beta}{4\beta}\right) & \text{if } d\xi \geq \beta \end{cases}$$

and $W_s = \sqrt{W_{Sx} \cdot W_{Sy}} = \sqrt{W_{S\eta} \cdot W_{S\xi}}$ (4.12)

The local slope of the interface is obtained from a point-wise second order polynomial fit after successful identification of the interface border[†] (Xu and Prince 1997, Scholz and Kähler 2004). With increasing flatness of the interface the curvature tends to zero, in which case a maximum stretching can be applied. The maximum length of the stretched window is then limited to ' $W_{s\eta} \approx SF_{\max}^{1/2} \cdot W_s$ ' with a corresponding minimum width of ' $W_{s\xi} \approx W_s \cdot SF_{\max}^{-1/2}$ ', where ' W_s ' symbolizes the side of a square window of equal area (4.12). When the radius of curvature becomes significantly smaller compared to the correlation window, such as for example near corners, the aspect ratio must tend to unity (Fig. 4.9-d). In this case the gradients in the spatial velocity distribution would anyway prohibit an accurate velocity measurement. For this reason, aspect ratios are set to unity within a radius of 45 pixels of detected corners (He and Yung, 2008).

The calculation of the displacement within the rotated (η, ξ)-grid requires an image intensity re-interpolation (Fig. 4.10). A B-spline interpolation scheme (Unser *et al.*, 1993^b) was implemented, constituting a trade-off between accuracy and computational effort. Rotation and iterative image deformation are combined in a single step, reducing

[†] It is interesting to note that the temporal evolution of a non-stationary interface can be successfully deduced by a combination of snakes and interpolation of the path-related frequencies obtained through Fourier Transforms (Abu-Gharbieh *et al.*, 2001).

both computation time and image degradation due to resampling (Scarano *et al.*, 2005). In addition the concept of intensity capping proposed by Shavit *et al.* (2007) was applied to further decrease the bias influence of bright flares. Overall the additional processing time imposed by the adaptive interface interrogation is negligible compared to the computationally more intensive direct correlation approach. The latter causes increases in computational effort typically in the order of 20%, but is only needed however in a small fraction of the PIV image where an interface is present. Moreover, the increase in computational effort can be deemed negligible compared to the expected drastic improvements in achievable spatial resolution.

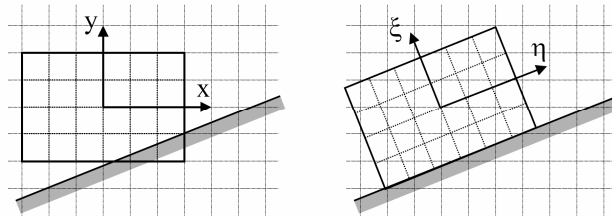


Fig. 4.10: Rotation of the correlation windows near interfaces requires re-interpolation of the original pixel intensities in the (x,y) coordinate system to the rotated (η,ξ) system.

4.7 Experimental assessment

4.7.1 Subsonic turbulent boundary layer over a flat plate

The improved robustness and resolution of the proposed technique in case of real experimental conditions is attested in the following with the study of a subsonic turbulent boundary layer over a flat plate.

- **Background**

When submerging a body within the flow, the fluid velocity will gradually tend towards the body's surface velocity. This change takes place in wall-normal distance and gives rise to so-called boundary layers (BL) schematically presented in Fig. 4.11-a. In most cases these layers are turbulent and contain a variety in flow scales. One of the pivot variables of a boundary layer is the wall-shear velocity ' u_τ ' which is a measure of the shear stress on the body's surface or in other words the viscous drag acting on the body. To estimate this velocity from accurate predictions of the velocity gradient, read displacement, near the wall are necessary which demands sufficient spatial resolution by means of small correlation windows. To give an indication, the boundary layer's wall-normal extent is illustrated in Fig. 4.11-b. Adrian (1997) argues that the spatial resolution can be controlled by meticulous selection of the field of view, i.e. the resolution can be improved by zooming in on a particular domain in the flow. In this case it would be the lower viscous sublayer of the boundary layer if only the wall-shear velocity would be of

interest. Accurate characterization of a boundary layer also requires its thickness ‘ δ ’ to be known for which a larger field of view is needed.

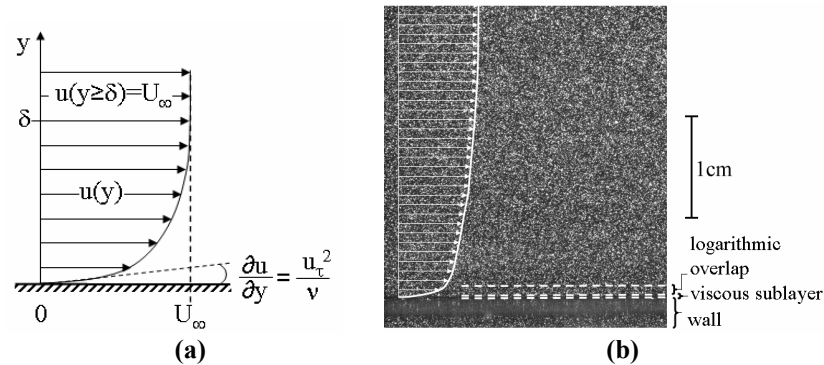


Fig. 4.11: (a) Theoretical boundary layer profile (b) PIV boundary layer image after contrast enhancement for clarity (Elsinga *et al.*, 2007).

Furthermore, the presence of strong light reflections and mirror images of particles commonly hampers a robust image analysis close to the interface. The presence of an interface within the experimental field of view further complicates the image processing by posing a signal truncation; the image area occupied by the object is without tracer particles. Whereas the lack of seeding particles imposes the use of larger interrogation windows, the boundary layer needs a higher sampling rate using smaller window sizes to resolve the flow fluctuations within. These are conflicting requirements for which a special treatment in the interrogation process is needed.

- **Experimental facility**

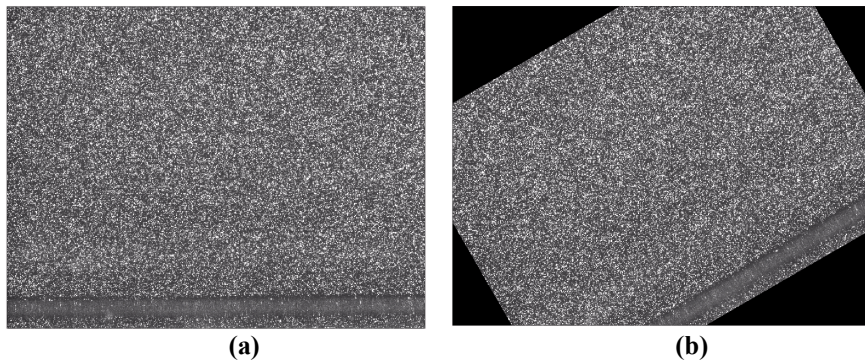


Fig. 4.12: Recordings of flat plate boundary layer experiment (a) original images (b) images rotated over 30 degrees.

Experiments on a turbulent boundary layer were conducted in a low speed wind tunnel with $40 \times 40 \text{ cm}^2$ test section and Plexiglas side-walls minimizing reflections (Fig. 4.12-a). The flow was seeded with particles of $1 \mu\text{m}$ in diameter, produced by a fog generator. A

Nd:Yag dual-head laser of 400mJ provided the illumination and a 12bit LaVision Imager Intense recorded the scattered light intensities. With a conversion factor of 1 pixel per $30\mu\text{m}$ in the image plane, the field of view corresponded to approximately $4.2\times 3.2\text{cm}^2$. The boundary layer was measured at a free-stream velocity of 9.8m/s. A tripping wire placed 2 meters upstream ensured a fixed location of the transition to the turbulent regime with a Reynolds number of $\text{Re}_\theta=1900$ based on the momentum defect thickness ' θ '. Further details regarding the experimental setup can be found in Elsinga *et al.* (2007).

- **Image evaluation and flow diagnostics**

The tests are performed on the original images providing a reference for the more difficult case where the wall is inclined over 30 degrees with respect to the CCD coordinates (Fig. 4.12-b). The proposed correlation method is expected to be invariant of any rotation of the system of axis. To provide a comparison, the same sets of images were analyzed with a more conventional procedure (referred to in the following figures as “conv.”) involving three iterative image deformation and refinement steps whereby correlation windows are placed on a Cartesian grid (Scarano and Riethmuller, 2000). Windows mutually overlapped by 75% and were correlated with the conventional FFT procedure.

Overall 100 images were used in the statistical analysis. To limit the influence of pixel-noise, background subtraction was performed prior to the correlation procedure as proposed by Wereley *et al.* (2002^b). To assess the measurement capacities individually of the different image interrogation metrologies, no-slip boundary conditions were neglected during iterative image deformation.

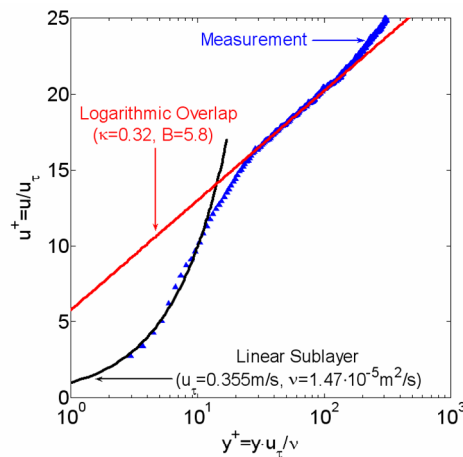


Fig. 4.13: Mean velocity profile obtained by ensemble correlation with superimposed law of the wall.

Reference values for the wall-friction velocity were obtained by analyzing the original images by means of ensemble cross-correlation (Meinhart *et al.*, 2000). Images were

iteratively deformed while simultaneously reducing the interrogation area, producing a wall-normal spatial resolution of around two wall units (WU). The value for the wall-friction velocity ' $u_\tau=0.355\text{m/s}$ ' was derived from a curve-fit of the inner-law to the resulting velocity profile (Fig. 4.13). Expressions for the inner variables and non-dimensional window size are given in (4.13) for conciseness.

$$u^+ = \frac{u}{u_\tau}, \quad y^+ = y \frac{u_\tau}{\nu}, \quad W_s^+ = W_s \frac{u_\tau}{\nu} \quad (4.13)$$

For the rotated images a typical distribution of 8000 correlation windows as applied by the improved adaptive interrogation methodology is depicted in Fig. 4.14-a. Hereafter the adaptive algorithm combined with adaptive interface interrogation and correlation enhancements will be referred to in the graphs by the synopsis "*adaptive+a.i.i.+enh.*". From a visual inspection the sampling is denser in an area parallel to the interface. The latter is put further into evidence by plotting the probability density function (PDF) of the distance between the sample, i.e. center of the correlation window, and the wall (Fig. 4.14-b). Combined with the algorithm's adaptivity of the sampling positions to the velocity fluctuations, a re-interpolation of the unstructured data to a Cartesian grid with approximately 1.5 WU (2 pixels) spacing was permitted.

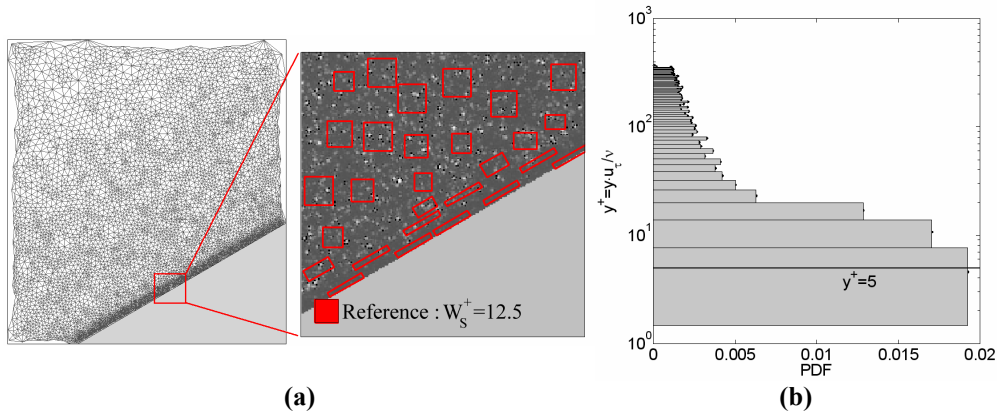


Fig. 4.14: Interrogation adaptivity (a) average window locations with zoom showing stretching and rotation of correlation windows (b) probability density function of the distance between the interface and sample locations.

Further rotation and stretching of the interrogation areas parallel to the inclined wall become prominent when zooming in on the interface (Fig. 4.14-a). The evolution of the tangent and normal correlation window sizes ' $W_{s\eta,\xi}^+$ ' (expressed in wall units) with normal distance from the wall is presented in Fig. 4.15-a. Within 11 WU windows remain constant in size with normal and tangent extensions of respectively 6.4 and 40 wall units, corresponding to a maximum stretching factor of around 6. Beyond, the window aspect ratio gradually decreases tending towards a square-shaped interrogation area at 50 WU (Fig. 4.15-b).

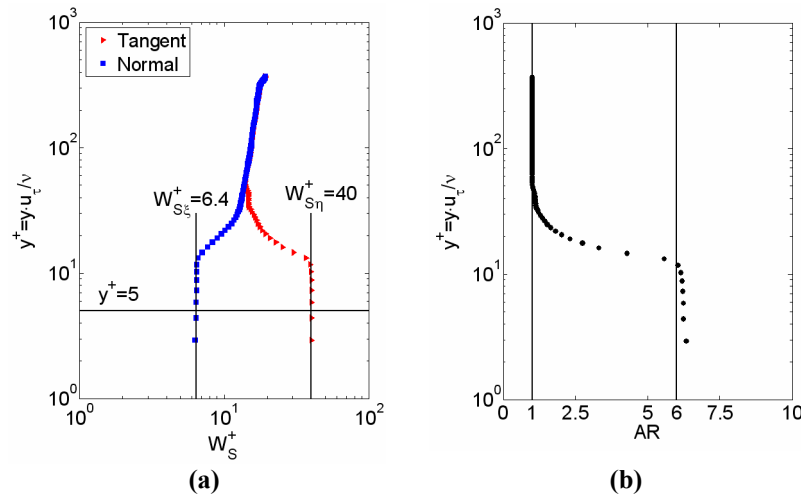


Fig. 4.15: Original boundary layer images: (a) evolution of the tangent and normal window sizes, expressed in wall units and (b) window aspect ratio as function of the wall-normal distance.

Averaged non-dimensional velocity profiles obtained by the extended adaptive and more conventional metrology are shown in Fig. 4.16-a for the original boundary layer images. In the latter approach window sizes of 12.5 WU and 24.2 WU (respectively 17 and 33 pixels) were applied globally. With an overlap coefficient of 75% this translated in a data-spacing of respectively 3.1 WU and 6 WU, compared to 1.6 WU with the adaptive scheme. Due to the large window sizes with respect to the viscous length scale ' ν/u_τ ' the conventional metrology is associated with insufficient resolution to measure the viscous sublayer (for which $y^+ \leq 5$). The resolution of the wall-adaptive approach on the other hand is sufficient to resolve the viscous sublayer (Fig. 4.14-b), yielding a $u^+ y^+$ profile fitting the theoretical models (Fig. 4.16-a). Implementation of the enhancements discussed within this chapter, being vector relocation and SME-DCC (hereinafter abbreviated to "*enh.*"), reforms the performances of the conventional interrogation approach in two ways. First, spatial resolution is increased through vector relocation, which is deducible in Fig. 4.16-a from the better fit of the non-dimensional profiles to both theory and results from adaptive interrogation. Second, the SME-DCC correlation scheme limits the number of erroneous vectors. The improved robustness is appreciable by plotting the RMS of the velocity component tangential to the wall (Fig. 4.16-b). Whereas previously the RMS evolved inversely proportional to the wall distance ' y/δ ' ($\delta \approx 24\text{mm}$), results now decrease near the wall and compare well with data reported by Klebanoff (1995). With decreasing window size the peak in RMS tends towards the adaptive measurement both in amplitude and spatial location, attesting the latter methodology to provide values representative of the investigated boundary layer.

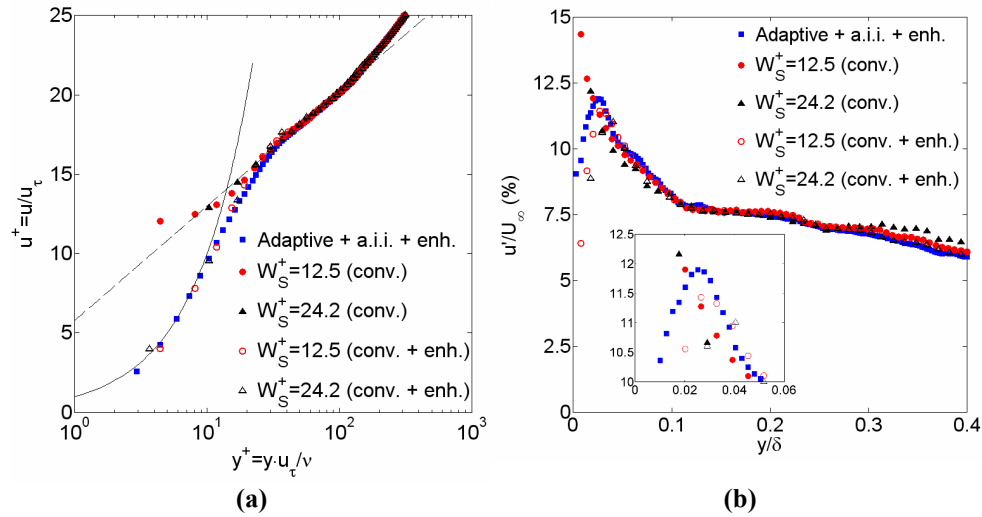


Fig. 4.16: Original boundary layer images: (a) mean velocity profile (b) profile of fluctuation in the wall-tangent velocity component. Image interrogation was performed by the adaptive approach combined with adaptive interface interrogation (*a.i.i.*) and correlation enhancements (*enh.*) (■), the conventional approach (*conv.*) (●,▲) and the conventional approach including correlation enhancements (*conv. + enh.*) (○,△).

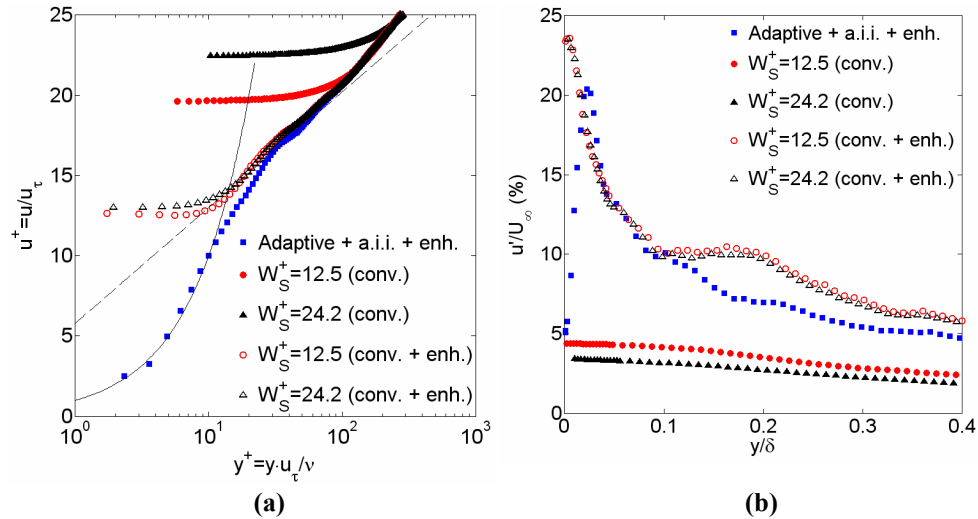


Fig. 4.17: Rotated boundary layer images: (a) mean velocity profile (b) profile of fluctuation in the wall-tangent velocity component. Image interrogation was performed by the adaptive approach combined with adaptive interface interrogation (*a.i.i.*) and correlation enhancements (*enh.*) (■), the conventional approach (*conv.*) (●,▲) and the conventional approach including correlation enhancements (*conv. + enh.*) (○,△). Profiles are undersampled for readability by a factor (a) 2 and (b) 3 if $y/\delta < 0.04$ or 9 otherwise.

Mean velocity profiles in inner-law scaling for the case of the rotated boundary layer images are presented in Fig. 4.17-a. Results from the discussed image interrogation

methodologies were re-interpolated to a pixel-wise grid beforehand allowing the extraction of the velocity data along a profile normal to the interface boundary. Conventional metrologies suffer from too poor resolution to resolve the linear sublayer (Fig. 4.17-a), proving them not to be conducive for PIV analysis in proximity of interfaces not aligned with the coordinates of the pixel-grid. Amelioration of the spatial resolution is achieved by incorporating vector relocation and SME-DDC in exchange of FFT. Whereas before a maximum WOR of 27% could be encountered, the WOR now spatially varies, making the correlation windows more susceptible to a strong reduction in effective correlation area (Fig. 4.9-a). In turn this increases the number of outliers and causes high RMS levels in the vicinity of the wall as shown in Fig. 4.17-b. A compromise is therefore needed in parameter settings (i.e. window size) to find a trade-off between spatial resolution and robustness. Compared to the original case (Fig. 4.16-a) the enhanced adaptive code on the other hand shows to return consistent results in mean velocity (Fig. 4.17-a) while retaining robustness (Fig. 4.17-b). Small dissimilarities between the velocity profiles are attributed first to uncertainties in wall-normal distance and second to poor image quality. The degradation in image signal is due to the performed morphological operation involving intensity re-interpolation. The latter further induces slightly enlarged window sizes away from the wall, modulating smaller fluctuations in the horizontal velocity component (Fig. 4.17-b). Near the interface the loss in signal explains the deviation of the u^+y^+ -profiles from the analytical function in the logarithmic overlap layer and the slightly higher amplitudes of the RMS distribution, while preserving the peak location.

4.7.2 Double compression ramp at Mach 7

To further attest the benefits of the correlation enhancements in wall-normal spatial resolution in vicinity of stationary interfaces, the case of a two-dimensional double ramp model with deflection angles of respectively 15° and 45° , placed inside a Mach 7 free stream (860 ± 10 m/s) is considered.

- **Background**

The flow over a double compression ramp configuration at Mach 7 constitutes a challenging application due to the presence of weak and strong shock waves at the leading edge of the ramp and at the second ramp respectively. When the leading edge shock interacts with the curved shock, an area is formed where complex flow features are to be expected (Olejniczak *et al.*, 1997).

After passing several oblique shocks, the flow close to the wall has a higher momentum compared to the flow behind the curved shock (Fig. 4.18). As a result, a jet-like contact surface is formed. The two layers are separated by slip-lines due to shock-shock interactions. The transition of these slip-lines into a shear layer causes the advent of large coherent turbulent structures downstream. Near the wall the flow undergoes separation on the first ramp with transition to turbulence in the form of recirculation (Ball and Korkegi, 1968). This small zone of lower velocities continues along the second ramp.

The numerical simulation of such flows is nowadays still very challenging and experimental techniques can barely visualize all the involved flow phenomena, not to mention the difficulty in measuring the finite separation zone near the ramp corner.

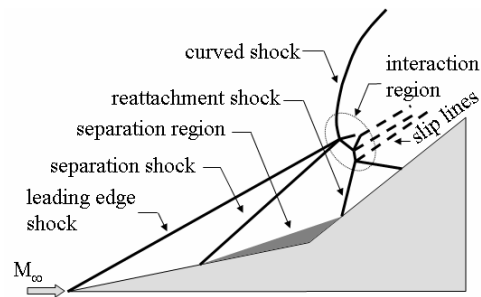


Fig. 4.18: Schematic shock pattern of the flow over a 15°-45° double-ramp at Mach 7.

- **Experimental facility**

A complete presentation of the experimental setup is described by Schrijer *et al.* (2006). Summarizing, experiments were conducted in a hypersonic facility based on the Ludwig tube concept. Titanium dioxide seeding particles with a median diameter of 400nm were introduced in the storage tube off-line by means of a high-pressure cyclone device. The procedure provided a relatively homogeneous seeding of the free-stream within a limited time interval (typically 20ms) during the windtunnel run. A Quanta Ray Spectra-Physics dual head Nd:Yag laser served as illumination source. Scattered light was digitally recorded by a LaVision Imager Intense CCD cameras with 600ns time separation between exposures. Approximately 32pixels covered one millimeter giving a field of view (FOV) of 4.3×3.3cm². The complex flow physics involved are visualized by the schlieren image presented in Fig. 4.19-a where the analyzed field of view is indicated by the white rectangle. Leading edge shock, curved compression shock and the interaction region between the two are distinguishable.

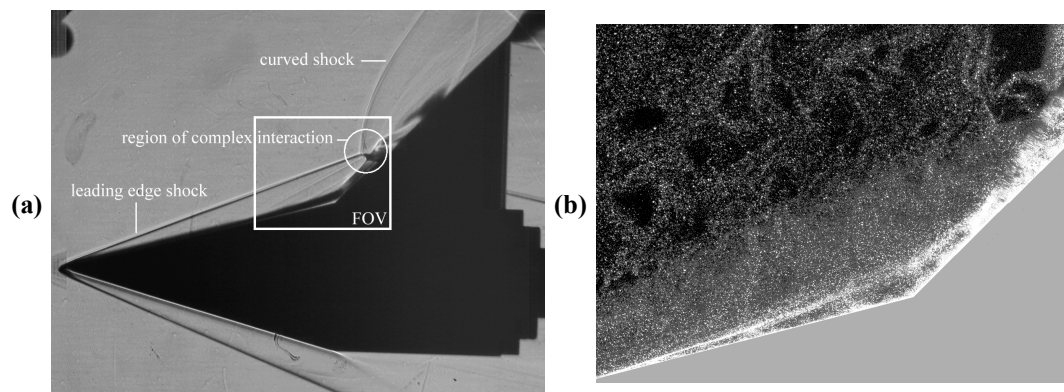


Fig. 4.19: (a) Schlieren image of the double wedge model at Mach 7 (b) Instantaneous PIV recording of the FOV (contrast has been enhanced for clarity).

- **Image evaluation and flow diagnostics**

Near the ramp corner the existence of boundary layer separation, reattachment and recirculation zones has been demonstrated extensively in both numerical and experimental studies (Korolev *et al.* 2002, Verma 2003, Fletcher *et al.* 2004, among others). However, detection of these phenomena with PIV measurements proves to be challenging. The strong spatial variations in seeding and flow velocity in the instantaneous PIV recording (Fig. 4.19-b) cause the cross-correlation to fail either because not enough tracers are encountered within the interrogation area or because the flow velocity is too inhomogeneous within it. Larger correlation window sizes lead to an increase in correlation reliability and dynamic range but simultaneously lowers spatial resolution (Scarano and Riethmuller, 1999). The latter explains why close to the wall, PIV measurements in general fail to sufficiently resolve the flow to infer small-scaled features. Besides the lack in tracer images due to large portions of the correlation windows overlapping the wall, strong reflections from the wall are encountered in the corner region. A strong bias of the measurements to zero is expected to appear in the proximity of the wall, which will further filter out smaller velocity fluctuations.

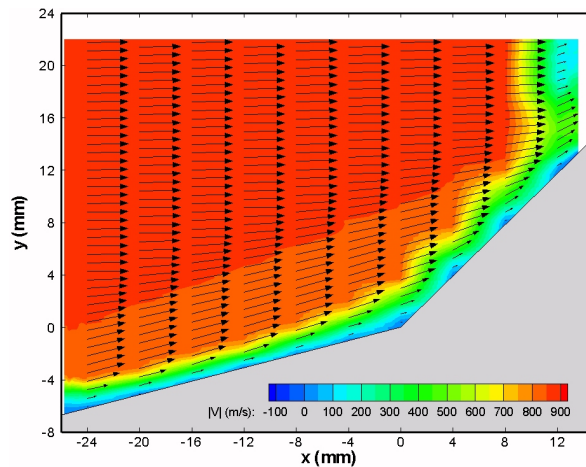


Fig. 4.20: Statistical mean of the total velocity for the FOV in Fig. 4.19-a.

An example of a statistical mean of the total velocity is presented in Fig. 4.20, taking into account 40 background subtracted (Wereley *et al.* 2002^b) image snapshots. Here the PIV analysis was performed placing correlation windows of 0.43mm^2 on a Cartesian grid with 0.19mm spacing. The included iterative window deformation and refinement in the interrogation process cause velocity profiles to tend towards the imposed no-slip condition at the wall. None of the streamlines indicate however presence of a recirculation zone (Fig. 4.21-a). Implementation of the SME-DCC routine and vector relocation is beneficial since the recirculation zone becomes discernible (Fig. 4.21-b). Still, only through the adaptive approach can both the dynamical range and spatial resolution be optimized by respectively maximizing the window size range and relocation

of the correlation windows (Theunissen *et al.*, 2006^b). With the imposed adaptivity criteria the proximity of the ramp is oversampled (0.06mm gridspacing) by correlation windows of $1.3 \times 0.3 \text{ mm}^2$, which are aligned with the interface. The enhancement in wall-normal spatial resolution is appreciable as the thin layer of recirculating flow near the interface is now sufficiently resolved (Fig. 4.21-c).

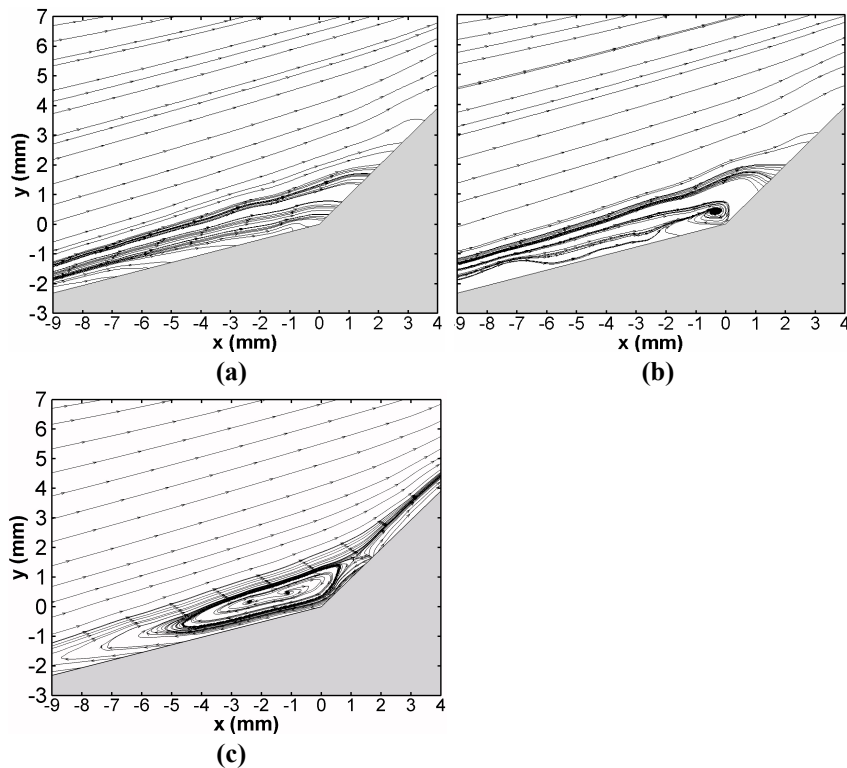


Fig. 4.21: Streamlines in vicinity of the ramp after analysis with (a) the conventional approach (b) the conventional approach including correlation enhancements (c) the adaptive approach combined with adaptive interface interrogation and correlation enhancements.

4.8 Conclusions

In proximity of a wall, conventional correlation methodologies suffer from large distortions in the correlation map due to signal truncation and reflections. In this chapter, several common image pre-processing, image processing and data post-processing routines are considered in the attenuation of the bias towards zero of the measured displacement and the probability of false peak detection. An assessment has been performed by means of Monte Carlo simulations with computer generated PIV images representative of fields of view involving static interfaces.

Local minimum intensity subtraction combined with equalization of the mean intensity throughout the image has been shown to be effective when reflections do not possess a temporal variation in intensity and image properties do not vary spatially. Under the opposed circumstances pixel-wise approaches are more appropriate in the removal of the artifacts from the images, but inherently degrade the signal of importance. There are numerous advanced image pretreatment methods, but all of them have some limit, where eventually the algorithms of this chapter will become meaningful. Furthermore, the problem of signal truncation remains and demands proper windowing techniques for correlation. Given wall overlap coefficients below 70%, correlation of only the signal containing area within the correlation window by means of direct cross-correlation proved to be most effective when symmetrically excluding the masked regions. Further repositioning of the obtained displacement vectors towards the geometrical center of the information containing section reduces the positional uncertainty and increases the spatial resolution. The shortcomings of the conventional methodologies, as well as the effectiveness of the proposed enhancements, have been attested by application to experimental images of a flat-plate turbulent boundary layer. Ameliorations in spatial resolution and robustness of the image analysis were appreciable.

Despite all efforts, even after implementation of the correlation enhancements, windows are still susceptible to a low spatial resolution and a lack in number of effective particle image pairs when the interface is misaligned with the CCD coordinates. This reduction in effective correlation area causes a growing probability of erroneous displacement vectors. An innovative interrogation method has therefore been presented with the intention to increase robustness and resolution. Besides the implementation of vector relocation and DCC-based image correlation near the interface, the method incorporated wall adaptivity in an automated manner. The enhanced interface treatment consisted of a) an increase in sampling rate in the vicinity of the wall, b) rotation of the correlation windows parallel to the interface and c) a reduction in wall-normal window size. Application of the proposed methodology to original and morphed flat plate boundary layer images has shown to yield consistent results both in velocity and turbulence intensity while retaining robustness. The benefits of the enhanced spatial resolution have been further demonstrated by comparing the PIV methodologies when applied to image recordings of a double compression ramp in a hypersonic flow. The adaptive approach was proven to possess sufficient spatial resolution to discern a recirculation zone near the corner, previously irresolvable by the conventional approach.

CHAPTER 5

STATISTICAL ADAPTIVITY IN PIV INTERROGATION[†]

Abstract

This chapter proposes an extension of the adaptive approach proposed afore to achieve an autonomous and robust adaptive interrogation method for PIV data sets with the focus on the determination of mean velocity fields. Under circumstances such as sub-optimal flow seeding distribution and large variations in the velocity field properties, neither multi-grid techniques nor adaptive interrogation with criteria based on instantaneous conditions offer enough robustness for the flow field analysis. A method based on the data ensemble to select the adaptive interrogation parameters, namely window size, aspect ratio, orientation, and overlap factor is followed in this study. Interrogation windows are sized and spatially distributed on the basis of the average seeding density and the gradient of the velocity field. Compared to the instantaneous approach, the ensemble-based criterion adapts the windows in a more robust way especially for the implementation of non-isotropic windows (stretching and orientation), which yields a higher spatial resolution. If the procedure is applied recursively, the number of correlation samples can be optimized to satisfy a prescribed level of window overlap ratio.

The relevance and applicability of the method are illustrated by an application to experimental data from a shock-wave-boundary layer interaction problem. Furthermore, the application to a transonic airfoil wake verifies by means of a dual-resolution experiment that the spatial resolution in the wake can be increased by using non-isotropic interrogation windows.

Nomenclature

δs	infinitesimally small area (pixels ²)
δU	instantaneous displacement corrections (pixels)
θ	correlation window orientation (radians)
λ_w	nearest neighbor sample spacing (pixels)

[†] This work has been partly published in Theunissen *et al.*, 2009, Experiments in Fluids.

Λ	Hessian eigenvalue
μ	velocity mean
(ξ, η)	coordinate system rotated over angle θ with respect to (x, y) system
σ	velocity standard deviation
σ_I	intensity standard deviation
φ	sampling rate (number of windows per pixel)
c	airfoil chord length
Conv.	Conventional image interrogation
$\det(X)$	determinant of matrix X
Ecc	correlation window eccentricity
H	Hessian matrix
I	image intensity
IA	Instantaneous Adaptivity
I_{thr}	threshold intensity
N	number of instantaneous data fields
$N_{\delta s}$	number of equidistant samples within an area δs
N_w	total number of correlation windows
s	shock-normal coordinate
SA	Statistical Adaptivity
S_d	signal source density
T_{aw}	adiabatic wall temperature (Kelvin)
T_e	temperature at boundary layer edge (Kelvin)
u', v'	fluctuating velocity components in horizontal and vertical direction
u_τ	wall-friction velocity
u_{eq}	van Driest equivalent velocity
$u_{n1,2}$	shock-normal velocity respectively upstream and downstream
U^*	filtered displacement field (pixels)
U_0	velocity defect in the wake
U_e	velocity at boundary edge
U_∞	free stream velocity
W_s	square correlation window size (pixels)
WOR	Window Overlap Ratio
\bar{X}	spatial average over a single instantaneous data field
$ X $	absolute value of variable X
$\langle X \rangle$	the ensemble-average value taken over N instantaneous data fields.

5.1 Introduction

The analysis of PIV recordings is nowadays fairly well established; the motion of particle images is obtained by multi-step cross-correlation analysis with typically square interrogation windows of decreasing size along the iterations. The multi-grid approach enables to overcome the $\frac{1}{4}$ rule (Keane and Adrian, 1990) and when window deformation

is applied, the effect of the in-plane velocity gradient is largely compensated (Huang *et al.* 1993^{a,b}, Scarano 2002). Nevertheless, the choice of some crucial parameters is left to the user, most important the size of the interrogation window. According to Adrian (1991) the correlation window should typically contain at least 8 particle image pairs. Although it is well known that the seeding density and the optical and digital resolution can be optimized through the appropriate choice of experimental parameters (e.g. magnification, numerical aperture, seeding concentration, light sheet thickness), it is very common to encounter the situation where not all parameters can be optimized. Moreover, it is not uncommon that for a given experiment no such thing as a single value for the window size, aspect-ratio and orientation, overlap factor can be found that optimizes the measurement performance (i.e. minimizes the measurement uncertainty and improves the confidence level). It has been shown for instance (Fouras and Soria, 1998) that the optimum flow sampling can be well controlled by the digital interrogation process. In the previous chapters, adaptive techniques have been introduced to remove the unnecessary constraint of a uniform size of the interrogation window (cf. Chapter 3) along with the possibility to implement non-isotropic spatial resolution (Scarano, 2003) and optimize it in a robust way for stationary interfaces (cf. Chapter 4). In the above mentioned approaches, the optimization is based on a single pair of images, which turns out to be particularly critical especially for the implementation of non-isotropic (elliptical) windows whereby the eccentricity and orientation depend upon the spatial second derivatives of the velocity field and are therefore prone to error propagation. Instead, the mean velocity field constitutes a suitable basis for the interrogation optimization in that the averaging process minimizes the influence of noise by taking into account its intrinsic stochastic nature (Westerweel, 2000).

Despite the difficulty of adapting the interrogation parameter to the image and flow field properties, the issue of obtaining an automatic (and possibly optimal) choice of the interrogation window is still relevant. The present study discusses the possible implementation in a *weaker form* when compared to the instantaneous approach, which is only based on the image and flow properties as obtained from the entire ensemble of recordings. Here the hypothesis is made that the measurement conditions remain unchanged during the recording time in such a way the information inferred from the ensemble will be relevant to the instantaneous pairs to a good extent. Moreover, in many industrial applications such as in aeronautics, the primary interest lies in the mean flow.

In the present work, the adaptive interrogation procedure is extended to include non-uniform sampling (resulting in a variable window overlap ratio) and interrogation window size and geometrical aspect ratio. These parameters are adapted to the ensemble-averaged particles image density (signal adaptivity). The adaptivity to the flow pattern is driven by the spatial variance and curvature of the mean velocity field. The effectiveness of the method is assessed with two experiments; first, a flow containing both normal discontinuities and a high rate of shear (shock-wave-boundary layer interaction) and second, a specific investigation of the flow behind a transonic airfoil performed simultaneously at two different resolutions to capture the momentum defect in the wake.

5.2 Proposed methodology

The measurement of time-averaged flow properties is of high relevance in turbulent flows. One of the parameters of interest, often beyond measurement capabilities, is the rate of strain associated with the mean velocity gradient for shear flows. The mean velocity gradient is furthermore in direct relation with the length scale of the turbulent fluctuations and the production of turbulent kinetic energy (cf. equation 6.5). As recently discussed by Astarita (2009) the modulation effects introduced by spatial averaging pose a general requirement to analyze at higher resolution sheared regions (shear layers), discontinuities (shock waves and interfaces) or highly curved regions (e.g. vortices).

In analogy with computational fluid dynamics (CFD) methods, the regions in the flow domain where the velocity field exhibits non-linear spatial variations can be considered as a good heuristic that indicates the regions that require grid refinement i.e. a high spatial resolution. The cross-correlation analysis in PIV returns in principle a spatially filtered measurement of the particle motion obeying the Navier-Stokes equations, with the filter being the interrogation area and to some extent the region in between neighbouring measurement points. Consequently this necessitates the need of an interrogation with adapted sampling locations instead of a conventional Cartesian approach.

The current method is built on the basis of the adaptive interrogation technique previously proposed (Chapter 3) where the main objective is to properly distribute in space the interrogation windows such to maximize the spatial resolution only within the flow regions that require it. The main difference with the previous approach is that the estimate for the required spatial resolution is obtained by the spatial standard deviation of the average velocities instead of the instantaneous velocity field. A linear combination of the velocity spatial variation (local variance) and the average image source density is used in order to produce a single normalized distribution for the spatial sampling rate ' ϕ ' (typically $\phi \ll 1$ expressed in vectors/pixel). A 2D transformation method (valid for planar PIV measurements) distributes the window locations according to this sampling rate. Additionally, the size of the interrogation window is chosen with inverse proportion to the seeding density and velocity local variance.

The adaptive interrogation performance can be further extended to incorporate non-uniform window shape and orientation as proposed by Scarano (2003). The indicator function for this optimization is provided by the second spatial derivatives of the velocity field. However, previous attempts to apply the non-isotropic resolution on an instantaneous basis showed that the velocity pattern is often too complex to perform such an optimization, and the measurement uncertainty and confidence level do not allow a correct estimation of the second derivatives of the velocity field. The concern is not only the presence of erroneous vectors, which could be efficiently removed by data validation (Westerweel and Scarano, 2005) but also the measurement precision needed to evaluate the second derivatives, limiting the approach of instantaneous adaptivity to window size and distribution only. A straightforward procedure to simplify the target flow pattern and overcome the adaptive interrogation parameters' sensitivity to measurement noise is to refer it to the time-averaged velocity vector field. This approach largely decreases the effect of outliers and instantaneous velocity fluctuations enhancing the overall robustness

of the process (Fig. 5.1) that estimates the target sampling rate ' ϕ ', window size ' WS ', window eccentricity ' Ecc ' and window orientation ' θ ', to tracer concentration (signal adaptivity) and spatial velocity variance (flow adaptation). Average correlation window settings and flow field are eventually obtained by averaging the ' N ' instantaneous interrogation parameters and velocity fields respectively. Within the remainder of this chapter the notation ' \bar{X} ' will imply the spatial average over a single instantaneous field while ' $\langle X \rangle$ ' indicates the ensemble-averaged value taken over N instantaneous fields.

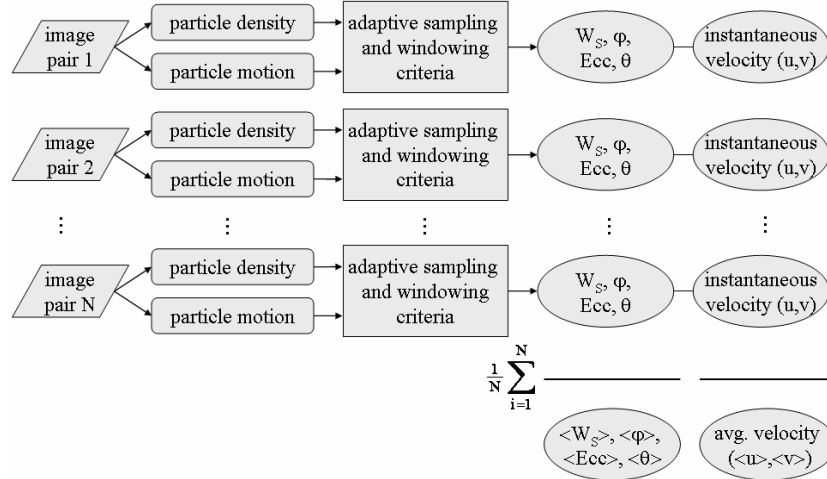


Fig. 5.1: Flow diagram of interrogation adaptation to instantaneous particle density and velocity pattern. A robust choice of the interrogation parameters is based on mean properties. Interrogation window characteristics and instantaneous velocity fields are determined for ' N ' individual image couples followed by an ensemble averaging.

Fig. 5.2 visually compares the application of two adaptive approaches to the case of the supersonic flow where a planar shock wave impinges on a solid flat wall where a turbulent boundary layer has fully developed. Details of the experiment are given in Humble *et al.* (2007). In Fig. 5.2-a, the instantaneous adaptivity process described in Fig. 5.1 is illustrated. The distribution of 9000 sampling locations is obtained considering data averaged from 400 instantaneous sampling distributions. Instead, the situation depicted in Fig.5.2-b is that obtained from the adaptive sampling directly based on the ensemble-averaged flow and image properties. The more distinct treatment of the potential flow regions and shocks and boundary layer in the second case is due to the fact that for ensemble-averaged information a higher refinement can be reliably imposed. It should be specified here that the region close to the wall (below the dashed red line), is refined with an interface-proximity-based criterion whereby the window shape and orientation are based on the distance from the wall and not on the velocity field (Chapter 4). This example already indicates the potential benefits of an ensemble-based adaptive criterion in terms of increased robustness. Moreover, once the initial difficulty of dealing with non-uniform data distribution is overcome, the approach offers advantages compared to a structured grid analysis with uniform spacing. Firstly, the distribution of correlation

windows shows more conformity to the underlying flow field. Additionally, the implemented adaptivity may offer a computational advantage when implemented, considering that a similar resolution is obtained by a uniform mesh with a total of over 30000 windows.

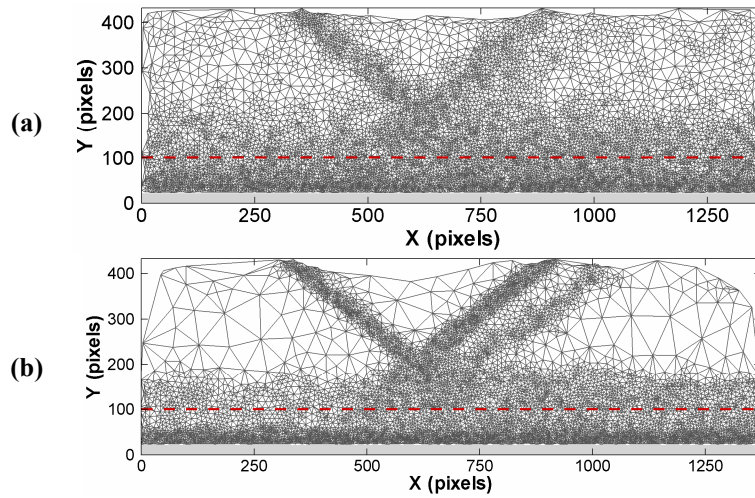


Fig. 5.2: Comparison of adaptive interrogation (sampling grid shown) for a shock wave boundary layer interaction experiment (9000 measurement points). Sampling locations are obtained (a) as the average of instantaneous adaptivity (Chapter 3) (b) from ensemble adaptivity (average flow field is assumed to be known)

The following objectives are finally put forward in the proposal of the new interrogation methodology;

- the interrogation approach must return a reliable mean velocity field with high resolution.
- the method must be robust with respect to outliers and spatial velocity variations especially in view of the required estimation of window shape and orientation.
- the spatial resolution both in terms of sample spacing and window size should be advantageous compared to image analyses implementing a Cartesian mesh.

Additionally, the method could potentially give a basis for a reduction of computational effort considering that the calculation of cross-correlation of measurement points may be chosen in a more flexible manner than for the Cartesian distribution.

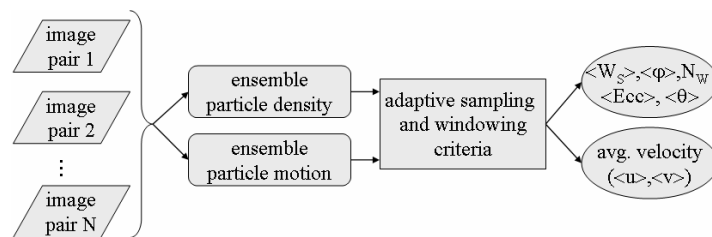


Fig. 5.3: Flow diagram of interrogation adaptation to ensemble particle density and motion. Adaptivity criteria are based on ensemble-averages.

In conclusion, the ensemble adaptivity translates the adaptivity criteria proposed in Chapter 3 to ensemble-averaged estimates for signal and flow adaptivity as schematically presented in Fig. 5.3. The statistical averaging operation will reduce the influence of random fluctuations in the tracer density and velocity field and strongly simplify the flow topology, thereby enabling the use of non-isotropic interrogation windows in a reliable manner. This variant, however, comes with the limitation that the increase in spatial resolution and robustness can only be obtained for the mean flow field. As will be shown in the remainder, the depicted procedure moreover allows an estimation of the necessary number of correlation windows to properly sample the image given a pre-defined window overlap ratio. Once the window characteristics have been determined, these remain unchanged throughout the analyses of the entire image set (Fig. 5.4). To obtain an average velocity field, the image interrogation itself can be performed either by means of ensemble correlation (Meinhart *et al.*, 2000) or by analysis of the image snapshots and averaging the instantaneous velocity data after applying data validation (Westerweel and Scarano, 2005).

Ensemble correlation maps peak at the most occurring (and most probable) displacement. Accordingly, ensemble correlation offers the advantage of yielding high signal-to-noise ratios and high reliability in the measured mean displacement, even in case of poor image quality. However, only when the velocity probability distribution function is symmetric around the maximum, the location of the peak with highest amplitude will correspond to the mean displacement. Moreover, one should retain in mind that the ensemble correlation approach can only be used efficiently with steady flows or exhibiting small fluctuations. The latter is a more strict constraint than that imposed to the currently proposed method, which can be also applied to turbulent flows with temporal fluctuations of the particle displacement exceeding a particle image diameter. Nevertheless, also in the current method, for the window characteristics derived from ensemble-averaged conditions to be correlated with the flow field at the varying instantaneous conditions, the flows should not exhibit fluctuations larger than typically 20 to 30%. For instance, the current approach would be adequate to treat wall-bounded turbulence and moderately separated flows (e.g. boundary layers, airfoils, cavities, slender obstructions). It is instead not appropriate in bluff-body wakes (e.g. Karman vortices past cylinders) or unsteady/pulsating jets, where the relative velocity fluctuations can attain levels of 100%. Still, the latter requirement is intended less strictly than that for ensemble correlation because the correlation peak is built for each individual pair of images.

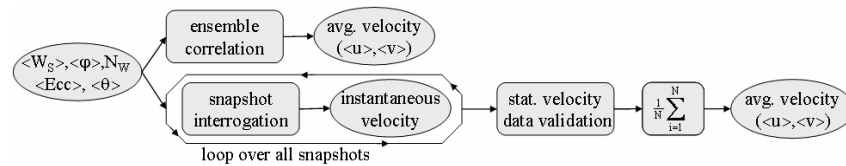


Fig. 5.4: Evaluation of average velocity fields for ensemble adaptive interrogation. The velocity field can be obtained either through ensemble correlation or by averaging the correlation of individual snapshots. Both approaches apply a-priori determined number of correlation windows, window sizes, sampling locations, eccentricity and orientation.

5.3 Implementation

5.3.1 Adaptive sampling and window sizing

The ensemble-averaged source density ' $\langle S_d \rangle$ ' is mapped through particle segmentation performed on the basis of an intensity threshold criterion. Pixel intensities exceeding the threshold intensity ' I_{thr} ' are classified as belonging to a particle image. In line with the work of Stitou and Riethmuller (2001), the intensity threshold is chosen from the ensemble-average intensity, ' $\langle I \rangle$ ', and RMS intensity fluctuations, ' σ_I ', calculated pixel wise;

$$I_{thr} = \langle I \rangle + 1.5 \cdot \sigma_I \quad (5.1)$$

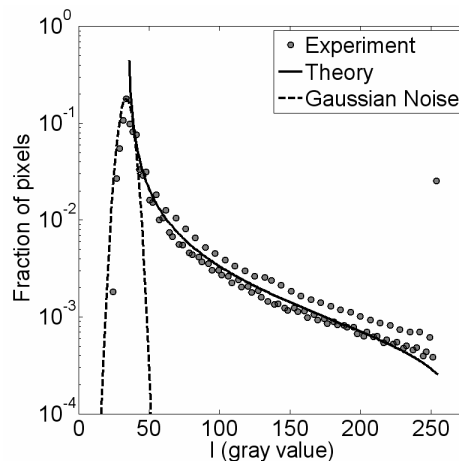


Fig. 5.5: Typical intensity histogram for a digital 8-bit PIV image (●). The dashed line assumes a Gaussian distribution for camera noise. The solid line is a theoretical reference (Westerweel 2000).

Following the work of Westerweel (2000), a typical intensity histogram of a digital PIV image is shown in Fig. 5.5. The distribution is composed of thermal camera noise (modeled by a normal function) and a theoretical probability distribution based on particle images following a Gaussian intensity distribution within a light sheet with a Gaussian profile. For such common probability functions, the selected factor of 1.5 ensures the probability of a pixel with a grey level intensity higher than the threshold defined in (5.1) to be noise always to be less than 10%. From the set of pixel intensities exceeding the threshold, only those constituting a spatially local maximum are considered as particle centroid. The segmentation takes into account image noise to be typically associated with low pixel intensities compared to those belonging to particle images. Furthermore, the correlation operation is known to be more sensitive to higher image intensities (Young *et al.*, 2004), which is translated into the threshold requirement of the important signal to be sufficiently discernible from the surrounding intensities. According to Keane and Adrian (1990) a prerequisite for reliable correlation is that each

interrogation window should contain at least 7 particle image pairs. Because a-priori the loss of particle pairs due to in-plane and out-of-plane motion and partial laser beam overlap is unknown, a safe estimate is to consider 20 particle images to typically ensure a sufficient number of particle image pairs. This requirement automatically sets a lower limit on the local size of the correlation windows.

To retrieve a first estimate of the average velocity field, an iterative analysis by cross-correlation is applied on a regular grid and with uniform window size (Fig. 5.6). Window sizes are reduced from 81 pixels to 31 pixels in two refinement steps with the WIDIM algorithm (Scarano and Riethmuller, 2000) maintaining a window overlap ratio 'WOR' of 50%. The choice of initial and final interrogation size provides a sufficiently large velocity dynamic range while maintaining sufficient robustness.

The second interrogation pass refines the measurement of the velocity field by adapting the window size, shape and distribution. The interrogation windows are distributed on an unstructured grid and have location and size prescribed by the outcome of the previous iteration. Note that the applied window characteristics are identical for each snapshot pair.

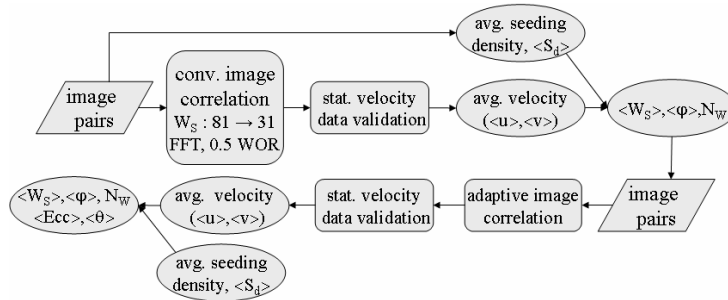


Fig. 5.6: Flow chart of the implemented methodology to estimate correlation window characteristics. A conventional interrogation routine is followed by adaptive interrogation of each couple of snapshots. The adaptive routine applies window sizes, sampling location and number of windows based on the average seeding density and average velocity field obtained from the conventional iteration.

5.3.2 Statistical validation

To minimize the detrimental effect of vector outliers in the determination of the mean flow field, a robust statistical data validation is necessary (Fig. 5.4). Displacement outliers are characterized as strong deviations in magnitude and direction from neighboring values (Westerweel, 1994). The anomaly can occur both spatially and over the sequence of recordings. Whereas in the former the vector differs from its spatial surrounding neighbors, sequence deviations imply that given a specific location in space, the obtained displacement estimate is unlikely to occur. Spatial deviations need to be identified within each instantaneous velocity field while improbable deviations require a statistical approach based on the local velocity probability density function.

In the current work, the procedure is based on the validation proposed by Heinz *et al.* (2002), assuming a normal probability density function for the local instantaneous

displacement. For each vector location '(x,y)', the Gaussian variance ' σ ' of the collection of instantaneous displacements '{U}' is determined. Samples exceeding in absolute value the collection's statistical mean ' μ ' by three times the standard deviation are excluded. The routine is then repeated for each vector in the validated collection of measurements until convergence in ' μ ' and ' σ ' is reached (Fig. 5.7). By repeating the above process for each sampling location, the combination of statistical, validated, means yields an average displacement field which will serve in the determination of window characteristics and image deformation field.

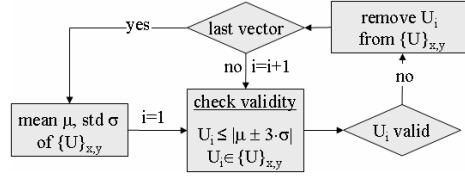


Fig. 5.7: Layout of iterative statistical vector validation; for a given sampling location (x,y), each instantaneous vector ' U_i ' is validated by considering the statistics ' μ ' and ' σ ' of the collection of (validated) instantaneous displacement measurements at the corresponding location.

5.3.3 Non-isotropic correlation

The non-isotropic window characteristics are expressed through the eccentricity and orientation angle. In the ensemble-based adaptive approach these quantities are based on a pixel-wise defined displacement field '<u>,<v>'' which is obtained by re-interpolating the average displacement field, defined at the correlation window locations, to each pixel by means of e.g. bi-linear interpolation. At each new window location selected from the ensemble-average sampling rate '<φ>', both eccentricity '<Ecc>' and orientation '<θ>' are derived for each displacement component from the maximum (' Λ_{\max} ') and minimum eigenvalues (' Λ_{\min} ') of the relevant Hessian matrix, 'H'. The latter is composed of the second spatial derivatives '<u>_{ii}' of the ensemble-averaged velocity components. The involved mathematical definitions are reported in Scarano (2003) and some results are reported here for the horizontal displacement component in (5.2), (5.3) and (5.4) for clarity.

$$\det(H - \bar{\Lambda}) = 0 \quad \text{where} \quad H = \begin{bmatrix} \langle u \rangle_{xx} & \langle u \rangle_{xy} \\ \langle u \rangle_{xy} & \langle u \rangle_{yy} \end{bmatrix} \quad \text{and} \quad \bar{\Lambda} = \begin{bmatrix} \Lambda_1 & 0 \\ 0 & \Lambda_2 \end{bmatrix} \quad (5.2)$$

$$\begin{cases} \langle \theta \rangle = \text{atan}\left(\frac{\langle u \rangle_{xy}}{\langle u \rangle_{xx} - \Lambda_{\max}}\right) + \pi & \text{if } \langle u \rangle_{xx} < \Lambda_{\max} \\ \langle \theta \rangle = \text{atan}\left(\frac{\langle u \rangle_{xy}}{\langle u \rangle_{xx} - \Lambda_{\max}}\right) & \text{else} \end{cases} \quad (5.3)$$

$$\langle \text{Ecc} \rangle = \frac{3}{4} \left(1 - \frac{\Lambda_{\min}}{\Lambda_{\max}}\right) \cdot e^{\frac{-1}{\Lambda_{\max} \cdot \langle W_S \rangle - 100}} \quad \text{where} \quad \begin{aligned} \Lambda_{\min} &= \min(\text{abs}(\Lambda_1), \text{abs}(\Lambda_2)) \\ \Lambda_{\max} &= \max(\text{abs}(\Lambda_1), \text{abs}(\Lambda_2)) \end{aligned} \quad (5.4)$$

Second order derivatives are provided at each pixel location by means of a parabolic Least-Square fit on the average pixel-wise displacement field. The fitting kernel size is set to 11-by-11 pixels and takes into account the variable sample spacing returned by the adaptive interrogation routine; regions with strong velocity variations are attributed the highest density of correlation windows with an average spacing of around 3 pixels. The fitting basis, which according to the theoretical considerations of Fouras and Soria (1998), should involve points lying within a radius of about 2 to 3 times the grid spacing, corresponds to a stencil of 11 pixels for the interpolated data at pixel resolution. An upper limit for the window eccentricity is set to $\frac{3}{4}$ (aspect ratio 4:1) following Scarano (2003). Because of the inflection point in the velocity profile across a shear layer or shock, the second derivatives tend to zero yielding zero eccentricity and undefined value of ‘ θ ’. To bridge the zero eccentricity gap, local eccentricity and angle are replaced by the maximum and mean value, respectively, within their immediate vicinity, followed by a sliding averaging operation to force regularity in the obtained distributions. The above is illustrated in Fig. 5.8 for the case of a shear-layer.

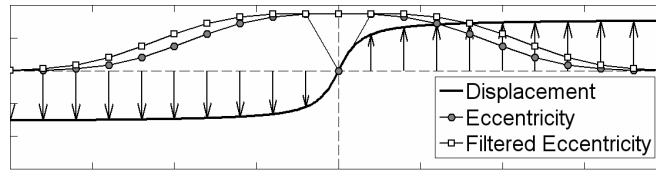


Fig. 5.8: Example of eccentricity filtering in case of a shear layer modeled by a hyperbolic tangent. Sampling locations are indicated by the arrows. To avoid zero eccentricity at the inflection point (\bullet), local eccentricity values are substituted by the maximum within their immediate vicinity (\square).

The extent of the interrogation window along the major ‘ ξ ’ and minor axis ‘ η ’ (Fig. 5.9) is given by

$$W_{S,\xi} = W_S \frac{1}{\sqrt{1-\text{Ecc}}} \quad \text{and} \quad W_{S,\eta} = W_S \sqrt{1-\text{Ecc}} \quad \text{with} \quad W_S = \sqrt{W_{S,x} \cdot W_{S,y}} \quad (5.5)$$

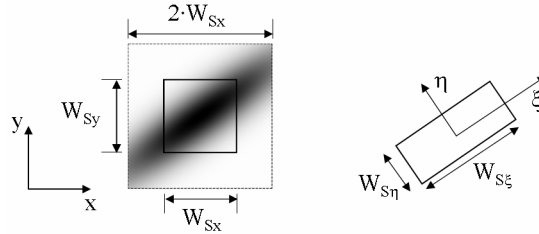


Fig. 5.9: Non-isotropic window by Gaussian weighting (Left) and by pixel grid rotation (Right).

Conventional interrogation methodologies adopt Gaussian intensity weighting functions to incorporate the window non-isotropy. Here interrogation windows need to be enlarged in order to limit the undesired truncation effects of the weighting functions and consequently augment the computational requirement. The current method instead involves a direct reshaping and rotation of the interrogation areas (Fig. 5.9), which does

not require the use of intensity weighting. The intensity re-interpolation is performed by means of quintic B-splines (Unser *et al.* 1993^{a,b}, Astarita and Cardone 2005).

5.3.4 Number of correlation windows

The adaptive placement of measurement points in the image offers the potential advantage of reducing the number of correlation windows in turn reducing the computational effort without overly compromising the measurement performance. The procedure locally associates an adequate number of correlation windows ‘ N_w ’ to the ensemble-average sampling rate ‘ $\langle\varphi\rangle$ ’ and window size ‘ $\langle W_s \rangle$ ’ while respecting an imposed mean window overlap ratio ‘ $\langle \overline{WOR} \rangle$ ’[†]. Currently the ratio has been set to 0.75 to reduce errors related to image deformation and maintain a high spatial resolution. This choice clearly privileges the aspect of measurement performance with respect to computational efficiency.

Both ‘ $\langle\varphi\rangle$ ’ and ‘ $\langle W_s \rangle$ ’ are functions of the spatial coordinates. Ideally, the number of equidistant samples ‘ $N_{\delta s}$ ’ located within a small area ‘ δs ’, centered on pixel coordinates ‘ (x_i, y_i) ’ can be approximated by ‘ $N_{\delta s}(x_i, y_i) = N_w \cdot \langle\varphi\rangle(x_i, y_i) \cdot \delta s$ ’, where ‘ N_w ’ is the overall total number of windows. The area ‘ δs ’ is sufficiently small to assume the sampling rate and window size distribution locally constant. According to Stephens (1972), the probability density function for the distance ‘ λ_w ’ describing the distance between the sampling locations then equals

$$f(\lambda_w) = 2 \cdot \left(\frac{\lambda_w}{\lambda_m}\right)^2 \cdot e^{-(\lambda_w/\lambda_m)^2} \quad \text{with} \quad \lambda_m = (\delta s / N_{\delta s})^{1/2} = (\langle\varphi\rangle \cdot N_w)^{-1/2} \quad (5.6)$$

The latter ‘ λ_m ’ represents the most probable nearest neighbor distance and will serve as an indicator of the local sample spacing. With the simplification of equidistant samples, the expression for the local window overlap ratio ‘ $\langle \overline{WOR} \rangle(x_i, y_i)$ ’ is given in equation (5.7) followed by the spatial averaged window overlap ratio ‘ $\langle \overline{WOR} \rangle$ ’ in equation (5.8). Because the number and location of the windows is not known initially, a recursive operation will be needed, minimizing ‘ $\langle \overline{WOR} \rangle$ ’ with respect to ‘ N_w ’. The method to project the sampling locations onto the spatial domain according to a given probability density function has been adopted from Secord *et al.* (2002).

$$\begin{aligned} \langle \overline{WOR} \rangle(x_i, y_i) &= 1 - \lambda_m(x_i, y_i) [\langle W_s \rangle(x_i, y_i)]^{-1} \\ &= 1 - \left[\sqrt{N_w} \cdot \sqrt{\langle\varphi\rangle(x_i, y_i)} \cdot \langle W_s \rangle(x_i, y_i) \right]^{-1} \end{aligned} \quad (5.7)$$

[†] Note that this estimator for ‘ N_w ’ is not suitable in case of individual snapshots, such as in Chapter 3. Because of its sensitivity to irregularities in the sampling and sizing distribution, the number of windows would be too dominated by local displacement outliers.

$$\overline{\langle \text{WOR} \rangle} = 1 - N_w^{-1} \sum_i^{N_w} \left[\sqrt{N_w \cdot \langle \phi \rangle(x_i, y_i) \cdot \langle W_s \rangle(x_i, y_i)} \right]^{-1} \quad (5.8)$$

Without loss of generality, a one dimensional example is considered in Fig. 5.10 assuming a line interval of 300 pixels (note that for the 1D case the area ' δs ' is also reduced in dimension and becomes a line segment yielding ' $\lambda_m = (\delta s / N_{\delta s})$ ' which allows omitting the square root in equation 5.7 and 5.8). For each ' N_w ', windows are spatially distributed according to the given PDF ' $\langle \phi \rangle$ ' and sized following the ' $\langle W_s \rangle$ ' function (Fig. 5.10-a). As ' N_w ' is gradually increased, the calculated ' $\overline{\langle \text{WOR} \rangle}$ ' will surpass the imposed ratio indicating a sufficient number of samples (Fig. 5.10-b).

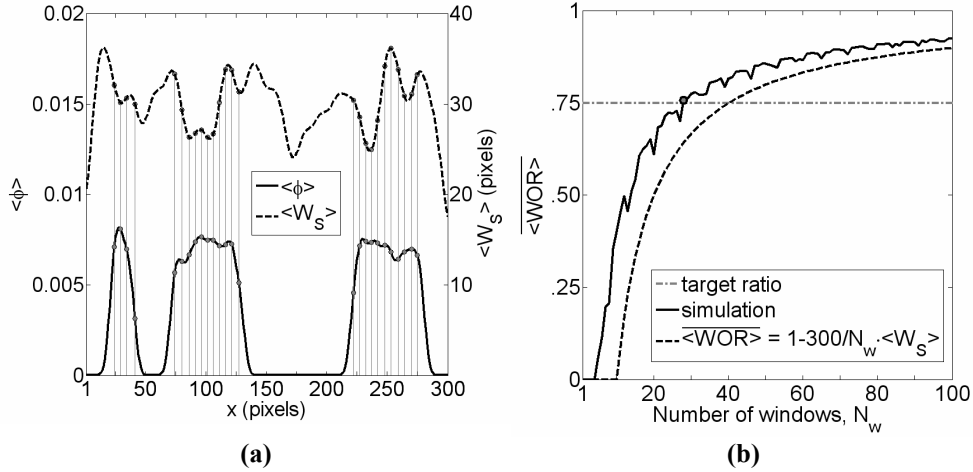


Fig. 5.10: (a) Imposed sampling distribution function and window size (b) Evolution of the spatially averaged mean window overlap ratio $\langle \text{WOR} \rangle$ versus the number of adopted windows. Sampling locations corresponding to $\langle \text{WOR} \rangle = 0.75$ are indicated by gray lines in (a).

5.3.5 Adaptive image snapshot interrogation

As mentioned in section 5.1 and shown in Fig. 5.4, the statistical approach requires the interrogation of snapshots once more using the parameters obtained from the ensemble-average analysis. In the following more detail is given concerning the implemented snapshot interrogation (Fig. 5.4 and Fig. 5.6). When opted for ensemble correlation, the routine shown in Fig. 5.11 remains unchanged except for postponing the search for the correlation peak after averaging of the instantaneous correlation maps.

Following the average spatial sampling and sizing distributions, ' $\langle \phi \rangle$ ' and ' $\langle W_s \rangle$ ', correlation windows are stretched and rotated according to the pre-determined eccentricity and orientation distributions, ' $\langle \text{Ecc} \rangle$ ' and ' $\langle \theta \rangle$ ', derived from the average velocity field, ' $\langle U \rangle$ '. The adopted number of correlation windows ' N_w ' follows from the procedure reported in the previous paragraph. To allow for instantaneous deviations ' δU ' from the average velocity, the interrogation consists of two iterations with the first cycle

applying twice the imposed window size ' $\langle W_S \rangle$ ' while leaving the location, orientation and eccentricity unchanged. A normalized cross-correlation coefficient is calculated either in a direct manner near interfaces or by means of Fourier transforms in the bulk of the flow (Chapter 4). To eliminate spurious vectors, validation of the instantaneous displacement vectors involves a signal-to-noise threshold, a normalized median test (Westerweel and Scarano, 2005) and a convergence test of the corrective displacements ' δU '. Detected outliers are replaced by an interpolated value in function of their natural neighbors (Sambridge *et al.*, 1995). The instantaneous displacement field is updated to allow the measurement of instantaneous deviations from the average flow field consistent with the concept of Reynolds decomposition into mean and fluctuating flow properties. The updated field is given by the initial average displacements of the previous iteration ' $\langle U \rangle$ ', modified by the instantaneous corrections ' δU ' for each individual image recording; ' $U = \langle U \rangle + \delta U$ '. The predictor field for image distortion was constructed by means of a linear interpolation of the filtered displacements ' U^* ' (Schrijer and Scarano, 2008) over all the pixels from the smoothed unstructured mesh of measurement points using the natural neighbors (Sambridge *et al.*, 1995).

The average velocity field is retrieved after statistical validation of the ensemble of instantaneous velocity fields.

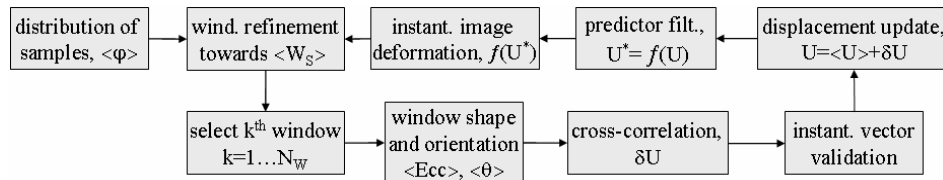


Fig. 5.11: Flow chart of the implemented adaptive interrogation of instantaneous image recordings (ensemble-based adaptive approach).

5.4 Experimental application

5.4.1 Shock-wave-boundary layer interaction

The performance of the proposed methodology is assessed through application on a set of experimental images of a shock-wave-boundary layer interaction (Humble *et al.*, 2007). The shock-wave-boundary layer interaction has been chosen as it represents a challenging test case considering the presence of strong velocity gradients and both spatial and temporal intermittent seeding densities. In addition, the formation of shocks requires a high spatial resolution and allows a thorough assessment of the proposed interrogation procedure. Experiments were conducted in a supersonic blow-down wind tunnel. A single-sided wedge with 10 degrees deflection angle was placed in the free stream at Mach 2.1 thus generating an oblique planar shock-wave. The latter impinges the fully developed turbulent boundary layer 20mm thick giving rise to a complex flow interaction. In total, 200 image pairs were utilized for the analysis.

To provide a reference, the image set is additionally analyzed by means of a conventional methodology based on the WIDIM algorithm (Scarano and Riethmuller, 2000). In the current analyses, two refinement steps were imposed leading to final window sizes of 21 pixels with 75% window overlap. Sampling locations correspond to the nodes of a Cartesian grid whereby window sizes and overlap factor are applied globally throughout the individual recordings and image set. The ensemble of velocity fields is post-processed afterwards to retrieve the mean flow field (cf. paragraph 5.3.2). A second iteration then repeats the image interrogation taking into account window eccentricity and orientation determined from the average velocity field.

In Fig. 5.12 the contours are shown of the horizontal velocity component following statistical adaptivity normalized with the free stream velocity. Incident shock and reflected shock are clearly distinguishable as well as the retarded flow within the boundary layer and at the interaction. The wall-adaptive image interrogation automatically makes a distinction between the wall region and free-stream (indicated by the dashed line). Near the interface, wall adaptivity (Chapter 4) will impose a larger number of stretched interrogation windows regardless of the seeding density. The adaptive interface interrogation consists of window stretching parallel to the wall while gradually reducing the interrogation area.

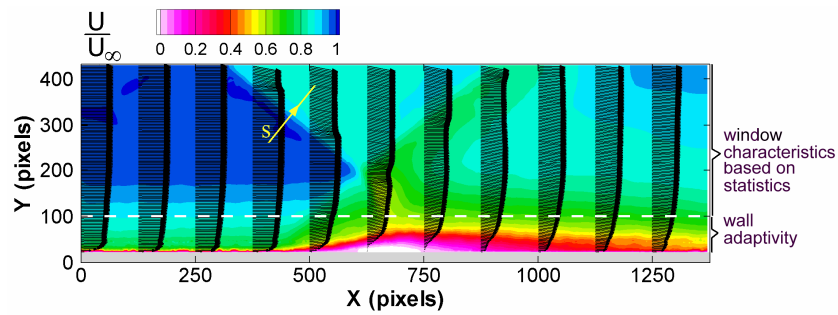


Fig. 5.12: Shock-wave-boundary layer interaction: ensemble-averaged velocity field. Horizontal velocity component color contours and wall-normal velocity vector profiles.

- ***Sampling distribution***

Figure 5.13 displays the spatial distribution of correlation windows as determined by the outcome of the process sketched in Fig. 5.3, 5.4 and Fig. 5.6. Clearly the distribution of interrogation windows follows the various flow features; the incoming and reflected shock, the expansion fan and the boundary layer. In this case, 9000 measurement points are included at an average window overlap ratio of 0.75 (Fig. 5.14). The strong reduction in sample spacing will reduce any limitation in spatial resolution inherent to coarse vectors spacing. Of importance is the fact that to reach the same overlap coefficient and spatial resolution in the shocks when adopting a structured grid, around 40000 correlation windows would be needed (Fig. 5.14), which typically puts the user with the trade-off between computational efficiency and the desired spatial resolution.

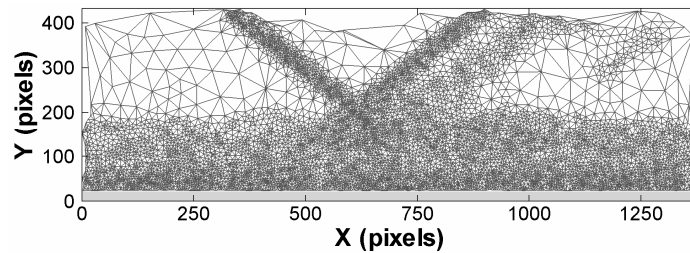


Fig. 5.13: Distribution of 9000 sampling locations according to statistical adaptivity.

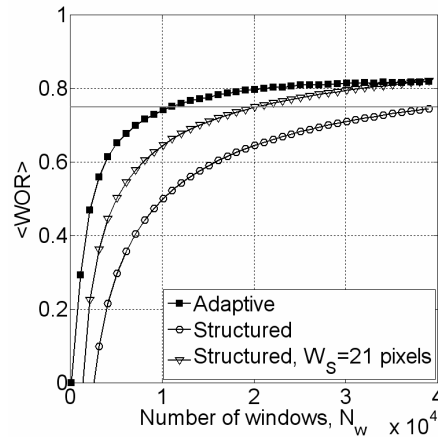


Fig. 5.14: Evolution of spatial averaged window overlap ratio with varying number of interrogation windows.

- **Interrogation window characteristics**

Besides a stretching of the correlation windows parallel to the shocks, non-isotropic window characterization imposes windows reduced in size to maximize the spatial resolution. Fig. 5.15-a depicts the eccentricity for the horizontal velocity component with some interrogation windows drawn at random locations. The eccentricity is clearly smeared across the shocks as a result of the filtering operations explained in paragraph 5.3.3. The square window sizes of 15 pixels in the vicinity of the shock combined with a typical maximum eccentricity of 0.5 yields a shock normal vector spacing of around 3 pixels. Near the wall a maximum stretching of 4 is imposed by wall adaptivity leading to wall-parallel window sizes of 37 pixels (Fig. 5.15-b) and 9 pixels in wall-normal direction.

With the conventional WIDIM analysis, windows of 21 pixels² were applied. When subjected to a second iteration including non-isotropic windows, a global window overlap factor of 0.75 combined with an eccentricity of 0.66 within the shock vicinity yield a resolution equal to that of the statistical adaptivity.

As a result, the velocity profile along the shock-normal abscissa 's' in Fig. 5.12, shows small differences between the following methods (Fig. 5.16): statistical adaptivity followed by correlation of the snapshots ('SA-snapshot'), statistical adaptivity followed

by ensemble correlation of the snapshots ('SA-ensemble'), interrogation with instantaneously determined adaptivity criteria ('IA') and the conventional technique ('Conv.') after the 1st and 2nd iteration. To avoid misunderstandings, it is stressed here that the 'IA' approach does not include non-isotropy in interrogation areas in that the extreme sensitivity in the determination of the optimum window eccentricity and orientation to velocity spatial fluctuations makes this option unmanageable.

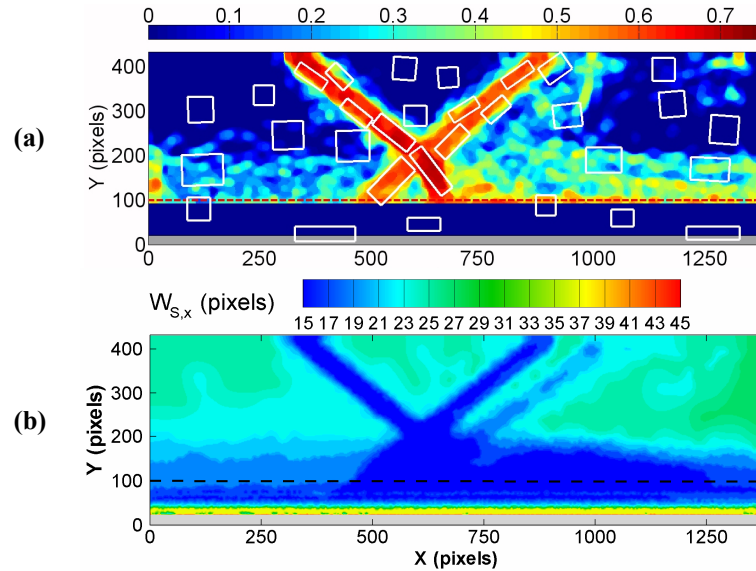


Fig. 5.15: (a) Correlation window eccentricity and orientation (window sizes are enlarged by factor 3 for readability) (b) window-size along major axis according to statistical adaptivity.

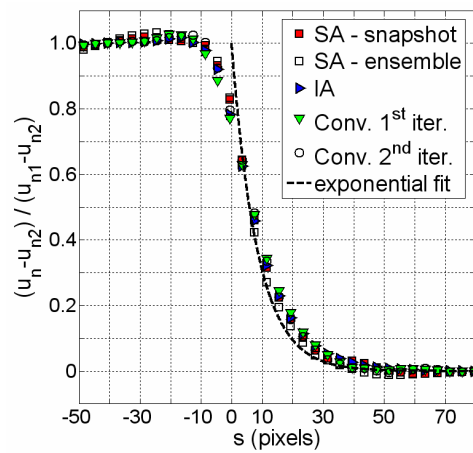


Fig. 5.16: Shock-normal velocity profile across the incident shock-wave ($u_{n1,2}$ represents the shock-normal velocity respectively upstream and downstream).

The reason for the marginal improvements is that the shock-wave was already well resolved within the digital recording, causing the measured shock profile to be dominated by the particle response as indicated by the exponential fit. The particle relaxation distance was estimated around 0.82mm, which is in reasonable agreement with the 0.76mm reported by Scarano and van Oudheusden (2003). It is worth noting that as such, the adaptive interrogation approaches are capable of returning the same measurement performance as the iterative multigrid analysis after a second iteration, with the advantage that a user input is not required for the selection of the window size.

- **Wall-adaptive interrogation**

Presented in Fig. 5.17 are the velocity profiles within the undisturbed boundary layer as returned by the various interrogation approaches, expressed in inner-law variables ‘ u^+ ’ and ‘ y^+ ’. Velocities are transformed into equivalent velocities following the concept of van Driest (5.9) to account for compressibility effects.

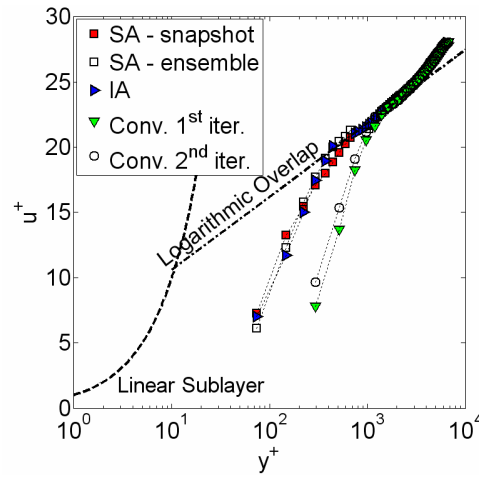


Fig. 5.17: Undisturbed boundary layer profile.

$$u_{eq} = \frac{U_e}{a} \cdot \sin^{-1} \left(a \frac{u}{U_e} \right) = u_\tau \cdot \left(\frac{1}{\kappa} \cdot \log(y^+) + B \right) \quad \text{with } a^2 = 1 - \frac{T_e}{T_{aw}} \quad (5.9)$$

$$\text{with } \kappa=0.41 \text{ and } B=5.0$$

For the current case the temperature at the edge of the boundary layer, ‘ T_e ’, reached 152K while the adiabatic wall temperature, ‘ T_{aw} ’, equaled 284K. The velocity at the boundary layer edge, ‘ U_e ’, was taken as 99% of the free stream velocity (525m/s). For further details the reader is referred to Humble *et al.* (2006). By zooming in on the boundary layer Humble *et al.* estimated the wall friction velocity, ‘ u_τ ’, with sufficient reliability to be 19.5 m/s.

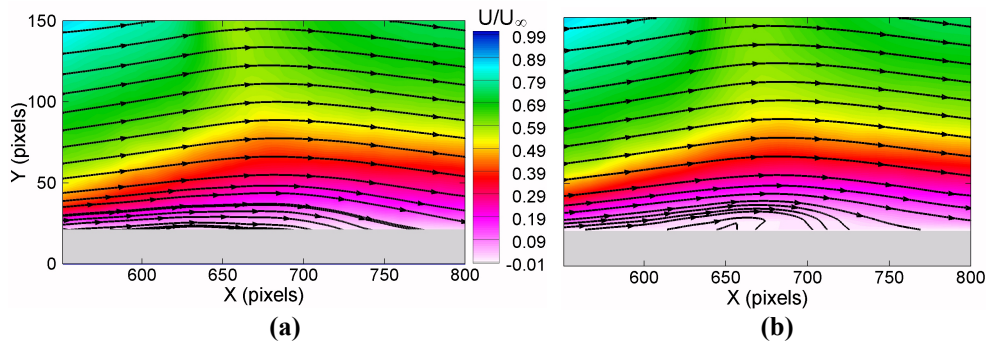


Fig. 5.18: Recirculation zone; streamlines and non-dimensional streamwise velocity component (a) Conventional (b) Statistically Adaptive interrogation approach with interface adaptivity.

None of the obtained velocity profiles correspond with the theoretical functions (Fig. 5.17) as a result of low digital resolution related to the large field of view covered compared to the boundary layer extension. According to Fig. 5.17 the conventional methodology performs worst but can slightly be improved by incorporating non-isotropy in window characteristics. Adaptation of the interrogation parameters to ensemble-averaged flow and signal conditions is almost identical to instantaneous adaptation which is caused by the imposition of equal wall adaptivity criteria (Chapter 4) for both approaches.

The improvement in wall resolution is further illustrated by observing the recirculation zone below the interaction region (Shapiro, 1953). While conventional image interrogation only hints at the presence of a separation bubble, the region of reverse flow becomes prominent only when applying wall adaptivity (Fig. 5.18).

- **Turbulence statistics**

Although the statistically adaptive approach is intrinsically appropriate for flows with only relatively small fluctuations this requirement can be partly relieved by building the correlation peak from individual pairs of images. In case of the shock-wave-boundary layer interaction, such fluctuations are limited[†] and as a result comparison of the Reynolds shear stresses with those stemming from the conventional technique shows an overall very good topological agreement (Fig. 5.19). Statistical adaptivity returns slightly noisier stress distribution with higher amplitudes especially in the reattached boundary layer and incident and reflected shock foot regions. The higher stress values are to be attributed to an improved spatial resolution which is further attested by the resolution of the expansion wave.

[†] According to the results of Humble *et al.* (2006), maximum fluctuations in ‘u’ and ‘v’ are in the order of respectively 20% and 10% of the freestream velocity (i.e. approximately 2 and 1 pixels respectively), which is sufficiently small to be adequately measured by correlation windows of 16 pixels in size (Fig. 5.15-b).

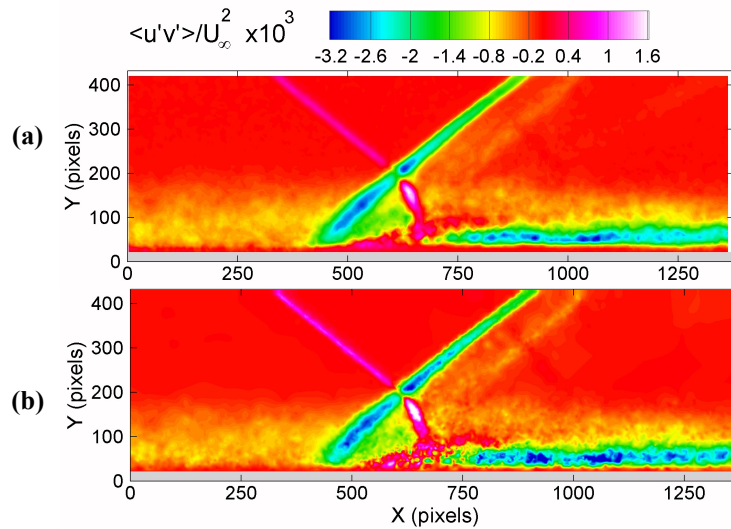


Fig. 5.19: Reynolds shear stress distribution obtained through (a) Conventional approach and (b) Ensemble-based adaptive interrogation methodology.

- **Potential saving in computation time**

Shock-normal velocity profiles and boundary layer profiles are presented for a varying number of correlation windows ‘ N_w ’ in Fig. 5.20. Two hundred image recordings were taken into account and analyzed with statistical adaptive interrogation followed by ensemble correlation (Fig. 5.4). The normalized CPU time is depicted in Fig. 5.20-a. A linear tendency can again be observed with increasing number of correlation windows. Imposing 1000 correlation windows clearly causes both the incident shock and boundary layer to be under-resolved (Fig. 5.20-b,-c). Convergence of the results for ‘ N_w ’ exceeding 5000 becomes evident as the remaining profiles superimpose nearly exactly. This result verifies the approach presented in paragraph 5.3.4 to be adequate in the selection of number of correlation windows.

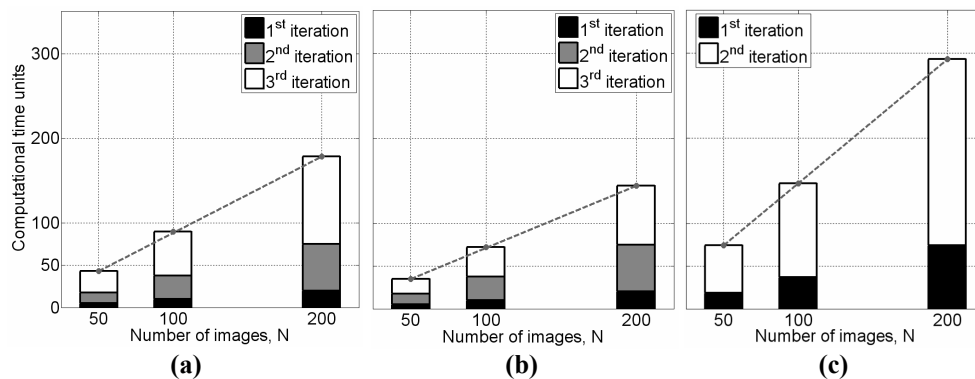


Fig. 5.21: Partition of computational effort. Statistical adaptivity with (a) snapshot correlation (b) ensemble correlation (c) conventional structured image analysis (final window size of 21 pixels with 75% mutual overlap).

Inherent to the possibility of reducing the number of required correlation windows, the proposed ensemble adaptivity offers the potential of lowering the computation time. To further advocate the possible computational benefits, the partition in CPU time for a varying extent of image set is considered in Fig. 5.21.

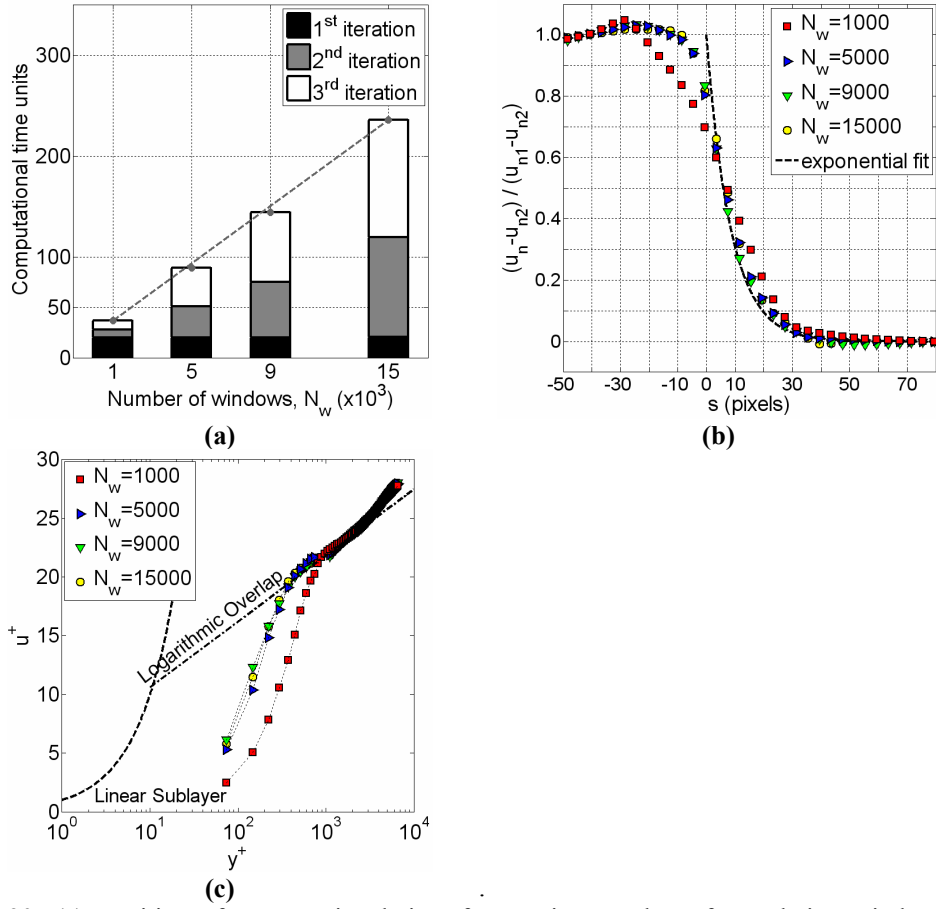


Fig. 5.20: (a) Partition of computational time for varying number of correlation windows (a) normalized, perpendicular velocity profile across the oblique shock-wave (c) undisturbed boundary layer profile in inner-law variables.

The total computational time is normalized by the time necessary to analyze a single snapshot with the instantaneous adaptivity approach. The latter serves as a reference unit. The first and second iterations refer to the analysis scheme presented in Fig. 5.6. Nine thousand correlation windows were involved. All image analyses methodologies obey a linear increase in CPU time with number of images as indicated by the dashed line. Once the window characteristics have been determined, ensemble correlation (Fig. 5.4) yields the lowest computational effort (Fig. 5.21-b). The slightly higher CPU time for the statistical adaptivity with snapshot correlation is attributed to the statistical vector validation routines. Still, statistical adaptivity yields a reduction in computational time of

a maximum factor 1.5 compared to the instantaneous approach. The conventional approach leads to a doubling of the CPU time when incorporating non-isotropic window characteristics (Fig. 5.21-c). Keeping in mind Fig. 5.14, the computational load will further increase when maintaining a spatial resolution equal to that achievable with the adaptive metrologies.

5.4.2 Transonic airfoil wake

- **Background**

When there is mixed sub- and supersonic local flow in the same flow field, transonic flow occurs. Transonic effects typically appear with free stream Mach numbers from 0.6 to 1.2. When the critical Mach number is reached, the flow becomes locally sonic at a single point on the airfoil surface. Further increasing the free stream velocity leads to the appearance of shock waves. Depending on the specific geometry of the airfoil and the Mach number, these shocks grow in strength and progress downstream (Fig. 5.22). Because of this spatial variation in flow conditions and flow phenomena, transonic flows are computationally challenging for numerical codes. The NACA0012 profile has become a benchmark case in the validation of the numerical predictions with experimental data being airfoil lift, drag and pressure distribution.

Apart from providing qualitative insight in the flow features through visualization, PIV allows the eduction of quantitative velocity data and turbulence statistics data. By making use of the aerodynamic governing equations, pressure and aerodynamic loads can be deduced from PIV data allowing the technique to be implemented for non-intrusive aerodynamic force characterization. This approach is appealing in that it establishes a direct link between flow behavior and forcing mechanisms. The method relies upon the application of control-volume approaches (van Oudheusden *et al.*, 2007) and requires velocity and its gradients as well as the velocity second moments, which are related to turbulent stresses, to be accurately determined on the outer contour of the control volume. Given the spatial and temporal intermittency of the seeding, its coherency and the various flow scales involved, the last point can and will be problematic for conventional image analysis.

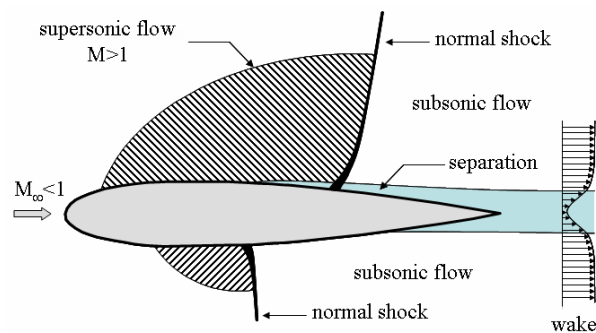


Fig. 5.22: Schematized flow pattern over a transonic airfoil.

As the air passes over the airfoil, it suffers a loss of momentum (Fig. 5.22). From this velocity deficit the profile drag per unit span can be inferred. Generally the wake flow is under-resolved as it occupies only a small portion of the total field of view (see Fig. 5.23). To extract the velocity profiles with sufficient accuracy and resolution, special measures during the image interrogation process are necessary.

- **Experimental facility**

The following test-case involves the wake behind a NACA-0012 airfoil with a chord length 'c' of 100mm. The model was placed at 1 degree angle of incidence within a transonic flow. One micron diameter DEHS droplets were introduced in the TST27 transonic blow-down type wind tunnel of Delft University of Technology, with a free-stream Mach number of 0.6. A Quantronix Darwin Duo Nd-YLF laser provided the necessary illumination with 200ns pulse duration at a repetition rate of 500Hz. The time separation between pulses was set to 6 micro-seconds yielding a free stream particle displacement of 1mm. The light sheet had a thickness of 2mm. Images were recorded by two Photron FastCAM SA1 CMOS with a light-sensitive sensor area of 1024×1024 pixels. Further details regarding the experimental campaign can be found in Ragni *et al.* (2009). Fig. 5.23 presents a typical PIV recording. The black areas in the central image portion are shadow regions created by the partially illuminated airfoil. Along with the straight wind tunnel walls on the top and bottom of the image, the outlines of the circular porthole can be observed.

In this experiment the measurement is performed simultaneously at two different values of the optical magnification, leading to a digital resolution of 6.6 pixels/mm and 33 pixels/mm for the fields of views of 150×150mm² (covering the entire airfoil) and of 30×30mm² (wake momentum defect) respectively. The availability of image recordings at different optical resolution was a unique opportunity to validate the present method in terms of attainable spatial resolution and compare it to the other approaches.

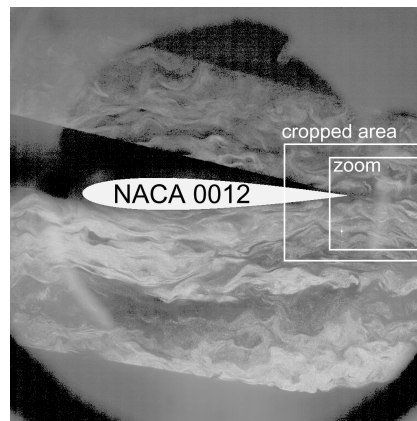


Fig. 5.23: Instantaneous PIV image of the airfoil with indicated field of views (Ashok *et al.*, 2008).

- *Image evaluation and flow diagnostics*

The inherent difference in adopted interrogation parameters by the conventional approach and statistically adaptive technique is illustrated in Fig. 5.24 for the cropped region shown in Fig. 5.23. The conventional technique applies square correlation windows of 25 pixels. In the ensemble-based adaptive technique the interrogation windows are sized, shaped and rotated. Large variations in the eccentricity are needed crossing the wake region due to the large curvature of the velocity profile. The interrogation windows are stretched and oriented approximately parallel to the airfoil chord to increase wall-normal resolution. As a result, the velocity profile in the boundary layer measured by the adaptive technique already shows a fuller shape, expected for the flow around this type of airfoil whereas the conventional method tends to over-estimate the momentum defect in the boundary layer. Besides the evident discrepancy in wake profile at the trailing edge, ensemble-based adaptivity yields wake profiles with a more clear momentum defect as opposed to the conventional approach when the large field of view is considered.

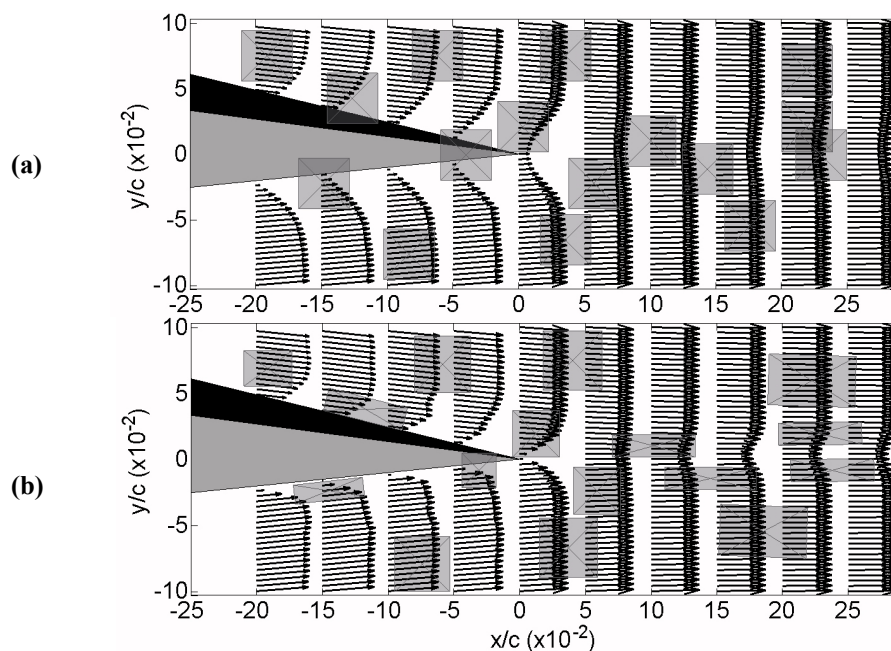


Fig. 5.24: Velocity profiles (5 grid units \approx 125m/s) and interrogation windows adopted by (a) conventional interrogation technique ($W_S=25$ pixels) and (b) statistically adaptive interrogation. The field of view corresponds to the cropped area shown in Fig. 5.23.

The achievable improvement in spatial resolution when the adaptivity criteria are based on statistical estimators is quantified in Fig. 5.25. Normalized axial velocity profiles (with free stream velocity ' U_∞ ') obtained from the small field of view in the wake are displayed for reference. At such high resolution, the wake zoom recordings analyzed with statistical adaptivity and the conventional interrogation technique only differ marginally, indicating

that the velocity profile can be well captured by the available optical resolution. Instead, a marked difference can be observed among the data obtained using the large field of view. In this case the conventional interrogation largely underestimates the momentum defect whereas the ensemble adaptive analysis closely follows the reference data except for the first profile closest to the trailing edge. The instantaneous adaptivity slightly outperforms the conventional approach as a result of the adaptive window sizing and distribution criteria but the error level remains unacceptably high. It is worth mentioning that the application of non-isotropic windows on the instantaneous images did not return reliable results with unrealistic distribution of the window eccentricity and orientation.

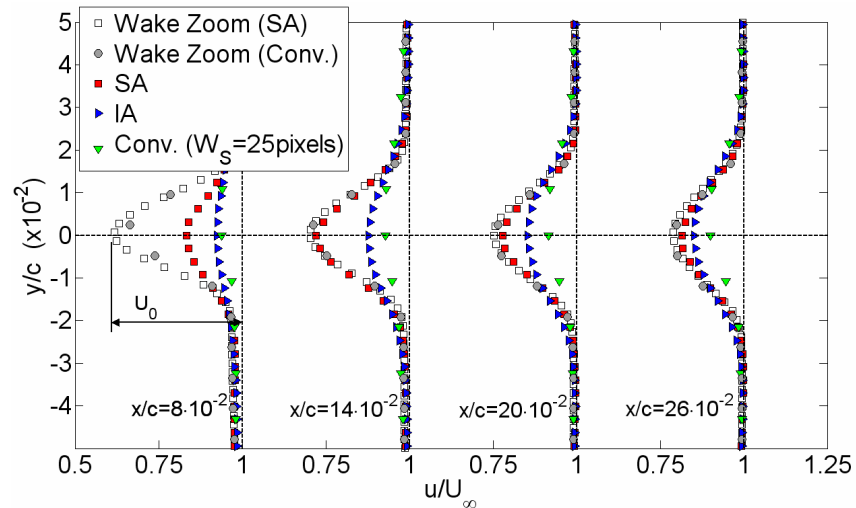


Fig. 5.25: Comparison of wake velocity profiles at several downstream distances ‘ x ’ from the trailing edge obtained by different interrogation methodologies; ‘SA’ statistical adaptivity, ‘IA’ instantaneous adaptivity, ‘Conv.’ conventional approach with windows of 25 pixels.

The wake velocity deficit ‘ U_0 ’ along the wake axis gradually decreases with downstream distance from the airfoil trailing edge while the wake width increases. Fig. 5.26-a depicts the evolution of the non-dimensional maximum velocity defect in the wake with downstream distance. Values are extracted from the zoomed wake measurements. The analytical function for a flat plate wake proposed by Weygandt and Mehta (1989) is plotted for comparison. For all downstream distances beyond 0.014 chord lengths, the statistical ensemble-based approach yields displacement estimates which agree with the reference data within 5% uncertainty for the large field of view (Fig. 5.26-b). The large differences near the airfoil between velocity profiles of the two fields of view are mainly ascribed to the correlation windows’ transversal size and partly to their length along the streamwise coordinate; near the wake origin the sharp (negative) velocity peak leads to underestimate of the momentum deficit. As the gradient reduces in strength with downstream distance, so does the error in the wake and the estimation of the momentum defect to infer the airfoil viscous drag.

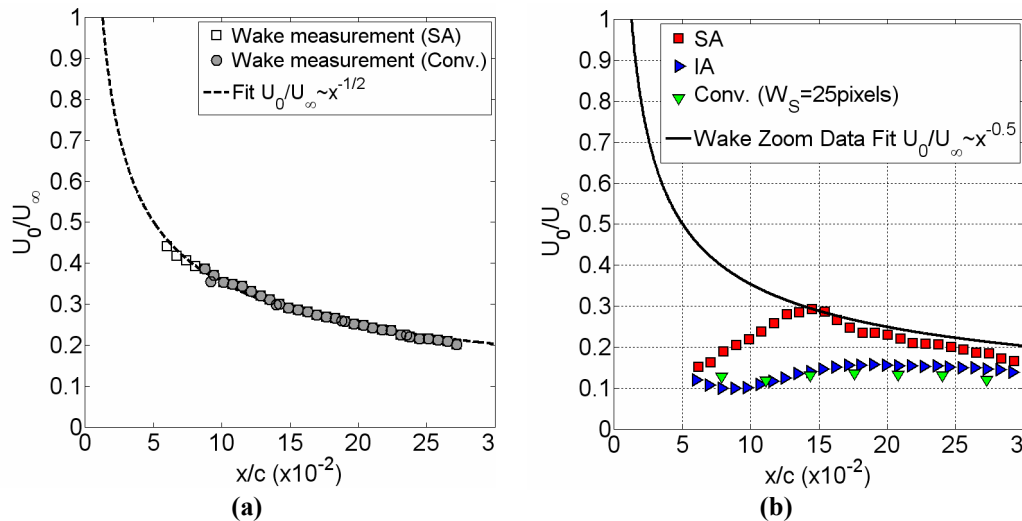


Fig. 5.26: Evolution of the velocity deficit amplitude in the wake with downstream distance (a) obtained from the zoomed field of view (measurements are under-sampled by a factor 8 for readability) (b) obtained from the large field of view (under-sampling by a factor 3 for clarity).

5.5 Conclusions

A variant of the spatially adaptive interrogation method has been proposed that increases the robustness of the previously introduced technique based on individual snapshots such to enable non-isotropic resolution in the interrogation method. The method that refines window size, shape/orientation and spatial distribution on the ensemble-averaged velocity field and image properties has been investigated and its performances directly assessed by experiments. The use of ensemble-averaged properties enables the reliable application of non-isotropic resolution in contrast to the instantaneous adaptive approach where the latter was impracticable. The procedure requires a first-guess average velocity field obtained by means of a conventional cross-correlation analysis. A second pass refines the window spatial distribution and size and shape. This approach allows to reduce the number of interrogation windows without overly compromising the measurement spatial resolution where needed.

Application to a shock-wave-boundary layer interaction flow demonstrates that the method correctly selects the regions where most measurement points need to be concentrated. A higher refinement ratio with respect to the instantaneous adaptivity is obtained. A dual-resolution experiment in the wake behind a transonic airfoil demonstrates that the spatial resolution across sheared regions is actually increased by the ensemble-based adaptivity technique, returning a momentum defect measurement in good agreement with reference data obtained in fully resolved conditions.

CHAPTER 6

EXPERIMENTAL ASSESSMENT OF ADAPTIVE PIV INTERROGATION

Abstract

In this chapter the adaptive interrogation principle is illustrated and its applicability assessed over three experimental cases; the backward facing step, the hypersonic flow over a sphere and an over-expanded supersonic jet. Rather than concentrating on specific bottlenecks, each of the cases offers a combination of processing difficulties allowing the assessment of adaptive interrogation as a whole.

Adaptivity is categorically demonstrated to be a consistent improvement over conventional uniform interrogation in terms of spatial resolution, computational efficiency and limited user input.

Nomenclature

γ	specific-heat ratio
Δ	shock stand-off distance (pixels or meter)
θ	shock angle (radians)
ν	kinematic viscosity (m^2/s)
τ_p	particle relaxation time (seconds)
τ_w	wall shear stress (Pascal)
a_e	exit speed of sound (m/s)
C	seeding concentration (particles per pixel ²)
C_f	wall friction coefficient
D	tunnel diameter (meter or pixels)
D_{noz}	nozzle exit diameter (meter or pixels)
D_{thr}	throat diameter (meter or pixels)
ER	channel expansion ratio
h	step height (meter or pixels)
H	channel height (meter or pixels)

IA	Instantaneous Adaptivity
M_∞	freestream Mach number
M_e	exit Mach number
P	turbulent kinetic energy production (m^2/s^3)
R	sphere radius / gas constant (meter or pixels / $\text{J}\cdot\text{kg}^{-1}\cdot\text{K}^{-1}$)
R_c	shock radius of curvature (pixels or meter)
SA	Statistical Adaptivity
T	static temperature (Kelvin)
T_t	total temperature (Kelvin)
u', v'	fluctuating velocity component (m/s or pixels)
u_n	shock-normal velocity (pixels or m/s)
$u_{n1,2}$	shock-normal velocity before, after the shock (pixels or m/s)
U_∞	freestream velocity (m/s or pixels)
W_S	correlation window size (pixels)
x_r	reattachment length (pixels or meter)
$\langle X \rangle$	ensemble average of variable X

6.1 Introduction

The previous chapters all focused on isolated problems in PIV image interrogation. Chapter 4 introduced the concept of adaptivity and applications involved mainly free flows without wall restrictions. The presence of interfaces was dealt with in chapter 5 whereas adaptivity in case of large data sets was topic in chapter 6.

In the following three experimental flow cases are considered to further illustrate the principle of adaptive interrogation parameters and to assess the viability of the proposed methodology; a sphere submerged in a hypersonic Mach 6 flow, a subsonic backward facing step at $Re_h \approx 5000$ and an over-expanded supersonic jet at Mach 3.75. Each of these cases poses different combinations of processing difficulties; the single snapshot of the sphere contains a curved interface with strong gradients in both seeding density and flow velocity, image recordings of the homogeneously seeded backward-facing step contain a variety in turbulent length scales with a simultaneous presence of an interface, the collection of supersonic jet images contain besides temporal and spatial variations in seeding density strong spatial gradients in velocity and non-homogeneity in image intensity. Given the generality of the experimental images considered and their associated difficulties, they are ideal to open the discussion on the performance of adaptive interrogation. Besides presenting the obtained velocity distributions, a more profound analysis is performed with the aim of extracting and evaluating those quantities typically of interest to the user performing such experiments. A short discussion on the performances and weaker points of adaptivity finalize the chapter.

6.2 Hypersonic sphere

6.2.1 Background

Because of the short testing times, typically in the order of milliseconds, short-time-duration facilities present experimental challenges because of the strong spatial and temporal gradients. PIV is ideally suited in such conditions by virtue of its capability to perform instantaneous and multi-component measurements of the velocity field.

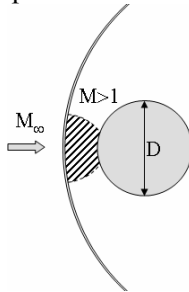


Fig. 6.1: Hypersonic flow over a sphere. The dashed area indicates the subsonic regime.

Its simplistic geometry has made the sphere very attractive in the validation of numerical codes. A sphere submerged in a high enthalpy flow is characterized by the formation of a curved bow shock (Fig. 6.1). Between this detached wave and the sphere's surface the flow attains subsonic, transonic and supersonic regimes. On the symmetry axis the flow is decelerated through a locally normal shock wave and then decelerates further in the subsonic flow region up to the stagnation point. Along the sphere's circumference the flow is accelerated and a boundary layer is formed. The subsequent strong spatial gradients in velocity and seeding density combined with the sharp velocity profile across the shock pose a challenge for the analysis of this type of recordings (Havermann *et al.*, 2002).

6.2.2 Experimental facility

Experiments were conducted in the short-time-duration shock tunnel at the French-German Research Institute of Saint-Louis (ISL). An intricate sequence of shock wave reflections pressurizes heated gas which is expanded in a convergent-divergent nozzle to supersonic velocities. Test times are in the order of two milliseconds during which the flow remains stationary. Further details on the ISL facility can be found in Haertig *et al.* (2002).

A sphere of 120mm in diameter was placed in a uniform flow of 1780m/s corresponding with a Mach number ' M_∞ ' of 6. Al_2O_3 particles acted as seeding in the PIV experiments. An Nd:Yag double-pulse laser provided the short illumination pulses with a separation time of 400 nano-seconds. Images were recorded by a sharpVISION 1300 DE camera. A field of view of $111 \times 89 \text{mm}^2$ was covered by an area of $1280 \times 1024 \text{pixels}^2$ yielding a recording resolution of $86.8 \mu\text{m}/\text{pixel}$ (Haertig *et al.*, 2005). A PIV snapshot is

shown in Fig. 6.2-a. The prominent detached bow shock stands out due to the significant gradient in particle concentration. The highest seeding density is achieved near the stagnation region and gradually decreases towards the meridian in accordance with the flow density. Shock theory predicts a density ratio in the order of 5 between upstream and downstream conditions while concentration estimates based on particle detection yield a ratio of 3 (Fig. 6.2-e). Particle segmentation criteria mentioned in Chapter 3 did on the other hand intend to single out only those tracer images with importance to the correlation result rather than accurately retrieving seeding concentration estimates.

6.2.3 Image evaluation

The contour plot of the streamwise velocity component is depicted in Fig. 6.2-b obtained from the analysis of a single snapshot (Fig. 6.2-a) with the adaptive interrogation procedure. Prior to the correlation operation a background removal sequence was performed by means of a minimum intensity filter. Within a moving window of 13×13 pixels² in size, the minimum intensities were subtracted from the original image. Subsonic and supersonic flow regimes are readily distinguishable as blue and red/green colored zones as well as the sphere's boundary layer. Patches of higher velocity are present in the freestream which correspond to poorer image quality and tend to appear also with more conventional analyses (Scarano and Haertig, 2003). In total, 10000 correlation windows sampled the velocity field with a minimal nearest neighbor distance of 2 pixels. Highest resolutions are desirable across the shockwave and close to the surface of the sphere which from the point of sample spacing is clearly achieved when observing the sampling rate depicted in Fig. 6.2-c. Simultaneously, elongated windows are applied near the sphere's surface aligned with its contours and sizes are reduced in the vicinity of the shock (Fig. 6.2-d). The free stream contains because of its low turbulence intensity large flow structures sufficing a few correlation points for adequate sampling. Figures 6.2-e and -f further explain the selection of sampling location; velocity variance imposes a higher sampling rate across the shock and interface with fewer points downstream of the shock and none upstream while seeding adaptivity forces the majority of points to be placed downstream of the detached shock. A clear contrast is visible between applied window sizes upstream and downstream of the shock. Flow regimes behind the shock span both sub- and supersonic requiring a denser sampling and reduced window sizes to cope with the smaller flow scales. Additionally, for typical concentration estimates of 0.06ppp and 0.03ppp downstream and upstream of the shock respectively, imposing at least 21 particle images per interrogation window yields basic correlation windows of around 1.6mm (≈ 19 pixels) and 2.3mm (≈ 26 pixels). Given the sphere's radius of 60mm this is in agreement with the window sizes presented in Fig. 6.2-d

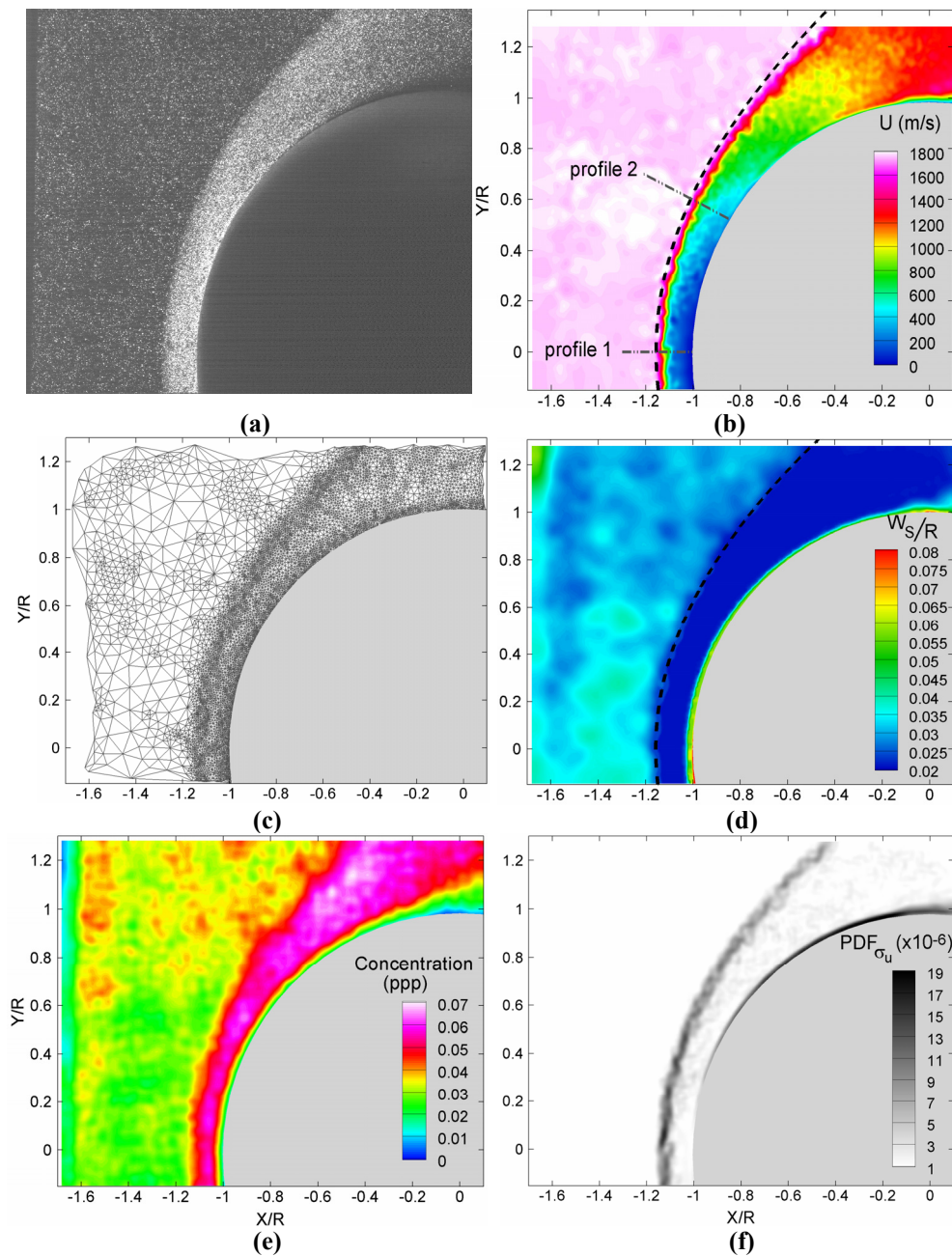


Fig. 6.2: Adaptive interrogation of the Mach 6 flow around a sphere (a) PIV snapshot (b) streamwise velocity distribution. The dashed line shows the predicted shock position according to Billig (1967) (c) spatial distribution of correlation windows (d) applied window sizes (in vicinity of the sphere ' W_s ' indicates the window size aligned with the sphere's surface) (e) measured particle concentration (f) probability density function based on velocity variance.

6.2.4 Flow diagnostics

In addition to window size and velocity contours, the theoretical shock-wave shape according to Billig (1967) has been plotted in Fig. 6.2-b and -d and shows good agreement with the measured gradient in velocity. The correlations for normal shock standoff distance ‘ Δ ’ and (x,y) coordinates of the shock in function of freestream Mach number ‘ M_∞ ’ and sphere radius ‘ R ’ are given by Billig (1967);

$$\Delta = 0.143 \cdot R \cdot e^{\frac{3.24}{M_\infty^2}} \quad \text{and} \quad x = -R - \Delta + R_c \cdot \frac{1}{\tan(\theta)^2} \left[\sqrt{1 + \frac{y^2 \tan(\theta)^2}{R_c^2}} - 1 \right] \quad (6.1)$$

where the Mach angle ‘ θ ’ and vertex radius of curvature ‘ R_c ’ are defined as

$$\theta = \sin^{-1}\left(\frac{1}{M_\infty}\right) \quad \text{and} \quad R_c = 1.143 \cdot R \cdot e^{\frac{0.54}{(M_\infty-1)^{1.2}}} \quad (6.2)$$

For the present case this yields a standoff distance of 9.4mm (≈ 108 pixels), a Mach angle of 9.6 degrees and a radius of curvature of 74.2mm (≈ 856.4 pixels).

A quantitative comparison is made with the conventional metrology adopting a structured sampling (cf. Chapter 2) with window sizes of 25 and 33 pixels and an overlap coefficient of 0.75. Velocity profiles are extracted across the shock at the locations indicated in Fig. 6.2-b where shock-wave positions were determined from (6.1) and (6.2). Profile 1 follows the stagnation streamline evidenced by the absence of a vertical displacement component (Fig. 6.3-a). While the velocity upstream of the shock ‘ u_{n1} ’ has been measured, the standoff distance is too small for the flow to reach the theoretical velocity ‘ u_{n2} ’ downstream of the normal shock. The velocity behind the normal shock is instead estimated from the isentropic shock relations;

$$\frac{u_{n2}}{u_{n1}} = \frac{2 + (\gamma - 1) \cdot M_\infty^2}{(\gamma + 1) \cdot M_\infty^2} \stackrel{M_\infty=6}{=} \stackrel{\gamma=1.4}{=} 0.1898 \quad (6.3)$$

Based on these profiles of the shock-normal velocities, particle relaxation times have been estimated to be around 2.28mm (1.82 μ s), the calculation procedure of which is recapitulated in Appendix B. This value agrees well with the theoretical 2.1mm reported by Havermann *et al.* (2002). Comparison with their estimated 1.8mm reveals an enhanced spatial response. The negligible difference between the different analysis methods hints that for the present case the measurement accuracy is limited by the particle tracers’ relaxation lengths. Converted into pixel units, the estimated particle relaxation length needed for the particle velocity to reach 50% of the downstream velocity equals around 40 pixels. Because of this considerable shock thickness, no improvements in shock resolution are to be expected when adopting window sizes below this limit value. A more

through elaboration is incorporated in Appendix B. Nevertheless, the adaptive interrogation methodology offers an important benefit in that it requires no user expertise and is able to provide identical results while offering a reduction in number of windows by respectively a factor 3 and 2 compared to the conventional approach.

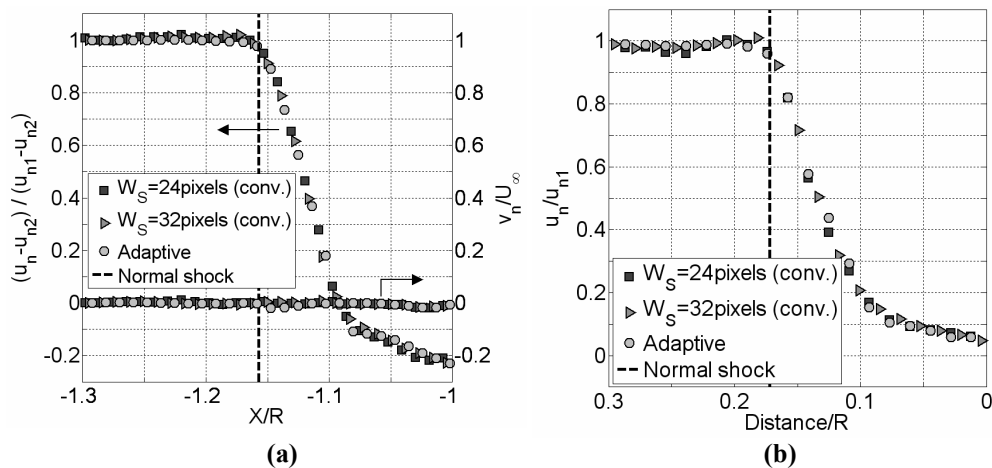


Fig. 6.3: Shock-wave normal velocity profiles (a) Profile 1 (b) Profile 2 (cf. Fig. 6.2-b).

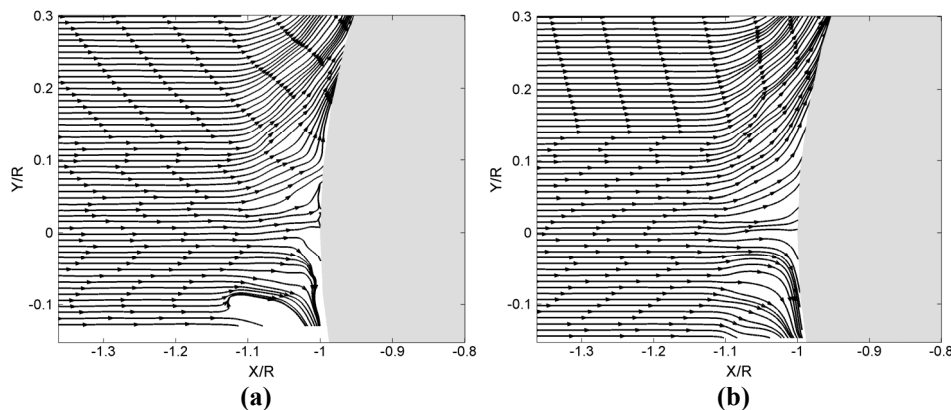


Fig. 6.4: Streamline pattern near stagnation point (a) adaptive interrogation (b) conventional interrogation with window sizes of $25 \times 25 \text{ pixels}^2$.

Figure 6.4 qualitatively displays the achievable gain of the adaptive interface treatment by comparing the streamline patterns near the stagnation point retrieved by adaptive interrogation and the conventional structured methodology adopting window sizes of $25 \times 25 \text{ pixels}^2$. In both cases the stagnation line can be traced. The pattern calculated from conventional data lacks however vertical symmetry in the immediate vicinity of the stagnation point. Streamline anomalies are clearly present caused by erroneous displacement estimates, especially near the interface. Streamlines based on image analysis utilizing self-adapted interrogation parameters on the other hand show a certain degree of smoothness and vertical symmetry. Moreover, close to the interface the

calculated trajectories are tangent to the sphere's surface as to be expected from the no-slip condition. Ipso facto, adaptive interrogation with the incorporation of interface treatment is preferential in the retrieval of the boundary layer around the curved surface.

6.3 Backward facing step flow

6.3.1 Background

Turbulent flow over a backward facing step is a widely used benchmark problem to evaluate the performance of turbulence models in the numerical prediction of separated flows. The flow over a backward-facing step has emerged as a prototype of a non-trivial yet simple geometry in which to examine the onset of turbulence as it embodies several important aspects of turbulent flow; separation, recirculation and reattachment. Statistically, a large recirculation region appears below the shear layer. Depending on the Reynolds number based on the step height and channel expansion ratio, a smaller recirculation zone is located near the step corner. As a result of Kelvin-Helmholtz instabilities, the shear layer emanating from the step edge breaks down into eddy structures and reattaches to the wall, downstream of which the boundary layer develops (Fig. 6.5-a). From the mean flow phenomena the obvious problematic appears of accurate representation of the shear layer because of the strong gradients in velocity which deteriorate the correlation quality.

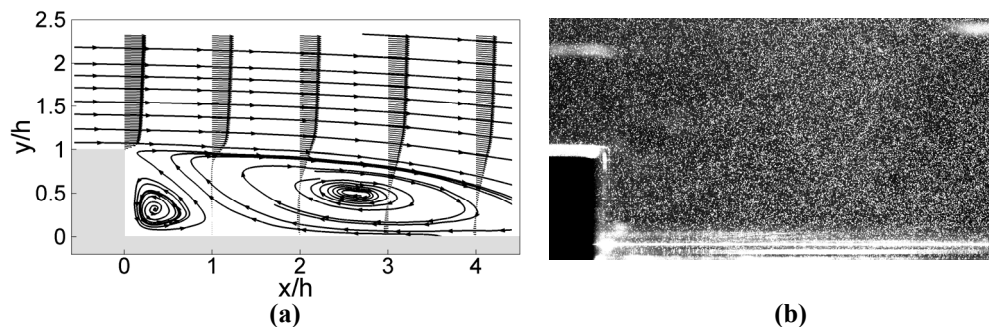


Fig. 6.5: Backward facing step for step height based Reynolds number of around 5000 (a) mean velocity field with stream lines (b) instantaneous PIV recording (contrast enhanced for clarity).

From an instantaneous point of view, the above phenomena can not be observed. The instantaneous flow fields are characterized by the formation, roll-up and shedding of spanwise vortical structures in the separated shear layer. Mainly these structures are responsible for growth of the shear layer and momentum transfer as indicated by the peaks in production of turbulent kinetic energy (Kostas *et al.* 2002, Scarano and Riethmuller 1999). The vortices are convected across the shear layer downstream and grow in size via pairing interactions (Schram *et al.*, 2004). The imposed, globally uniform, interrogation parameters are thus not necessarily conform to the instantaneous

flow variations and a general optimization of the analysis is needed. Characterization of turbulence furthermore requires accurate displacement measurements (Christensen, 2004), a minimization of the modulation factor inherent to cross-correlation (Piirto *et al.*, 2003) and a high spatial resolution. The higher the resolution, the smaller the turbulent scales taken into consideration and the more realistic the flow estimates. The latter is especially important in the determination of turbulent quantities such as e.g. energy dissipation, kinetic energy production, etc. (Baldi and Yianneskis, 2004). While large correlation windows ensure robustness, the latter requirement translates into reduced window sizes. In that perspective, the ratio between size of the sensing domain and relevant flow scale i.e. the Kolmogorov scale should ideally not exceed unity. Simultaneously, this poses stringent requirements on the tracer spacing which ultimately determines the lower resolution limit.

Last but not least, the backward facing step has a strong three-dimensional character which translates into convection of seeding in spanwise direction. PIV experiments consisting of a single camera will suffer from degradation of the results as a result of out-of-plane motion. Moreover, capturing the reattachment point while maintaining a sufficiently large physical sensing domain imposes stringent requirements on the interrogation methodology not to mention the apparent image aberrations and velocity gradients near the wall (Fig. 6.5-b).

6.3.2 Experimental facility

The backward facing step geometry was created by an expansion of the main channel by a factor ' $ER=(H+h)/H$ ' of 1.2. The symbol ' H ' refers to the height of the windtunnel section (10cm) upstream of the step with height ' $h=2\text{cm}$ '. A turbulent boundary layer was triggered upstream of the step with a thickness of $1.2\cdot h$ visible from the velocity profile extracted a half step height upstream of the sudden expansion (Fig. 6.7-a). A freestream velocity of 3.75m/s and 2cm step height yielded at ambient temperature ($\nu=1.52\times 10^{-5}\text{ m}^2/\text{s}$) a nominal Reynolds number ' $Re_h=U_\infty\cdot h/\nu$ ' of around 5000.

The air flow was seeded by silicon oil droplets of $1\mu\text{m}$ diameter in average. A classical optical arrangement consisting of a cylindrical and spherical converging lens transformed the light beam emanated by a double pulsed Nd:Yag laser into a thin light sheet about 1mm thick. Images focused in the test-section's mid-plane were captured by a 12bit PCO Sensicam ($1280\times 1024\text{ pixels}^2$) at an acquisition frequency of 5Hz. With an image separation time of $165\mu\text{s}$ and calibration factor of $\approx 78\cdot 10^{-3}\text{ mm/pixels}$ maximum tracer displacements were set to orders of magnitude of 8 pixels. To allow a statistical analysis the image set consisted of 320 snapshot. An exemplary instantaneous snapshot is illustrated in Fig. 6.5-b.

6.3.3 Image evaluation

The ensemble average over 320 instantaneous interrogation locations is depicted in Fig. 6.6-a along with the sampling locations as predicted by statistical adaptivity in Fig.

6.6-b. The dense meshes stemming from wall adaptivity are clearly visible in both approaches. Although instantaneous adaptivity imposes a slightly elevated sampling density in the separated shear layer, the degree of clustering with respect to the freestream and region of secondary recirculation near the step base is more pronounced in the statistical approach (Table 6.1). Given the low levels in longitudinal and transversal velocity fluctuations near the step base and freestream the second interrogation mesh (Fig. 6.6-b) can be considered to be more appropriate. With exception of some isolated patches in the undisturbed boundary layer, an adopted instantaneous sampling rate (Fig. 6.6-c) shows a high degree of similarity with the statistically adaptive version (Table 6.1). Considering the homogeneity in seeding density, the distribution of correlation windows is dominated by velocity variance. The latter is confirmed when visually comparing the projected window locations with the probability density functions in spatial velocity variance (Fig. 6.6-c vs. -e and Fig. 6.6-b vs. -f). Notice how the velocity variance in case of statistical adaptivity is a smoothed version of the instantaneous data field.

Both figures 6.6-a and -b show the squared window sizes ($W_s = W_{sx}^{1/2} \cdot W_{sy}^{1/2}$) normalized by the step height at random locations. Adaptivity automatically sets a dynamic range in interrogation window dimensions with reduced sizes in the separated shear layer and increased sizes in the freestream and secondary recirculation near the bottom of the step corner. Near the interface, non-isotropic correlation windows are applied with reduced wall-normal extents (Fig. 6.6-g) and maximum eccentricity factors of 0.75 yielding a maximum stretching factor of 4. Typical window sizes are one to two orders of magnitude smaller with respect to the step height. A quantitative comparison between the squared window sizes utilized in instantaneous and statistical adaptivity reveals an overall size ratio of ~ 1.7 . This discrepancy is related to the methodologies fundamental difference in quantifying the signal density[†]. With instantaneous adaptivity spatial variations in intensity prescribe the particle identification while in statistical adaptivity temporal fluctuations are key factor. Even though the corresponding probability distributions are nearly identical, intensities categorized as spatially local maxima at a particular time instant do not necessarily constitute temporal maxima. Consequently, the signal quantization philosophies yield different seeding concentration estimates as illustrated by Fig. 6.6-d. Statistical adaptivity partially compensates the inherent loss in spatial resolution due to enlarged window sizes by incorporating window non-isotropy (Fig. 6.6-g). Window eccentricity and re-orientation is applied in flow areas with strong spatial gradients in mean velocity, i.e. the separated shear layer (Fig. 6.6-h), while square windows are applied in the free stream.

[†] Subsequent image recordings are non-correlated since the acquisition rate of 5Hz is one order of magnitude smaller than the frequency based on the characteristic time scale $(h/U_\infty)^{-1} = 187.5\text{Hz}$. Accordingly, particle motion has no influence in the statistically determined intensity threshold for particle image identification (cf. section 5.3.1).

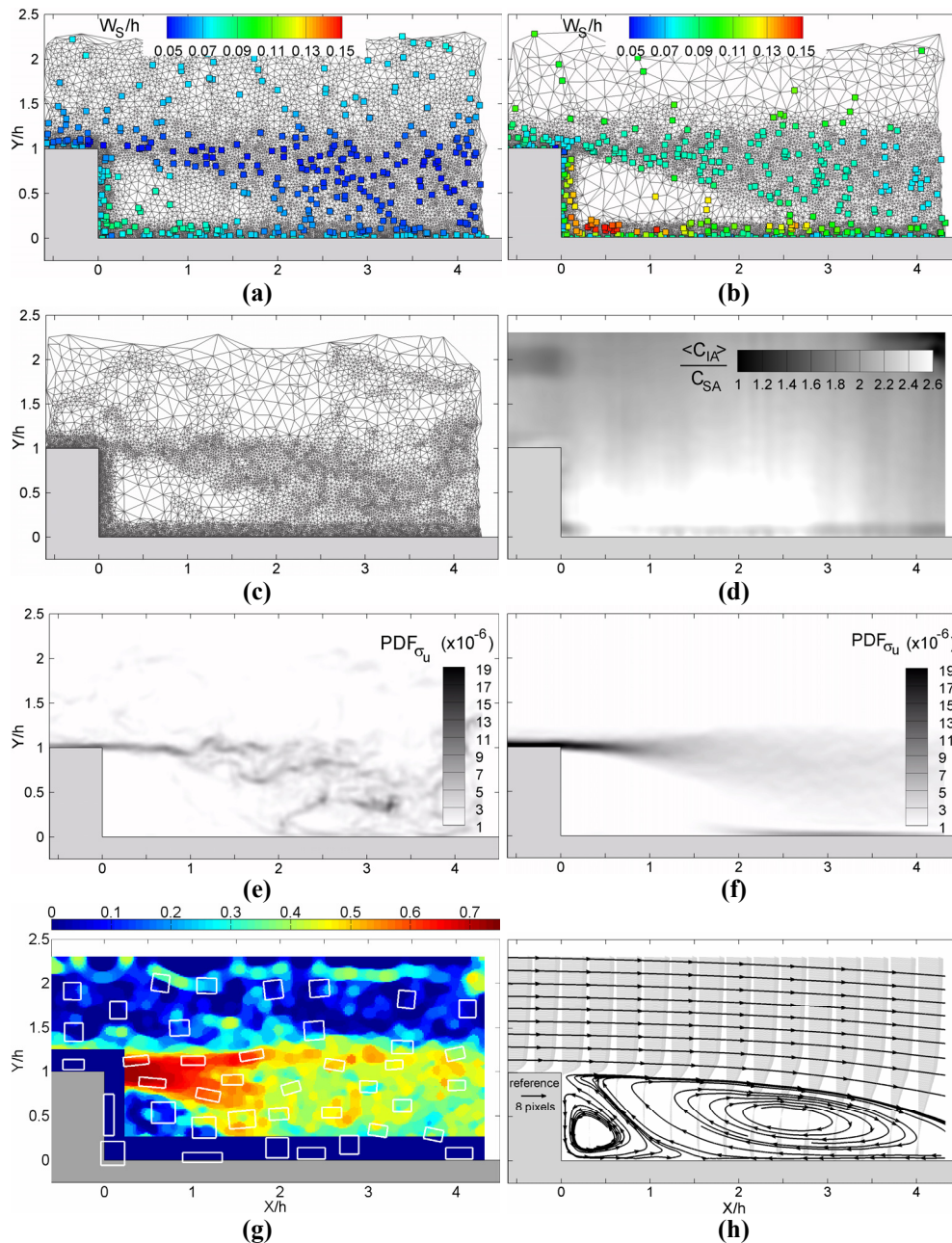


Fig. 6.6: Backward facing step ($Re_h \approx 5000$). Interrogation mesh and squared window sizes (a) ensemble averaged instantaneous adaptivity (b) statistical adaptivity (c) instantaneous sampling grid (d) ratio in concentration estimates from instantaneous adaptivity (ensemble averaged) and statistical adaptivity. PDF in velocity variance (e) instantaneous (f) statistical adaptivity. (g) Contour of eccentricity and sampled window orientation in horizontal velocity component (scaled window sizes by factor 3 for clarity). (h) Flow topology measured with statistical adaptivity.

Table 6.1 recapitulates the discussed interrogation parameters in different flow areas adopted by the image analysis methodologies considered. The mean flow topology of the separated region from the statistical technique is illustrated in Fig. 6.6-h. The main recirculation originating from the separation point at the step edge and the secondary recirculation in the bottom corner of the step are visible.

Table 6.1: Approximate adopted interrogation parameters normalized by step height (correlation window size ' W_s ' and sample spacing ' λ_w ') in Instantaneous Adaptivity (IA), the ensemble average ($\langle IA \rangle$), Statistical Adaptivity (SA) and a conventional approach (Conv.) with final correlation windows of 17 pixels and 75% window overlap.

	$W_s/h (\times 10^{-2})$				$\lambda_w/h (\times 10^{-2})$			
	IA	$\langle IA \rangle$	SA	Conv.	IA	$\langle IA \rangle$	SA	Conv.
Freestream	7.3	7.3	10	6.6	17	6.4	21	1.9
Shear layer $x/h < 1$	5	5	16.2 \times 4	6.6	1.7	2.4	1.7	1.9
$x/h > 1$	5	5	11 \times 6	6.6	2.9	2.7	2.7	1.9
Wall region	9.9 \times 4.9	9.9 \times 4.9	14.1 \times 7	6.6	1.1	1.1	1.1	1.9

Besides the two adaptive approaches, the image set was analyzed by the conventional interrogation technique discussed in Chapter 2 for different spatial resolution. Square window sizes of 17 and 33 pixels ($W_s/h \approx 0.066$ and $W_s/h \approx 0.13$) were utilized yielding for a constant window overlap ratio of around 0.7 a vector spacing of 5 and 9 pixels respectively. It is worthy of notice that while the adaptive analyses involved 8000 correlation windows, the uniform approach utilized 32000 and 10000 windows respectively. The reduction in necessary correlation operations while maintaining, if not improving, performances emphasizes the possible computational advantage offered by adaptivity.

6.3.4 Flow diagnostics

- *Velocity and vorticity profiles*

Velocity profiles in mean streamwise component at different locations downstream of the step are presented in Fig. 6.7-a. The profile extracted at ' $x/h = -0.5$ ' attests a boundary layer thickness or approximately 1.2 step heights. For abscissae exceeding one step height transversal gradients have become visibly smaller (Fig. 6.6-h). Given the comparable sampling resolution in terms of window sizes and vector spacing, differences between interrogation techniques will thus become negligible. Closer towards the step edge, the strongest velocity gradients are encountered. Because of slight reduction in vector spacing and correlation window size in the direction normal to the mean flow, statistical adaptivity yields marginally higher velocity gradients followed by instantaneous adaptivity (Fig. 6.7-b). The effects of enlarged interrogation areas and vector spacing are evidenced by the appreciable reduction in measurable gradient when applying window sizes of 33 pixels ($W_s/h \approx 0.13$). The discrepancy between the numerical results obtained

by Le *et al.* (1997) and PIV results stem from variations in inlet conditions (according to Piirto *et al.*, 2003). In effect, observing the data extractions at ‘ $x/h=0.5$ ’ measured profiles are “fuller” with respect to their numerical counterpart, indicating a more developed turbulent boundary layer. According to Isomoto and Honami (1989) this explains the observed shortened reattachment length.

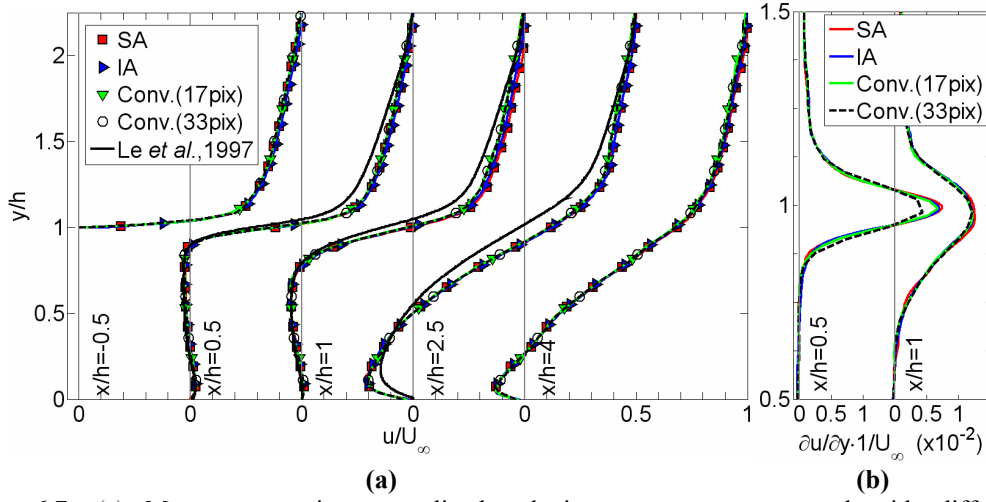


Fig. 6.7: (a) Mean streamwise normalized velocity component measured with different interrogation methodologies at various abscissae (b) Normalized mean transversal gradient in streamwise velocity at different downstream locations.

- ***Skin friction coefficient***

The distribution of the measured skin friction coefficient, which has been derived from the ensemble average flow fields using (6.4), is plotted in Fig. 6.8-a against the direct numerical simulation of Le *et al.* 1997) and BFS-related PIV experiments of Jovic and Driver (1994). The velocity gradient was evaluated by linear fitting through the two lowest positions in the measurement grid. The mean reattachment location for the current PIV measurements has been estimated at 5.4 step heights[†]. This estimate is lower compared to other values found in literature for reasons explained above but remains within the limits ‘ $4.86 \leq x_r \leq 7.86$ ’ reported by Le *et al.* (1997).

$$C_f = \frac{\langle \tau_w \rangle}{\frac{1}{2} \rho U_\infty^2} = \frac{2\nu}{U_\infty^2} \frac{\partial \langle u \rangle}{\partial y} \quad (6.4)$$

[†] Because the PIV field of view did not cover the reattachment location (see Fig. 6.6-h), the reattachment length was estimated on the basis of the evolution in skin friction factor. The proposed estimate for ‘ x_r ’ resulted in the best agreement between the reference evolutions (Le *et al.* 1997 and Jovic and Driver 1994) and the present PIV measurement analyses.

Small positive values of ' C_f ' close to the step indicate the presence of the corner eddy while the negative values refer to the main recirculation bubble. The minimum friction coefficient is typically located around ' $x/x_f \approx 0.6$ '. Conventional metrologies clearly underestimate the trough value with errors in function of the applied wall-normal window size. This problem of insufficient spatial resolution in the measurement of velocity gradients at the wall has been successfully addressed by implementing wall adaptivity (cf. Chapter 4). Friction coefficients measured by adaptive metrologies are in good agreement with reference values. The marginally higher coefficient measured with instantaneous adaptivity is attributed to the slightly lower wall-normal correlation window extents (Table 6.1).

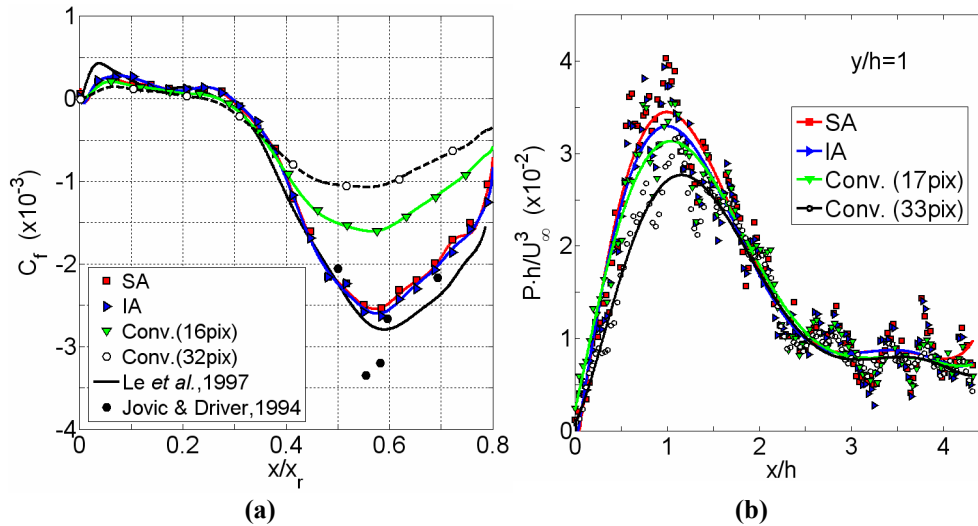


Fig. 6.8: (a) Distribution of wall friction coefficient (data is undersampled for readability). (b) Evolution of the normalized turbulent kinetic energy production extracted at ' $y/h=1$ ' with downstream distance. Solid lines serve as mere indication and are determined from low order spline fitting.

- ***Turbulent kinetic energy production***

Figure 6.8-b reports the turbulent kinetic energy production defined in (6.5) along ' $y/h=1$ '. Despite significant data scatter[†], general tendencies are visible and permit an assessment of the interrogation routines' proficiency in turbulence characterization. The main part of the energy production occurs in a region situated along the mean stream separation streamline (Kostas *et al.*, 2002). Arguing that according to Fig. 6.4-h the latter

[†] The scatter is believed to be the result of the uncertainty in the estimation of the statistical quantities. According to Benedict and Gould (1996) the fractional error in $\overline{u'u'}$ at a 95% confidence level is related to the number of flow fields ' N ' by $\sim 2.77 \cdot N^{-1/2}$. If this error is used as a mere indicator for the relative error in P , errors easily in excess of 15% ($N=320$) can be expected.

has descended by less than 10% of the step height at 'x/h=2', the extraction at 'y/h=1' will serve the current purpose. Large velocity gradients occur close to the step edge and cause the maximum production to be localized within the shear layer extending from 'x≈h' to 'x≈2h'. Beyond, the turbulent kinetic energy production decreases to a rather uniform level. This is in accordance with Fig. 6.8-b.

$$P = -\langle u'u' \rangle \cdot \frac{\partial \langle u \rangle}{\partial x} - \langle v'v' \rangle \cdot \frac{\partial \langle v \rangle}{\partial y} - \langle u'v' \rangle \cdot \left(\frac{\partial \langle u \rangle}{\partial y} + \frac{\partial \langle v \rangle}{\partial x} \right) \quad (6.5)^\dagger$$

Results obtained by the conventional techniques confirm the tendency of a drop in peak amplitude in estimated turbulence production with decreasing spatial resolution (Pirto *et al.*, 2003). For 'x/h>>1' the interrogation parameters with signal and flow dependency were reported to be nearly identical to those imposed by the conventional technique applying correlation window sizes of 17 pixels. This explains why the production estimates in those areas are nearly identical for the three analyses (Table 6.1). However, near the step edge where velocity gradients are largest, the ability to measure a higher energy production emphasizes the relaxation of the limits on spatial resolution by the adaptive metrologies and in particular the statistical adaptive technique. The ability of this technique to measure the small fluctuations despite a solid foundation in ensemble averaging is attributed to the implemented interrogation routine (cf. Fig. 5.4); the mean flow field serves as a first estimate for image distortion after which images are re-interrogated to accommodate for small deviations from this average.

6.4 Over-expanded supersonic jet

6.4.1 Background

The term over-expanded is referred to when the pressure within the exit nozzle is lower compared to the outer atmospheric pressure. To equate this pressure difference between exhaust and atmosphere the flow is subjected to a sequence of contractions and expansion (Norman and Winkler, 1985). The method by which the flow accomplishes these compressions and expansions is through different kinds of waves that form the basis of supersonic fluid dynamics. Among these types of waves are oblique and normal shock waves, Prandtl-Meyer expansion and compression waves (Fig. 6.9-a).

[†] Under the assumption of dealing with an ergodic process, the ensemble average ' $\langle X \rangle$ ' will be equivalent to the time average ' \overline{X} ' taken over a sufficiently long time interval. The time interval is such that it contains a great number of characteristic time-scales and hence statistically independent measurements (see also Chapter 7).

The PIV recording of a supersonic over-expanded jet flow issuing from a conical nozzle at Mach 3.75 is presented in Fig. 6.9-b (Jerónimo *et al.*, 2002). The first normal shock (Mach disk) is discernible by the variation in density. Outside of the characteristic shock cell pattern of the over-expanded jet, less seeding is present, giving rise to distinctive differences in image intensity. The large flow rates in supersonic flows involve significant seeding quantities in a flow field that is subjected to large displacement gradients across shocks and expansions. Therefore uniform seeding concentrations of good quality are very difficult to obtain as can be verified from Fig. 6.9-b. The presence of both inhomogeneous seeding concentrations and the rapid change in flow scales across the displacement discontinuities, make that supersonic flows are challenging for the viability of PIV interrogation routines.

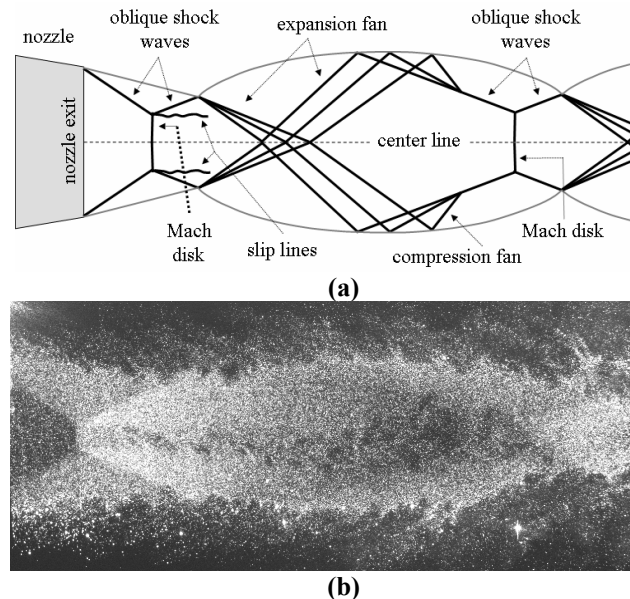


Fig. 6.9: (a) Idealistic wave structures in an over-expanded jet (b) experimental PIV recording of an over-expanded jet at Mach 3.75 (contrast enhanced for clarity).

6.4.2 Experimental facility

The supersonic over-expanded jet flow was issued from a conical nozzle with exit diameter ' D_{noz} ' of 17.3mm and throat diameter ' D_{thr} ' of 5.85mm. With a pressure ratio between stagnation chamber and ambient of 25, the exit velocity corresponded to a Mach number of 3.75 (Jerónimo *et al.*, 2002). Upstream of the nozzle, air was mixed with sub-micron oil particles generated by a modified Laskin's nozzle seeding generator. The laser sheet with a thickness of 0.5mm was generated by a sequence of cylindrical and spherical lenses. An Nd:Yag laser pulsed with regular intervals of 0.5 μ s provided the necessary light source. Images were acquired at a frequency of 8.2Hz with a 12bits PCO Digital Camera. The imaged area was approximately 4 \times 2cm² and sampled by a sensor area of

1280×544pixels² or an optical resolution of around 34μm per pixel. More information concerning the experimental campaign can be found in Jerónimo *et al.* (2002).

6.4.3 Image evaluation

- ***Correlation window distribution***

The characteristic shock cell patterns of the over-expanded jet are emphasized by gradients in seeding density (Fig. 6.9-b). Despite the fact that seeding was introduced upstream of the nozzle, tracers are present outside the jet although in minor quantity. This spreading of seeding is caused by turbulent mixing layers. Real supersonic jets differ from such idealizations sketched in Fig. 6.9-a in that they do not have sharp, stable boundaries but turbulent boundaries where jet and ambient gases mix. These mixing layers, which grow as a result of Kelvin-Helmholtz instabilities, progressively eat their way into the jet core. When they reach the axis of the jet several nozzle diameters downstream the flow is subsonic and fully turbulent (Love *et al.*, 1959). The presence of such a turbulent shear layer complicates the distribution of sampling locations. High values in velocity variance will be found near the normal and oblique shocks where the flow decelerates and in the shear layers where the flow is turbulent. These zones are accordingly attributed a higher sampling rate leaving the bulk part under-sampled as attested by Fig. 6.10-b. This would be an ideal distribution of samples to characterize the shear layers if not for the then far from optimal seeding conditions. One way of circumventing this drawback inherent to the imposed adaptivity criteria is to impose a dynamic threshold on the intensity (cf. Chapter 3 – paragraph 3.4.1). Regions of higher light scattering amplitude now correspond to the flow features of interest (cf. Fig. 3.8) and gain the largest share in interrogation areas (Fig. 6.10-c).

To provide a more general solution without the need of dynamic intensity thresholding (cf. paragraph 3.4.1) and give the spatial variation in flow length scales (i.e. velocity variance) more weight in the choice of sampling locations, a statistical approach is more conducive. Fig. 6.10-d displays the unstructured grid generated following ensemble adaptivity. The turbulent outer edge of the jet and incident and reflected shocks are more pronounced compared to Fig. 6.10-c specifically further downstream of the nozzle. Considering the case dependent tweaking of the intensity threshold level and mainly owing to the current interest in the jet excluding its boundary (because the local imaging conditions do not allow a high information density anyway), a cropping of the images offers a more consistent solution. Mach disk, reflected shocks and expansion fan can be unmistakably identified from the average instantaneous correlation window distribution (Fig. 6.11-a). Regions of high velocity gradients become even further pronounced in case of ensemble statistics (Fig. 6.11-b) and are clearly emphasized by the Reynolds shear stresses (Fig. 6.11-c) and window size distribution (Fig. 6.11-d). Notice how regions partially overlapping the jet's boundary are consistently attributed a higher sampling density.

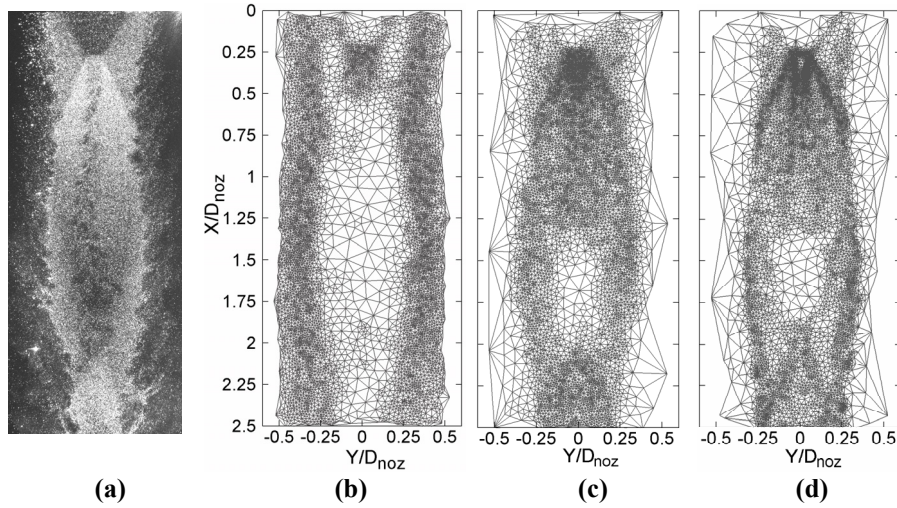


Fig. 6.10: (a) Typical instantaneous PIV image of the over-expanded jet. Images are rotated over 90 degrees and contrast enhanced for visual clarity. Flow goes from top to bottom. (b) Ensemble averaged distribution of 8000 correlation windows without (c) with intensity dynamic threshold. (d) Correlation window locations predicted by statistical adaptivity.

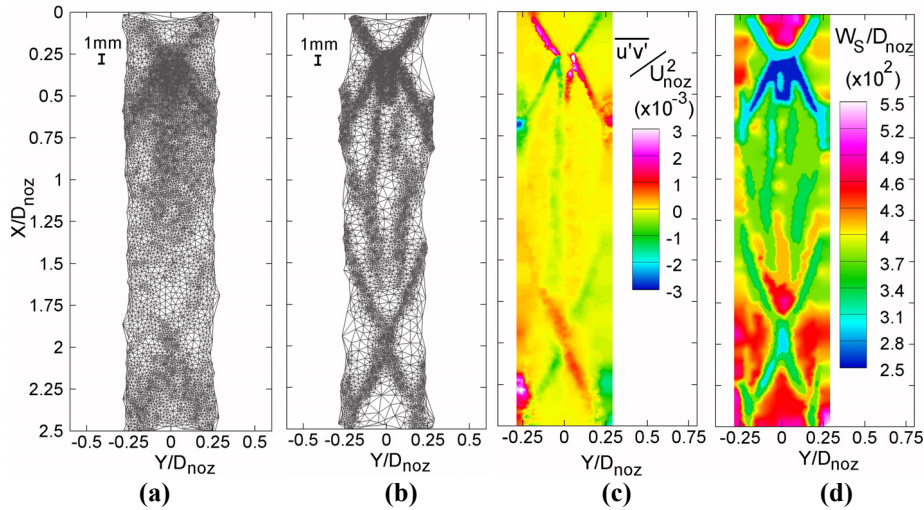


Fig. 6.11: (a) Ensemble average of instantaneous distribution of correlation windows (b) correlation window locations predicted by statistical adaptivity (c) normalized Reynolds shear stress and (d) normalized correlation window sizes obtained by the ensemble adaptive interrogation metrology.

- **Qualitative flow diagnostics**

Wave structures within the supersonic core are buffeted by the turbulent boundary layer causing an oscillation in the normal shock location. Jerónimo *et al.* (2002) estimated the amplitude to be in the order of 1mm. These dimensions are in agreement with the

streamwise extent of the region with high sampling density in the vicinity of the Mach disk and reflected shocks (Fig. 6.11-b). The spatial variation in shock locations is further illustrated by observing two instantaneous unstructured grids (Fig. 6.12). Between the estimated shock locations (red lines) a clear spatial shift is present. Compared with the more concentrated sampling density obtained by ensemble adaptivity the instantaneous distribution of windows resembles a spatially smeared version exactly due to these oscillations (Fig. 6.11-a vs. -b). In the mean flow field these fluctuations are averaged out, which is why the shock locations are well defined in case of ensemble adaptivity. From this aspect, the inherent adaptivity criteria are able to take into account the fluctuations in shock locations whereas the rigid sampling locations imposed by conventional interrogation are unable to cope with the temporal variations in flow scales.

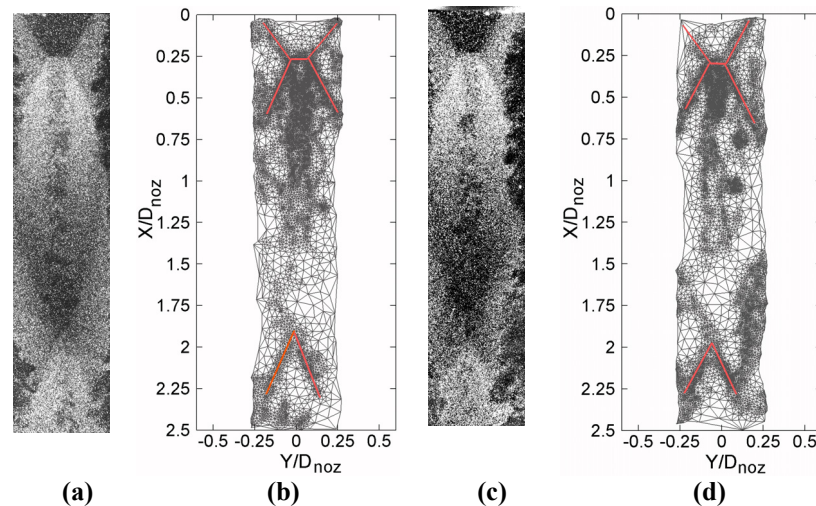


Fig. 6.12: (a)-(c) Cropped instantaneous PIV images of the over-expanded jet (contrast enhanced) (b)-(d) Corresponding sampling grids imposed according to instantaneous adaptivity. Red lines are estimated shock locations inferred from velocity variance.

6.4.3 Flow diagnostics

- **Instantaneous vorticity**

One of the advantages of instantaneous adaptivity lies in the reduction of vorticity. Fig. 6.13 considers the instantaneous vorticity distribution for the image depicted in Fig. 6.10-a calculated by a conventional metrology adopting windows sizes of 23 pixels ($W_s/D_{noz} \approx 4.5 \times 10^{-2}$) on a structured grid and the adaptive technique with interrogation parameters based on instantaneous seeding and flow conditions (e.g. Fig. 6.12 and Fig 6.13-d). While the flow behind the normal shock is subsonic, it is still supersonic behind the oblique shocks. This velocity discontinuity gives rise to slip-lines emanating from the intersection points of the oblique shocks with the Mach disk (Yüceil *et al.*, 2000). The shear layers grow and merge at the jet's centerline to develop as a wake. Both

metrologies are able to capture the above flow phenomena and clearly indicate the slip-lines to originate from the triple points (i.e. the intersection between incident shock, reflected shock and Mach disk). Albeit the vorticity fields show a general agreement, vorticity peaks predicted by adaptive interrogation attain higher amplitudes attributed to enhanced sampling by means of reduced window sizes (Fig. 6.13-d). Additionally the regions upstream of the Mach disk and vicinity of the second cell pattern show more spurious vorticity peaks in case of the conventional approach which are apt to stem from a higher degree of erroneous fluctuation in displacement measurements.

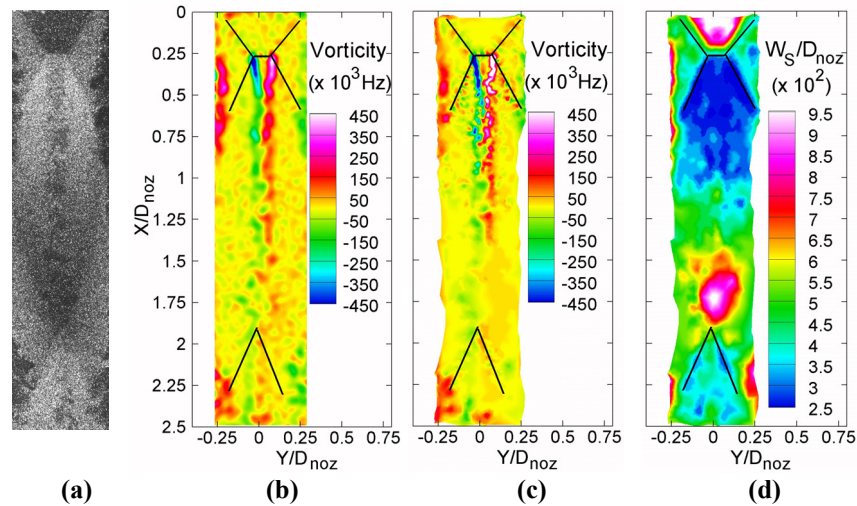


Fig. 6.13: (a) Contrast enhanced cropped instantaneous PIV image of the over-expanded jet. Corresponding instantaneous vorticity field calculated by (b) uniform interrogation ($W_s/D_{noz} \approx 0.045$) (c) instantaneous adaptivity. (d) Utilized window sizes based on (a) by adaptive interrogation in the calculation of vorticity.

- ***Average shock-normal velocity profiles***

Although the instantaneous adaptivity can be considered as a conducive technique in the retrieval of instantaneous flow fields, it suffers from too strong oscillations in applied window sizes and sampling locations to provide a robust basis for ensemble statistics; the averaged sampling distribution shows quite a degree of smoothing (Fig. 6.11-a) and instantaneous window sizes are strongly directed by seeding density (compare e.g. Fig. 6.13-d with -a). Moreover, the instantaneous sampling distributions vividly suffer from local anomalies caused by occasional erroneous vectors. Compared to instantaneous adaptivity a statistical approach has the advantage of being less susceptible to extrema in deduced tracer concentration. When considering multiple image exposures isolated events have a low probability of occurrence which automatically minimizes their influence and allows a consistent sizing of the interrogation areas as illustrated by Fig. 6.11-d. Discussion of statistical quantities hereafter will therefore involve only the statistically adaptive and conventional metrology with the former adopting ensemble correlation.

From the known nozzle exit area to sonic throat area and total temperature (T_t) of 290 Kelvin, the corresponding Mach number can be calculated to be 3.77 from equation (6.6). Substitution of the available data; $T_t=290\text{K}$, $\gamma=1.4$ and $R=287.04\text{ J}\cdot\text{kg}/\text{K}$, in (6.7) yields a corresponding velocity of 655 m/s. The evolution of velocity and ratio in nozzle areas with exit Mach number is plotted in Fig. 6.11.

$$\frac{D^2(x)}{D_{\text{thr}}^2} = \frac{1}{M_e(x)} \left[\frac{2}{\gamma+1} \left(1 + \frac{\gamma-1}{2} M_e^2(x) \right) \right]^{\frac{\gamma+1}{2(\gamma-1)}} \quad (6.6)$$

$$u_e = M_e \cdot a = M_e \cdot \sqrt{\gamma \cdot R \cdot T} = \sqrt{\gamma \cdot R \cdot T_t} \cdot M_e \cdot \left(1 + \frac{\gamma-1}{2} M_e^2 \right)^{-\frac{1}{2}} \quad (6.7)$$

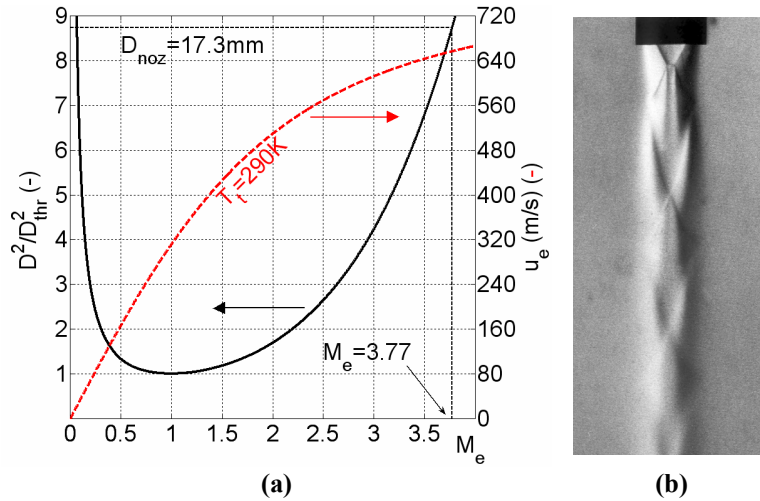


Fig. 6.14: (a) Evolution of velocity and the ratio between nozzle and throat area in function of the Mach number based on preservation of entropy (b) Schlieren image of the over-expanded jet (taken from Jerónimo *et al.*, 2002).

Maximum displacements measured are however in the order of 633 m/s. The discrepancy stems from boundary layer separation inside the nozzle which is a phenomenon well demonstrated numerically by e.g. Xiao *et al.* (2007). The separation is indicated by observing the Schlieren image in Fig. 6.14-b showing the oblique shocks not to be formed at the nozzle exit. As separation occurs, the formation of oblique shocks and Mach disks translates further upstream. Following the isentropic considerations in Fig. 6.14-a, this upstream shift towards a narrower cross-section is accompanied by a reduction in velocity and Mach number. Based on Fig. 6.14-a and given the measured displacement value, a conditional Mach number in the order of 3.33 was attained. Normal shock relations predict a downstream Mach number of 0.46 or a velocity of 153.4 m/s.

Overlaying the mean jet's centerline velocities measured by the conventional metrology and the adaptive evaluation technique adopting ensemble adaptivity, illustrates

the enhanced resolution of the latter approach (Fig. 6.15-a). While the conventional approach inherits a measurement error of 75% in shock downstream velocity, adaptive interrogation settings combined with correlation window eccentricities in the order of 0.7 reduce this error to a mere 0.31%. Resolution improvements are further emphasized by the capability in adequately representing the velocity gradients across the Mach disk as illustrated by Fig. 6.15-b.

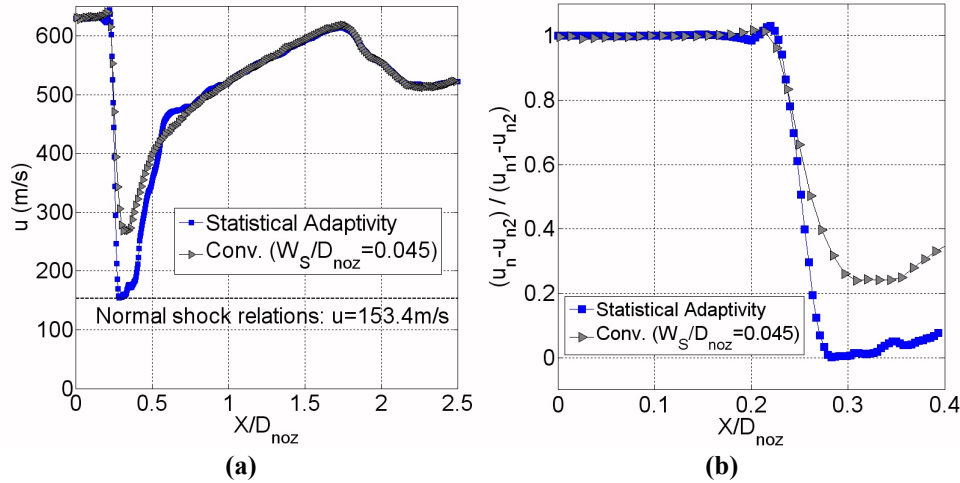


Fig. 6.15: Over-expanded jet (a) Average centerline ($Y/D_{noz}=0$) velocity measurements (b) shock normal velocity profiles obtained by the conventional interrogation procedure and the discussed approach with statistical adaptivity (u_{n2} has been set equal to the theoretical value of 153.4 m/s).

Across the incident oblique shock both interrogation approaches yield a ratio of particle relaxation distance to nozzle diameter of 0.0167 (Fig. 6.16-a). Normalized window sizes ' W_s/D_{noz} ' are in the order of 0.029 for the adaptive (cf. Fig. 6.11-d) and 0.045 for the conventional metrology. Because the hypothetical shock thickness of 0.046 nozzle diameters[†] is larger than, respectively nearly equal to the adopted the adopted correlation windows, the achieved resolution in measured velocity across the shock has been prescribed by respectively particle relaxation and interrogation window sizing. Supporting this conclusion, based on the (normal) shock velocity profile across the Mach disk measured by the adaptive evaluation an equal relaxation distance is obtained (Fig. 6.16-b). Once more the adopted window sizes of ' $W_s/D_{noz}=0.025$ ' are sufficiently small to conclude that the present enhancement in resolution by the adaptive technique can be attributed to the reduction in window size and augmented sampling. In case of the conventional image analysis on the other hand, the observed smoothing in the velocity

[†] Due to their finite response the tracer particles need 0.046 nozzle diameters downstream of the shock for the velocity to be reduced by a factor e^{-4} . This distance can be used as an estimate of the measured shock thickness although the real thickness is of course a couple of orders smaller (cf. Appendix B).

profile depicted in Fig. 6.15-b is caused by the enlarged interrogation window sizes ($W_s/D_{noz}=0.045$) and sampling spacing, not by particle inertia.

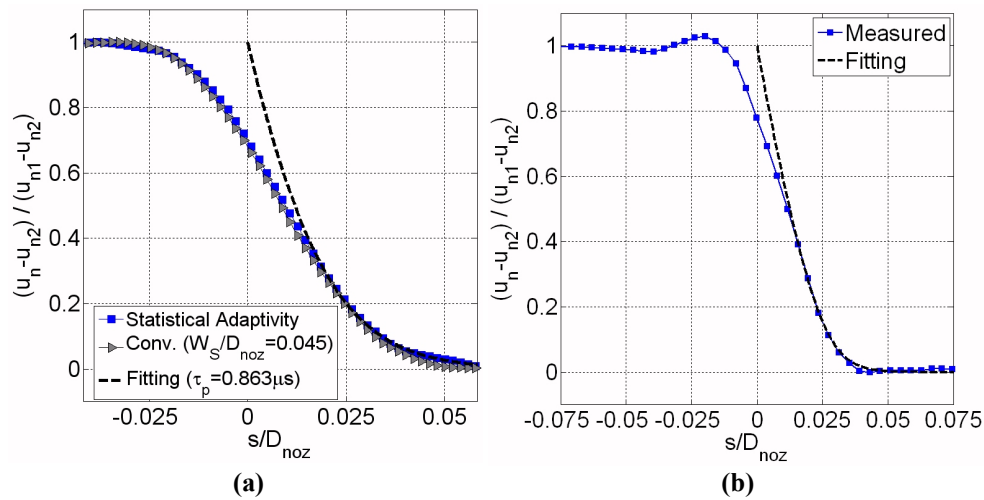


Fig. 6.16: Over-expanded jet (a) velocity profiles across the incident oblique shock near the nozzle exit (b) normal shock velocity profiles obtained by statistically adaptive interrogation.

In the vicinity of the second Mach disk the obtained results by the two image evaluation procedures were, although no results have been presented, almost identical despite a reduced correlation window size and eccentricity factor of around 0.4 imposed by the adaptive technique. Because of viscous effects the jet tends to subsonic, turbulent conditions with downstream distance. Following the first Mach disk the sequence of characteristic cells no longer contain a normal shock as indicated by the Schlieren image (Fig. 6.14-b) but yield a diffused interaction region of the oblique shocks. Consequently, steep gradients in velocity are no longer present.

6.5 Discussion

Besides optical resolution, particle spacing and particle relaxation time proved to be the defining limiting factor in spatial resolution on several occasions. They are moreover considered as the ultimate limits in achievable resolution. This is however mostly the case in academic environments where experiments are meticulously prepared to measure the largest dynamic spatial range possible. In the majority of less specialized experiments, the resolution related to image interrogation routine was previously dictated by (a) the correlation window sizes, set uniformly throughout the image and chosen properly to ensure sufficient robustness and (b) the vector spacing. Now adequate sizing and sampling alleviate the limits imposed by these interrogation parameters and omit the need of a trade-off between robustness and resolution.

Examining the case of the backward facing step flow several step heights downstream, direct improvements in terms of spatial resolution were not always very pronounced in the free flow. Here imaging and seeding conditions permitted the uniformly set interrogation parameters to yield the highest possible resolution without compromising robustness. However, coming to those settings requires a certain user expertise but is in the majority of cases the result of laborious trial and error. From this angle adaptivity offers benefits to both user-types. The amount of user interference is minimized however for what concerns the correlation window settings (size, overlap, eccentricity, orientation). In turn this, let's call it user friendliness, will make the utilization of PIV more attractive to a broader and often inexperienced public i.e. the industry. The user is offered a potential reduction in computational effort by minimizing the number of necessary interrogation windows thanks to flow adaptation while maintaining robustness and resolution. More important is the freedom allowed in spatial variation in window shape, which in case of present interfaces has been demonstrated conclusively to yield considerable improvements.

The idea of a completely autonomous interrogation routine must be omitted though since there will be continuous need for user input. Flow features of interest are rarely isolated events which complicates an automated identification of the image region of interest to analyze. The case of the supersonic over-expanded jet can be considered as a textbook example on conflicts in interest; while the turbulent shear layer was in this work of no importance it might have been in a different study. When subjected to scrutiny the proposed sampling distribution obtained from instant adaptivity (cf. Fig. 6.10-b) would have been ideal. The question then poses how to translate such dubious requirements into a single, generally valid adaptation criterion. The answer is quite simple; there is no such manner. After all, the next experimentalist in line might have slightly optimized the seeding by injecting tracers also in the outer jet flow with the intention of accurately characterizing only the mixing layer and has no interest in the shock pattern. A third one might be interested in correlating the spatial oscillation in Mach disk with the jet edge instabilities. Consider as a second example a PIV campaign held within an experimental wind tunnel facility. While the walls of a windtunnel allow in one experiment a boundary layer characterization they do not require special treatment when the same field of view contains an airfoil profile. Given such identical circumstances from an image point of view (equal seeding densities, illumination, recording device...), the disparate and often opposing interests of the user cannot be converted into a unique criterion such that the algorithm is able to automatically understand the user's interests in every specific situation. Instead, the proposed adaptivity criteria comply with typical user requirements; *in general* the boundary layer enveloping an interface needs to be well resolved, research *typically* focuses on turbulent flow characterized by velocity fluctuations, compressibility effects in supersonic flow *generally* require higher spatial resolution because they need to be well represented etc.

6.6 Conclusions

The adaptive interrogation routines proposed within this dissertation have been applied to the following experimental flows; a hypersonic sphere, a backward-facing step and a supersonic jet. Besides numerical and analytical references, the obtained results have been compared to those of conventional, uniform image evaluation.

In case of the hypersonic sphere at Mach 6, resolution across the bow shock was limited by tracer response and adaptivity did not yield any net improvement despite a reduction in number of utilized windows by a factor 2. Near the curved interface the adaptive approach returned nevertheless a more physical streamline pattern compared to the conventional approach.

Highest velocity gradients immediately behind the backward facing step were measured with the adaptive techniques on the account of enhanced spatial resolution. Statistical adaptivity revealed to be most adequate in estimating the production of turbulent kinetic energy. Because of proper seeding and lower amplitudes in velocity fluctuations improvements became marginal further downstream but with a beneficial reduction in number of correlation windows by a factor 4. The functionality of wall adaptivity was further illustrated by the ability to measure peaks in wall shear friction coefficient matching numerical simulations.

All adaptive methodologies had difficulties in properly sampling image recordings of the over-expanded supersonic jet as a result of a conflict in interest; poor signal quality vs. typical user requirements. Images were overall better evaluated by means of statistical adaptivity compared to instantaneous adaptivity owing to an enhanced sampling and window sizing. These benefits lead to improved measurement of the steep velocity gradient across shocks compared to uniform interrogation.

CHAPTER 7

STATISTICAL ANALYSIS OF PIV MEASUREMENTS[†]

Abstract

An original application to Time-Resolved PIV of an existing method for confidence level and error determination, called dependent bootstrapping is shown. Due to the high sampling frequencies the measured velocity samples are no longer uncorrelated making classical statistical procedures not applicable. Examples show that the various ways in calculating the number of independent samples based on the autocorrelation function question the reliability of the rarely, if ever, mentioned confidence levels in literature. Instead, the dependent bootstrapping technique reports consistent results of confidence estimates for both correlated and uncorrelated PIV velocity samples making this technique robust and general for further applications. The step-by-step description of the dependent circular block bootstrap implementation is given, including an estimator for the autocorrelation's randomness. The practical application and viability of the method are illustrated by two experimental cases.

Nomenclature

$1-\alpha$	confidence level
γ	measure of autocorrelation function noisiness
Δt	sampling time (seconds)
μ	estimated value of the true mean μ_x (arbitrary units)
μ_B	mean of the ensemble of bootstrap replications (arbitrary units)
μ_x	true mean of variable x (arbitrary units)
ξ	desired statistical parameter (arbitrary units)
ξ_{est}	statistical estimator of ξ (arbitrary units)
ρ_x	autocorrelation coefficient
σ	estimated value of the true standard deviation σ_x (arbitrary units)
σ_B	variance of the ensemble of bootstrap replications (arbitrary units)

[†] This work has been partly published in Theunissen *et al.*, 2008, Experiments in Fluids.

σ_x	true standard deviation of variable x (arbitrary units)
τ_{\max}	maximum time-lag in the calculation of the ρ_x (seconds or samples)
b	block length (samples)
B	number of bootstrap replications
erf	error-function
f(X)	probability density function of variable X
h	step height of the backward facing step (meter or pixels)
LSQ	Least-Squares
m_x^n	n^{th} order statistical moment of variable X
N	number of recorded samples
N_{eff}	number of recorded independent samples (effective sample size)
PDF	Probability Density Function
PIV	Particle Image Velocimetry
R	autocorrelation function
std	standard deviation
t	Student t-value
T	recording time (seconds)
T^*	integral time-scale (seconds)
X	observed variable (arbitrary units)

7.1 Introduction

Beside instantaneous velocity information, statistical descriptions can be extracted from the large number of analyzed PIV measurements. With the exception of turbulence-related research, these statistical quantities are very often limited to lower order moments[†], in particular the mean flow field and fluctuating flow field or standard deviation. A fundamental principle of experimental science is that no real measurement is infinitely precise, but instead must necessarily include a degree of uncertainty in the value. Indeed quantitative evaluations from PIV images suffer from various sources of corruption acting on the instantaneous displacement estimates. Among these are the obvious degenerations in image quality, measurement errors inherent to the applied correlation technique and effects originating from the finite extent of the interrogation windows. A possible indicator of the former are the readily available signal-to-noise ratios while the second error can only be assessed by means of computer generated PIV images with imposed displacement fields (e.g. McKenna and McGillis, 2002). Combined with well-defined experimental conditions, corrections can be inferred which attenuate the limitations in spatial resolution inherent to the PIV technique (Lavoie *et al.*, 2007). Eventually also the finite recording time and number of measurement repetitions play an

[†] the n^{th} order moment ‘ m_x^n ’ of a PDF ‘ $f(x)$ ’ is defined as
$$m_x^n = \int_{-\infty}^{+\infty} x^n f(x) dx .$$

important role which is often overlooked. The following analogy clarifies; measuring the outside temperature with an accurate or less precise thermometer in a region where the temperature fluctuates daily will either way yield an erroneous estimate of the average monthly temperature if the measurement is conducted one-off. Even if multiple measurements are performed, but in a short time span of e.g. 1 hour, the extracted mean will still not be conclusive. On the other hand, in a place with nearly no temperature variations, the single measurement will provide a good representation of the average temperature. Estimates of confidence levels and statistical error must therefore complement the description of the extracted statistical parameters to give an indication of their reliability.

Commonly used by the PIV community are standard expressions which follow large sampling (central limit) theory where the signal is conjectured to be normally distributed (Bendat and Piersol 1966, Benedict and Gould 1996). These express the uncertainty in the estimation of mean and standard deviation of a signal from a measurement to be related to the number of uncorrelated samples, the local level of signal fluctuation and to a given confidence percentile $(1-\alpha)$;

$$\mu_x = \mu \pm Z_\alpha \frac{\sigma_x}{\sqrt{N_{\text{eff}}}} \quad \text{and} \quad \sigma_x = \sigma \pm Z_\alpha \frac{\sigma_x}{\sqrt{2 \cdot N_{\text{eff}}}} \quad \text{and} \quad 1 - \alpha = \text{erf}\left(\frac{Z_\alpha}{\sqrt{2}}\right) \quad (7.1)$$

where N_{eff} refers to the number of uncorrelated samples. Given the local turbulence intensity σ_x/μ_x , the necessary number of independent samples to obtain a predefined fractional error and confidence level in the measurement of the statistical variables can be derived from (7.1) (Riethmuller and Lourenco, 1981), as depicted in Fig. 7.1. Note that justified on the account of dealing with large data sets, the signal's true standard deviation σ_x and mean μ_x can be replaced by their estimated values σ and μ in the expression of the confidence interval.

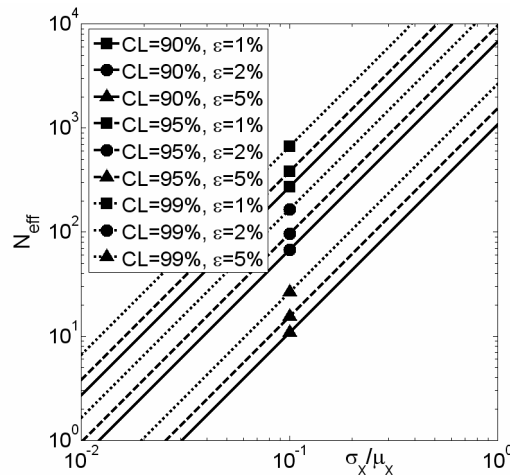


Fig. 7.1: Necessary effective sample size versus agitation level for varying confidence level and error percentages on the mean value estimate.

While these simplified equations are correct for typical turbulent flows having a normal shaped probability density (Tennekes and Lumley, 1972), Benedict and Gould (1996) report high inaccuracies when the probability distributions of the variables in question deviate from normality. Though normality can be easily verified by means of e.g. a Jarque-Bera test (Jarque and Bera, 1980), it is too often blindly assumed (Garcia *et al.*, 2006).

For general PIV applications where the characteristic flow time-scales lie below the typical laser's repetition time of the order of 0.1 second (Raffel *et al.*, 1998), ' N_{eff} ' is identical to the number of flow fields ' N ' (Grant *et al.* 1992). In cases where recorded flow behavior shows strong spatial dependence, temporal over-sampling concomitant to the larger flow-characteristic time-scales might occur and undermine this conjecture. Because recording images of the seeded flow at high sampling frequencies allows an accurate description of the signal both in the amplitude and time/frequency domain, Time-Resolved PIV (TR-PIV) has gained growing interest in the PIV community. As a consequence of the short time interval between image recordings the obtained flow fields can no longer be considered independent and ' N_{eff} ' remains to-be determined. The estimation of the undeterminable effective sample size is therefore considered to be of importance in future applications.

To estimate the number of independent samples from the recorded observation, information concerning the integral time-scale is necessary (Bruun, 1995). In literature a diversity exists in possible time-scale definitions, which may lead to error estimates varying as much as one order of magnitude when applied to a typical TR-PIV measurement. A first estimate of the time-scale can be made based on a dimensional analysis and Taylor's hypothesis. A diversity exists however in how to define the typical length-scale. In the case of the Backward Facing Step for example, the characteristic length-scale can be defined on the basis of the step height or the re-attachment length. The second method constitutes inferring the integral time scale ' T^* ' directly from estimates of the effective sample size ' N_{eff} ' using the sampling interval ' Δt ' as ' $T^* = N_{\text{eff}} \times \Delta t$ '. Thiébaux and Zwiers (1984) attempted a variety of techniques to determine the effective sampling size from the observed sequence. They concluded the precisions of the estimates to be dependent on the stochastic structure of the observed process and in some cases on the length of the available sample. Effective sample size estimations from the power spectrum showed a large diversity in precision and well-converged results in the low-frequency part were required in order to limit inaccuracies when extrapolating to zero frequency. The third and most common approach involves the autocorrelation function. In theory the time-scale can be determined from the integral of the autocorrelation function defined for an infinite number of time-lags, read recording time;

$$T^* = \int_0^{+\infty} \rho_x(\tau) \cdot d\tau \quad \text{and} \quad \rho_x(\tau) = \frac{R(\tau)}{R(0)} \quad (7.2)$$

In practice however the finite measurement time prohibits an autocorrelation extending to infinity. Furthermore, to obtain an unbiased estimate of the autocorrelation function, the

number of possible lags taken into account in the calculation of the autocorrelation is limited (Bruun, 1995). Denoting the number of samples contained within recording time 'T' by 'N' with sampling time-interval ' Δt ', expressions for the unbiased autocorrelation and coefficient are respectively

$$R(k\Delta t) = \frac{1}{N-k} \sum_{i=1}^{N-k} (X_i - \overline{X_N})(X_{i+k} - \overline{X_N}) \text{ and } \rho_x(k\Delta t) = \frac{R(k\Delta t)}{R(0)}$$

for $k=0 \dots \tau_{\max}/\Delta t$ where $\overline{X_N} = \frac{1}{N} \sum_{i=1}^N X_i$ (7.3)

Various alternative definitions have been proposed for the time-scale (Fig. 7.6): e.g. the time-lag needed by the autocorrelation to reach an amplitude of e^{-1} , the time lag at which the first zero is reached or the necessary number of lags to reach the minimum of the negative part of the correlation function (Tritton 1988; 'O'Neill *et al.* 2004). To demonstrate the diversity in resulting time-scales, time-resolved PIV measurements performed in air at a sampling frequency of 1.7kHz in a diverging channel are considered. The channel is 0.7m long with 0.079m hydraulic diameter at the inlet and 6 degrees total aperture angle. Further details on the setup can be found in Di Sante *et al.* (2008). The considered sample is recorded at a Reynolds number of 6300 (based on hydraulic diameter and mean velocity at the channel inlet), midway between inlet and outlet at 2.5mm from the lateral wall (i.e. pressure side). Figure 7.2 shows the velocity versus time in the turbulent boundary layer. The evolution of the integral time-scale ' T^* ' is shown in Fig. 7.3 as function of the sample length 'T'.

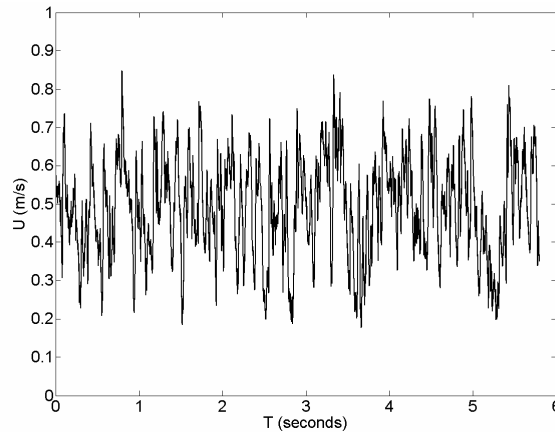


Fig. 7.2: Time history record of turbulent boundary layer velocity measurements performed at a sampling frequency of 1.7kHz in the diverging channel described by Di Sante *et al.* (2008).

The sensitivity of the time-scale estimate to the considered sampling time and number of applied time lags is indicated by the large scatter and variation in Fig. 7.3. Note that the integral of the autocorrelation could even lead to negative values of the integral time-

scale. Since the time-scale clearly cannot be based on the autocorrelation in a reliable way, the standard expressions for fractional error and uncertainty (Bendat and Piersol, 1966) mentioned in (7.1) will lead to very different results. In the best case convergence in mean values and decrease in the scatter around with sample size can be demonstrated to follow a power-function (Ullum *et al.*, 1998).

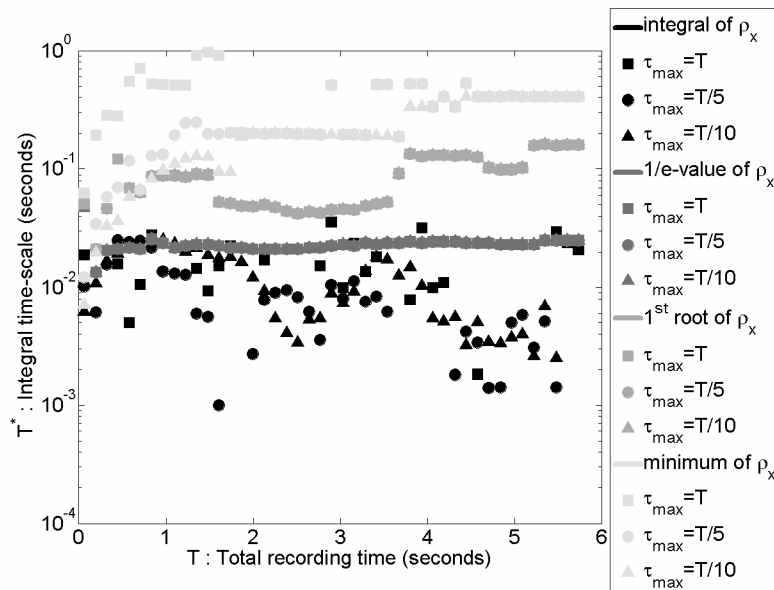


Fig. 7.3: Estimated integral time-scale ' T^* ' as a function of record length ' T ' and applied maximum time-lag ' τ_{max} ' in the calculation of the autocorrelation.

To circumvent the above bottlenecks, an original application of a technique is proposed, whose results have been shown to be consistent for any degree of correlation between the measured velocity samples. Commonly known as dependent bootstrapping in the econometric community (Politis and White, 2004), this resampling technique has to the best of the author's knowledge never been applied before to PIV data in the determination of error and confidence level.

In this chapter the dependent bootstrapping technique is first explained followed by a step-by-step description of the method of implementation. The applicability of the dependent bootstrapping technique is illustrated by two experimental cases involving correlated and uncorrelated PIV data.

7.2 Dependent circular block bootstrap

The basic idea behind bootstrapping is to replace the original sample record by numerous bootstrap replicates (typically larger than 1000 according to Garcia *et al.*, 2006) of the same length (Fig. 7.4). Each series consists of randomly selected samples

with replacement from the original observation. From each of the bootstrap series the parameter of interest is calculated, which allows an estimate of the parameter's probability distribution. As such, bootstrapping offers the possibility to calculate statistical moments with simultaneous errors and confidence levels provided that the recorded sample is a good approximation of the true signal distribution.

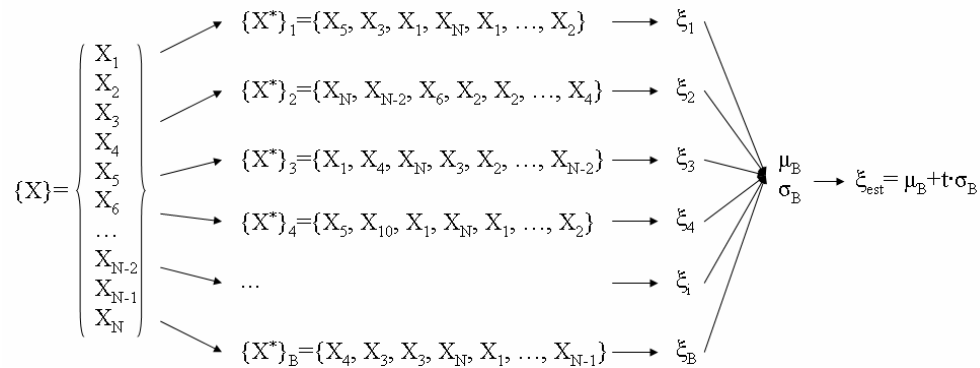


Fig. 7.4: Principle of bootstrapping. The statistical quantity ‘ ξ ’ is determined for each of the total ‘ B ’ generated pseudo-series $\{X^*\}$. From the collection of ‘ ξ_i ’ values, the mean and standard deviation of the ‘ ξ ’ distribution can be calculated and used in the estimation of the true ‘ ξ ’ value.

Convergence in the Fast Fourier Transform diagram can be used as indication for a sufficient cut-off time (Doebelin, 1990). The traditional simple bootstrap resampling scheme fails however to provide consistent results in the case of even weakly dependent processes (Singh, 1981). Künsch (1989) modified the bootstrap resampling algorithm to be applicable to correlated sample records; blocks of consecutive observations are selected rather than individual samples. This method of bootstrapping results in the lowest mean square errors in the variance compared to the other bootstrapping methodologies even for moderate sample sizes. As mentioned in Young (1994), the block length remained a crucial parameter to tune. Politis and White (2004) proposed an automatic procedure for its calculation compensating for the correlated nature of the original signal. Garcia *et al.* (2006) validated the moving block bootstrap with automatic block length calculation using both analytical data and experimental data and observed very good agreement. This method is hereafter applied to PIV data with the further improvement of implementing the circular block bootstrap (Politis and White, 2004). The latter methodology ensures all samples to have equal probability of being chosen.

7.3 Dependent circular bootstrap implementation

The summary of the practical implementation of the dependent circular block bootstrap procedure with automatic block length selection according to Politis and White (2004) is given hereafter. The procedure has been extended to include a possible, empirical, estimator of the autocorrelation's randomness. The quantization is based on strong

fluctuations yielding high second order derivatives with respect to the auto-correlation range.

- a. Calculation of the unbiased autocorrelation function 'R' of the signal (7.4). The maximum time-lag considered is half the sampling time since at higher lag number the autocorrelation becomes less accurate.
- b. Quantify the autocorrelation's randomness as

$$\gamma = \frac{\sum_{k=2}^{\tau_{\max}/\Delta t} |R(k\Delta t) - 2 \cdot R((k-1)\Delta t) + R((k-2)\Delta t)|}{(\max(R) - \min(R)) \cdot \left(\frac{\tau_{\max}}{\Delta t} - 3\right)} \quad (7.4)$$

When $\gamma > 0.1$ the autocorrelation suffers from a strong oscillating behavior, indicating a very low degree of correlation between the samples (see e.g. Fig. 7.8-a). A conservative unit block-length is opted for in that case ignoring steps 'c' and 'd'.

- c. Finding the smallest lag 'm' for which the 'K' consecutive values of the autocorrelation coefficient ' ρ_x ' satisfy $|\rho_x(m+k)| \leq c \left(\frac{\log N}{N}\right)^{1/2}$ with $k=0,1,\dots,K$ and $K = \max\left(5, (\log N)^{1/2}\right)$. The constant 'c' is generally set equal to two.
- d. Calculation of the optimal block length 'b';

$$b = N^{1/3} \left(\sqrt{6} \frac{\sum_{k=-2m}^{2m} \lambda\left(\frac{k}{2m}\right) \cdot k \cdot R(k)}{R(0) + 2 \sum_{k=-2m}^{2m} \lambda\left(\frac{k}{2m}\right) R(k)} \right)^{2/3} \quad (7.5)$$

$$\text{with } \lambda\left(\frac{k}{2m}\right) = \begin{cases} 1 & \text{if } 0 \leq \left|\frac{k}{2m}\right| \leq \frac{1}{2} \\ 2\left(1 - \left|\frac{k}{2m}\right|\right) & \text{if } \frac{1}{2} \leq \left|\frac{k}{2m}\right| \leq 1 \\ 0 & \text{otherwise} \end{cases}$$

- e. Construction of the wrapped data series $\{X_1, \dots, X_{N+b-1}\}$ where $X_{N+k} = X_k$
- f. Dividing the wrapped observation into 'N' consecutive blocks of length 'b'. Construction of 'B' pseudo series by selecting for each series 'N/b' blocks randomly and with replacement.
- g. Calculating for each series the parameter of interest ' ξ_i ' where $i=1,2,\dots,B$
- h. Calculation of the mean ' μ_B ' and variance ' σ_B^2 ' of the 'B' number of bootstrapped parameters ' ξ_i '.
- i. The estimate ' ξ_{est} ' of the true parameter value ' ξ ' is defined in (7.6) where 't' refers to the Student t-value (dependent of B) corresponding to a given bound in confidence.

$$\xi_{\text{est}} = \mu_B \pm t \cdot \sigma_B \quad (7.6)$$

Note that the above procedure may lead to an estimate of the effective sample size irrespective of the definition of integral time-scale by assuming equality[†] between the fractional error in first moment following from (7.1) and (7.6)

$$t \frac{\sigma_B}{\mu_B} = Z_\alpha \frac{\sigma}{\mu_B} \frac{1}{\sqrt{N_{\text{eff}}}} \rightarrow N_{\text{eff}} = \left(\frac{Z_\alpha \sigma}{t \sigma_B} \right)^2 \quad (7.7)$$

7.4 Practical examples

The implemented bootstrap methodology is a point-wise technique. To obtain an overall view of the statistical error and uncertainty of a complete field of view, the procedure referred to in the previous paragraph must be repeated at each sampling location, for which a collection of ‘N’ values are available from the set of instantaneous flow fields (Fig. 7.5). Without loss of generality the practical examples hereafter will concentrate however on the application to individual sampling positions.

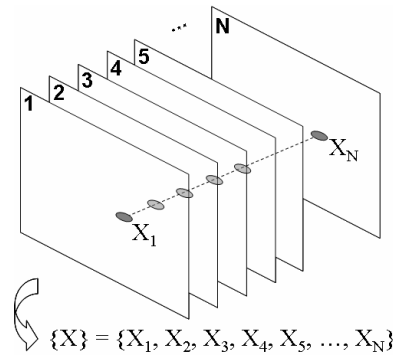


Fig. 7.5: For each sample point within the flow field ‘N’ realizations are available. For each collection of values the bootstrap technique must be applied.

7.4.1 Time-resolved PIV in a diverging channel flow

To demonstrate the efficacy and simplicity of the improved circular block bootstrap method, an error analysis for the above mentioned time-resolved sample record (see Fig. 7.2, total recording time of 5.74 seconds corresponding to around 10000 sample values) has been carried out. Figure 7.6-a presents the autocorrelation function where the locations corresponding to the different time-scale definitions mentioned in the

[†] this implicitly assumes the signal to have a Gaussian probability density distribution.

introduction (see also Fig. 7.3) are plotted for clarity. A decay of the autocorrelation coefficient, typical of turbulent velocity measurements (Tennekes and Lumley, 1972) can be observed.

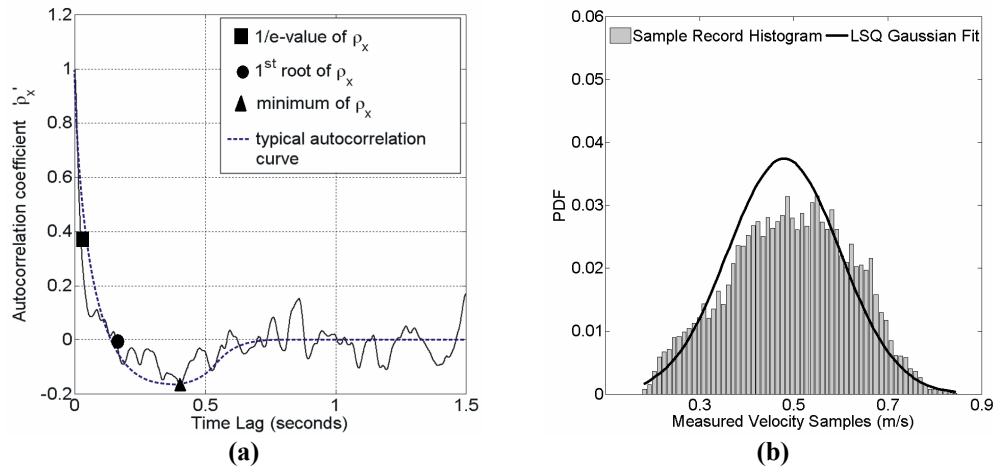


Fig. 7.6: (a) Autocorrelation function for the first 1.5 seconds time lag of the signal depicted in Fig. 7.1. The dashed line sketches a typical correlation shape of turbulent data. Symbols indicate the locations used to determine the various integral time-scales. (b) Histogram of the sample record of Fig. 7.1. The solid line represents a Least-Squares Gaussian fit of the histogram.

Table 7.1: Mean values and errors comparison for a TR-PIV sample. Quotes are in ‘m/s’.

Arithmetic mean	Standard Statistical Method				Bootstrap Method
	integral ($T^*=0.0210s$)	1/e ($T^*=0.0252s$)	1 st root ($T^*=0.1600s$)	1 st minimum ($T^*=0.4057s$)	
all samples	all samples				all samples
$0.4926 \pm ?$	$0.4958 \pm 4.3\%$	$0.4930 \pm 4.8\%$	$0.5467 \pm 10.6\%$	$0.6003 \pm 25\%$	$0.4925 \pm 3.9\%$

When using all samples in the computation of the arithmetic mean no error estimate can be assessed. Mean values and fractional error estimates, obtained from standard statistical methods (Riethmuller and Lourenco, 1981), show a large variation according to the different definitions of integral time-scale (table 7.1). Fractional errors, at 95% confidence level, ranged from $\pm 4.3\%$ to $\pm 10.6\%$ and even $\pm 25\%$, making the error determination to be depending on the arbitrary choice of the experimentalist. Furthermore, the histogram of the sample record (Fig. 7.6-b) clearly undermines the assumption of signal normality on which the standard methods are based. With bootstrapping on the other hand a mean value almost equal to the arithmetic mean was retrieved but with a single error estimate.

Following the circular block bootstrap procedure described in the third section, the block length was calculated automatically to be 247 samples. In total 3000 pseudo series (‘B’) were generated, resulting in a Gaussian distributed bootstrapped mean velocity (Fig. 7.7-a). The latter ensures the validity of a central-limit theorem for the considered statistic

of interest, while the decay in the autocorrelation function demonstrates the fulfillment of mixing conditions[†]. Combined, these two requirements ensure the validity of applying dependent block bootstrapping technique for the sample-mean statistic (Politis and White, 2004). The dependency of the bootstrap result on the number of bootstrap repetitions is presented in Fig. 7.7-b. Results in both mean and standard deviation of the bootstrap statistic's density distribution varied in the order of 10^{-4} m/s after 3000 repetitions, ensuring it to be a sufficient number to obtain a reliable estimate of the distribution.

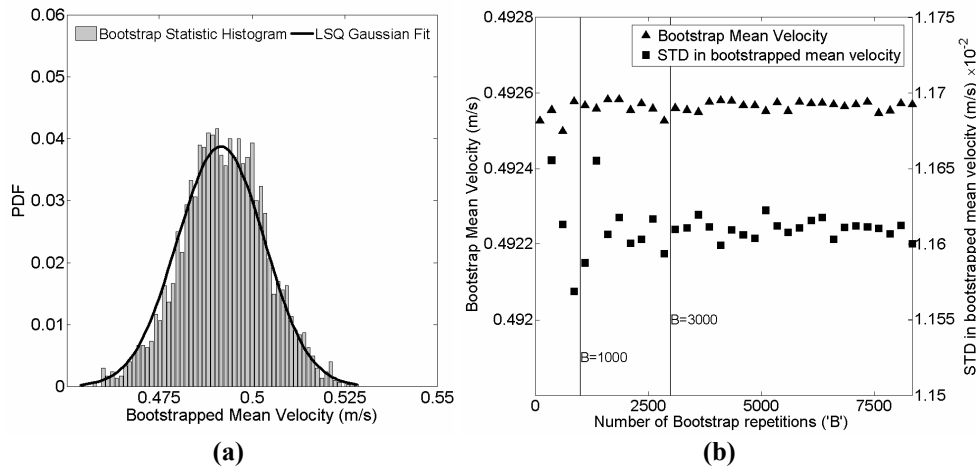


Fig. 7.7: (a) Histogram and Least-Squares Gaussian fit of the bootstrapped mean velocity (b) Evolution of the mean and standard deviation of the distribution of the bootstrapped statistic as a function of the number of bootstrap repetitions.

7.4.2 Classic PIV in a backward facing step flow

The generality of the bootstrap methodology is further assessed by applying it to the backward facing step flow at a step height-based Reynolds number of 5000 (cf. section 6.3). Using a classical (not time-resolved) PIV system, images were recorded at a frequency of 10Hz ensuring all measurements to be uncorrelated. A point inside the shear layer ($x/h=1$, $y/h=1$)[‡] has been selected. Independence between the observations is verified by the rapid decay of the sample record's autocorrelogram (Fig. 7.8-a). Based on Fig. 7.8-a, samples can be considered as uncorrelated when separated by at least one sampling interval (equal to 0.1 seconds). Under these conditions and given the signal's PDF to approach a normal distribution (Fig. 7.8-b), standard statistical methods are known to give reliable results.

[†] Loosely speaking mixing conditions imply processes with decaying auto-covariance function .

[‡] See point 'b' in Fig. A.3-a.

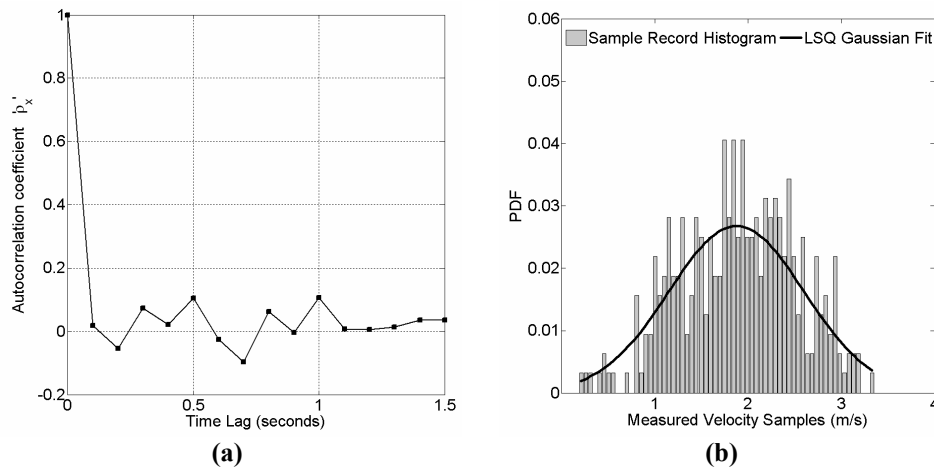


Fig. 7.8: Velocity measurements within the turbulent shear layer of a backward facing step with a classical PIV system (a) Autocorrelation function of the sample record (b) Histogram of the observations. The solid line represents a Least-Squares Gaussian fit of the histogram.

Both statistical techniques returned equivalent values (table 7.2) proving the block bootstrap method to yield consistent results, insensitive to the degree of correlation between the samples. The latter complies with the automatic selection of a block length ‘b’ equal to unity when proceeding according to paragraph 7.3. Slight differences between the techniques are to be ascribed to the strong parametric assumption concerning the signal (i.e. normality) by the common statistical technique. It should be clear that these differences will increase with the order of the statistical moment.

Table 7.2: Mean and maximum fractional error at 95% confidence level calculated for a backward facing step flow. Quotes are in ‘m/s’.

	Number of measurement samples involved in estimation				
	20	80	160	240	320
Bootstrap	1.7699 ± 10.1%	1.7314 ± 6.3%	1.8254 ± 4.3%	1.8463 ± 3.6%	1.8905 ± 3.0%
Standard	1.7709 ± 12.4%	1.7303 ± 7.8%	1.8249 ± 5.2%	1.8478 ± 4.3%	1.8904 ± 3.6%

For the sake of completeness the evolution of the bootstrap result of the mean velocity of all 320 samples as function of the number of bootstrap repetitions ‘B’ is presented in Fig. 7.9-a. Generation of 3000 pseudo data series corresponds again to a reasonable trade-off between computation time and sufficient number of samples for a reliable estimate of the bootstrapped statistic’s PDF. The bootstrapped mean velocity follows once more a Gaussian distribution (Fig. 7.9-b), which together with the fast decay of the correlogram permits dependent bootstrapping in the estimation of the true mean velocity and simultaneous uncertainties at given confidence levels (Politis and White, 2004).

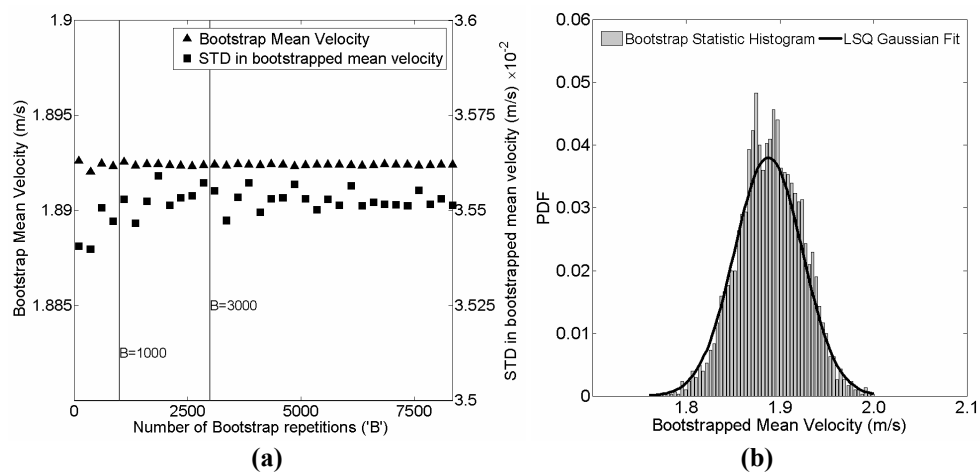


Fig. 7.9: (a) Evolution of the mean and standard deviation of the distribution of the bootstrapped statistic as a function of the number of bootstrap repetitions (b) Histogram and Least-Squares Gaussian fit of the bootstrapped mean velocity.

7.5 Conclusions

In conclusion, results obtained by dependent circular block bootstrapping with automatic block length selection have been shown to be insensitive to the degree of correlation between the samples thus proving to be a robust and globally applicable method in the statistical analysis of PIV data. Moreover the method does not require any parametric assumption concerning the signal and is consistent, in that error estimates decrease with increasing number of measurement samples.

CHAPTER 8

SUMMARY AND PERSPECTIVES

Abstract

This chapter contains a summary of the globally adaptive interrogation methodology and the accompanying achievements put forward in this dissertation. The current position of the approach with respect to existing techniques is discussed as well as its potentials. With more advanced measurement techniques the adaptivity criteria can be refined to be more robust. There is room for improvement in the sense that the level of adaptivity can be expanded but the philosophy of adaptive image interrogation has been substantiated to be a versatile and powerful concept offering many advantages. This assertion augurs and ascertains adaptive processing likely to become the next standardization in the near future of image velocimetry processing.

PIV has reached without doubt a mature level of standardization. Developments in both hardware and software do not stop and the technological advances give rise to ever more powerful variants of the image velocimetry metrology. These are accordingly subjected to experimental flow fields of growing intricacy. In view of such advancements it is considered worthwhile to discuss after a summary of the presented work, the potential and possible prospects of the adaptive interrogation philosophy put forward within this dissertation.

8.1 Summary

As an experimental tool, Particle Image Velocimetry has quickly superseded traditional point-wise measurements. The inherent image processing has become standardized though the performances are strongly dependent on user experience. Moreover, the arduously selected image interrogation parameters are applied uniformly throughout the image snapshots and image sequence but seldom comply with the observed fluid's convective motion, spatial distribution in length scales or signal distribution. Instead, a degree of adaptation in the image analyses is required to estimate

the velocity field underlying the image recordings as accurate as possible and preferably within an automated fashion.

A variety of correlation methodologies exist each conducive for specific cases. Here, the aim has been a global solution which through adaptivity of the interrogation parameters (window size, location and overlap) remains adequate in the majority of encountered problems. This dissertation proposes to go in line of a recursive approach autonomously adapting to both signal and flow conditions. Correlation window location, number and size are regulated taking into account seeding quantity and flow fluctuation magnitude; high image densities and/or regions with strong flow gradients lead to a clustering of smaller interrogation windows. Signal quantization is based on individual particle image segmentation while spatial variance in velocity served as a heuristic for flow adaptation. The implementation of the proposed technique further requires specialized interpolation schemes and sample projection techniques to account for the non-Cartesian sampling grid.

One of the main practical problems tackled is that of the user faced with a necessary trade-off between spatial resolution and robustness. The new interrogation method surpasses the compromise and places more and smaller windows where the flow requires it and seeding allows it. Vice versa, less of these unnecessary small windows are placed in regions where the flow does not require it (i.e. absence of gradients or fluctuations in velocity). As such mechanisms influencing correlation robustness i.e. lack in seeding or strong gradients, are decoupled. Performances of the adaptive approach were assessed by means of synthetic images of isotropic turbulence and experimental images of a turbulent shock-wave boundary layer interaction at Mach 2.1 and illustrated the improvements to be less pronounced in case of optimal recording conditions and optical resolution, albeit the limited user dependency offered a net improvement. However, the enhancements in spatial resolution were emphasized when applied to vortical flows behind a transport aircraft and a circular cylinder ($Re_D \approx 2000$) where vector spacing and window dimensions are pivotal in accurate vorticity education.

The second problem is posed in the vicinity of interfaces where large distortions are present in the correlation maps stemming from signal truncation across the walls and reflections. While adequate image pretreatment, advanced correlation schemes and vector repositioning ameliorate spatial resolution and robustness, the rigidity of the correlation windows in conventional correlation methodologies has been proven to be generally inappropriate. An innovative interface treatment has been proposed incorporating wall adaptivity in an automated manner by gradually increasing the sampling rate in the vicinity of the wall, rotating the correlation windows parallel to the interface and reducing wall-normal window sizes. When applied to original and morphed flat subsonic boundary layer images ($Re_\theta = 1900$) consistent improvements in resolution and robustness were obtained. Even more persuasive was the new ability to discern a recirculation zone near the corner of a double compression ramp in a hypersonic (Mach 7) flow, previously irresolvable by the conventional approach.

The interrogation approach with adaptation based on instantaneous conditions proved so far to yield convincing results especially in the presence of strong velocity gradients. Nevertheless, under circumstances such as sub-optimal flow seeding distribution and

large variations in the velocity field properties neither multi-grid techniques nor adaptive interrogation offer a robust estimate of the flow field. A variant of the spatially adaptive interrogation method is proposed that refines window size, shape, orientation and spatial distribution based on the ensemble averaged velocity field and image properties. The use of ensemble averaged properties enables the reliable application of non-isotropic resolution in contrast to the instantaneous adaptive approach where the latter is impracticable. This approach additionally allows to reduce the number of interrogation windows without overly compromising the measurement spatial resolution where needed. Application to a shock-wave boundary layer interaction flow demonstrated that the method correctly selects the regions where most measurement points need to be concentrated. A superior refinement ratio with respect to the instantaneous adaptivity was found. A dual-resolution experiment in the wake behind a transonic (Mach 0.6) airfoil confirmed that the spatial resolution in sheared regions can be significantly enhanced by the statistical adaptivity technique, which returned a momentum deficit in good agreement with reference data obtained in fully resolved conditions.

Further applications included within the dissertation elaborately assessed the enhanced performances of all adaptive interrogation methodologies discussed over conventional techniques. The image data sets consisted of an over-expanded supersonic jet (Mach 3.75), a hypersonic sphere (Mach 6) and rearward facing step ($Re_h \approx 5000$).

Extending the concept of statistical robustness, the application of a well-known statistical technique has been proposed for the extraction of mean data in PIV. The principle and proficiency were demonstrated through conventional PIV measurements of a backward facing step flow ($Re_h \approx 5000$) and time-resolved measurements in a diverging channel ($Re = 6300$).

8.2 Perspectives

8.2.1 PIV in the fast lane

The computational power of computers follows an exponential growth. At the rate of a doubling in computational performance about every two years, one is tempted to question the importance of the proposed doctoral work and stick with conventional routines while imposing an over-sampling.

The development in PIV hardware has not been dormant but has instead been boosting in performance owing to the unstoppable technological advancements. Lasers are becoming ever more powerful with decreasing pulse durations and are even capable of repetition rates of Mega- to Giga-Hertz. Owing to advanced electronics digital CCD cameras equipped with 2000×2000 pixels² sensor areas are becoming more common. Not only has the optical spatial resolution improved over the years, so has the temporal resolution. Conventional PIV systems based on Nd:YAG lasers and CCD cameras typically acquire flow information at a rate of 5 Hz. Now acquisition at rates up to 1000 times faster. High speed cameras are on the market allowing recording frequencies in the

order of 20000 frames per second. Albeit such magnitudes of frame grabbing frequencies are inherently at the cost of higher levels of shot noise and enlarged dimensions of the sensor elements, these cameras may soon be expected to have performances superior to present-day standards.

From this aspect, the amount of retrieved data also grows proportional with hardware capacity. Moreover, high repetition systems allow the extraction of time-derivates since the measurements are time-resolved and provide the necessary tools for space-time correlations, the temporal and 2D spatial tracking of coherent flow structure etc. While this aids in understanding the underlying flow phenomena, it also implies an extensive and time-consuming data post-processing, despite ever faster computers. Reduction of computational effort will therefore always remain pivotal, and as demonstrated, one possible way of achieving this goal has been identified as adequately sampling the flow with a reduced number of correlation windows. In addition, the optimized interrogation parameters will certainly improve spatial resolution and simultaneously the level of detail in which the investigated flow can be studied.

8.2.2 An everlasting yearn for more spatial resolution

When it comes to spatial resolution one tendency is clear; one can never have enough. The reason is straightforward; the higher the spatial resolution, the better one can resolve the smallest scales. One way of improving the optical resolution (i.e. the number of pixels per unit of distance) is the application of microscopes. Already long-distance microscopic PIV has shown a great potential for the measurement of very small flow scales and for high-resolution measurements of the velocity profile close to the wall. Even in these cases the significance of the chapter dealing with wall adaptivity retains its momentum as the importance of vector relocation and aligning the correlation windows with the wall interface were categorically illustrated.

While applying large magnifications factors is very suited to study isolated flow phenomena, the majority of PIV experiments involve sampling all flow scales simultaneously i.e. from the macro- to the micro-scale. Here an area of the size of the largest scale has to be observed with the resolution of the smallest scale. Wall adaptivity has already attested to be capable of improving robustness and resolution near interfaces but the consistent advances in digital resolution may provide a second solution. Large format cameras with up to 10 million pixels are already available on the market increasing the pixel to millimeter conversion ratio. Especially for industrial applications this is a more attractive solution since recordings may cover large fields of view with adequate resolution to resolve the smaller scales. The general limitations in spatial resolution inherent to PIV will still be present though. Tracers must be properly spaced though keeping in mind Nyquist's sampling criterion. Assuming the seeding quality to be appropriate, suitable processing parameters will be pivotal owing to the presence of a legion of flow scales; too large correlation windows with respect to the flow scale yield too strong modulation factors and especially strong velocity gradients require a high density of small correlation windows. This is only achievable by means of adaptive interrogation and is a valid assertion even for techniques touching the bounds of optical

resolution such as Microscopic PIV. From this point of view, the philosophy and ideas put forward within this dissertation will undoubtedly gain importance and always be advantageous to some degree.

8.2.3 Extended adaptivity

When images are of poor quality accuracy becomes inferior to robustness and a third adaptivity criterion is needed[†]. In case of sub-optimal PIV recordings, ensemble correlation has proven to be very efficient but when exactly do we use ensemble correlation? How do we know averaging the correlation maps works well when images are very noisy (low signal-to-noise), when seeding density is low (low concentration) or when the flow is expected to be rather stationary (low acceleration)? The answer is experience. Similarly, the experienced user knows that when tracer spacings ' λ_p ' are in the order of typical correlation window sizes, individual particle tracking will enhance the spatial resolution compared to statistical (i.e. correlation) operators[‡], but at the loss of some precision. Additionally, if hybrid tracking techniques are excluded because of the low seeding concentration, the tracer displacements ' Δx ' must be smaller than the spacing between tracers to restrict ambiguity in particle pairing. To retain a sufficient probability in detecting the individual particle image and with sufficient accuracy, the image noise must be within bounds (high signal-to-noise ratios). Neural networks can be trained to do the decision making for us (Grant and Pan, 1997) but a sequence of yet undefined criteria will be required to direct the network's choices. An exemplary flowchart capturing the tendencies mentioned above is outlined in Fig. 8.1 taking into account the source density ' N_s ', image density ' N_I ' (cf. Chapter 1), signal-to-noise ratio ' SNR ', flow acceleration ' u_{tt} ', particle displacement ' Δx ' and tracer spacing ' λ_p '.

Here adaptive interrogation may provide a relaxation in dependency on the a-priori unknown flow velocity and acceleration in that it is able to yield autonomously more robust velocity estimates with a higher resolution compared to conventional interrogation procedures. In turn, the selection of proposed interrogation procedures in Fig. 8.1 can be reached within a recursive structure where the adaptive routine encompasses all techniques. Statistical adaptivity already attested to be suitable under sub-optimal conditions and it will only be a slight step to further incorporate particle tracking. Given that acceleration, concentration and image quality may show spatial variations throughout an image, so will the eventually adopted correlation technique (standard vs. ensemble correlation, window vs. single point ensemble correlation, correlation vs. particle tracking) thus adding an extra degree of adaptivity.

[†] The first two criteria refer to flow and signal adaptivity

[‡] Recall that the need of in average at least 7 particle image doublets per correlation window to retrieve reliable correlation functions (Keane and Adrian, 1992) directly prescribes the lower bound in window size.

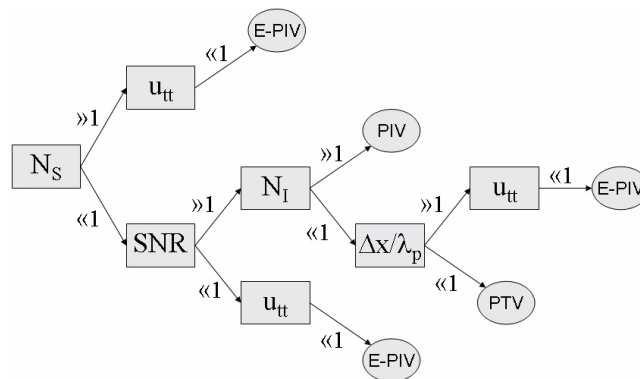


Fig. 8.1: Example flowchart relating imaging, seeding and flow conditions to the preferential correlation technique (E-PIV stands for Ensemble PIV).

Not only PIV hardware undergoes evolution, but also the PIV technique itself. In his quest to understand the physics behind his observations the experimentalist has unrelentingly attempted to maximize the information quantity extractable from the PIV measurements. Seeing that originally the PIV technique yielded two velocity components within a plane while the majority of applications involve fully three dimensional motion and temporal evolutions, a multitude of PIV variants have arisen such as Stereo-PIV to measure the third velocity component and Time-Resolved PIV to have temporal resolution. The principle of all the techniques remains the same however; extracting information from the recordings. Concomitantly, the proposed philosophy of adapting the image interrogation to both flow and seeding conditions remains applicable. The advantage of the improved techniques with respect to their classical variant is the availability of additional information to make the adaptive procedure more robust.

In time-resolved PIV use is already made of the temporal resolution to enhance the measurement dynamic range and accuracy (Hain and Kähler, 2006). In stereoscopic PIV two cameras image the illuminated flow particles from different angles, which may aid in the signal quantization since the influence of random camera noise can be minimized. Moreover, quantitative estimates of the out-of-plane velocity may be incorporated in adequate sampling of the flow. The more out-of-plane motion, the larger the correlation windows since the inherent loss of tracers degrades the correlation signal and consequently the measurement reliability and accuracy. Such a procedure where the correlation windows are adapted to the measurement error and velocity gradients has already been proposed by Becker *et al.* (2008). Combining such an approach with signal adaptivity will be arduous though because of user ambiguity coming back into play; one user is keen on retaining accurate measurements even if it means sacrificing resolution while another praises resolution despite a loss in accuracy.

8.2.4 Adaptivity philosophy in 3D

The main limiting factor for the planar approach consists in the fact that the motion across the plane cannot be represented as accurately as the motion within the plane. This

drawback, and because of the technological advances in PIV hardware, has led to the development of the 3D (or 4D) metrology (time-resolved) tomographic PIV (Elsinga *et al.*, 2006). This technique yields a fully three-dimensional representation of the velocity field related to the observed phenomenon. In view of the sparse nature of the seeding distribution in Tomo PIV and the possibility of a fully three dimensional flow characterization, the adaptivity criteria proposed within this thesis may yield an improvement in the 3D spatial resolution which currently is rather limited. Moreover, as adequate sampling locations can be chosen, the number of correlation volumes can be reduced which leads to a further decrease in computational time. In the 2D PIV variant, the adaptive algorithm is currently based on seeding concentration estimates obtained from an identification of the individual particle images. These estimates are not trivially obtained from the reconstructed tomographic particle image distributions due to parasitic reconstruction artifacts in the form of so called ghost particles. Without doubt these will introduce erroneous concentration estimates leading to false boundaries in sampling volumes. Therefore it is essential to define a signal adaptivity criterion based on a different set of criteria rather than counting individual particles. Furthermore, in planar PIV the velocity gradients are a good measure of the involved flow length scales. Tomographic PIV results contain a fully three dimensional representation of the flow velocity distribution which allows flow adaptation to be more precise if the related criteria are redefined.

Further accuracy and resolution improvements are expected by extending (now standard) 2D processing schemes to volume processing. Such a line of thought is followed in Appendix C where the feasibility of 3D weighting functions is investigated.

REFERENCES

- Abu-Gharbieh R, Hamerneh G, Gustavsson T and Kaminski C F, 2001, Flame front tracking by laser induced fluorescence spectroscopy and advanced image analysis, *Optics Express*, 8, 278-287
- Adrian R J and Yao C-S, 1984, Development of pulsed laser velocimetry (PLV) for measurement of turbulent flow, *In: Proceedings of the eighth Symp. on turbulence*, September 1983, ed. Reed X B, Patterson Jr. G K and Zakin J L, 170-186
- Adrian R J, 1991, Particle-imaging techniques for experimental fluid mechanics, *Annual review of Fluid Mechanics*, 23, 261-304
- Adrian R J, 1997, Dynamic ranges of velocity and spatial resolution of particle image velocimetry, *Measurement Science and Technology*, 8, 1393-1398
- Adrian R J, Christensen K T, Soloff S M and Meinhart C D, 1998, Decomposition of turbulent fields and visualization of vortices and turbulent momentum transport, *8th Int. Symp. on Flow Visualization*, Sorrento, Italy, 01-04 September
- Adrian R J, 2005, Twenty years of particle image velocimetry, *Experiments in Fluids*, 39, 159-169
- Agüí J C and Jiménez J, 1987, On the performance of particle tracking, *Journal of Fluid Mechanics*, 185, 447-468
- Amidor I, 2002, Scattered data interpolation methods for electronic imaging systems: a survey, *Journal of Electronic Imaging*, 11-2, 157-176
- Ashok A, Ragni D, van Oudheusden B W and Scarano F, 2008, Transonic airfoil aerodynamic characterization by means of PIV, *In: 14th Int. Symp. on application of laser techniques to fluid mechanics*, Lisbon, Portugal, 07-10 July
- Astarita T and Cardone G, 2005, Analysis of interpolation schemes for image deformation methods in PIV, *Experiments in Fluids*, 38, 233-243
- Astarita T, 2007, Analysis of weighting windows for image deformation methods in PIV, *Experiments in Fluids*, 43, 859-872
- Astarita T, 2009, Adaptive space resolution for PIV, *Experiments in Fluids*, 46, 1115-1123
- Baivier C, 2006, Adaptation de la technique de vélocimétrie par images de particules à l'étude d'écoulements à grande échelle : validation expérimentale, *Final year thesis*, Université de Liège and von Karman Institute for Fluid Dynamics
- Balakumar B J and Adrian R J, 2004, Particle-image velocimetry measurement in the exhaust of a solid rocket motor, *Experiments in Fluids*, 36, 166-175

- Baldi S and Yianneskis M, 2004, On the quantification of energy dissipation in the impeller stream of a stirred vessel from fluctuating velocity gradient measurements, *Chemical Engineering Science*, 59, 2659-2671
- Ball K O W and Korkegi R H, 1968, An investigation of the effect of suction on hypersonic laminar boundary-layer separation, *AIAA Journal*, 6, 239-243
- Becker F, Wieneke B, Yuan J and Schnörr C, 2008, Variational correlation approach to flow measurement with window adaptation, *In: 14th Int. Symp. on laser applications to fluid mechanics*, Lisbon, Portugal, 7-10 July
- Beloki Perurena J, Asma C O, Theunissen R and Chazot O, 2008, Experimental investigation of liquid jet injection into Mach 6 hypersonic crossflow, *Submitted to Experiments in Fluids*
- Bendat J S and Piersol A G, 1966, Measurement and Analysis of Random Data, New-York, John Wiley & Sons
- Benedict L H and Gould R D, 1996, Towards better uncertainty estimates for turbulence statistics, *Experiments in Fluids*, 22, 129-136
- Billig F S, 1967, Shock-wave shapes around spherical- and cylindrical-nosed bodies, *Journal of spacecraft and rockets*, 4, 822-823
- Boillot A and Prasad A K, 1996, Optimization procedure for pulse separation in cross-correlation PIV, *Experiments in Fluids*, 21, 87-93
- Brücker C, 1997, 3-D scanning PIV applied to an airflow in a motored engine using digital high-speed video, *Measurement Science and Technology*, 8, 1480-1492
- Bruun H H, 1995, Hot-wire Anemometry – Principles and Signal Analysis, Oxford University Press, 405-445
- Christensen K T, 2004, The influence of peak-locking errors on turbulence statistics computed from PIV ensembles, *Experiments in Fluids*, 36, 484-497
- Cohn R and Koochesfahani M M, 2000, The accuracy of remapping irregularly spaced velocity data onto a regular grid and the computation of vorticity, *Experiments in Fluids*, 29, 61-69
- Cowen E A and Monismith S G, 1997, A hybrid digital particle tracking velocimetry technique, *Experiments in Fluids*, 22, 199-211
- Depardon S, Lasserre J J, Boueilh J C, Brizzi L E and Borée J, 2005, Skin friction pattern analysis using near-wall PIV, *Experiments in Fluids*, 39, 805-818
- Devlin K J, 2002, The millennium problems: the seven greatest unsolved mathematical puzzles of our time, Basic Books, 131-155
- Di Florio D, Felice F D and Romano G P, 2002, Windowing, reshaping and re-orientation interrogation windows in particle image velocimetry for the investigation of shear flows, *Measurement Science and Technology*, 13, 953-962
- Di Sante A, Theunissen R and Van den Braembussche R A, 2008, A new facility for time-resolved PIV measurements in rotating channels, *Experiments in Fluids*, 44, 179-188
- Dodgson N A, 1997, Quadratic interpolation for image resampling, *IEEE Transactions on Image Processing*, 6-9, 1322-1326
- Doebelin E O, 1990, Measurement Systems – Application and Design, Fourth Edition, McGraw Hill, 169-182

- Dong S and Meng H, 2001, Chebyshev spectral method and Chebyshev noise processing procedure for vorticity calculation in PIV post-processing, *Experimental Thermal and Fluid Science*, 24, 47-59
- Elsinga G E, Kuik D J, van Oudheusden B W and Scarano F, 2007, Investigation of the three-dimensional coherent structures in a turbulent boundary layer, *45th AIAA Aerospace Sciences Meeting*, Reno, NV, USA, AIAA-2007-1305
- Elsinga G E, Scarano F, Wieneke B, van Oudheusden B W, 2006, Tomographic particle image velocimetry, *Experiments in Fluids*, 41, 933-947
- Elsinga G E, van Oudheusden B W and Scarano F, 2005, Evaluation of aero-optical distortion effects in PIV, *Experiments in Fluids*, 39, 246-256
- Etabari A and Vlachos P P, 2005, Improvements on the accuracy of derivative estimation from DPIV velocity measurements, *Experiments in Fluids*, 39, 1040-1050
- Fawcett P A and Komerath N M, 1991, Spatial correlation velocimetry in unsteady flows, *In: 29th Aerospace sciences meeting AIAA91-0271*, Reno, Nevada, USA, 7-10 January
- Flack R D Jr, 1975, The application of a Laser Doppler Velocimeter (LDV) in interpreting turbulent structure, PhD Thesis, Purdue University, West Lafayette
- Fletcher A J P, Ruban A I and Walker J D A, 2004, Instabilities in supersonic compression ramp flow, *Journal of Fluid Mechanics*, 517, 309-330
- Fore L B, Tung A T, Buchanan J R and Welch J W, 2005, Nonlinear temporal filtering of time-resolved digital particle image velocimetry data, *Experiments in Fluids*, 39, 22-31
- Foucaut J M and Stanislas M, 2002, Some considerations on the accuracy and frequency response of some derivative filters applied to particle image velocimetry vector fields, *Measurement Science and Technology*, 13, 1058-1071
- Fouras A and Soria J, 1998, Accuracy of out-of-plane vorticity measurements derived from in-plane velocity field data, *Experiments in Fluids*, 25, 409-430
- Garcia C M, Jackson P R and Garcia M H, 2006, Confidence intervals in the determination of turbulence parameters, *Experiments in Fluids*, 40, 514-522
- Garcia S A P, van Beeck J, Rambaud P and Olivari D, 2002, Numerical and experimental modeling of pollutant dispersion in a street canyon, *Journal of Wind Engineering and Industrial Aerodynamics*, 90, 321-329
- Graftieaux L, Michard M and Grosjean N, 2001, Combining PIV, POD and vortex identification algorithms for the study of unsteady turbulent swirling flows, *Measurements Science and Technology*, 12, 1422-1429
- Grant I and Pan X, 1997, The use of neural techniques in PIV and PTV, *Measurement Science and Technology*, 8, 1399-1405
- Grant I, Owens E and Yan Y Y, 1992, Particle image velocimetry measurements of the separated flow behind a rearward facing step, *Experiments in Fluids*, 12, 238-244
- Guezennec Y G and Kiritsis N, 1990, Statistical investigation of errors in particle image Velocimetry, *Experiments in Fluids*, 10, 138-146
- Gui L and Merzkirch W, 2000, A comparative study of the MQD method and several correlation-based PIV evaluation algorithms, *Experiments in Fluids*, 28, 36-44
- Gui L and Wereley S T, 2002, A correlation-based continuous window-shift technique to reduce the peak-locking effect in digital PIV image evaluation, *Experiments in Fluids*, 32, 506-517

- Gui L, Wereley S T and Kim Y H, 2003, Advances and applications of the digital mask technique in particle image velocimetry experiments, *Measurement Science and Technology*, 14, 1820-1828
- Haertig J, Havermann M, Rey C and George A, 2002, Particle image velocimetry in Mach 3.5 and 4.5 shock-tunnel flows, *AIAA Journal*, 40, 1056-1060
- Haertig J, Havermann M, Rey C and George A, 2005, Application of Particle Image Velocimetry to high-speed supersonic flows, *In: PIVNET II Int. workshop on the application of PIV in compressible flows*, Delft, The Netherlands, 6-8 June
- Hain R and Kähler C J, 2007, Fundamentals of multiframe particle image velocimetry (PIV), *Experiments in Fluids*, 42, 575-587
- Hall E L, 1979, Computer image processing and recognition, Academic Press, New York, 88-94
- Hart D P and Meinhart C, 2003, Improved SNR by combining ensemble averaging and zero-order correlation, *In: FEDSM'03 4th ASME JSME Joint Fluids Engineering Conference*, Honolulu, Hawaii, USA, 6-11 July
- Hassan Y A and Canaan R E, 1991, Full-field bubbly flow velocity measurements using a multiframe particle tracking technique, *Experiments in Fluids*, 12, 49-60
- Havermann M, Rey C and Haertig J, 2002, Application de la PIV à l'étude des écoulements à très haute vitesse produits par une soufflerie à choc, *In: 8^{ième} Congres francophone de vélocimétrie laser*, Orsay, France, 17-20 September
- He X C and Yung N H C, 2008, A corner detector based on global and local curvature properties, *Optical Engineering*, 47, DOI 10.1117/1.2931681
- Hecht E, 2002, Optics-4th edition, Addison Wesley Longman Inc.
- Heinz O M, Ilyushin B B and Markovich D M, 2002, PIV-data validation algorithm based on statistical analysis for ensemble of turbulent velocity fields, *In: 11th Int. Symp. on applications of laser techniques to fluid mechanics*, Lisbon, Portugal, 8-11 July
- Honkanen M and Nobach H, 2005, Background extraction from double-frame PIV images, *Experiments in Fluids*, 38, 348-362
- Huang H T, Fiedler H E and Wang J J, 1993a, Limitation and improvement of PIV part I: limitation of conventional techniques due to deformation of particle image patterns, *Experiments in Fluids*, 15, 168-174
- Huang H T, Fiedler H E and Wang J J, 1993b, Limitation and improvement of PIV part II: particle image distortion, a novel technique, *Experiments in Fluids*, 15, 263-273
- Huang H, Dabiri D and Gharib M, 1997, On errors of digital particle image velocimetry, *Measurement Science and Technology*, 8, 1427-1440
- Humble R A, Scarano F, van Oudheusden B W and Tuinstra M, 2006, PIV measurements of a shock wave/turbulent boundary layer interaction, *In: 13th Int. Symp. on applications of laser techniques to fluid mechanics*, Lisbon, Portugal, 26-29 June,
- Humble R A, Scarano F, van Oudheusden B W, 2007, Particle image velocimetry measurements of a shock wave/turbulent boundary layer interaction, *Experiments in Fluids*, 43, 173-183

- Isomoto K and Honami S, 1989, The effect of inlet turbulence intensity on the reattachment process over a backward-facing step, *Journal of Fluid Mechanics*, 111, 87-92
- Jarque C M and Bera A K, 1980, Efficient tests for normality, homoscedacity and serial independence of regression residuals, *Economics Letters*, 6, 255-259
- Jeong J and Hussain F, 1995, On the identification of a vortex, *Journal of Fluid Mechanics*, 285, 69-94
- Jerónimo A, Riethmuller M L and Chazot O, 2002, PIV application to Mach 3.75 overexpanded jet, *In: 11th Int. symp. on application of laser techniques to fluid mechanics*, Lisbon, Portugal, 8-11 July
- Jiménez J and Agüí J C, 1987, Approximate reconstruction of randomly sampled signals, *Signal Processing*, 12, 153-168
- Jonassen D R, Settles G S and Tronosky M D, 2006, Schlieren "PIV" for turbulent flows, *Optics and Lasers in Engineering*, 44, 190-207
- Jones N L, Davis R J and Sabbah W, 2003, A comparison of three-dimensional interpolation techniques for plume characterization, *Ground Water*, 41-4, 411-419
- Jovic S and Driver D M, 1994, Backward-facing step measurements at low Reynolds number, $Re_h=5000$, *NASA Technical Memorandum 108807*
- Kähler C and Scholz U, 2006, Transonic jet analysis using long-distance micro-PIV, *In: 12th Int. Symp. on flow visualization*, Göttingen, Germany, 10-14 September
- Kähler C J, Sholz U and Ortmanns J, 2006, Wall-shear-stress and near-wall turbulence measurements up to single pixel resolution by means of long-distance micro-PIV, *Experiments in Fluids*, 41, 327-341
- Katkovnik V, Egiazarian K and Astola J, 2002, Adaptive window size image de-noising based on intersection of confidence intervals (ICI) rule, *Journal of Mathematical Imaging and Vision*, 16, 223-235
- Keane R D and Adrian R J, 1990, Optimization of particle image velocimeters. Part I: double pulsed systems, *Measurement Science and Technology*, 1, 1202-1215
- Keane R D and Adrian R J, 1992, Theory of cross-correlation analysis of PIV images. *Applied Scientific Research*, 49, 191-215
- Keane R D, Adrian R J and Zhang Y, 1995, Super-resolution particle imaging velocimetry, *Measurement Science and Technology*, 6, 754-768
- Khoo B C, Chew Y T and Li G L, 1997, Effects of imperfect spatial resolution on turbulence measurements in the very near-wall viscous sublayer region, *Experiments in Fluids*, 22, 327-335
- Kim B J and Sung H J, 2006, A further assessment of interpolation schemes for window deformation in PIV, *Experiments in Fluids*, 41, 499-511
- Klebanoff P S, 1955, Characteristics of turbulence in a boundary layer with zero pressure gradient, *Naca Report 1247*
- Korolev G L, Gajjar J S B and Ruban A I, 2002, Once again on the supersonic flow separation near a corner, *Journal of Fluid Mechanics*, 463, 173-199
- Kostas J, Soria J and Chong M S, 2002, Particle image velocimetry measurements of a backward-facing step flow, *Experiments in Fluids*, 33, 838-853

- Kundu P K and Cohen I M, 2002, Fluid Mechanics – second edition, Elsevier Science (USA)
- Künsch H, 1989, The jackknife and the bootstrap for general stationary observations, *Annals of Statistics*, 17, 1217-1241
- Lavoie P, Avallone G, De Gregorio F, Romano G P and Antonia R A, 2007, Spatial resolution of PIV for the measurement of turbulence, *Experiments in Fluids*, 43, 39-51
- Le H, Moin P and Kim J, 1997, Direct numerical simulation of turbulent flow over a backward-facing step, *Journal of Fluid Mechanics*, 330, 349-374
- Lecordier B and Trinité M, 2003, Advanced PIV algorithms with image distortion validation and comparison using synthetic images of turbulent flow, *In: 5th Int. Symp. on particle image velocimetry*, Busan, Korea, 22-24 September
- Lecordier B and Trinité M, 2006, Accuracy assessment of image interpolation schemes for PIV from real images of particles, *In: 13th Int. Symp. on Applications of laser techniques to fluid mechanics*, Lisbon, Portugal, 26-29 June
- Lecordier B, Demare D, Vervisch L M J, Réveillon J and Trinité M, 2001, Estimation of the accuracy of PIV treatments for turbulent flow studies by direct numerical simulation of multi-phase flow, *Measurement Science and Technology*, 12, 1382-1391
- Lecordier B, Lecordier J C and Trinité M, 1999, Iterative sub-pixel algorithm for the cross-correlation PIV measurements, *In: 3rd Int. Workshop on PIV 99*, Santa-Barbara, USA, 16-18 September
- Lehmann T M, Gönner C and Spitzer K, 2001, Addendum: B-spline interpolation in medical image processing, *IEEE Transactions on Medical Imaging*, 20-7, 660-665
- Lienhard, J, 1966, Synopsis of Lift, Drag, and Vortex Frequency Data for Rigid Circular Cylinders, Washington State University, College of Engineering Bulletin No. 300
- Lin H J and Perlin M, 1998, Improved methods for thin, surface boundary layer investigations, *Experiments in Fluids*, 25, 431-444
- Lindeberg T, 1993, On scale selection for differential operators, *In: 8th Scandinavian Conference on Image Analysis*, Tromso, Norway, 25-28 May
- Lindken R and Merzkirch W, 2002, A novel PIV technique for measurements in multi-phase flows and its application to two-phase bubbly flows, *Experiments in Fluids*, 33, 814-825
- Lindken R, Poelma C and Westerweel J, 2003, Compensation for spatial effects for non-uniform seeding in PIV interrogation by signal relocation, *In: 5th Int. Symp. on particle image velocimetry*, Busan, Korea, 22-24 September
- Lourenco L and Krothapalli A, 1995, On the accuracy of velocity and vorticity measurements with PIV, *Experiments in Fluids*, 18, 421-428
- Lourenco L M and Krothapalli A, 2000, True resolution PIV: a mesh-free second-order accurate algorithm, *In: 10th Int. Symp. on applications of laser techniques in fluid mechanics*, Lisbon, Portugal, 10-13 July
- Lourenco L, 2000, Recent methods and current trends in PIV data processing, *In: Particle image velocimetry and associated techniques, von Karman Institute for Fluid Dynamics Lecture Series*, ed.: Riethmuller M L, 17-21 January
- Love E S, Grigsby C E, Lee L P and Woodling M J, 1959, Experimental and theoretical studies of axisymmetric free jets, *NASA Technical Report R-6*

- Lucas B D and Kanade T, 1981, An iterative image registration technique with an application to stereo vision, *In: Proceedings DARPA Image Understanding Workshop*, April 1981, 121-130
- Luff J D, Drouillard T, Rompage A M, Linne M A and Hertzberg J R, 1999, Experimental uncertainties associated with particle image velocimetry (PIV) based vorticity algorithms, *Experiments in Fluids*, 26, 36-54
- Malik N A, Dracos T and Papantoniou D A, 1993, Particle tracking velocimetry in three-dimensional flows – Part II: particle tracking, *Experiments in Fluids*, 15, 279-294
- Marxen M, Sullivan P E, Loewen M R and Jähne B, 2000, Comparison of Gaussian particle center estimators and the achievable measurement density for particle tracking velocimetry, *Experiments in Fluids*, 29, 145-153
- McKenna S P and McGillis W R, 2002, Performance of digital image velocimetry processing techniques, *Experiments in Fluids*, 32, 106-115
- Meinhart C D, Wereley S T and Santiago J G, 2000, A PIV algorithm for estimating time-averaged velocity fields, *Journal of Fluids Engineering*, 122,
- Melling A, 1997, Tracer particles and seeding for particle image velocimetry, *Measurement Science and Technology*, 8, 1406-1416
- Meynart R, 1983, Instantaneous velocity field measurements in unsteady gas flow by speckle velocimetry, *Applied Optics*, 22-4, 535-540
- Miozzi M, 2005, Direct measurement of velocity gradients in digital images and vorticity evaluation, *In: 6th Int. Symp. on Particle Image Velocimetry*, Pasadena, California, USA, 21-23 September
- Mitchell D P and Netravalli A N, 1988, Reconstruction filters in computer graphics, *Computer graphics*, 22-4, 221-228
- Nogueira J, Lecuona A and Rodríguez P A, 1999, Local field correction PIV: on the increase of accuracy of digital PIV systems, *Experiments in Fluids*, 27, 107-116
- Nogueira J, Lecuona A and Rodríguez P A, 2001, Identification of a new source of peak locking, analysis and its removal in conventional and super-resolution PIV techniques, *Experiments in Fluids*, 30, 309-316
- Nogueira J, Lecuona A, Rodríguez P A, Alfaro J A and Acosta A, 2005, Limits on the resolution of correlation PIV iterative methods. Practical implementation and design of weighting functions, *Experiments in Fluids*, 39, 314-321
- Norman M L and Winkler K-H A, 1985, Supersonic jets, *Los Alamos Science*, 12, 38-72
- 'O'Neill P L, Nicolaidis D, Honnery D and Soria J, 2004, Autocorrelation functions and the determination of integral length with reference to experimental and numerical data, *In: 15th Australasian Fluid Mechanics Conference*, Sydney, Australia, 13-17 December
- Ohmi K and Li H-Y, 2000, Particle-tracking Velocimetry with new algorithms, *Measurement Science and Technology*, 11, 603-616
- Okamoto K, Nishio S, Saga T and Kobayashi T, 2000, Standard images for particle-image velocimetry, *Measurement Science and Technology*, 11, 685-691
- Okutomi M and Kanade T, 1992, A locally adaptive window for signal matching, *Int. Journal of Computer vision*, 7-2 143-162

- Olejniczak J, Wright M J and Candler G V, 1997, Numerical study of inviscid shock interactions on double-wedge geometries, *Journal of Fluid Mechanics*, 352, 1-25
- Pierce W F and Delisi D P, 1995, Effect of interrogation window size on the measurement of vortical flows with digital particle image velocimetry, *In: Proceedings of the Seventh Int. Symp. on Flow Visualization*, ed. Crowder J P, Seattle, Washington, USA, 11-14 September, 728-732
- Piirto M, Saarenrinne P, Eloranta H and Karvinen R, 2003, Measuring turbulence energy with PIV in a backward-facing step flow, *Experiments in Fluids*, 35, 219-236
- Politis D N and White H, 2004, Automatic block-length selection for the dependent bootstrap, *Econometric Reviews*, 23-1, 53-70
- Prasad A K, 2000, Stereoscopic particle image velocimetry, *Experiments in Fluids*, 29, 103-116
- Press W H, Teukolsky S A, Vetterling W T and Flannery B P, 1992, Numerical recipes in C – second edition, Cambridge University Press, 108
- Quénot G M, Pakleza J and Kowalewski T A, 1998, Particle image velocimetry with optical flow, *Experiments in Fluids*, 25, 177-189
- Ragni D, Ashok A, van Oudheusden B W and Scarano F, 2009, Surface pressure and aerodynamic loads determination of a transonic airfoil based on particle image velocimetry, *Measurement Science and Technology*, 20, 074005
- Raffel M, Willert C E and Kompenhans J, 1998, Particle image velocimetry – a practical guide, Springer-Verlag, Berlin Heidelberg
- Riethmuller M L and Lourenco L, 1981, Measurement in particulate two-phase flows, *In: Laser velocimetry, von Karman Institute for Fluid Dynamics Lecture Series*, ed.: Riethmuller M L, 23-27 February
- Riethmuller M L and Planquart P, 2006, A new PIV technique for very large heat-induced flow fields, *In: Int. heat transfer conference*, Sydney, Australia, 13-18 August
- Roesgen T, 2003, Optimal subpixel interpolation in particle image velocimetry, *Experiments in Fluids*, 35, 252-256
- Rohály J, Frigerio F, Hart D P, 2002, Reverse hierarchical PIV processing, *Measurement Science and Technology*, 13, 984-996
- Ronneberger O, Raffel M and Kompenhans J, 1998, Advanced evaluation algorithm for standard and dual plane particle image velocimetry, *In: 9th Int. Symp. on Applications of Laser Techniques to Fluid Mechanics*, Lisbon, Portugal, 13-16 July
- Rossow V J, 1999, Lift-generated vortex wakes of subsonic transport aircraft, *Progress in Aerospace Sciences*, 35, 507-660
- Roth G I and Katz J, 2001, Five techniques for increasing the speed and accuracy of PIV interrogation, *Measurement Science and Technology*, 12, 238-245
- Ruan X, Wu F and Yamamoto F, 2003, Precision of direct measurement of vorticity from digital particle images, *Measurement Science and Technology*, 14, 1314-1320
- Ruwet V, Corieri P, Theunissen R, Ma B, Darquenne C and Riethmuller M L, 2008, Flow of aerosol in a 3D alveolated bifurcations: experimental measurements by Particle Image Velocimetry (PIV) and Particle Tracking Velocimetry (PTV), *14th Int. Symp. on applications of laser techniques to fluid mechanics*, Lisbon, Portugal, 7-10 July

- Saarenrinne P, Piirto M and Eloranta H, 2001, Experiences of turbulence measurement with PIV, *Measurement Science and Technology*, 12, 1904-1910
- Sakumar N, Moran B and Belytschko T, 1998, The natural element method in solid mechanics, *Int. Journal for Numerical Methods in Engineering*, 43, 839-887
- Sambridge M, Braun J and McQueen H, 1995, Geophysical parameterization and interpolation of irregular data using natural neighbours, *Geophysical Journal Int.*, 122, 837-857
- Scarano F and Haertig J, 2003, Application of non-isotropic resolution PIV in supersonic and hypersonic flows, *In: 5th Int. Symp. on particle image velocimetry*, Busan, Korea, 22-24 September
- Scarano F and Riethmuller M L, 1999, Iterative multigrid approach in PIV image processing with discrete window offset, *Experiments in Fluids*, 26, 513-523
- Scarano F and Riethmuller M L, 2000, Advances in iterative multigrid PIV image processing, *Experiments in Fluids*, 29, 51-60
- Scarano F and van Oudheusden B W, 2003, Planar velocity measurements of a two-dimensional compressible wake, *Experiments in Fluids*, 34, 430-441
- Scarano F, 2002, Iterative image deformation methods in PIV, *Measurement Science and Technology*, 13, 1-19
- Scarano F, 2003, Theory of non-isotropic spatial resolution in PIV, *Experiments in Fluids*, 35, 268-277
- Scarano F, 2004, On the stability of iterative PIV image interrogation methods, *In: 12th Int. Symp. on the application of laser techniques to fluid mechanics*, Lisbon, Portugal, 12-15 July
- Scarano F, 2008, Overview of PIV in supersonic flows, *In: Particle image velocimetry – new developments and recent applications*, ed.: Schröder A and Willert C E, Springer
- Scarano F, David L, Bsibsi M and Callaud D, 2005, S-PIV comparative assessment: image dewarping+misalignment correction and pinhole+geometric back projection, *Experiments in Fluids*, 39, 257-266
- Scholz U and Kähler C J, 2004, Automated image processing and segmentation for mask generation for PIV, *In: 12th Int. Symp. on Applications of Laser Techniques to Fluid Mechanics*, Lisbon, Portugal, 12-15 July
- Schram C, Rambaud P and Riethmuller M L, 2004, Wavelet based eddy structure eduction from a backward facing step flow investigated using particle image velocimetry, *Experiments in Fluids*, 36, 233-245
- Schrijer F F J and Scarano F, 2008, Effect of predictor-corrector filtering on the stability and spatial resolution of iterative PIV interrogation, *Experiments in Fluids*, 45, 927-941
- Schrijer F F J, Scarano F and van Oudheusden B W, 2006, Application of PIV in a Mach 7 double-ramp flow, *Experiments in Fluids*, 41, 353-363
- Schröder A, Geisler R, Henning A, Wieneke B, Elsinga G E and Scarano F, 2008, Lagrangian and Eulerian views into a turbulent boundary layer flow using time-resolved tomographic PIV, *In: 14th Int. Symp. on application of laser techniques to fluid mechanics*, Lisbon, Portugal, 7-10 July

- Secord A, Heidrich W and Streit L, 2002, Fast primitive distribution for illustration, *13th Eurographics Workshop on Rendering*, ed. P Debevec and S Gibson
- Shankar P N and Deshpande M D, 2000, Fluid mechanics in the driven cavity, *Annual review of Fluid Mechanics*, 39, 93-136
- Shapiro A H, 1953, The dynamics and thermodynamics of compressible fluid flow, Volume II, The Ronald press company, New York
- Shavit U, Lowe R J and Steinbuck J V, 2007, Intensity capping: a simple method to improve cross-correlation PIV results, *Experiments in Fluids*, 42, 225-240
- Shi J and Tomasi C, 1994, Good features to track, *IEEE Conference on Computer Vision and Pattern Recognition*, Seattle, USA, 21-23 June
- Shinnee A-M, Bugg J D and Balachandar R, 2004, Variable threshold outlier identification in PIV data, *Measurement Science and Technology*, 15, 1722-1732
- Sibson R, 1981, A brief description of natural neighbour interpolation, *In: Interpreting Multivariate Data*, ed. Barnett V., 21-36
- Simpson A, Planquart P and Riethmuller M L, 2005, Application of PIV to very large flow fields, *In: 8th Int. Symp. on fluid control, measurement and visualization*, Chengdu, China, 22-25 August
- Simpson R B, 1994, Anisotropic mesh transformations and optimal error control, *Applied Numerical Mathematics*, 14, 183-198
- Singh K, 1981, On the asymptotic accuracy of Efron's bootstrap, *Annals of Statistics*, 9, 1187-1195
- Soria J, 1996, An investigation of the near wake of a circular cylinder using a video-based digital cross-correlation particle image velocimetry technique, *Experimental Thermal and Fluids Science*, 12, 221-233
- Spedding G R and Rignot E J M, 1993, Performance analysis and application of grid interpolation techniques for fluid flows, *Experiments in Fluids*, 15, 417-430
- Spencer A and Hollis D, 2005, Correcting for sub-grid filtering effects in particle image velocimetry data, *Measurement Science and Technology*, 16, 2323-2335
- Stanislas M and Monnier J C, 1997, Practical aspects of image recording in particle image velocimetry, *Measurement Science and Technology*, 8, 1417-1426
- Stanislas M, Okamoto K and Kähler C, 2003, Main results of the first international PIV challenge, *Measurement Science and Technology*, 14, 63-89
- Stanislas M, Okamoto K, Kähler C J and Westerweel J, 2005, Main results of the second international PIV challenge, *Experiments in Fluids*, 39, 170-191
- Stanislas M, Okamoto K, Kähler C J, Westerweel J and Scarano F, 2008, Main results of the third international PIV Challenge, *Experiments in Fluids*, 45, 27-71
- Stephens J J, 1972, Distance distributions for randomly distributed data, *Monthly weather review*, 100, 60-61
- Stitou A and Riethmuller ML, 2001, Extension of PIV to super resolution using PTV, *Measurement Science and Technology*, 12, 1398-1403
- Stitou A, 2003, Development of a hybrid PIV-PTV super resolution method – application to separated flows, PhD-thesis, Université Libre de Bruxelles and von Karman Institute for Fluid Dynamics

- Stüer H and Blaser S, 2000, Interpolation of scattered 3D PTV data to a regular grid, *Flow, Turbulence and Combustion*, 64, 215-232
- Susset A, Most J M, Honoré D, 2006, A novel architecture for a super-resolution PIV algorithm developed for the improvement of the resolution of large velocity gradient measurements, *Experiments in Fluids*, 40, 70-79
- Takehara K and Etoh T, 1999, A study on particle identification in PTV – particle mask correlation method, *Journal of visualization*, 1-3, 313-323
- Tennekes H and Lumley J L, 1972, A first course in turbulence, The MIT Press, Cambridge, Mass.
- Theunissen R, Buchmann N, Corieri P, Riethmuller M L and Darquenne C, 2006^a, Experimental investigation of aerosol deposition in alveolar lung airways, *In: 13th Int. Symp. on applications of laser techniques to fluid mechanics*, Lisbon, Portugal, 26-29 June
- Theunissen R, Scarano F, Riethmuller M L and Jérónimo A, 2005, Application of an adaptive windowing and sampling PIV interrogation method to a supersonic jet flow, *In: PIVNET II Int. Workshop on the Application of PIV in Compressible Flows*, Delft, The Netherlands, 6-8 June
- Theunissen R, Schrijer F F J, Scarano F and Riethmuller M L, 2006^b, Application of adaptive PIV interrogation in a hypersonic flow, *In: 13th Int. Symp. on Applications of Laser Techniques to Fluid Mechanics*, Lisbon, Portugal, 26-29 June
- Theunissen R, Stitou A and Riethmuller ML, 2004, A novel approach to improve the accuracy of PTV methods, *In: 12th Int. Symp. on applications of laser techniques to fluid mechanics*, Lisbon, Portugal, 12-15 July
- Thévenaz P, Blu T and Unser M, 2000, Interpolation revisited, *IEEE Transactions on Medical Imaging*, 19-7, 739-758
- Thiébaux H J and Zwiers F W, 1984, The interpretation and estimation of effective sample size, *Journal of Climate and Applied Meteorology*, 23, 800-811
- Tokumar P T and Dimotakis P E, 1995, Image correlation velocimetry, *Experiments in Fluids*, 19, 1-15
- Triguí A, 2005, Natural neighbour coordinates on irregular staggered grids, Studienarbeit Nr. 1967, University of Stuttgart, Institut für Parallele und Verteilte Systeme, Abteilung Simulation großer Systeme
- Tritton D J, 1988, Physical fluid dynamics – second edition, Oxford Science Publications, 306-308
- Tsuei L and Savas Ö, 2000, Treatment of interfaces in Particle Image Velocimetry, *Experiments in Fluids*, 29, 203-214
- Ullum U, Schmidt J J, Larsen P S and McCluskey D R, 1998, Statistical analysis and accuracy of PIV data, *Journal of Visualization*, 1-2, 205-216
- Unser M, Aldroubi A and Eden M, 1993^a, B-spline signal processing: part I-theory, *IEEE Transactions on Signal Processing*, 41-2, 821-832
- Unser M, Aldroubi A and Eden M, 1993^b, B-spline signal processing: part II-efficient design and applications, *IEEE Transactions on Signal Processing*, 41-2, 834-848

- Usera G, Vernet A, Ferré J A, 2004, Considerations and improvements of the analysing algorithms used for time resolved PIV of wall bounded flows, *In: 12th Int. Symp. on Applications of Laser Techniques to Fluid Mechanics*, Lisbon, Portugal, 11-15 July
- Van Dyke M, 1988, *An album of fluid motion*, The Parabolic Press, Stanford, California, 63
- van Ertbruggen C, Corieri P, Theunissen R, Riethmuller M L and Darquenne C, 2008, Validation of CFD predictions of flow in 3D alveolated bend with experimental data, *Journal of Biomechanics*, 41, 399-405
- van Oudheusden B W, Scarano F, Roosenboom E W m, Casimiri E W F and Souverein L J, 2007, Evaluation of integral forces and pressure fields from planar velocimetry data for incompressible and compressible flows, *Experiments in Fluids*, 43, 153-162
- Vedula P and Adrian R J, 2004, Optimal solenoidal interpolation of turbulent vectors: application to PTV and Super-resolution PIV, *In: 12th Int. Symp. on application of laser techniques to fluid mechanics*, Lisbon, Portugal, 12-15 July
- Vennemann P, Kiger K T, Lindken R, Groenendijk B C W, Stekelenburg-de Vos S, ten Hagen T L M, Ursem N T C, Poelmann R E, Westerweel J and Hierck B P, 2006, In vivo micro particle image velocimetry measurements of blood-plasma in the embryonic avian heart, *Journal of Biomechanics*, 39, 1191-2000
- Verma S B, 2003, Experimental study of flow unsteadiness in a Mach 9 compression ramp interaction using a laser schlieren system, *Measurement Science and Technology*, 14, 989-997
- VKI LS, 1986, Flow visualization and digital image processing, ed. Buchlin J M, *von Karman Institute for Fluid Dynamics—Lecture Series*, 9-13 June
- Wereley S T and Meinhart C D, 2001, Second-order accurate particle image velocimetry, *Experiments in Fluids*, 31, 258-268
- Wereley S T, Gui l and Lee S Y, 2002^a, Digital filters for reducing background noise in micro PIV measurements, *In: 11th Int. Symp. on application of laser techniques to fluid mechanics*, Lisbon, Portugal, 8-11 July
- Wereley S T, Gui L and Meinhart C D, 2002^b, Advanced algorithms for microscale particle image velocimetry. *AIAA*, 40-6, 1047-1055
- Wernet M P, 2005, Symmetric phase only filtering: a new paradigm for DPIV data processing. *Measurement Science and Technology*, 16, 601-618
- Westerweel J and Scarano F, 2005, Universal outlier detection for PIV data, *Experiments in Fluids*, 39, 1096-1100
- Westerweel J, 1993, Digital particle image velocimetry – theory and application, PhD thesis, Delft University Press
- Westerweel J, 1994, Efficient detection of spurious vectors in particle image velocimetry data, *Experiments in Fluids*, 16, 236-247
- Westerweel J, 1997, Fundamentals of digital particle image velocimetry, *Measurement Science and Technology*, 8, 1379-1392
- Westerweel J, 1998, Effect of sensor geometry on the performance of PIV interrogation, *In: 9th Int. Symp. on application of laser techniques to fluid mechanics*, Lisbon, Portugal, 13-16 July

- Westerweel J, 2000, Theoretical analysis of the measurement precision in particle image velocimetry, *Experiments in Fluids*, 29, 1-12
- Westerweel J, 2007, On velocity gradients in PIV interrogation, *Experiments in Fluids*, 44, 831-842
- Westerweel J, Dabiri D and Gharib M, 1997, The effect of a discrete window offset on the accuracy of cross-correlation analysis of digital PIV recordings, *Experiments in Fluids*, 23, 20-28
- Westerweel J, Draad A A, van der Hoeven J G Th and van Oord J, 1996, Measurement of fully-developed turbulent pipe flow with digital particle image velocimetry, *Experiments in Fluids*, 20, 165-177
- Weygandt J H and Mehta R D, 1989, Asymptotic behaviour of a flat plate wake, *Joint institute for aeronautics and acoustics*, JIAA TR-95
- White F M, 1991, Viscous fluid flow – second edition, McGraw-Hill Inc., pg.479
- Wieneke B and Susset A, 2004, Higher PIV accuracy by optimization of interrogation window size and shape, *Pivnet T5/ERCOFTAC SIG 32, 7th Workshop on PIV*, Lisbon, Portugal
- Willert C E and Gharib M, 1991, Digital particle image velocimetry, *Experiments in Fluids*, 10, 181-193
- Willert C E, 2000, Evaluation of digital PIV recordings, *In: Application of particle image velocimetry - theory and practice*, Course Notes, DLR Göttingen, Germany, 6-10 March
- Willert C E, 2009, Advanced image analysis for particle image velocimetry part I: processing individual PIV recordings, *In: Recent advances in Particle Image Velocimetry, von Karman Institute for Fluid Dynamics Lecture Series*, ed.: Riethmuller M L, 26-30 January
- Williamson C H K, 1996, Vortex dynamics in the cylinder wake, *Annual review of Fluid Mechanics*, 28, 477-539
- Xiao Q, Tsai H M and Papamoschou D, 2007, Numerical investigation of supersonic nozzle flow separation, *AIAA*, 45, 532-541
- Xu C and Prince J L, 1998, Snakes, Shapes, and Gradient Vector Flow, *IEEE transactions on image processing*, 7, 359-369
- Yoon S S and Heister S D, 2004, Analytical formulas for the velocity field induced by an infinitely thin vortex ring, *Int. Journal for Numerical Methods in Fluids*, 44, 665-672
- Young C N, Johnson D A and Weckman E J, 2004, A method to anchor displacement vectors to reduce uncertainty and improve particle image velocimetry results, *Measurement Science and Technology*, 15, 9-20
- Young G A, 1994, Bootstrap: More than a Stab in the Dark?, *Statistical Science*, 9-3, 382-415
- Yüceil K B, Ötügen M G and Arik E, 2000, Underexpanded sonic jets: a PIV study, *In: 10th Int. Symp. on application of laser techniques to fluid mechanics*, Lisbon, Portugal, 10-13 July
- Zhou T and Shimada K, 2000, An angle-based approach to two-dimensional mesh smoothing, *In: 9th Int. Meshing Roundtable*, New Orleans, Louisiana, USA, 2-5 October

APPENDIX A

ADAPTIVE IMAGE EVALUATION: LITERATURE SURVEY

Abstract

The following appendix elaborates on the implementation of the adaptivity criteria and interrogation routines presented in Chapter 4. Various methodologies covering signal quantization, data interpolation and vorticity education are briefly discussed and evaluated based on their conduciveness for the applications presented within the thesis framework. Particle identifications proves to be the most straightforward and consistent approach in the determination of the signal content. Because of its robustness and locality Natural Neighbour interpolation has been selected for redistribution of data while Least-Squares polynomial fitting of velocity data with a 7×7 base kernel ensures smooth and accurate vorticity estimates.

Nomenclature

λ	eigenvalue
Δ	grid/sample spacing (pixels or meters)
ω_{bias}	bias error in vorticity (pixel/pixel or Hz)
ω_{exact}	exact vorticity value (pixel/pixel or Hz)
ω_z	out-of-plane vorticity component ; $\omega_z = \partial v / \partial x - \partial u / \partial y$ (pixel/pixel)
d_p	particle image diameter (pixels)
G	intensity derivative matrix
h	step height of the backward facing step (meter or pixels)
$I_{\text{min,max}}$	minimum, respectively maximum pixel intensity
I_{noise}	noise intensities
I_{part}	particle intensities
L	characteristic length scale (arbitrary unit)
N_p	number of particle images
N_s	source density
$u_{\text{fit}}, v_{\text{fit}}$	velocity components obtained through fitting (pixels or m/s)

$\text{var}(X)$	variance in variable X (arbitrary unit)
$\langle X \rangle$	ensemble average value of variable X (arbitrary unit)

A.1 Introduction

In Chapter 4 an adaptive image interrogation procedure was proposed. Opposed to the classical approach where correlation windows are placed on the nodes of a structured Cartesian grid, the sampling locations are projected in the interrogation domain following a probability density distribution. One of the parameters describing this pdf is the amount of signal contained within the image. In PIV the signal relates to recorded particle images as they constitute the fundamental sampling of the unknown velocity distribution. Their number plays an important role in the robustness of the image analysis. Interrogation windows must contain a certain number of particle images to yield a reliable correlation, which imposes stringent limitations on the window dimensions and inherently the potential spatial resolution. A method of quantifying the source density is therefore in order. This is the topic of discussion in the first paragraph.

Once the velocity estimates are retrieved, redistribution onto a structured grid is often compulsory to facilitate the post-processing. The implemented PDF-weighted projection of the sampling locations inherently signifies an additional complexity since the samples' spatial separation no longer follows an analytical description, a bottleneck typically encountered in e.g. LDV measurements. Similar problems have been tackled in the geodesic and meteorological community where measurements are always unevenly spaced be it across the globe surface or in altitude. An array of interpolation techniques exist which, and this is akin to vorticity estimates, each has optimal performances under specific conditions. In the current framework the implemented routines must be as general and globally applicable though. One therefore has to keep in mind, that the chosen procedures for data interpolation and vorticity estimation within this reported work might not be optimal for specific conditions but that they offer a broadly applicable solution.

A.2 Signal quantization

In the following a closer look is taken at advantages and disadvantages of estimators for the signal density alternative to straightforward particle image segmentation.

A.2.1 Feature tracking

PIV has a close resemblance to feature tracking given that the correlation operator searches for a minimum in disparity between two intensity distributions. According to Okutomi and Kanade (1992) precise determination of disparity in feature tracking is difficult though and unreliable either due to insufficient signal variation relative to noise

or too much disparity fluctuation within the window. Shi and Tomasi (1994) therefore select features providing sufficient information for the measurement and having high probability of success in tracking based on the eigenvalues of the intensity derivative matrix presented in equation (A.1) (taking only affine motion into account).

$$G(i, j) = \sum_{k=i-\frac{w_s}{2}}^{k=i+\frac{w_s}{2}} \sum_{m=j-\frac{w_s}{2}}^{m=j+\frac{w_s}{2}} \begin{bmatrix} \frac{\partial^2 I}{\partial x^2}(k, m) & \frac{\partial I}{\partial x} \frac{\partial I}{\partial y}(k, m) \\ \frac{\partial I}{\partial x} \frac{\partial I}{\partial y}(k, m) & \frac{\partial^2 I}{\partial y^2}(k, m) \end{bmatrix} \quad (\text{A.1})$$

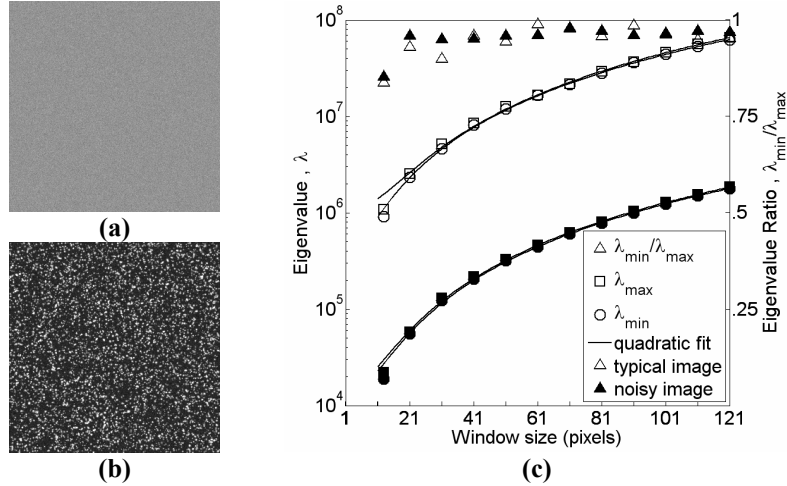


Fig. A.1: Computer generated images of (a) white noise (b) a typical PIV image. (c) Computed eigenvalues according to (A.1). Full and hollow symbols refer to respectively the noisy and typical PIV image.

Both eigenvalues must be large to ensure sufficient exclusion of image noise influences. Small eigenvalues imply a uniform intensity profile while large values indicate a pattern which can be tracked reliably. The ratio of eigenvalues should remain however close to unity to avoid unidirectional intensity profiles. From this point of view, the considered eigenvalues could in principle serve as an indicator of the amount of signal available and allow an estimate of the appropriate correlation window size. This approach has however several important drawbacks. As can be deduced from the diagram in Fig. A.1, eigenvalue ratios close to unity are obtained not only for typical particle images, but also for randomized pixel intensities, i.e. white noise. Both image types yield eigenvalues with quadratic dependency in window size. A threshold criterion is therefore the only measure of discriminating between noise and signal of interest. The criterion will however be case-dependent, impeding the current objective of global signal adaptation. The strong reflections encountered near the boundary of a submerged body during PIV experiments are accompanied by a high and low eigenvalue due to their edge-like appearance. This will additionally hamper the use of a global threshold throughout the image and will furthermore cause selected windows to be concentrated near the interfaces leaving the bulk flow under-sampled. Moreover, no adequate window size can be inferred

from the depicted relation between eigenvalues and window size while it is well-known from Keane and Adrian (1992) that the lower limit in size is prescribed by the number of tracer images necessary to yield a reliable correlation.

A.2.2 Image statistics

Though the most straightforward estimate of seeding concentration can be based on the recorded intensity amplitudes[†] (Garcia *et al.*, 2002), the involved technique suffers from numerous sources of measurement error (Stitou, 2003). Such errors include effects of electronic noise, the truncation of particle images due to the finite dimensions of the sliding analysis area, the out-of-plane extension of the light sheet, the dependency of the scattered intensity on the observation angle, etc. Instead, given ideal recording conditions (i.e. in absence of noise) and mono-phase PIV images Westerweel (2000) expresses the source density 'N_s' in terms of the image contrast defined as the ratio between intensity spatial variance and mean intensity (A.2). Monte Carlo simulations based on computer generated images verify this relation (Fig. A.2).

$$\frac{\sqrt{\text{var}(I)}}{\langle I \rangle} = \frac{\sqrt{\text{var}(I_{\text{part}}) + \text{var}(I_{\text{noise}})}}{\langle I_{\text{part}} \rangle + \langle I_{\text{noise}} \rangle} \stackrel{I_{\text{noise}}=0}{=} \frac{\sqrt{\text{var}(I_{\text{part}})}}{\langle I_{\text{part}} \rangle} = \frac{1}{\sqrt{N_p \frac{\pi}{4} d_p^2}} = \frac{1}{\sqrt{N_s}} \quad (\text{A.2})$$

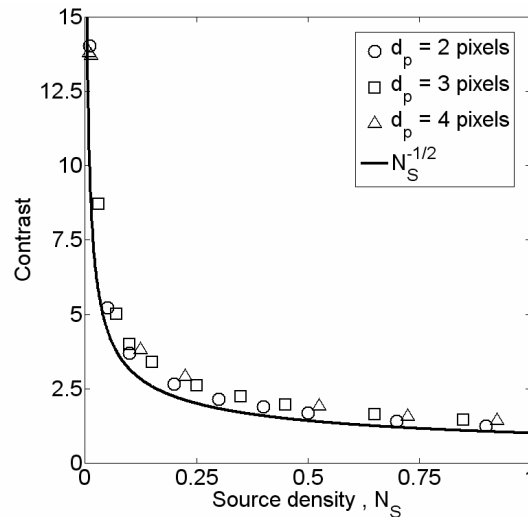


Fig. A.2: Evolution of image contrast vs. source density for different particle image diameters in case of ideal computer generated PIV images.

[†] The denser the seeding, the brighter the image and vice versa. By measuring the total intensity captured by a window moving across the recorded image, the seeding concentration can be estimated.

Based on (A.2) the number of recorded particle images ‘ N_p ’ can be evaluated after introduction of the particle diameter ‘ d_p ’. In practice the particle image diameters are unknown a-priori but can be assumed to vary around 3 pixels in mean value as this is the most common value and smallest size to minimize the peak-locking effect (Westerweel, 1998). Although the approach has been successfully applied (Theunissen *et al.*, 2005), typical recording conditions are far from ideal. Since parasitic image noise and the signal particle image intensities are uncorrelated stochastic variables, the image contrast will involve both mean and RMS noise level (A.2). As a result, estimation of source density from the image contrast becomes impossible due to the present inability of accurate noise characterization.

A.2.3 Particle image segmentation

The methodologies discussed above both offer the advantage of speed and are very adequate in estimating the amount of signal providing the image recording is not degraded by noise. Although cameras are nowadays equipped with cooling thereby reducing the thermal noise, parasitic noise influences stemming from the experimental facility itself (e.g. spurious light sources, reflections, etc.) are not so easily wavered. As a result, a more robust technique must be adopted and one of the possible candidates is straightforward particle identification. Although it has been many a subject of discussion and research in particle tracking techniques, one must bear in mind that the present issue is not accuracy, but robustness. Accurate particle localization is only essential to have precise velocity estimates when tracking individual tracers. The implemented particle segmentation routine is described in further detail in Chapter 3.

A.3 Data interpolation

This paragraph aims at scrutinizing several popular data interpolation schemes abundantly available in literature. Interpolation by means of global basis functions[†] will be discarded because of their high dependency upon the measurement density (Spedding and Rignot 1993). Turning therefore to weighted interpolation, the interpolated value ‘ f_p ’ at location ‘P’ can in general be rewritten as an average of ‘n’ neighboring data values ‘ f_i ’, weighted by coefficients ‘ w_i ’ whose definition depends on the adopted interpolation scheme;

$$f_p = \sum_{i=1}^n w_i f_i \quad (\text{A.3})$$

[†] The basic idea is to select a basis function ‘ F_i ’ and determine the coefficients ‘ w_i ’ based on the given data points ‘ f_i ’ such that the interpolated value is given as ‘ $f_p = \sum w_i F_i$ ’. The difficulty lies in the appropriate selection of ‘ F_i ’. An example of such a basis function are Splines.

A.3.1 Adaptive Gaussian Windowing averaging (AGW)

In the popular adaptive Gaussian window averaging methodology proposed by Agüi and Jiménez (1987), weighting coefficients are derived from a Gaussian kernel centered on the point of interest. The window size was prescribed as 1.24 times the unstructured sample spacing (i.e. particle image spacing), independent of the characteristic length scale of the assumed sinusoidal-like flowfield. Having to sum over all samples within the observation volume can introduce however a considerable smoothing due to the inherent non-locality of the scheme (Spedding and Rignot, 1993). In particle tracking related measurements, the limited bandwidth of the interpolation method can however be advantageous in reducing the influence of the random error (Theunissen *et al.*, 2004)

A.3.2 Polynomial fitting

Cohn and Koochesfahani (2000) considered the concept of polynomial fitting which can be rewritten in the form of equation (A.3) through Lagrange's formula (Press *et al.*, 1992). They concluded a 4th order polynomial to produce the most accurate remapping. However, for this least-squares fit to be well determined, at least 81(!) samples would have to be taken into account, disabling the reconstruction of high frequency fluctuations due to smoothing. Instead a second order polynomial would be more favorable at the expense of only a slight increase in bias and rms errors providing fulfillment of the Nyquist sampling criterion. The latter agrees with the findings of Jiménez and Agüi (1987) and Stüer and Blaser (2000) who both conclude lower order interpolation to yield suitable performances at adequate sampling densities compared to higher order schemes. Concluding, the strict requirements on original velocity data density inhibits a universal applicability of polynomial fitting; each sample spacing prescribes an optimal order of the polynomial which in turns goes with an ideal extent of the fitting base.

A.3.3 Kriging interpolation

Kriging interpolation involves a set of linear regression routines, minimizing the estimation variance from a predefined covariance model (Jones *et al.*, 2003). From the scatter point set to be interpolated, a variogram is constructed through determination of the variance[†] of each point with respect to the other data points as a function of their inner-distance. Based on the model variogram, which mathematically describes the trend in the experimental variogram[‡], the interpolation weights are computed. The fact that as such the degree of correlation between samples is taken into account, thereby minimizing

[†] The variogram used here is defined as $\gamma(\Delta) = \frac{1}{N(\Delta)} \sum (u_i - u_j)^2$; the variogram for a particular sample spacing ' Δ ' is the averaged difference squared of the velocity or displacement values over all the data pairs separated by approximately that spacing.

[‡] e.g. a straight line, an exponential function, etc.

the influence of redundant information, makes kriging an interpolation method worth the interest. The variograms of three locations in the case of a backward facing step (step height 'h' based Reynolds number $Re_h=5000$) is depicted in figure A.3-a. Point 'a' is located within the free stream while 'b' and 'c' are situated within the shear layer and boundary layer respectively. The corresponding variograms in Fig. A.3-b show a rather smooth evolution up to a normalized sample spacing of around 0.8, 0.5 and 0.4 respectively, after which the tendency becomes erratic. A model variogram taking into account all samples will therefore not yield an apposite representation of the degree of correlation between the neighboring points. Instead the number of neighboring samples to consider is critical and appears to be dependent on the character and spatial location within the flow. Furthermore, the determination of the experimental and model variogram must be repeated for each velocity component of the nodes within the unstructured grid, which then allows the derivation of the weights. As mentioned by Sibson (1981), the computational effort thus involved makes the technique quite unattractive.

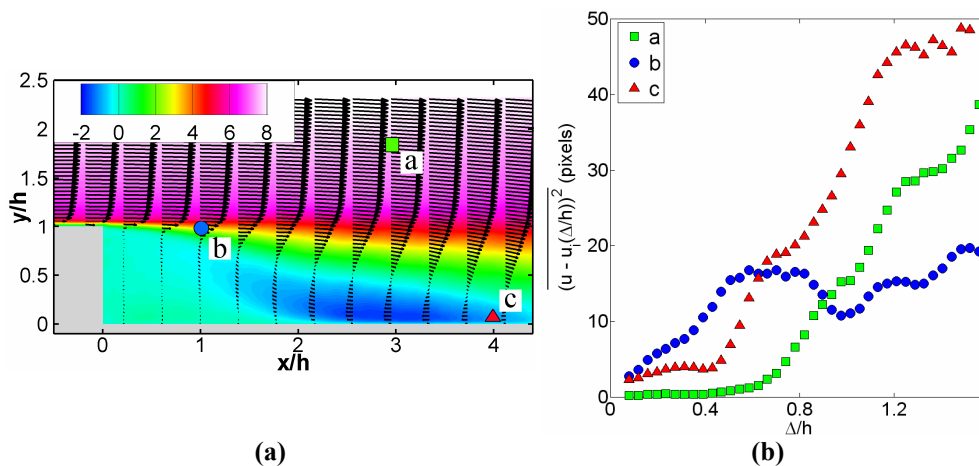


Fig. A.3: (a) Backward facing step flow at $Re_h \approx 5000$. Contours of the horizontal velocity component, expressed in pixels (b) Variogram of points 'a', 'b' and 'c'. 'h' and ' Δ ' denote the step height and sample spacing respectively.

A.3.4 Natural Neighbor interpolation (NN)

In view of the data density variation, natural neighbor interpolation (NN) will prove to be a more robust and conducive interpolant as remarked by Amidror (2002). Natural neighbor interpolation overrides the classical attribution of larger importance/weights to closer nodes compared to those placed at larger distances by defining the weights by an appropriate measure of the occupied space. Weights are based on both topological relationships and areas of influence, making the approach local (Sibson, 1981). Further properties of NN interpolation include linear completeness; constant functions and original data at the reference nodes are exactly reproduced. Furthermore, the interpolation

schemes guarantee smoothness (hence continuous differentiability) everywhere with exception of the nodes. Further details on the implementation can be found in Chapter 3.

A.4 Post-processing: vorticity calculation

If the vorticity field is known, a great deal of information can be obtained about the investigated flow. Metrologies have been reported in literature rendering velocity estimates superfluous (Ruan *et al.*, 2003); rather than extracting the out-of-plane vorticity component from the estimated velocity distribution, the average rotational angle of particles from one pattern into its counterpart from consecutive particle recordings is evaluated. The current objective is however to estimate the vorticity field with reasonable accuracy from PIV-based velocity measurements, discarding momentarily the filtering effect of the underlying velocity field as a result of the limited spatial resolution inherent to the finite interrogation window (Pierce and Delisi, 1995).

A.4.1 Differential schemes

Besides techniques incorporating the philosophy of Stokes' theorem and the definition of circulation (Raffel *et al.* 1998, Luff *et al.* 1999, Graftieaux *et al.* 2001), numerical derivative calculations are ingrained in the estimation of vorticity. Foucaut and Stanislas (2002) characterized the performance of a variety of differential schemes in the extraction of the out-of-plane vorticity component. As anticipated by Lourenco and Krothapalli (1995), the optimal choice of derivative filter in the deduction of vorticity turned out to be linked to a-priori knowledge of vortex characteristics, spatial resolution and measurement noise. Overall, the second-order central difference scheme presented the best trade-off in performance between bias and random error in vorticity at the expense of erratic vorticity fields due to noise amplification (Raffel *et al.*, 1998). The latter is attested in Fig. A.4 considering the vorticity contours of an Oseen-Lamb vortex field (201×201 pixels² field of view, 60 pixels core radius and peak vorticity of 0.2 pixels/pixels) superimposed with random displacement noise of maximum 0.01 pixels in amplitude.

A.4.2 Least-squares fitting

In an attempt to reduce the error's dependency on sampling resolution and random measurement noise Etabari and Vlachos (2005) propose a 4th order noise-minimizing compact-Richardson scheme after extensive comparison of differential schemes. An alternative approach towards reducing the effect of noise can be achieved by fitting an analytic polynomial to the discrete velocity field in a least-squares sense (Cohn and Koochesfahani 2000, Fouras and Soria 1998). To achieve a second order accuracy, it is assumed that the displacement field is well described locally by a second-order polynomial. The derivative is then obtained by an analytical derivation of the fitted function.

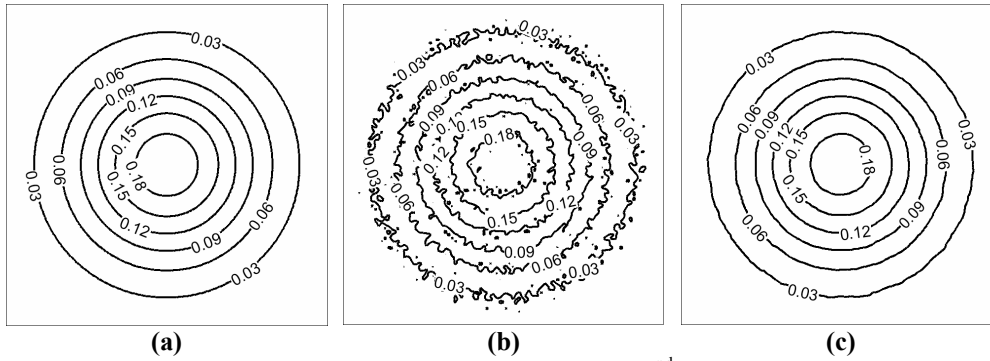


Fig. A.4: Vorticity contours (a) imposed (b) obtained through 2nd order central difference (c) least-squares fit (21 points).

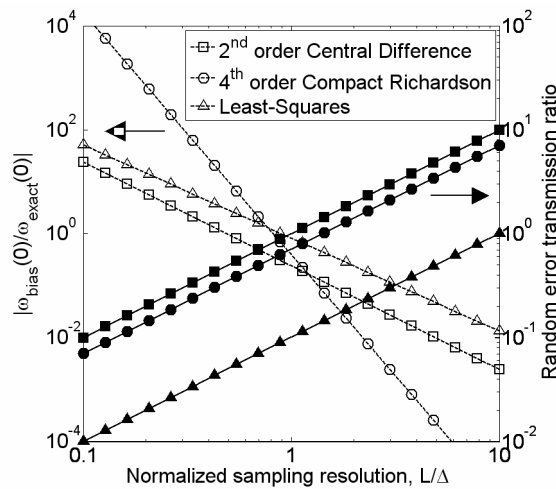


Fig. A.5: Normalized peak bias vorticity error (hollow) and random error transmission ratio (filled) as function of the normalized velocity sampling resolution.

All studies manifest the opposing dependency of the bias error in vorticity peak and random vorticity error with normalized sampling resolution dependency. The normalized spatial sampling resolution is here defined as the number of sampling points with spacing ‘ Δ ’ per characteristic flow scale ‘ L ’. Low resolution leads to low random vorticity errors but higher bias errors at the peak vorticity location while the converse applies at high resolutions. The tendencies are graphically captured in Fig. A.5 where the bias error in vorticity and the transmission coefficient for the random vorticity error are plotted in function of normalized sampling resolution. The transmission coefficient represents the amplification of the velocity random error in the vorticity estimation. Although the proposed 4th order compact derivation of Etabari and Vlachos (2005) yields the lowest bias in peak vorticity providing an adequate sampling (Fig. A.5), the scheme requires an extensive stencil size (81×81). This questions the achievable final resolution considering the assessment was performed on isolated vortex models. Fig. A.5 further attests second-

order central differentiation of the discrete velocity field to yield an adequate choice in derivation scheme. However, in this work the least-squares approach has been deemed more suitable as it offers comparable error-related properties while omitting noise amplification inherent to derivative operations (Fig. A.4-c). Having redistributed the unstructured data towards a Cartesian grid of spacing 'h', datapoints lying within the isotropic rectangular grid extending two to three grid spaces from the point of interest are taken into account in the determination of the coefficients defining the applied parabolic model functions (Lourenco, 2000);

$$\begin{aligned} u_{\text{fit}}(x, y) &= a_u x^2 + b_u y^2 + c_u xy + d_u x + e_u y + f_u \\ v_{\text{fit}}(x, y) &= a_v x^2 + b_v y^2 + c_v xy + d_v x + e_v y + f_v \end{aligned} \quad (\text{A.4})$$

yielding

$$\omega_z(x, y) = \frac{\partial v_{\text{fit}}}{\partial x} - \frac{\partial u_{\text{fit}}}{\partial y} = (2a_v x + c_v y + d_v) - (2b_u y + c_u x + e_u) \quad (\text{A.5})$$

Following the procedure described by Fouras and Soria (1998), the dependency on sampling resolution of the random error transmission ratio and vorticity bias error for the afore-mentioned model functions are depicted in Fig. A.5.

As a first additional remark, the least-squares operator does not require the velocity vector field to be sampled on an evenly spaced grid contrary to finite differencing, which in the present case can be of great benefit.

Second, the natural neighbor interpolation allows a direct computation of the first order derivatives (Miozzi, 2005). Nevertheless, smoother results for derivative operations were obtained by 2nd order least-squares fitting.

Third, Dong and Meng (2001) propose an original technique deploying the Chebyshev spectral method. While combined with the Chebyshev noise processing procedure, the accuracy in vorticity estimation is greatly enhanced in comparison to the least-squares method, the technique requires a specific distribution of the original grid points rendering the methodology solely suitable for wall-bounded flows.

APPENDIX B

PIV RESOLUTION ACROSS NORMAL SHOCKS

Abstract

Particle inertia is the primary factor limiting the achievable resolution in PIV when dealing with strong velocity discontinuities such as shock-waves. The appendix therefore starts with a recapitulation of the equations quantifying the particle response to a normal shock-wave. However, even if the particles respond perfectly, the finite resolution inherent to the interrogation process influences the achievable spatial resolution. These resolution limits are evinced by a simplistic model of the correlation operator as a moving average filter. Monte-Carlo simulations however show the shock response of the image evaluation methodology to be better than the simplistic representation. In addition, an automated routine is proposed to extract shock position and particle relaxation distance from the measured velocity distribution.

Nomenclature

δ_s	shock thickness (meters or pixels)
Δ	difference between estimated and measured relaxation distance (pixels)
μ	dynamic fluid viscosity ($\text{kg}\cdot\text{m}^{-1}\cdot\text{s}^{-1}$)
ν	kinematic fluid viscosity ($\text{m}^2\cdot\text{s}^{-1}$)
ξ	particle relaxation distance (pixels or meter)
ρ	flow density ($\text{kg}\cdot\text{m}^{-3}$)
ρ_p	particle density ($\text{kg}\cdot\text{m}^{-3}$)
τ	particle relaxation time (seconds)
a	speed of sound (m/s)
C_D	particle drag coefficient
d_p	particle diameter (pixels)
M	Mach number upstream and downstream of the shock respectively
Re_p	particle Reynolds number ($Re_p = d_p \cdot V \cdot \nu^{-1}$, with V the relative velocity between particle and fluid)
t_p	tracer travel time starting from shock position (seconds)

u_n	shock-normal flow velocity (pixels or m/s)
$\overline{u_n}$	measured flow velocity through cross-correlation (pixels or m/s)
u_n^*	normalized velocity jump across shock
u_p	tracer velocity (pixels or m/s)
W	Lambert function
W_s	correlation window size (pixels)
x	distance (pixels or meter)
x_ξ	measured relaxation distance (pixels or meter)
x_p	distance downstream of shock, traveled by tracers (pixels or meter)
x_r	random location (pixels)
x_s	measured shock location (pixels)

Subscripts

1,2	upstream and downstream of the shock
e	estimated value from fitting procedure

B.1 Introduction

Supersonic flows are characterized by the presence of shock-waves and expansion waves across which the flow properties and streamlines change in a discontinuous manner in contrast to the smooth, continuous variations in subsonic flows. These discontinuities are further emphasized by strong gradients in density, both spatial and temporal, and are thus easily distinguishable within the captured recordings. A shock wave has a finite but very small thickness caused by packing of the molecules during the compression process. Traversing the shock, the fluid tries to redistribute density, pressure, velocity etc. evenly; a process governed by fluid viscosity. In fact the shock thickness ' δ_s ' can be expressed in terms of upstream fluid viscosity and velocity jump (Kundu and Cohen, 2002);

$$\delta_s \sim \frac{\nu}{\Delta u} \quad (\text{B.1})$$

For a Mach number of 6 at sea-level conditions ($\nu = 1.46 \cdot 10^{-5} \text{m}^2/\text{s}$, $a_\infty = 340.29 \text{m/s}$) this results in a normal shock thickness of approximately 8 nano-meters ($8 \cdot 10^{-6} \text{mm}$). In other words, over 8 nano-meters the velocity jumps from 2042m/s to 388m/s (cf. equation 6.3). Adequate optical resolution where the shock would cover at least one sensor element (1 pixel $\approx 6 \cdot 10^{-6} \text{m}$) would require almost impossible magnification factors in the order of 10^3 . In practical terms, the flow variation across a shock will therefore appear as a discontinuity of infinitely small thickness in the PIV image recordings.

The eduction of flow velocities with the PIV technique is based on the interrogation of the particle image recordings by means of correlation windows which should contain a sufficient number of particles images to ensure reliability in the results. Consequently, one of the limitations in the techniques' spatial resolution is defined by the spatial density of particle images. This poses a problem considering non-uniform particle seeding densities because of the compressible flow features. The velocity returned from the correlation operator common in PIV image analyses is inherently an ensemble average of the particle velocities. The degree to which the instantaneous velocity distributions are spatially low-pass filtered depend on the size of the correlation windows. Additionally, due to the finite time response of the tracers (Melling, 1997), the exponential decay of the tracer velocity in case of steep velocity gradients (e.g. across a shock wave) causes the measured flow velocity discontinuity to be smeared.

The two main limits in achievable resolution with PIV i.e. tracer inertia and image interrogation are discussed within this appendix. It goes without saying that experimental parameters such as recording frequency and exposure time (Scarano, 2008), not to mention the aberrations stemming from gradients in refractive index (Elsinga *et al.*, 2005) are of importance too as they have a strong influence the correlation quality. However, a treatise on their influence would fall beyond the scope here and is accordingly discarded. Throughout the following elaboration, conditions identical to those reported for the hypersonic sphere (cf. Chapter 6) will be applied.

B.2 Tracer response

When neglecting buoyancy, gravity and external forces the steady state particle trajectory is prescribed as

$$\frac{du_p}{dt} = \frac{u - u_p}{\tau} \quad \text{with} \quad \frac{1}{\tau} \approx \frac{3}{4} \cdot C_D \cdot \text{Re}_p \cdot \frac{\mu}{\rho_p \cdot d_p^2} \quad (\text{B.2})$$

where ' τ ' represents the characteristic particle relaxation time, ' u ' the fluid velocity and ' u_p ' the particle's velocity[†]. In case of a shock with normal velocities ' u_{n1} ' and ' u_{n2} ' respectively upstream and downstream, consecutive integration of equation (B.2) yields the following expressions for particle velocity and position in function of time ' t_p ';

$$u_p = u_{n2} + (u_{n1} - u_{n2}) \cdot e^{-\frac{t_p}{\tau}} \quad \text{and} \quad x_p = u_{n2} \cdot t_p + (u_{n1} - u_{n2}) \cdot \tau \cdot \left(1 - e^{-\frac{t_p}{\tau}}\right) \quad (\text{B.3})$$

[†] Note that under Stokes conditions the drag coefficient $C_D=24/\text{Re}_p$ which after substitution gives back equation (1.3)

Both equations can be combined to eliminate the terms containing ‘ t_p ’ and express the velocity discontinuity across the shock in terms of the particle position;

$$\frac{u_p - u_{n2}}{u_{n1} - u_{n2}} = \frac{1}{\frac{u_{n1} - u_{n2}}{u_{n2}}} W\left(\frac{u_{n1} - u_{n2}}{u_{n2}} \cdot e^{-\frac{u_{n1}}{u_{n2}} \frac{x_p}{u_{n1}\tau} + \frac{u_{n1} - u_{n2}}{u_{n2}}}\right) \quad (\text{B.4})$$

where ‘ W ’ refers to the Lambert W function[†] and the included velocity ratios are prescribed by normal shock relations. Because this equation does not have a readily available solution, the particle’s response in PIV applications is conveniently quantified by the relaxation distance ‘ ξ ’ required for the particle velocity lag after the shock to be reduced by a factor e^{-1} (Melling, 1997);

$$\frac{u_p}{u_{n1}} = \frac{u_{n2}}{u_{n1}} + \left(1 - \frac{u_{n2}}{u_{n1}}\right) \cdot e^{-1} \quad \text{or} \quad \frac{u_p - u_{n2}}{u_{n1} - u_{n2}} = e^{-1} \quad (\text{B.5})$$

Quantifying the relaxation length itself is accomplished through substitution of ‘ t_p ’ by ‘ τ ’ and ‘ $x_p = \xi$ ’ in equation (B.3).

$$\xi = u_{n1} \cdot \left[1 + \left(\frac{u_{n2}}{u_{n1}} - 1\right) \cdot e^{-1}\right] \cdot \tau \quad (\text{B.6})$$

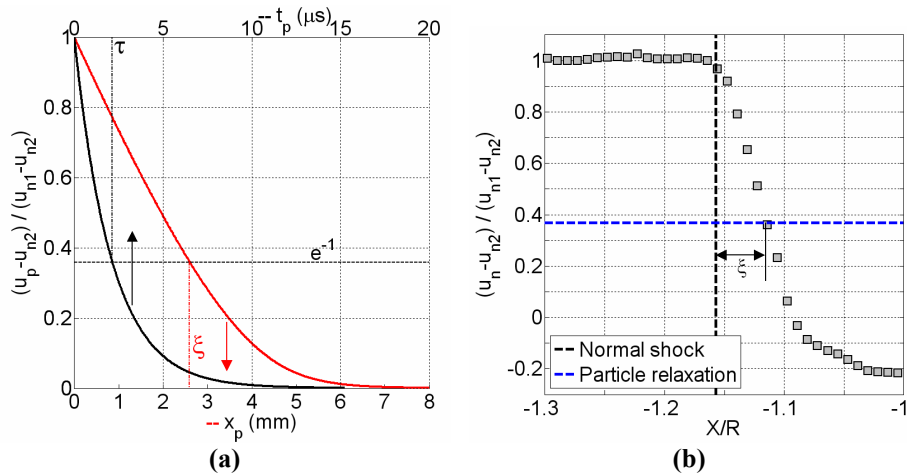


Fig. B.1: (a) Velocity jump across a normal shock in function of relaxation length and time (b) Experimental velocity jump across a shock (hypersonic sphere cf. chapter 7).

[†] Equation (B.3) can be simplified into the form ‘ $a \cdot \ln(y) - y = b$ ’ where ‘ $y = e^{-t_p/\tau}$ ’, with the solution ‘ $y = -a \cdot W(-a^{-1} \cdot e^{b/a})$ ’.

An example is shown in Fig. B.1-a for a Mach 6 flow ($u_{n2}/u_{n1}=0.1898$) with an upstream velocity of 1780m/s. Relaxation length was set to 2.6mm translating into a relaxation time of 2.1 μ s. As illustrated, even in case of an ideal normal shock, particle inertia will prevent the measurement of an infinitely thin shock thickness. If the upper shock bound can be estimated by assuming the velocity ratio ' $(u_n-u_{n2})/(u_{n1}-u_{n2})$ ' to have been reduced to e^{-4} (or ' $t_p=4\cdot\tau$ '), the measurable shock thickness can be expressed as in (B.7). For this example it yields ' $\delta_s|_{e^{-4}}=6.5\text{mm}$ '.

$$\delta_s|_{e^{-4}} = 4 \cdot u_{n2} \cdot \tau + (u_{n1} - u_{n2}) \cdot \tau \cdot (1 - e^{-4}) = u_{1n} \cdot \tau \cdot \frac{2(4+e^{-4}) + (5\gamma-3-e^{-4})M_\infty^2}{(\gamma+1)M_\infty^2} \quad (\text{B.7})$$

In Fig. B.1-b the shock-normal velocity profile for the hypersonic sphere (cf. Chapter 6) is repeated. The blue dashed line indicates the particle relaxation velocities defined by equation (B.5). The relaxation length can readily be extracted from the graphs as the intersection between the measured and relaxation velocity. Once ' ξ ' is known, inversion of (B.6) leads to the relaxation time.

B.3 Image evaluation limits to PIV shock resolution

B.3.1 Model shock response for ideal tracers

In practice, the physical dimensions of the shock thickness are negligible to those of the correlation windows, allowing the velocity jump across to be considered ideal. In its basic form, the correlation operator applied in PIV to estimate the tracer displacement within an interrogation window has a spatial response similar to that of a moving averaging filter. With the sketch in Fig. B.2-a and taking into account variations in density across the shock to weigh the up- and downstream velocities, the returned mean velocity by the linear operator is analytically given by

$$\overline{u_n} = \frac{\rho_1 u_{n1} \left(\frac{W_s}{2} - x\right) + \rho_2 u_{n2} \left(\frac{W_s}{2} + x\right)}{\rho_1 \left(\frac{W_s}{2} - x\right) + \rho_2 \left(\frac{W_s}{2} + x\right)} \quad (\text{B.8})$$

Addressing continuity and normal shock relations, the normalized velocity jump is simplified to

$$\frac{\overline{u_n} - u_{n2}}{u_{n1} - u_{n2}} = \left[1 + \frac{W_s + 2 \cdot x}{W_s - 2 \cdot x} \cdot \frac{(\gamma + 1) \cdot M_1^2}{2 + (\gamma - 1) \cdot M_1^2} \right]^{-1} \quad (\text{B.9})$$

Equation (B.9) has been graphically represented in Fig. B.2-b simulating the ideal case (gradients across the shock are described by a step function) with an upstream Mach number of 6. With increasing window size the shock resolution worsens; the shock thickness is identical to W_S . Effects of finite resolution are more pertinent upstream compared to downstream.

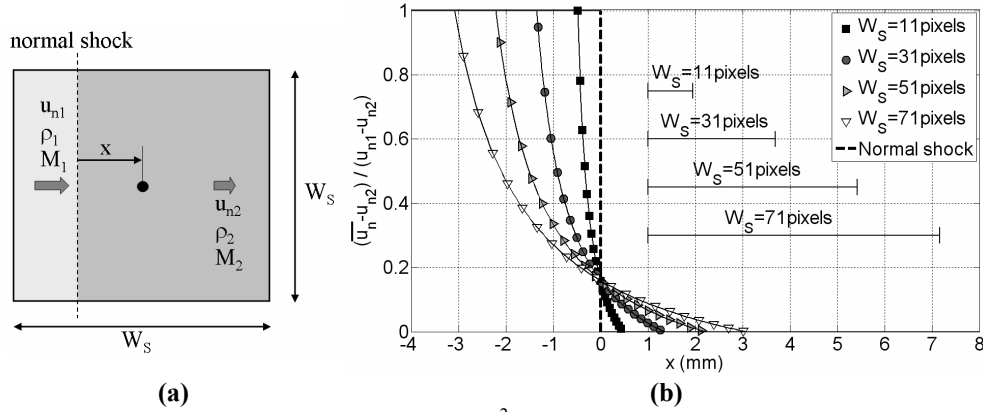


Fig. B.2: (a) Correlation window of area W_S^2 overlapping an infinitely thin normal shock (dashed line) with upstream velocity, density and Mach number respectively u_{n1} , ρ_1 and M_1 . The geometrical center of the window is indicated by \bullet . (b) Evolution of normalized velocity across a normal shock ($M_1=6$) according to (B.9) (conversion factor: $86.6\mu\text{m}/\text{pixel}$).

B.3.2 Interrogation intrinsic shock response for ideal tracers

Monte-Carlo simulations have demonstrated the spatial response, even of the conventional interrogation method, to be superior to that of a moving averaging filter. To quantify the enhanced performances in case of a normal shock, the interrogation routine described in Chapter 2 has been applied to synthetic PIV images. Computer generated images simulated the case of a normal shock with freestream Mach number 6 taking into account gradients in density ($\rho_2/\rho_1 \approx 5.3$) and velocity (Fig. B.3-a). The upstream flow contained a concentration of 0.1ppp of particle images 3 pixels in diameter. Tracers were assumed ideal (0 relaxation length). The interrogation was performed within a recursive structure imposing window overlap coefficients of 0.9 to avoid resolution limits imposed by inadequate vector spacing.

Although not presented, simulations involving various shock strengths resulted in non-dimensional velocity profiles almost identical to those displayed in Fig. B.3. With the analytical profiles according to (B.9) overlaid, Fig. B.3-b attests to the non-linear character of the correlation operator. For a window size of 11 pixels good agreement is observed with the analytical solution. While a general strong disparity is present in velocity evolution, the general tendency remains evident nonetheless; larger correlation windows yield poorer spatial resolution. Similar to the theoretical analysis above, resolution effects are most pronounced upstream of the shock.

In case of ideal flow seeding particles the achievable spatial resolution can be roughly scaled with the interrogation window size. For the current case of the hypersonic sphere, the shock thickness was estimated to be around 6.5mm (B.7). According to Fig. B.4 the shock is smeared over one window size as a result of purely the PIV image analysis. In case of small interrogation areas, the main factor limiting the achievable resolution across the normal shock will thus be the tracer response function.

Regarding the response of the correlation approach to the discontinuity in velocity and density, each of the plotted velocity profiles contains undulations which tend to increase in wavelength and amplitude proportional to the correlation window size. These oscillations are inherent to the applied local velocity predictor filtering. Although not presented, the ringing disappears when adopting the integral predictor (Scarano, 2004). Typically, a local displacement predictor is chosen for nevertheless since it will generally yield higher accuracy.

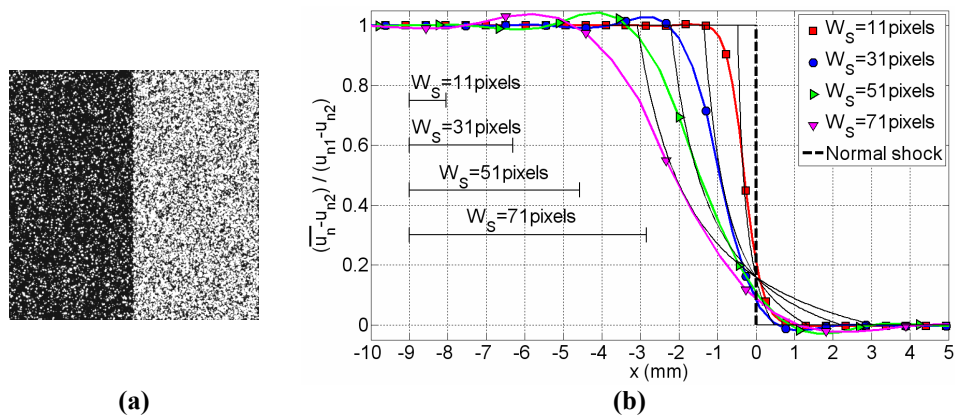


Fig. B.3: (a) Computer generated PIV image simulating a normal shock ($M_\infty=6$) (b) Shock response of the interrogation metrology described in Chapter 2 imposing different window sizes (conversion factor: 1pixel = 86.8 μ m). Solid black lines correspond to Fig. B.2-b.

B.3.3 Model shock response for real tracers

Fig. B.4 integrates particle response and moving averaging (correlation) operator, once again for the case of a Mach 6 flow with an upstream velocity of 1780m/s and particle relaxation length of 2.6mm. For the smaller window sizes i.e. $W_S=11, 31$ pixels, the measured profile covers 6 to 2 window lengths starting from the estimated shock location ($x=0$ mm) respectively before attaining the flow velocity downstream. Velocity gradients are reduced with respect to Fig. B.2-b stemming from a smooth particle path allowing a more accurate representation. About half a window size upstream of the normal shock, measured velocities start to decrease as a result of the averaging effect. Compared to Fig. B.2 the effects of finite spatial resolution are less prominent.

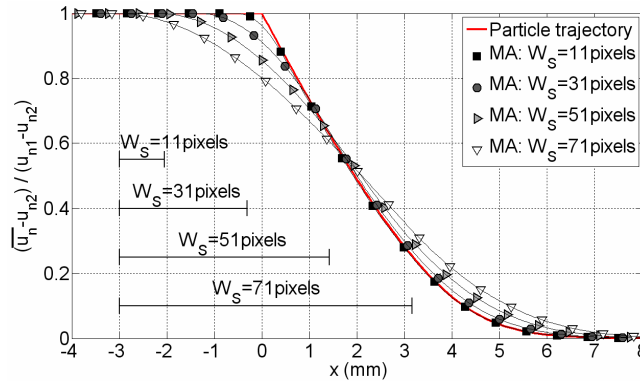


Fig. B.4: (Red line) Simulated particle velocity (2.6mm relaxation distance) in case of a normal shock with 1780m/s upstream velocity (Mach 6) following equation (B.4). Symbols simulate the particle velocity including resolution effects (i.e. moving average filtering).

B.4 Shock position retrieval

The seamless transition between upstream flow and shock response shown in Fig. B.4 caused by averaging inhibits an accurate localization of the original discontinuity. Furthermore, the byzantine Lambert function of (B.4) does not lend itself very well to a functional fitting. Consequently, neither the particle relaxation length ' ξ ' nor time can be explicitly inferred from the obtained velocity profiles without a user-defined shock location.

An iterative procedure is proposed to estimate the shock position and relaxation time automatically based on the knowledge of an exponential decay in normalized velocity with particle travel time. The different steps in the routine are itemized below, starting from the measured spatial evolution in velocity and shock normal velocities up- and downstream;

- a. A point ' x_r ' sufficiently upstream of the shock is randomly picked and will serve as future reference for the estimated particle relaxation length ' x_ξ ' (Fig. B.5).
- b. A first estimate of the shock location is made. If ' x_s ' denotes the shock location with respect to ' x_r ' then the particle will travel a distance ' $x = x_p + x_s$ ' in a time ' $t = t_p + t_s$ ' with ' $t_s = x_s / u_{n1}$ ' (Fig. B.5). Note that ' x_p ' is given by (B.3).
- c. The distance ' x_ξ ' can be readily extracted from the measured velocity profile across the shock according to the e^{-1} criterion. With ' x_s ' estimated with respect to the reference point ' x_r ', the relaxation length ' ξ ' can be calculated as ' $\xi = x_\xi - x_s$ '.
- d. (B.6) converts the relaxation length into a relaxation time ' τ '.
- e. Since ' $x_p = x - x_s$ ' and ' $t_p = t - x_s / u_{n1}$ ', (B.3) can be defined in terms of variables ' x ' and ' t '. Solving (B.3) for ' t ' effectively transforms the measured velocity profile from the spatial domain into the time domain, similar to Fig. B.1-a.
- f. Because the tracer velocity behind the shock location follows an exponential function (B.3), the measured velocity profile, which is now transformed to vary with time, can be fitted with ' $e^{-t/\tau e}$ '.

- g. This results in a new estimate for the particle time response ' τ_e ' and the relaxation distance ' ξ_e ' using (B.6).
- h. The discrepancy ' Δ ' between the estimates relaxation distances ' ξ_e ' and ' $\xi = x_\xi - x_s$ ' is then used to update the shock location estimate ' x_s '. The routine re-iterates from step b until convergence in ' Δ ' is reached.

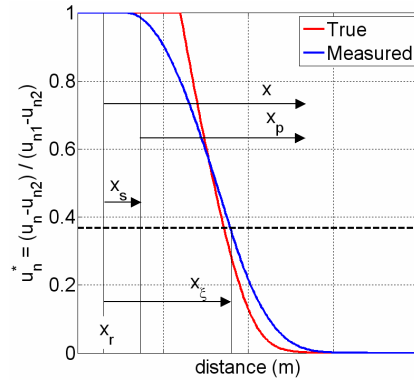


Fig. B.5: Graphical representation of the most important variables in the iterative procedure to estimate shock location and particle relaxation distance from measured data.

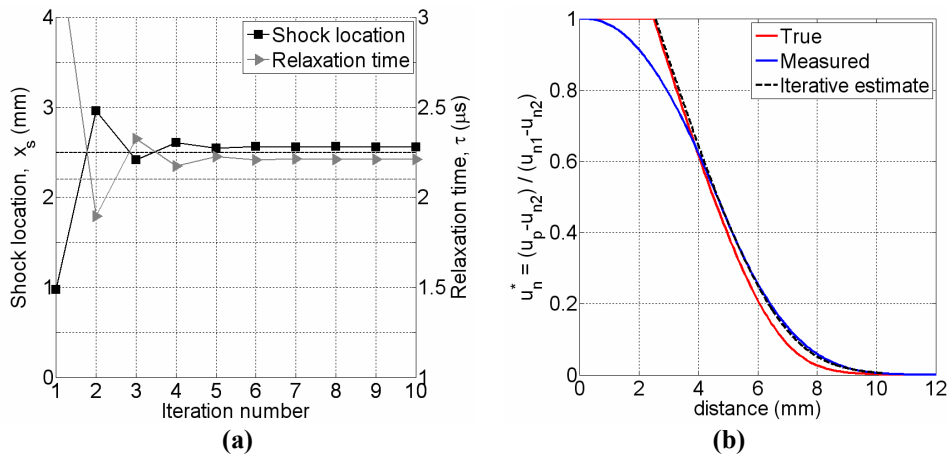


Fig. B.6: (a) Iterative convergence in estimated shock location and relaxation time (b) Obtained exponential fit from the iterative routine.

An assessment is performed on the example encountered in Fig. B.5 for the case of $W_S=51$ (Fig. B.6). The correct shock location is quickly retrieved, whereas slightly more iterations are needed to reach a stable estimate of the relaxation time (Fig. B.6-a). Both show a residual error caused by fitting errors stemming from deviations on the measured profile from the exponential function. As the applied window size reduces by means of e.g. adaptive interrogation, the measurement will veer towards the true value (cf. Fig. B.4) leading to a reduction in the error mentioned afore. The correspondence between final result of the fitting procedure, true profile and measured velocity profile is presented

in Fig. B.6-b. While the shock position matches with the true one, the lower portion of the iterative result is in good agreement with the measured velocity profile.

B.5 Conclusions

Particle inertia and interrogation window size have been effectively identified as limiting factors in the spatial resolution of PIV across a normal shock. Incorrect velocity estimates are returned in the area downstream of a shock due to particle lag. On the other hand, even if the particle responds correctly, interrogation window sizes will impact on the velocity estimates upstream of the shock due to averaging effects. From analytical considerations and Monte-Carlo simulations, the resolution imposed by the interrogation process itself was shown to be proportional to the correlation window size.

Efforts to enhance the spatial resolution in the presence of a shock by decreasing the applied correlation window size are futile when the resolution is limited by the particle response. It is important to emphasize that to come to such a conclusion, the latter demands an evaluation of equation B.7 and its comparison with the physical dimensions of the interrogation area.

APPENDIX C

ROBUST IMAGE EVALUATION FOR SUB-OPTIMAL PIV RECORDINGS

Abstract

The competence of Particle Image Velocimetry as measurement technique has inevitably lead to its advent in large field-of-views such as e.g. the study of natural convection within enclosed rooms where image and recording conditions are encountered which are below optimal for typical PIV analyses. To retrieve valuable and robust velocity information from the collection of image recordings one therefore refers to ensemble correlation. In the following a processing routine is presented incorporating the enhancements reported in Chapter 2 combined with ensemble correlation. The proposed approach's performances are demonstrated through the application to experimental flows and are compared to that of the statistically adaptive routine discussed in Chapter 5.

C.1 Introduction

Since Willert and Gharib (1991) introduced the concept of digital image analysis in PIV, implementation of Fast Fourier Transforms (FFT) in the correlation operations has become widely accepted. Rather than convoluting in the spatial domain, operating in the frequency domain by means of FFT drastically reduces the execution time. FFT-based correlation remains however sensitive to lack in seeding density and poor image quality on the basis of individual snapshots (Keane and Adrian, 1990). Stemming from a low, inhomogeneous image density or high intensity noise level, spurious peaks will appear in the correlation map causing a low measurement reliability and high occurrence of outliers. For quasi-steady flow conditions the underlying flow velocity can still be deduced by means of correlation function averaging. Meinhart *et al.* (2000) introduced the concept of ensemble correlation which consists in averaging the correlation map of the individual snapshots prior to locating the correlation peak. Especially in the estimation of the convection of larger flow structures, ensemble correlation proves to be a useful tool (Fig.

C.1). For these kind of applications small scale turbulent structures are no longer of interest. Instead the displacement of the larger, more energetic, structures is estimated.

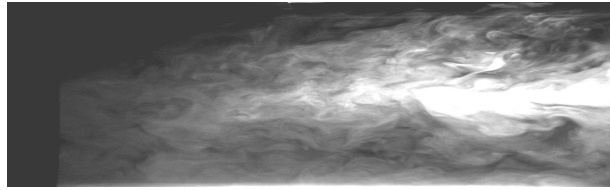


Fig. C.1: Example of typical image for large scale PIV.

In the following an image evaluation routine is presented, incorporating simultaneously the ensemble correlation approach and iterative window deformation with refinement. The combination yields a net improvement in spatial resolution while retaining a high confidence level in obtained results. Following the implementation, the viability of the metrology is demonstrated by the application to three experimental flow fields; uniform smoke flow, Stokes' flow through an annular bent tube and liquid cross-flow in a hypersonic flow.

The image evaluation can be further extended to incorporate a degree of freedom in the selection of correlation window location and sizing as reported in Chapter 5. To assess the performance of statistical adaptivity in case of sub-optimal image recordings a comparison is finally made for the case of an alveolated tube with Reynolds number approaching unity.

C.2 Implementation

The flow chart of the recursive structure is displayed in Fig. C.2. With exception of the correlation step the interrogation sequence is identical[†] to the evaluation of individual snapshots with the WiDIM algorithm (Scarano and Riethmuller, 2000). Simultaneous and gradual reduction in size of the interrogating windows (windows are halved in both directions) yields a finer resolution in space. Compared to one step interrogation methods this adopted approach thus increases the spatial resolution.

When evaluating digital PIV recordings with conventional correlation algorithms, a sufficient number of particle images per interrogation window is required to perform a reliable cross-correlation. The common procedure to enhance the quality of the spatial-average displacement in case of low image density or poor image quality for quasi-steady

[†] Owing to the emanation of correlation DC components by the ensemble operation, the retrieval of sub-pixel accuracy in peak location demands a modification in the definition of signal-to-noise ratio. Keane and Adrian (1990) define it as the ratio between the highest and second highest correlation peak. As the ensemble averaged correlation map is likely to contain a single dominant peak, the definition of the above ratio has been altered to involve the highest peak and the map average.

flow types is to average the spatial correlation of corresponding interrogation domains in successive image pairs. Denoting ‘ $\phi(m,n)$ ’ as the correlation function of a single image pair, the average (or ensemble) correlation function for ‘ N ’ PIV recording pairs is given by Wereley *et al.* (2002^b) as

$$\phi_{\text{ens}}(m, n) = \frac{1}{N} \sum_{k=1}^N \phi_k(m, n) \quad (\text{C.1})$$

This procedure is generally called ensemble correlation and causes the random noise peaks to be significantly reduced through the averaging operation while enhancing the recurring signal peak (Fig. C.2).

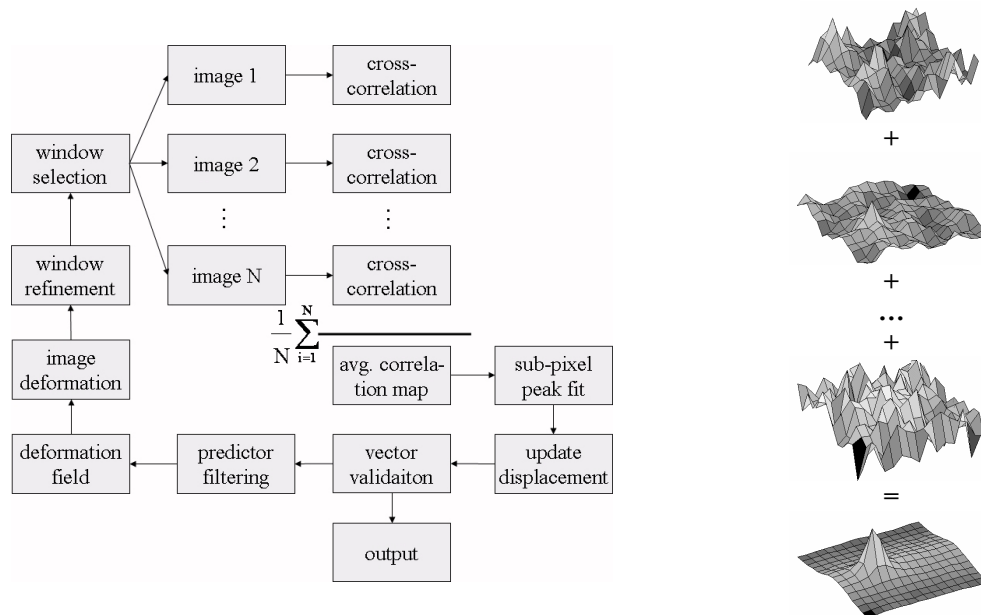


Fig. C.2: (Left) Block diagram of ensemble correlation implemented within a recursive structure. (Right) Through ensemble averaging of the instantaneous correlation maps, the DC displacement component becomes evident.

C.3 Experimental applications

C.3.1 Large scale wind tunnel

Experiments were conducted in a large-scale wind tunnel facility with a test section area of $1 \times 1.3 \text{ m}^2$. Seeding was introduced through a rake emitting smoke rather than individual tracers (see Fig. C.1). The latter implies the use of a light sheet with dimensions in the order of the large smoke structures. A thin laser sheet hampers the

continuous recording of the structures due to out-of-plane motion. Images were recorded by a PCO Pixelfly camera (1392×1024 pixels²) at an optical resolution of almost one to one; 0.965mm per pixel. Because the experimental setup demands multiple specific adjustments compared to a typical PIV setup, a detailed treatise lays beyond the present scope. Information regarding necessary modifications in the experimental setup of a large-scale PIV experiment can be found in Simpson *et al.* (2005) and Riethmuller and Planquart (2006).

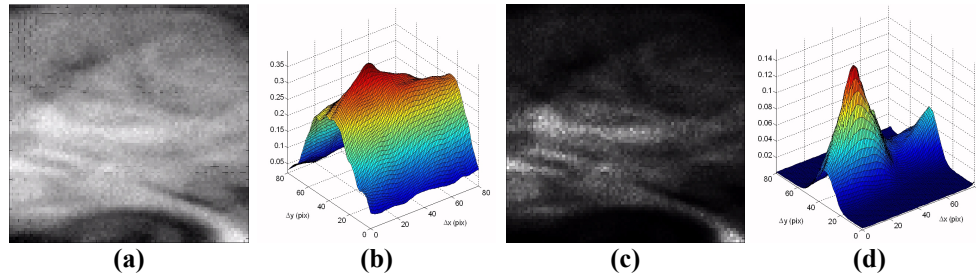


Fig. C.3: (a) interrogation area containing a smoke structure (b) corresponding average correlation function of 200 images (c) intensity distribution after contrast correction (d) corresponding correlation function.

A typical interrogation area partially covering a smoke structure is presented in Fig. C.3-a. Individual tracer images can no longer be identified. Scattered intensities are instead merged into a continuous intensity surface. Correlation maps are consequently absent of distinct peaks (Fig. C.3-b) causing a drop in reliability of the estimated displacements. As the Gaussian fitting functions are generally no longer adequate to retrieve the sub-pixel peak location, the accuracy of the displacement estimates decreases. This attenuation in relative measurement error has been experimentally demonstrated by Baivier (2006). By changing the image contrast (Fig. C.3-c) however smoke patterns of high intensity amplitude can be emphasized and tracked yielding eminently distinct peaks (Fig. C.3-d). The question remains how to choose the severity of the contrast correction. On one hand the strong spatial intensity gradients constitute good features to track (cf. Appendix A), but lead on the other hand to a low information density since only specific regions are interrogated. Up to now a general rule remains absent and the applied image pre-processing steps generally depend strongly on the user and image quality.

An alternative to correlation is optical flow (Quénot *et al.*, 1998) given the continuous intensity distributions. Optical flow has the advantage of yielding higher spatial and temporal resolution with respect to ensemble averaging. For the current purposes however optical flow will not be discussed further within this appendix.

C.3.2 Alveolated bend[†]

This paragraph reports the experimental investigation conducted in a model of the alveolar lung region. The airway generation was modeled by a curved pipe with cylindrical cavities representing the alveolar structures. Silicone was used as carrier fluid with iron particles of $20\mu\text{m}$ in diameter acting as tracers. A continuous Innova 70C Argon laser supplied the coherent light source which was shaped into a thin laser sheet of 1mm at the symmetry plane by an optical assembly. The scattered light intensities were recorded by a 12bit PCO Sensicam camera, with a separation time of around $570\mu\text{s}$. An instantaneous PIV recording is presented in Fig. C.4-a. At a conversion rate of 14.4 pixel per millimeter, the image size of 1056×672 pixels² corresponded with an imaged area of 73×47 mm². For further details see Theunissen *et al.* (2006^a).

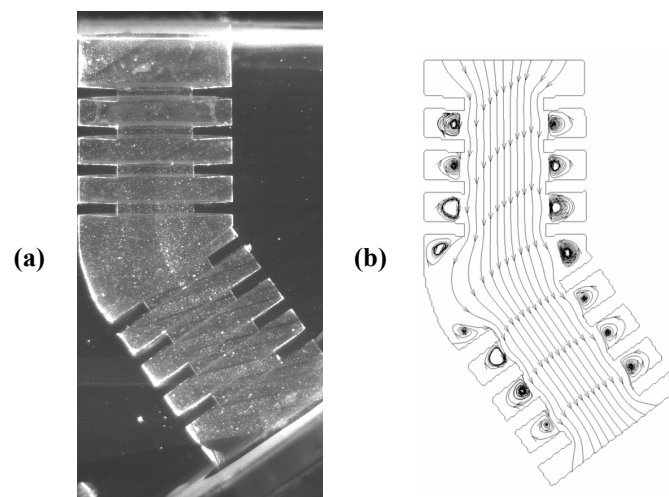


Fig. C.4: (a) Instantaneous PIV recording of the flow in the alveolated tube at $Re=0.069$ (b) streamline pattern.

Initially interrogation windows of 80×80 pixels² are applied and reduced to final windows of 20×20 pixels² (1.4×1.4 mm²) in three iterations. Fig C.4-b depicts the streamline pattern. Tubular vortices are found in the corners of the outer radius of the bend which then merge into a larger vortex when reaching the inner radius. Although the velocity inside the alveoli is about two orders of magnitude smaller compared to the mean lumen velocity, through the advanced interrogation methodology even these slow rotating fluid elements can be properly identified. Compared to CFD calculations (van Ertbruggen *et al.*, 2008) data agreed to within 1% in the central tube and 15% in the alveolar cavities.

[†] This paragraph has been partly published in van Ertbruggen *et al.*, 2008, Journal of Biomechanics

Considering the harsh image conditions this demonstrates the conduciveness of the iterative ensemble correlation technique for data extraction in case of quasi-steady flows.

C.3.3 Liquid ejection in a hypersonic cross-flow[†]

Water is ejected from a flat plate positioned in a hypersonic flow at Mach 6. Halogen lamps provided the necessary background illumination. The negative images are recorded by a Phantom V7.0 digital high speed camera in order to capture the highly unstable process of clump detachment and droplet formation downstream of the injection point. A typical image is shown in Fig. C.5-a and scarcely reminds a typical PIV recording with individual particle images. Inherent to the high speed camera's large pixel size, the image covers a mere 208×128 pixels² and is degraded by camera shot noise (for further details, the reader is referred to Beloki *et al.*, 2008). However, as cross-correlation allows the tracking of features, the shadows cast by the water can be tracked to give an estimate of the flow albeit mean conditions. Final window sizes of 17×17 pixels ($1.37 \times 1.37 \text{mm}^2$) were applied in the analysis with an overlap factor of around 80% yielding a vector spacing of 3 pixels (0.24mm). In total, 500 image couples were considered. Fig. C.5-b shows streamtraces plotted onto the ensemble averaged intensities. Deflection of the jet due to the high pressure distribution on its surface above the injection point is noticeable. Approximately 11 orifice diameters downstream all vertical motion of the liquid jet's large structures is diverted into horizontal direction. This flow case demonstrates the capability of ensemble correlation to provide displacement estimates for dimensional analyses despite high noise levels, poor illumination and untraditional seeding.

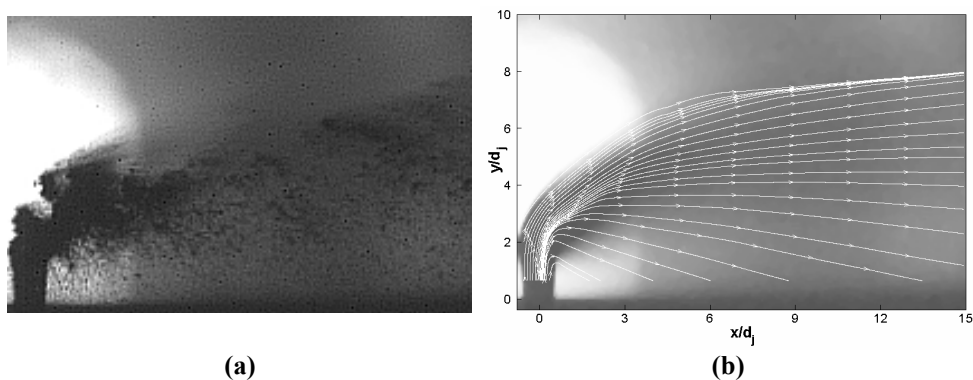


Fig. C.5: Vertical injection of a liquid jet (shadow area) into a hypersonic crossflow (a) sample image recording (b) streamline pattern. The orifice diameter is symbolized by ' d_j '.

[†] This work has been partly published in Beloki *et al.*, 2008, Experiments in Fluids.

C.4 Adaptivity in robust image evaluation: application to an alveolated tube

The interrogation routine depicted in Fig. C.2 applies correlation windows with fixed uniform and large size, which are typically placed on the nodes of a structured grid. In typical PIV recordings where homogeneous seeding and illumination are present, particle images are distinct and image noise is minimal, the above restrictions cause results to be often of poor resolution, as discussed in the previous chapters.

The adjustment of sampling density and window sizes to ensemble data offers an extra improvement in spatial resolution as described in Chapter 5. To evaluate such enhancements in the case of sub-optimal PIV conditions, a comparison between the ensemble multigrid correlation and the statistically adaptive routine is made in this paragraph for the case of an alveolated tube.

It is important to bear in mind that signal adaptivity, as currently implemented, is based on the principle of counting individual particle images. For images such as Fig. C.1 and Fig. C.5 signal quantization will have to be based on a different concept (see e.g. Appendix A). This is however not discussed in further detail in this paragraph.

C.4.1 Background

Lungs intrinsically consist of a complex system of dichotomic branches. Especially the lower alveolar airways where gas exchange between lungs and blood takes place are of special interest in studies involving the effect of environmental hazards to humans such as e.g. air pollution. As a result of the tubular dimensions in the order of micro-meters, in vitro studies are impossible. Numerical calculations are the only option but lack a thorough validation. An initial study at the von Karman Institute within a collaboration of the University of San Diego (California, USA) involved PIV experiments on symmetric alveolated bifurcations simplifying the alveolated airway geometry (Ruwet *et al.*, 2008). A quasi Stokes-flow complied with the alveolar conditions. With Reynolds numbers in the order of unity characterizing the flow, turbulence is out of the picture. Consequently parabolic Poiseuille-like velocity profiles (van Ertbruggen *et al.*, 2007) are transmitted throughout every daughter branch.

The image analysis does not pose serious problems at first sight especially since flow fluctuations are negligible. Besides strong light reflections near the tubular walls, the main problem arises in measuring the slowly rotating fluid motion within the annular structures shown in Fig. C.4. Moreover, these areas contain a low signal density since the Stokes regime hinders entrapment of seeding particles. Here adapted correlation functions must be applied to counteract the inferior image and seeding quality.

C.4.2 Experimental facility

Experiments were conducted in a optically accessible 3D model of acinar lung bifurcations representative of airway lumen in generations 20, 21 and 22 of the human

lung. Tubes of 20mm in diameter were surrounded by three cylindrical cavities of 45mm in diameter representing the alveoli. The current area of interest is schematized in Fig. C.6-a. To permit Reynolds number (based on the main tube diameter) in the order of 0.1, silicon oil served as carrier fluid with neutrally buoyant iron particles of 20 μ m acting as seeding. The light source was provided by a continuous Innova 70C Argon laser, conveniently transformed into a thin laser sheet in the model's mid-(or bifurcation) plane. A digital PCO Pixelfly camera recorded the scattered light intensities during 5 milliseconds at an acquisition rate of 10Hz. The digital images had a typical resolution of 1392 \times 724 pixels² covering a field of view of \sim 37.6 \times 19.8 mm² (conversion: \sim 0.027 mm/pixel). The reader is referred to Ruwet *et al.* (2008) for further details on the experimental campaign.

In Fig. C.6-b image snapshots are subtracted by a background image (cf. section 1.5) and superposed. The deformation of the partitions is clearly visible. A recirculation flow with clear core region is positioned in the centre of each cavity while a curvilinear streamline near the opening implies little convective change with the main tubular flow. Within the annular extremities the rotational motion is characterized by velocities in the order of 10⁻³mm/s. The superposition of images further emphasizes the poor optical access within the annular extremities. In the vicinity of the dividing walls strong light reflections and refractions are present and few tracers can be distinguished.

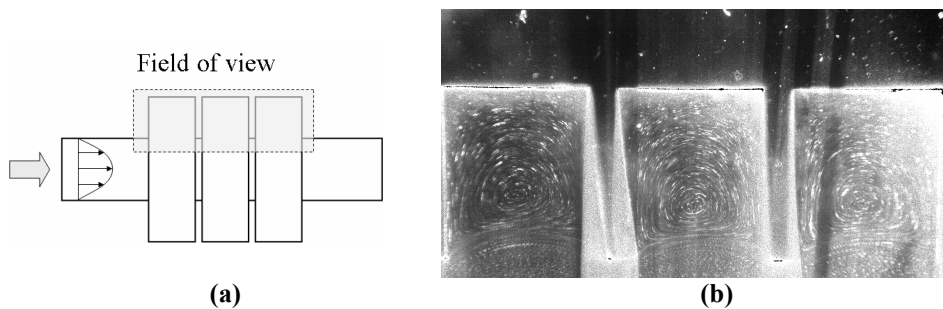


Fig. C.6: (a) Schematic of the investigated field of view (b) Recirculation zones and curvilinear streamlines near the opening become distinguishable when overlaying 50 image snapshots (after contrast enhancement for clarity).

C.4.3 Image evaluation

The combination of displacements which are fractions of the particle image diameters and poor image quality complicates the image analysis by means of straight-forward correlation. Instead, techniques based on ensemble averages will be more conducive as stated by Meinhart *et al.* (2000). For this reason the image set comprising 50 instantaneous recordings was analyzed by the statistical interrogation approach adopting the ensemble correlation routine (cf. Fig. 5.4). With 8000 correlation windows an average window overlap ratio of 71% was achieved. The automatically determined interrogation mesh is presented in Fig. C.7-a. Dense concentrations of correlation windows are imposed in the vicinity of the static walls (wall adaptivity) with fewer samples near the

outer annular perimeters and clustering towards the central tube. The latter is in agreement with the appearance of the strongest velocity gradients (Fig. C.7-b). Core regions of the rotational flow are however always comprised within the regions of dense sampling (compare the location of the rotation centers indicated by the closed streamlines in Fig. C.7-b with the mesh in Fig. C.7-a) and are analyzed with correlation windows reduced in size ranging between 11 pixels ($\approx 0.3\text{mm}$) and 15 pixels ($\approx 0.4\text{mm}$). The central regions of the cylindrical extremities are typically attributed windows in the order of 21 pixels ($\approx 0.57\text{mm}$).

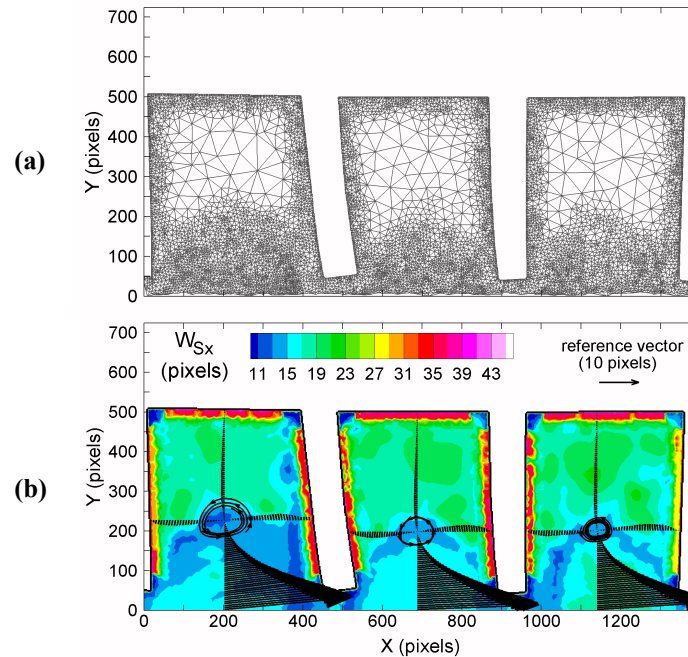


Fig. C.7: Analysis of image recordings of the alveolated tube with the statistical approach; (a) adopted interrogation mesh (b) imposed window sizes (in horizontal direction or parallel to the wall) with extracted velocity profiles across the rotation centers as indicated by the closed streamlines.

The more conventional, interrogation methodology was applied for comparison (cf. Fig. C.2). Robust velocity information within square windows placed on the nodes of a Cartesian grid was retrieved by means of ensemble correlation. Iterative window deformation and refinement was incorporated to yield sufficient spatial resolution. Final window sizes of 17×17 pixels² ($\approx 0.57 \times 0.57$ mm²) were applied in the analysis with an overlap factor of around 80% yielding a vector spacing of 4 pixels ($\approx 0.11\text{mm}$) or around 62000 vectors.

C.4.4 Flow diagnostics

Vertical profiles across the vortex cores of the horizontal velocity component retrieved by the present statistical and more conventional approach are depicted in Fig. C.8-a. All profiles share topological similarities with lid-driven cavity flows (Shankar and Deshpande, 2000). Both adaptive and structured approaches yield results which nearly superpose perfectly which indicates the adaptive sampling rate to be sufficient even in the more sparsely sampled regions (Fig. C.7-a).

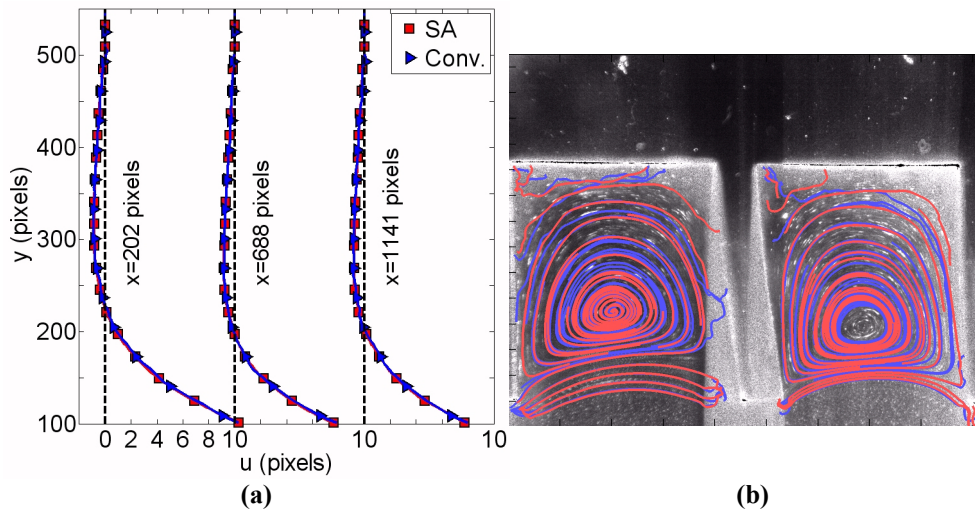


Fig. C.8: (a) Vertical profiles across the vortex cores (Fig. C.7-a) of the horizontal velocity component predicted by Statistical Adaptivity (referred as “SA”) adopting ensemble correlation (cf. Fig. 5.5) (—) and more “conventional” ensemble correlation (—) (b) Superposition of streamlines for the first two annular rings (see a) for color coding).

Streamline patterns in the first annular cavities are compared in Fig. C.8-b. As a result of extremely low seeding density and image quality reliable velocity estimates are lacking in the vicinity of the walls and produce erroneous streamlines. Under such severe conditions wall adaptivity does not pose an outcome as illustrated. Nevertheless, the streamline pattern returned by ‘SA’ in wall-vicinity overall shows a higher degree of smoothness and physical relevancy. In the vortex core’s environs on the other hand both interrogation methodologies are overall in close agreement; streamlines are smooth and follow the particle image traces (with exception of the spirals which are numerical artifacts related to the plotting of streamlines).

Although the results of the adaptive routine are only marginally improved compared to those of the structured approach, the achieved reduction in correlation windows by a factor 8 and the autonomous selection of interrogation parameters without a loss in accuracy or spatial resolution can be considered as an important improvement.

C.5 Conclusions

To retrieve robust velocity information from a succession of poor quality images, an analysis metrology based on ensemble correlation has been proposed. To obtain sufficient spatial resolution, iterative window deformation and refinement have been incorporated. The evaluation routine has been applied to several experimental images degraded by low image density and quality and has proven to be efficient in the eduction of the average convective motion in quasi-steady flows or at least an estimate of macroscopic flow scales.

Implementation of adaptivity in sampling density and correlation window sizing lead to marginal improvements in resolution and accuracy whereas the autonomous selection of interrogation parameters and force reduction in number of interrogation windows can be considered as important advances.

Still, continuous intensity distributions produce smooth correlation maps which decrease the estimation accuracy and require a-priori image enhancement. Further efforts may concentrate on automatic adaptive image pre-processing routines and/or the application of optical flow.

APPENDIX D

NON-ISOTROPIC WEIGHTING FUNCTIONS IN TOMOGRAPHIC PIV

Abstract

Tomography PIV has appeared very recently in the scenario of 3D measurement techniques. The metrology's widespread acknowledgement in industrial environments remains currently hampered though by its severe hardware requirements as well as computational cost. Moreover, the involved image processing is still in its infancy which explains the interrogation routines' current lack in spatial resolution. Nevertheless, Tomo-PIV may rely on and benefit from achievements in planar PIV. In the following a possible criterion for interrogation volume non-isotropy is proposed based on vorticity. The effectiveness of the reported approach to enhance measurement accuracy and spatial resolution is demonstrated by its application to the synthetic flow field induced by a vortex ring.

Nomenclature

$\varepsilon_{u,v,w}$	relative measurement error in u-, v- and w- velocity component with respect to the true values (voxels)
σ	vortex radius (voxels)
ω	true, imposed vorticity (voxels/voxels)
ω_m	measured vorticity (voxels/voxels)
ω_{peak}	true, imposed peak vorticity (voxels/voxels)
R	vortex ring radius (voxels)
(u, v, w)	velocity along the axis of the (x,y,z) coordinate system (voxels)
u_θ	angular velocity (voxels)
W_S	cube interrogation volume window size (voxels)
$W_{S_{\xi,\eta,\zeta}}$	correlation window size along major and minor axes (voxels)

D.1 Introduction

The main limiting factor for the planar approach consists in the fact that the motion across the plane cannot be represented as accurately as the motion within the plane. Insights on the instantaneous 3D structure of turbulent flows are lacking as the involved motion can only be partly captured by the current planar PIV techniques. Moreover because of the finite extent of the light sheet thickness, particle out-of-plane motion yields an unrecoverable loss in correlation signal, limiting the dynamic range of the measurement.

In order to overcome the current limitations a breakthrough in the direction of full 3D measurement capabilities is needed. Tomography PIV has appeared very recently in the scenario of 3D measurement techniques (Elsinga *et al.*, 2006). Rather than a sheet, a fluid volume is now illuminated. Scattered particle intensities are recorded simultaneously from several viewing directions using multiple CCD cameras. The 3D particle distribution is then reconstructed as a 3D light-intensity distribution from the obtained projections through an intricate reconstruction algorithm. The interrogation procedure to extract the displacement estimates is based on the traditional correlation operator extended to three dimensions. Since it has been applied to several aerodynamic problems, the present state-of-the-art for tomographic PIV reveals major bottlenecks on the side of hardware requirements as well as in computational cost. Moreover, the spatial resolution is quite limited owing to the finite extent of the interrogation volumes, but can be increased and controlled through the use of weighting functions (Astarita, 2006) during the calculation of the 3D correlation coefficient. Scarano (2003) introduced the concept of non-isotropic intensity weighting functions in planar PIV related to flow curvature to increase both accuracy and spatial resolution. However, each velocity component required a repetition of the interrogation routine, which in case of Tomo-PIV would infer a tripling of the computational effort.

The idea proposed in this appendix adopts the philosophy of intensity weighting but bases the involved coefficients on a single parameter, vorticity, to limit the required computational time while enhancing spatial resolution. The effectiveness of the approach is demonstrated by the application to a synthetic ring vortex.

D.2 Non-isotropic weighting

The proposed weighting is based solely on vorticity and originates from the consideration of the Oseen-Lamb vortex extended to three dimensions (Fig. D.1-a). The use of a single parameter to describe the weighting function for each velocity component rather than evaluating for each component individually offers a strong computational benefit. While the vorticity vector in turbulent flows may spatially vary in both magnitude and direction, locally these variations are considered small, resembling the situation illustrated in Fig. D.1-a (with exception of the axis extents). Accordingly, gradients and curvature in velocity in the direction of the vorticity vector ($\vec{\omega}$) can be

considered to be locally zero and are restricted to perpendicular planes. This already favors a weighting function with major axis aligned with the vorticity vector (Fig. D.1-b).

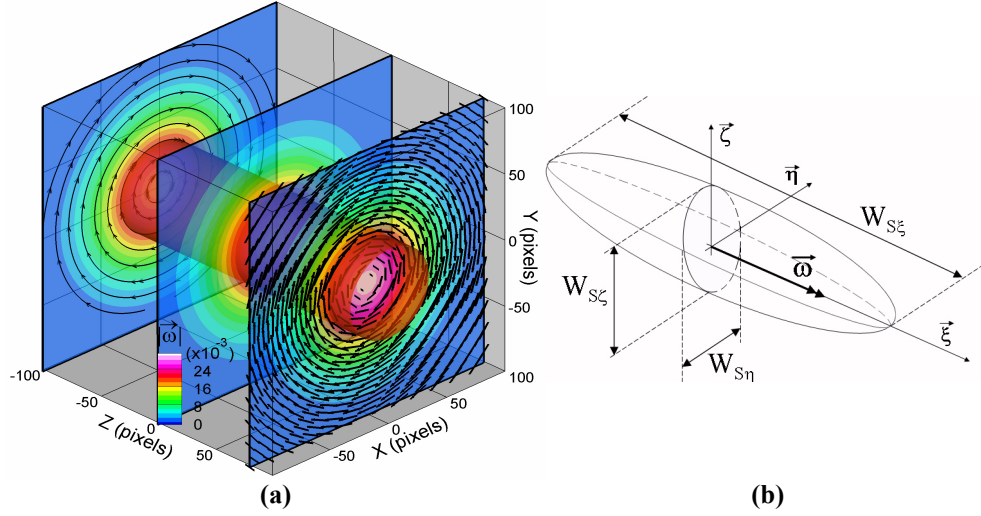


Fig. D.1: (a) Oseen-Lamb vortex model extended to 3D. The vorticity vector ' $\vec{\omega}$ ' is aligned with the Z-axis (b) Definition of axes and window sizes. The major axis of the windowing function is aligned with the vorticity vector.

With the assumption of rigid body rotation around the vorticity vector, the spatial extents of the correlation windows must be minimal within the planes perpendicular to the vorticity vector to improve both measurement accuracy and spatial resolution. While further window non-uniformity can be imposed for the remaining window extensions, this has currently been left out of consideration adopting the following aspect ratio between the interrogation window dimensions

$$\frac{W_{S\xi}}{W_{S\eta}} = \frac{W_{S\xi}}{W_{S\zeta}} = 1 + 3 \frac{|\vec{\omega}|}{|\vec{\omega}_{\text{peak}}|} \quad \text{and} \quad W_{S\xi} \cdot W_{S\eta} \cdot W_{S\zeta} = W_S^3 \quad (\text{D.1})$$

where the ξ -coordinate is aligned with the vorticity vector and ' W_S ' is the cube window size.

The non-isotropic window shapes are imposed by means of elliptical Gaussian weighting functions applied to the square interrogation windows. Identical to the proposal of Scarano (2003) the Gaussian variances are prescribed by twice the window sizes determined in (D.1).

D.3 Performance assessment

D.3.1 Synthetic flow field generation

The performance of the proposed weighting is illustrated through the application to a ring vortex. While analytically more sound formulas exist for the ring vortex induced velocity field (e.g. Yoon and Heister, 2004), they are mostly based on the Biot-Savart law for infinitely thin vortex rings and consequently prescribe unphysical (infinite) velocities on the ring itself. For this reason in the following the flow field has been generated adopting the Oseen-Lamb vortex model (D.2) centered on the perimeter of a ring of radius $R=50$ pixels (see Fig. D.2)

$$\mathbf{u}_\theta = \frac{\omega_{\text{peak}}}{2} \frac{\sigma^2}{r} \left(1 - e^{-\frac{r^2}{\sigma^2}} \right) \quad (\text{D.2})$$

The vortex radius ' σ ' has been set to 50 pixels and a peak vorticity ' ω_{peak} ' of 32×10^{-3} voxels/voxels has been adopted.

The ring's axis of symmetry has been aligned with the Z-axis. At any location 'p' the velocity is assumed to be induced only by those points on the ring's circumference lying within the plane determined by the point in question and the Z-axis (Fig. D.2-a). For the schematic cartooned in Fig. D.2-a the corresponding locations are indicated by '1' and '2'. To make the ring stationary, velocities in Z-direction are subtracted by the ring's self-induced velocity (equation (D.2) with $r=2 \cdot R$). A three dimensional representation of the imposed flow field complete with streamtraces and vorticity magnitude contours is given in Fig. D.2-b.

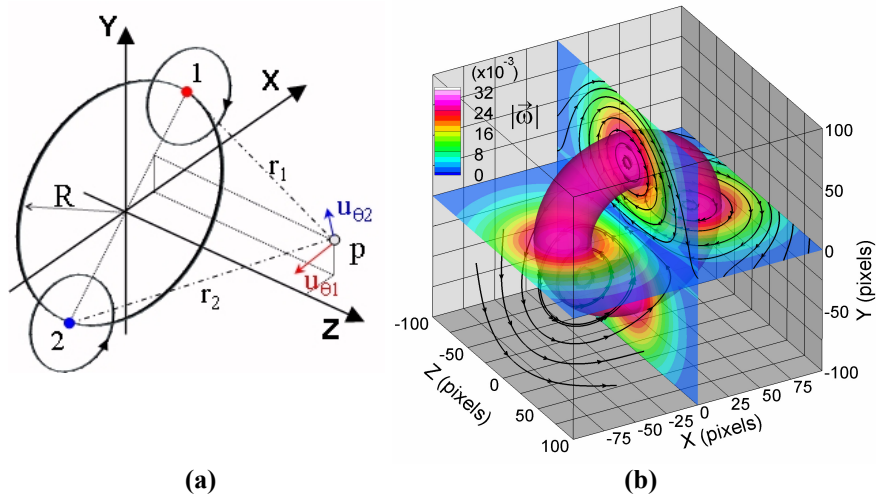


Fig. D.2: (a) Schematic of the synthetic vortex ring (b) Simulated flow field with vorticity contours and vorticity iso-surface ($|\vec{\omega}|=28 \times 10^{-3}$).

D.3.2 Results

To simulate the image interrogation process, the correlation operator has been modeled as a moving average filter. Velocities are calculated every 4 pixels corresponding to the vector spacing obtained by correlation volumes of $17 \times 17 \times 17$ voxels³ with an overlap ratio of 75%.

The adopted elliptical Gaussian windowing functions are illustrated in Fig. D.3. Near the outer regions, where the vorticity attains low magnitudes, the weighting functions are spherical shaped. Towards the ring vorticity increases and the shapes become elliptical with the axis of maximum eccentricity tangent to the ring's perimeter.

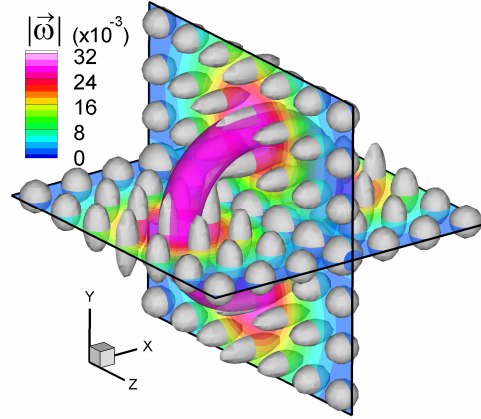


Fig. D.3: Elliptical shaped weighting functions prescribed by (D.1) with vorticity contours and iso-surface.

The advantages of non-isotropic correlation volumes become qualitatively visible by observing the obtained flow fields (Fig. D.4). Straightforward, the moving average operation yields a consistent sub-estimation of the vorticity. The effects are most prominent near the vortex cores. Besides slight alterations in streamtraces, a distorted (squared) vortex ring shape is obtained (Fig. D.4-a). Applying a weighted averaging on the other hand allows a flow measurement returning results in better agreement with the imposed values (Fig. D.4-b).

A quantitative comparison between the two approaches is presented in Fig. D.5. Histograms of the relative error, with respect to the imposed values, in the most relevant flow statistics are extracted and proclaim the improvement in accuracy. Whereas the standard filter produced relative displacement errors up to 30% to 40%, weighting reduces the errors to orders of 0%-10%.

The improved spatial resolution is further proclaimed by the shift in normalized vorticity error from 5% to 0% with an accompanying force reduction in distribution width (Fig. D.5-d).

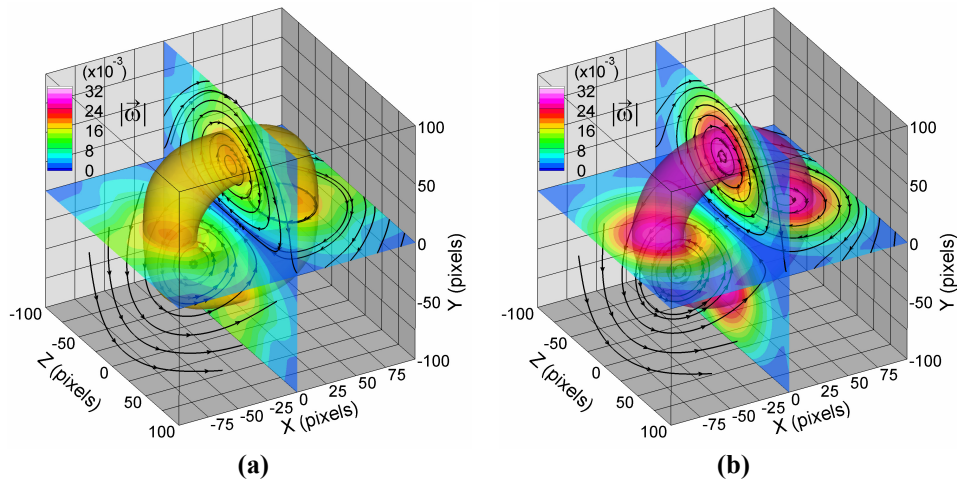


Fig. D.4: Measured vortex ring flow fields vorticity contours and iso-surface with interrogation volumes of 17^3 voxels³ (a) moving average (b) weighted moving average.

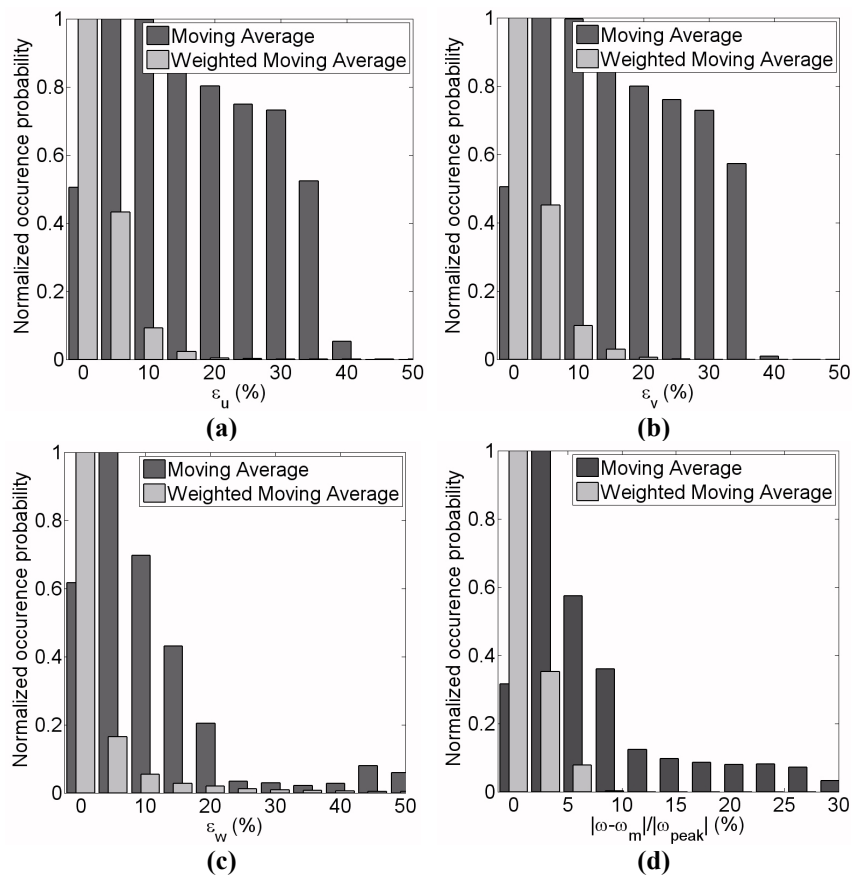


Fig. D.5: Relative errors in displacements along (a) X-axis (b) Y-axis (c) Z-axis (d) Normalized error in vorticity.

D.4 Conclusions and prospects

This appendix reports on an idea to enhance the spatial resolution in tomographic PIV while limiting the additional computational efforts. The proposed approach applies weighting functions with alignment and aspect ratios predicted by vorticity. Test on the artificial flow field of a vortex ring attested the improvement in accuracy (relative errors decreased from ~30% to ~10%) and spatial resolution (error in vorticity decreased from ~5% to ~2%)

Currently only eccentricity between major and minor axis of interrogation volume non-isotropy have been considered. Further non-uniformity in correlation volume extensions perpendicular to the vorticity vector may be incorporated. Possible criteria may be either gradients in velocity (Di Florio *et al.*, 2002) or in vorticity. Compared to the former, vorticity derivatives offer the advantage of taking indirectly flow curvature into consideration which, as mentioned many a times, is strongly related to spatial resolution.

NEDERLANDSTALIGE

SAMENVATTING

ADAPTIEVE BEELDANALYSE VOOR PIV - TOEPASSING OP SAMENDRUKBARE STROMINGEN EN GRENSVLAKKEN -

Als experimenteel hulpmiddel heeft PIV snel traditionele punt gewijze meetmethoden vervangen. De inherente beeldverwerking is gestandaardiseerd geworden hoewel de prestaties sterk afhankelijk zijn van gebruikerservaring. Voorts worden de vaak met moeite geselecteerde parameters voor de beeldverwerking uniform toegepast over gehele momentopnamen maar voldoen zij zelden aan de waargenomen convectie van de vloeistof, de ruimtelijke verdeling van lengteschalen of de distributie in signaal. In plaats daarvan is een zekere mate van aanpassing in de beeldanalyse vereist om het snelheidsgebied dat aan de beeldopnamen ten grondslag ligt zo nauwkeurig mogelijk te schatten en bij voorkeur in een geautomatiseerde structuur.

Er bestaat een verscheidenheid in correlatiemethodologieën elk bevorderlijk in slechts specifieke gevallen. Hier is het doel nu een globale oplossing te bekomen welke door aanpassing van de beeldverwerkingsparameters (venstergrootte, plaatsing en overlapping), grotendeels adequaat blijft. Deze verhandeling stelt voor om in de richting van iteratieve procedures te gaan waar automatische aanpassing plaatsvindt, gebaseerd op stromings en signaal condities. De plaatsing van de correlatievensters, hun aantal en grootte wordt bepaald door rekening te houden met de hoeveelheid aanwezig signaal en schommelingen in het snelheidsveld. Hoge beeld dichtheden en/of regio's met sterke snelheids gradiënten leiden tot een groepering van kleine vensters in de beeldanalyse. De kwantificatie van het signaal is gebaseerd op detectie van individuele deeltjes in de beeldopnames terwijl ruimtelijke variatie in de snelheid dienst doet als indicator voor aanpassing aan de stroming. De implementatie van de voorgestelde techniek vereist gespecialiseerde interpolatieschemas en ruimtelijke projectie van de vensterlocaties om op die manier rekening te houden met hun niet-Cartesiaanse verdeling.

Één van de belangrijkste praktische problemen welk is aangepakt, is dat van de gebruiker die geconfronteerd wordt met een noodzakelijk compromis tussen ruimtelijke

resolutie en robuustheid. De nieuwe beeldverwerkingsmethode omzeilt de evenwichtige wisselwerking en plaatst meer kleinere vensters daar waar de stroom het vereist en het signaal het toelaat. Vice versa worden minder van deze onnodige kleine vensters geplaatst in gebieden waar de strooming het niet nodig heeft (d.w.z. ontbreken van gradiënten of schommelingen in de snelheid). Op die wijze vindt een loskoppeling plaats van mechanismes die de robuustheid van de correlatie kunnen beïnvloeden. De prestaties van de adaptieve benadering werden beoordeeld door middel van computer gegenereerde beelden van isotrope turbulentie en experimentele opnames van een turbulente interactie tussen schokgolf en grenslaag (Mach 2.1). Aangetoond werd dat verbeteringen minder uitgesproken zijn in geval van optimale opnames en optische resolutie, hoewel de beperking in de gebruikersinteractie een netto verbetering met zich meebracht. Desondanks werden de verbeteringen in ruimtelijke resolutie benadrukt door toepassing op wervelstromingen achter een transportvliegtuig en een cirkelvormige cylinder ($Re_h \approx 200$) waar de korte afstand tussen de vectoren en kleine dimensies van de vensters garant staat voor een nauwkeurige schatting van de vorticeiteit.

Het tweede probleem stelt zich in de nabijheid van grensvlakken waar grote verstoringen aanwezig zijn in de correlatiefuncties als gevolg van bruuske signaalbeïndiging langs de muren en lichtreflecties. Hoewel adequate beeldbehandeling voorafgaand aan de correlatie en vector herpositionering een verbetering tot stand brengen in de ruimtelijke resolutie en robuustheid, is bewezen dat de starheid van de correlatievensters in de conventionele correlatiemethoden een nefaste invloed hebben. Een innovatieve behandeling van grensvlakken is voorgesteld waarin adaptiviteit is opgenomen op een geautomatiseerde manier door het geleidelijk verhogen van het aantal vensters in de nabijheid van de muur, het draaien van de correlatievensters: parallel aan het grensvlak en het verminderen van de grootte loodrecht op de wand. Bij toepassing op originele en getransformeerde beelden van een subsonische grenslaag over een vlakke plaat ($Re_\theta \approx 1900$) werden consistente verbeteringen in de resolutie en robuustheid vastgesteld. Nog overtuigender was de nieuwe mogelijkheid om de recirculatie te meten in de hoek van een dubbele compressie glooiing in een hypersonische stroming (Mach 7), terwijl deze eerder onoplosbaar was met een conventionele benadering.

De ondervragingsmethodologie waarbij de parameters worden aangepast aan momentane condities bleek tot dusver overtuigende resultaten op te leveren vooral in aanwezigheid van snelheidsgradiënten. Desondanks kunnen noch multi-grid technieken noch de adaptieve routine robuuste schattingen maken van het snelheidsveld indien er sprake is van sterke schommelingen in de snelheidsverdeling van het stromingsveld of een niet-optimale verdeling van signaal. Een variant van de adaptieve ondervragingstechniek is voorgesteld waarbij venstergrootte, vorm, richting en ruimtelijke verdeling worden verfijnd aan de hand van het gemiddelde stromingsveld en beeldeigenschappen. Het gebruik van zulke gemiddelden laat een betrouwbare toepassing toe van niet-isotrope resolutie in tegenstelling tot momentane aanpasbaarheid waar zulke resolutie niet haalbaar is. Deze benadering laat bovendien toe het aantal correlatievensters te beperken zonder de nodige ruimtelijke meetresolutie in het gedrang te brengen. Toepassing op de grenslaag-schokgolf interactie toonde aan dat de methode correct die zones selecteert waar het meeste aantal meetpunten moet worden geplaatst. Een experiment met

verschillende opname resoluties in het kielzog achter een transsoon (Mach 0.6) vleugelprofiel bevestigde dat de ruimtelijke resolutie in regio's met schuifstromen beduidend verbeterd kan worden door de statistisch adaptieve techniek. Het gemeten impulsafname kwam goed overeen met de referentie data uit de opnamen met hoge resolutie.

De verbeterde prestaties van alle adaptieve ondervragingsmethodologieën in vergelijking met conventionele technieken werden uitvoerig besproken en aangetoond met behulp van verdere toepassingen. De uitgebreide serie beeldopnamen bestond uit een supersonische straalstroom (Mach 3.75), een hypersonale bal (Mach 6) en een achterwaartse stap ($Re_h \approx 5000$).

Het concept van statistische robuustheid is verder uitgebreid door het voorstel een bekende statistische techniek toe te passen in PIV voor het afleiden van gemiddelde gegevens. Het principe en de toepasbaarheid werden aangetoond met conventionele PIV metingen van een achterwaarts gekeerde stap ($Re_h \approx 5000$) en de stroming in een divergerend kanaal met voldoende resolutie in tijd ($Re = 6300$).

CURRICULUM VITAE

Raf Theunissen was born the 1st of November 1978 in Genk (Belgium). In 1996 he graduated from the Sint-Jan Berchmanscollege in Genk as *head of class* in the Mathematics-Science program. Having finished his secondary school Raf went to study Aerospace Engineering at the University of Technology in Delft (The Netherlands). His compulsory internship was completed at the von Karman Institute in Brussels (Belgium). Supervised by Prof. van Beeck, Raf applied PIV to two-phase flashing jets. In 2003 Raf finished his master's thesis entitled "Improvements in Hybrid PIV/PTV algorithms and droplet sizing" at the same institute under the guidance of Prof. Riethmuller and Prof. Scarano. This work earned him his Master's degree in 2003 which he received with the notion *cum laude*. In the same year he started the Diploma Course with a project "Experimental investigation of aerosol deposition in lung airways" at the von Karman Institute under the supervision of Prof. Riethmuller. The following year Raf finished his DC course *with honours* and received the *award for best public presentation*. The four year PhD program was initiated in 2004. All work was performed at the von Karman Institute in collaboration with TU-Delft and Vrije Universiteit Brussel (IWT SBO project) under the close supervision of Prof. Scarano and Prof. Riethmuller. The findings of his work are reported within this thesis. During his PhD Raf participated in international conferences and published articles in renowned international journals. Along with his work, Raf supervised students and gave courses on Particle Image Velocimetry. On several occasions he acted on behalf of Prof. Riethmuller for the von Karman Institute at international contract meetings, representing the von Karman Institute.

As of February 2009 Raf Theunissen is employed as a gasturbine performance engineer in Alstom Switzerland (Ltd.) located in Baden.

Awards

1. Award for best public presentation – von Karman Institute for Fluid Dynamics. Diploma Course 2003-2004
2. The 2007 *Measurement Science and Technology* Outstanding Paper Award for the paper "An adaptive sampling and windowing interrogation method in PIV"

List of Publications

Journals (First Author)

1. Theunissen R, Scarano F and Riethmuller M L, 2008, Spatially adaptive PIV interrogation based on data ensemble, *Experiments in Fluids*, DOI 10.1007/s00348-009-0782-7
2. Theunissen R, Scarano F and Riethmuller M L, 2008, On improvement of PIV interrogation near stationary interfaces, *Experiments in Fluids*, 45, 557-572
3. Theunissen R, Di Sante A, Riethmuller M L and Van den Braembussche R, 2007, Confidence estimation using dependent circular bootstrapping: application to the statistical analysis of PIV measurements, *Experiments in Fluids*, 44, 591-596
4. Theunissen R, Scarano F and Riethmuller M L, 2007, An adaptive sampling and windowing interrogation method in PIV, *Measurement Science and Technology*, 18, 275-287

Journals (Co-Author)

1. Ma B, Ruwet V, Corieri P, Theunissen R, Riethmuller M L and Darquenne C, 2009, CFD Simulation and Experimental Validation of Fluid Flow and Particle Transport in a Model of Alveolated Airways, *Journal of Aerosol Science*, 40, 403-414
2. Perurena B J, Asma C O, Theunissen R, Chazot O, 2009, Experimental investigation of liquid jet injection into Mach 6 hypersonic crossflow, *Experiments in Fluids*, 46, 403-417
3. Di Sante A, Theunissen R, Van den Braembussche R, 2007, A new facility for time-resolved PIV measurements in rotating channels, *Experiments in Fluids*, 44, 179-188
4. van Ertbruggen C, Corieri P, Theunissen R, Riethmuller M L and Darquenne C, 2008, Validation of CFD predictions of flow in 3D alveolated bend with experimental data, *Journal of Biomechanics*, 41, 399-405

Contribution to books

Theunissen R and Riethmuller M L, 2008, Particle Image Velocimetry in lung bifurcation models, *In: Particle image velocimetry – new developments and recent applications*, ed.: Schröder A and Willert C E, Springer

Contribution to conferences and workshops (First Author)

1. Theunissen R, 2009, Adaptive-interrogation algorithms, *von Karman Institute for Fluid Dynamics Lecture Series; Recent advances in Particle Image Velocimetry*, Brussels, Belgium, 26-30 January

2. Theunissen R, 2009, Treatment of fluid-solid interfaces, *von Karman Institute for Fluid Dynamics Lecture Series; Recent advances in Particle Image Velocimetry*, Brussels, Belgium, 26-30 January
3. Theunissen R, Scarano F and Riethmuller M L, 2008, Statistical adaptivity in PIV interrogation, *14th International symposium on applications of laser techniques to fluid mechanics*, Lisbon, Portugal, 7-10 July
4. Theunissen R, Scarano F and Riethmuller M L, 2008, Improvement of PIV interrogation near stationary interfaces, *EWA International workshop on advanced measurement techniques in aerodynamics*, Delft, The Netherlands, 31 March – 1 April
5. Theunissen R, Scarano F and Riethmuller M L, 2007, Improvement of cross-correlation robustness and resolution near stationary interfaces, *7th International symposium on particle image velocimetry*, Rome, Italy, 11-14 September
6. Theunissen R, Schrijer F F J, Scarano F and Riethmuller M L, 2006, Application de la PIV adaptative dans un écoulement hypersonique, *10^{ième} Congrès francophone de vélocimétrie laser*, Toulouse, France, 19-22 September
7. Theunissen R, Corieri P, Riethmuller M L, van Ertbruggen C and Darquenne C, 2006, Trajectoires d'aérosols dans un tube courbe alvéolé : mesure de vitesse par PIV et suivi des aérosols par PTV, *10^{ième} Congrès francophone de vélocimétrie laser*, Toulouse, France, 19-22 September
8. Theunissen R, Schrijer F F J, Scarano F and Riethmuller M L, 2006, Application of adaptive PIV interrogation in a hypersonic flow, *13th International symposium on applications of laser techniques to fluid mechanics*, Lisbon, Portugal, 26-29 June
9. Theunissen R, Buchmann N, Corieri P, Riethmuller M L and Darquenne C, 2006, Experimental investigation of aerosol deposition in alveolar lung airways, *13th International symposium on applications of laser techniques to fluid mechanics*, Lisbon, Portugal, 26-29 June
10. Theunissen R and van Beeck J P A J, 2006, Particle sizing under PIV conditions: from single diffraction peaks to glare-spots, *PIVNET 2 Workshop on the latest application and development of particle sizing techniques in conjunction with PIV*, C.I.R.A. Icing Wind Tunnel, Capua, Italy, 10-11 April
11. Theunissen R, Scarano F and Riethmuller M L, 2005, An adaptive windowing and sampling PIV interrogation method, *6th International symposium on particle image velocimetry*, Pasadena, California, USA, 21-23 September
12. Theunissen R, Scarano F, Riethmuller M L and Jerónimo A, 2005, Application of an adaptive windowing and sampling PIV interrogation method to a supersonic jet flow, *PIVNET II International workshop on the application of PIV in compressible flows*, Delft, The Netherlands, 6-8 June
13. Theunissen R, Stitou A and Riethmuller M L, 2005, Increasing accuracy in super-resolution PIV, *AVT-124 Specialists meeting on recent developments in non-intrusive measurement technology for military application on model- and full-scale vehicles*, Budapest, Hungary, 25-29 April

14. Theunissen R, Corieri P and Riethmuller M L, 2004, Aerosol deposition in a physical model of human pulmonary airways, *EUROMECH Colloquium N°456–Experimental and computational biofluid mechanics*, Aachen, Germany, 4-5 October
15. Theunissen R, Stitou A and Riethmuller M L, 2004, Approche nouvelle pour l'amélioration de l'incertitude de mesure en PTV, *9^{ème} Congrès francophone de vélocimétrie laser*, Bruxelles, Belgique, 14-17 September
16. Theunissen R, Corieri P and Riethmuller M L, 2004, Application de la technique PTV à la modélisation d'écoulements d'aérosols dans voies aériennes pulmonaires, *9^{ème} Congrès francophone de vélocimétrie laser*, Bruxelles, Belgique, 14-17 September
17. Theunissen R, Stitou A and Riethmuller M L, 2004, A novel approach to improve the accuracy of PTV methods, *12th International symposium on applications of laser techniques to fluid mechanics*, Lisbon, Portugal, 12-15 July

Contribution to conferences and workshops (Co-Author)

1. Ruwet V, Corieri P, Theunissen R, Ma B, Darquenne C and Riethmuller M L, 2008, Flow of aerosol in a 3D alveolated bifurcations: experimental measurements by Particle Image Velocimetry (PIV) and Particle Tracking Velocimetry (PTV), *14th International symposium on applications of laser techniques to fluid mechanics*, Lisbon, Portugal, 7-10 July
2. Stitou A, Theunissen R and Riethmuller M L, 2003, Advances in hybrid PIV-PTV techniques and application to vortical flows, *EUROPIV2 Workshop on PIV*, Zaragoza Spain, 31 March – 1 April
3. Stitou A, Theunissen R and Riethmuller M L, 2003, Application of hybrid PIV-PTV algorithm to vortical flows, *5th International symposium on particle image velocimetry*, Pusan, South-Korea, 22-24 September
4. Yildiz D, Theunissen R, van Beeck J P A J and Riethmuller M L, 2002, Understanding of dynamics of a two-phase flashing jet using multi-intensity-layer PIV and PDA, *11th International symposium on application of laser techniques to fluid mechanics*, Lisbon, Portugal, 8-11 July